FORSCHUNGSZENTRUM ROSSENDORF
Mitglied der Wissenschaftsgemeinschaft Gottfried Wilhelm Leibniz

WISSENSCHAFTLICH-TECHNISCHE BERICHTE
FZR-380
Juni 2003
ISSN 1437-322X

Institute of Safety Research

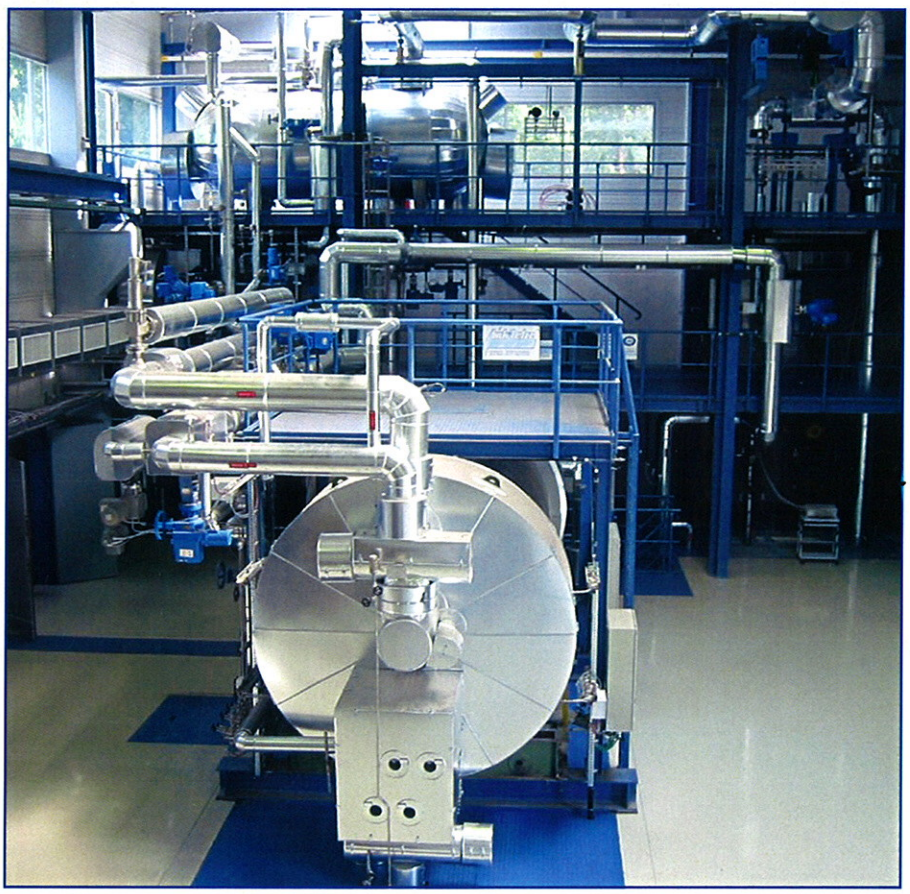

Annual Report 2002

FORSCHUNGSZENTRUM ROSSENDORF
Mitglied der Wissenschaftsgemeinschaft Gottfried Wilhelm Leibniz

WISSENSCHAFTLICH-TECHNISCHE BERICHTE

FZR-380

Juni 2003

Annual Report 2002

Institute of Safety Research

Editors:

Prof. Frank-Peter Weiß

Priv.-Doz. Dr. Udo Rindelhardt

CONTENTS

Preface

The Institute of Safety Research (ISR) is one of the five scientific institutes of Forschungszentrum Rossendorf e.V.. The Forschungszentrum Rossendorf is a member of the scientific association named after Gottfried Wilhelm Leibniz. As such it is basically funded by the Federal Ministry of Education and Research and by the Saxon Ministry of Science and Arts with 50% each.

The work of the institute is directed to the assessment and enhancement of the safety of technical plants and to the increase of the effectiveness and environmental sustainability of those facilities. Subjects of investigations are equally nuclear plants and installations of process industries. To achieve the goals mentioned, the institute is mainly engaged in two scientific fields, i.e. thermal fluid dynamics including magneto - hydrodynamics (MHD) and materials/components safety.

Together with the Dresden Technical University and with the Zittau University of Applied Sciences the ISR represents the East German Center of Competence in Nuclear Technology being a member of the national nuclear competence network (Kompetenzverbund Kerntechnik). As such the ISR also takes care for the conservation and promotion of expertise in nuclear engineering.

At the end of 2002, the institute can look back again at the acquisition of many research grants and scientific contracts with the industry. 34% (2,57 Mio Euro) of the total budget came from such external funding sources with 26% from research grants of the Federal Government, the Free State of Saxony and the European Union. 5% of the funding originated from Deutsche Forschungsgemeinschaft (DFG) and 3% from contracts with the industry (see also the attached graphs). The absolute level of external funding is the same as in previous years.

In the reporting period, the ISR performed 9 meetings and workshops with international participation. It is especially worth mentioning the NEA OECD workshop on "Numeric simulation of accident scenarios in BWRs", the 5th MHD-days devoted to “Geo-and astrophysical MHD”, and the 5th workshop “Development and application of two-phase flow measuring techniques”.

The completion of the construction of our new thermal hydraulic two-phase flow test facility TOPFLOW is the main scientific and technological success of the institute in 2002. Measurements were started at TOPFLOW on transient air-water flows in vertical tubes with a diameter of up to 200mm. With the greatest diameters investigated, strongly deformed large size bubbles were detected by the novel wire mesh instrumentation. Those bubbles freely move over the pipes cross section. This type of flow was measured for the first time with such a high resolution in space and time. TOPFLOW is to strengthen the national and international position of the ISR in the field of two phase flow modeling. The work is substantially supported by a 4 years project granted by the reactor safety fund of BMWA (Bundesministerium für Wirtschaft und Arbeit).

The investigation of dynamic thermal hydraulic flow maps resulted in a set of experimentally validated equations that describe the forces which act on bubbles in a vertical flow depending on bubble size and radial location. The experimental results are available now also for the

development of CFD[1] codes. The work was performed in the framework of a project that was funded by BMWA, too.

The development of the On-line-Monitoring-System MoSys was completed. MoSys was transferred to the industrial partner DEGUSSA. The system enables an effective and safe controlling of complex chemical processes at industrial conditions, which could be proven during two production campaigns.

The post irradiation investigations of the irradiation program “Rheinsberg” were finished. The change of strength and toughness properties of the different RPV materials caused by neutron irradiation were measured under hot cell conditions. Structural analyses were additionally performed of all material heats. Clear correlations were found between the embrittlement and the volume fraction of the irradiation induced microstructural defects. It was for the first time, that such correlations could be presented for VVER steels.

The application range of Ultrasonic Doppler-Velocimetry (UDV) for the measurement of velocity fields in opaque liquids could successfully be extended to high temperature metal melts. For that special acoustic wave guides were developed and tested in the MHD department. The measurements were performed in different metal melts with temperatures up to 750 °C.

The ISR is proud of the fact that its members E. Altstadt and H.-G. Willschütz received the research award 2002 of Forschungszentrum Rossendorf for their work on modeling the RPV behavior during severe core melt accidents. The developed models consider both, the thermal fluid dynamics of the melt pool in the lower RPV calotte and the thermo-mechanics of the RPV. By applying a new algorithm creeping could be described uniformly in the whole range of relevant temperatures and stresses. The model was successfully applied for the interpretation of model experiments performed at the Royal Institute of Technology Stockholm. The validated model was used to assess the efficiency of additional mechanical measures like a creep stool that takes the weight of the RPV and the internal melt pool when the creep deformation of the RPV exceeds a certain level. It could further be shown that external pit flooding extends the time till RPV failure significantly and so allows for additional accident management measures.

[1] Computational Fluid Dynamics

Distribution of funding sources 2002

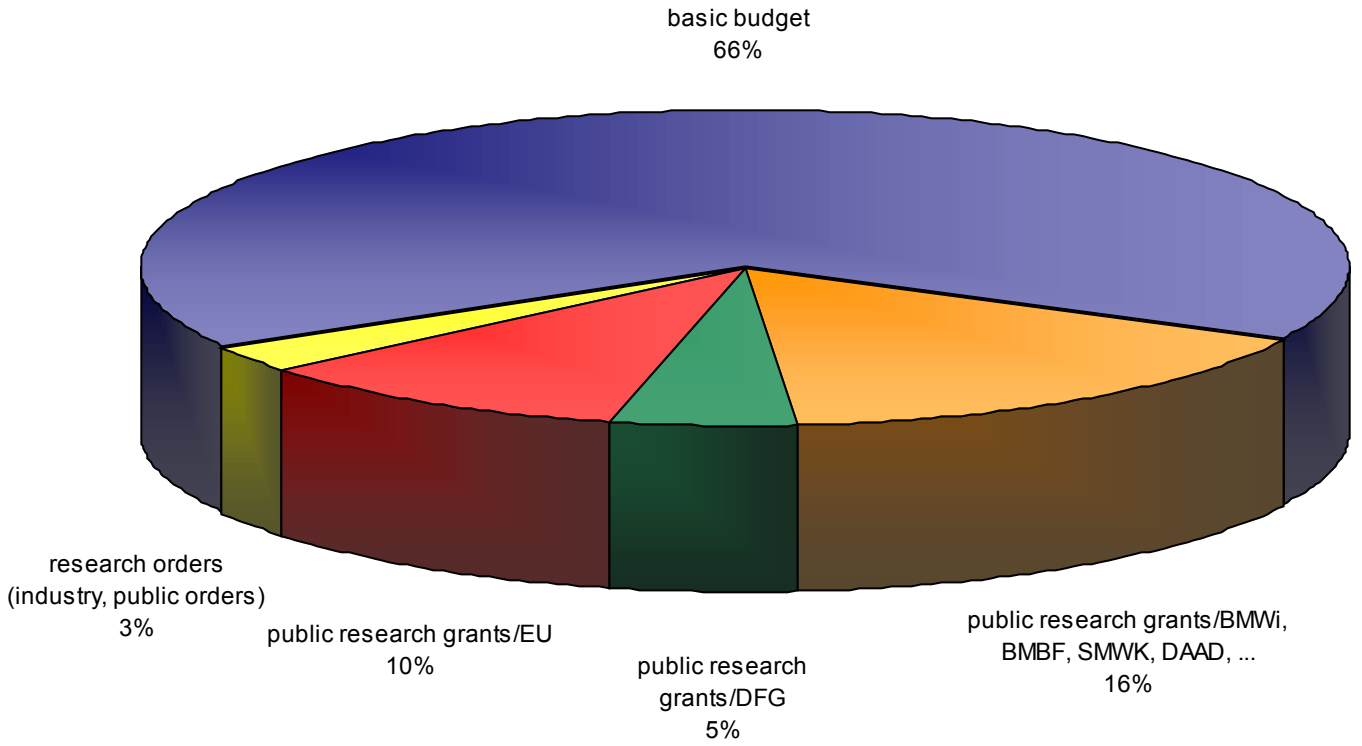

Deployment of funding on the tasks/projects 2002

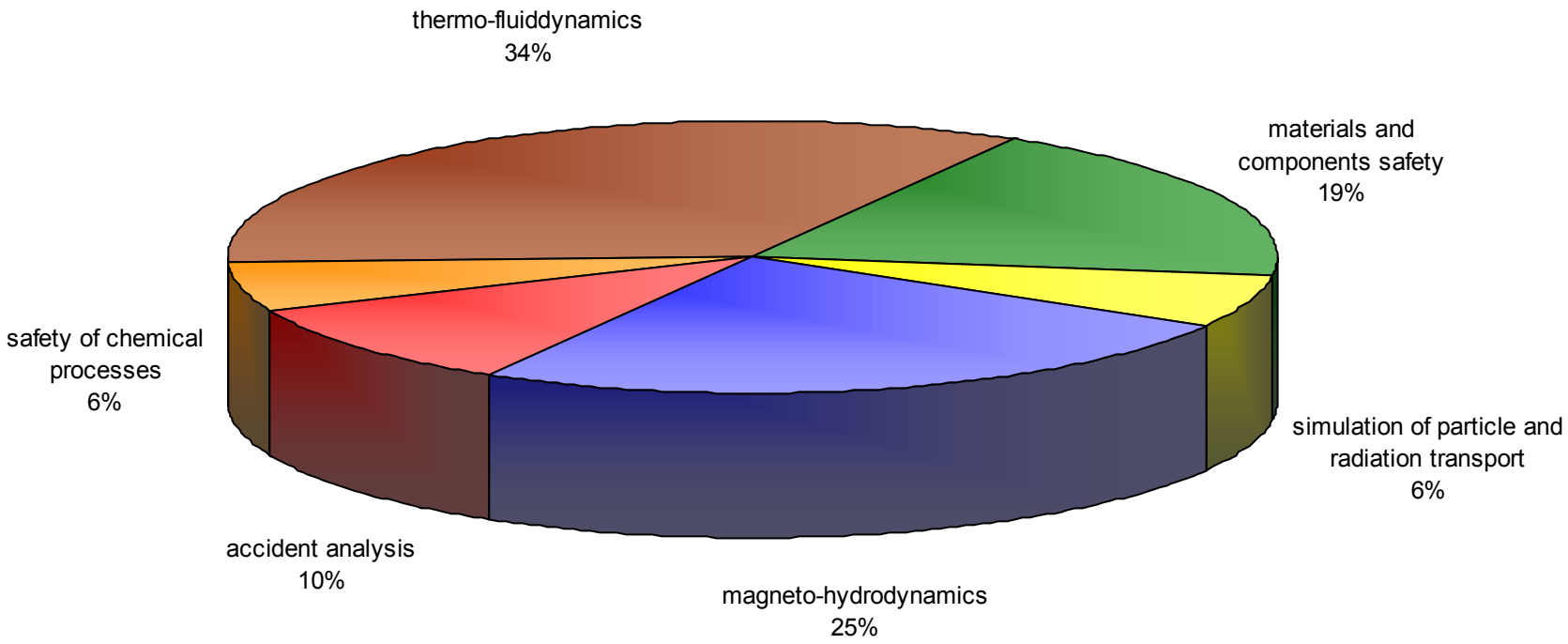

Selected reports

TOPFLOW TESTS ON THE STRUCTURE OF THE GAS-LIQUID INTERFACE IN A LARGE VERTICAL PIPE

Horst-Michael Prasser, Matthias Beyer, Arnd Boettger, Helmar Carl, Dirk Lucas, Andreas Schaffrath, Peter Schuetz, Frank-Peter Weiss, and Jochen Zschau

1. Introduction

TOPFLOW is an acronym deduced from Transient TwO Phase FLOW Test Facility [1, 2]. It is designed for generic and applied studies of transient two phase flow phenomena in power and process industries. The fluid is either steam-water or air-water mixture. TOPFLOW stands in the tradition of single-effect tests in large-scale models of safety relevant components of nuclear plants. The new test facility in Rossendorf was constructed using parts of NOKO, a test facility, which was successfully operated at the Forschungszentrum Jülich [3]. NOKO was dismantled in 2001, the electrical heater and the condenser tank were transferred to the new site in Rossendorf and completed by a number of new components. In the end of 2002 the facility was commissioned and reached its working parameters of 7 MPa and the corresponding saturation temperature of 286 °C.

After this, first tests were carried out that aimed at studying the structure of a gas-liquid two-phase flow in pipes of large diameter. For this purpose, an air-water flow in the large vertical test section of TOPFLOW was studied using a wire-mesh sensor [4, 5]. Its high spatial and temporal resolution allow to obtain time sequences of instantaneous gas fraction distributions over the entire cross section that reflect the shape and extension of the gas-liquid interface in great detail. The data is used for the visualisation of the two-phase flow structure as well as to obtain void fraction profiles and bubble size distributions [6, 7]. Additionally to earlier described methods, a new visualisation technique is presented, that consists in the creation of virtual side projections of the flow. Using these three evaluation methods, new insights are brought into the structure of two-phase flow in large pipes. The comparison with earlier tests in a 51.2 mm pipe revealed scaling effects.

2. Test section DN 200

The test pipe has an inner diameter is 194.1 mm and a total height of 9 m. Close to the lower end a gas injector is located (Fig. 1). A tube is bend into the main flow direction, forming a coaxial segment which has a perforated head to inject the air. The perforation consists of three rings, each with 20 orifices of 6 mm diameter (Fig. 2). Above the perforated region the injector head has a conical part in order to reduce the formation of vortices due to flow separation effects.

The new wire-mesh sensor (Fig. 3) comprises a matrix of 64x64 measuring points that are scanned at 2500 Hz. The large number of electrode wires allows to achieve a resolution of 3 mm in the entire cross section. The sensor is mounted into a flange connection 1000 mm below the upper end of the test section. The distance between gas injection and the measuring plane of the wire-mesh sensor was z_{wms} = 7660 mm.

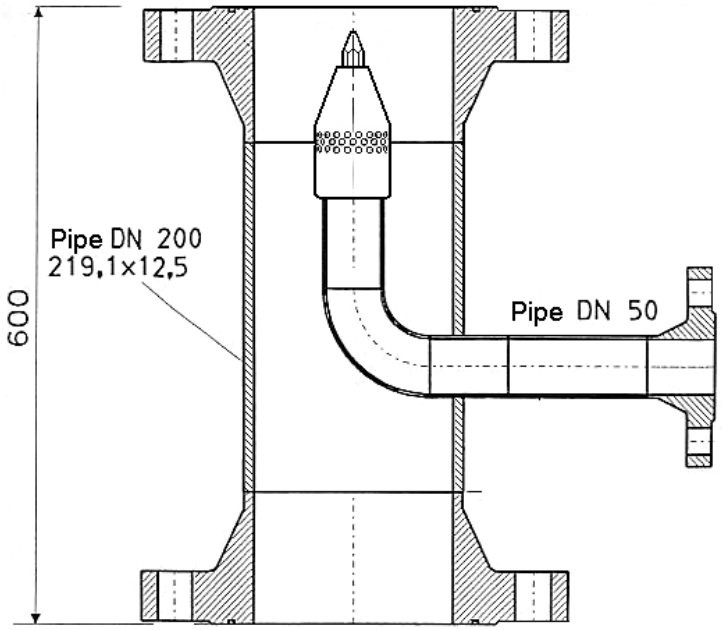

Fig. 1: Gas injection device in the DN200 test pipe

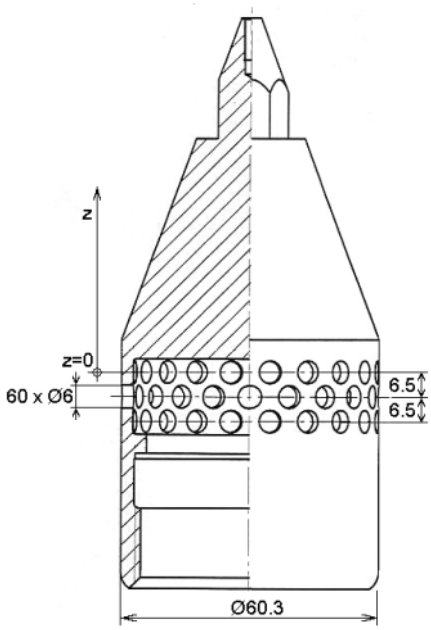

Fig. 2: Gas injection head

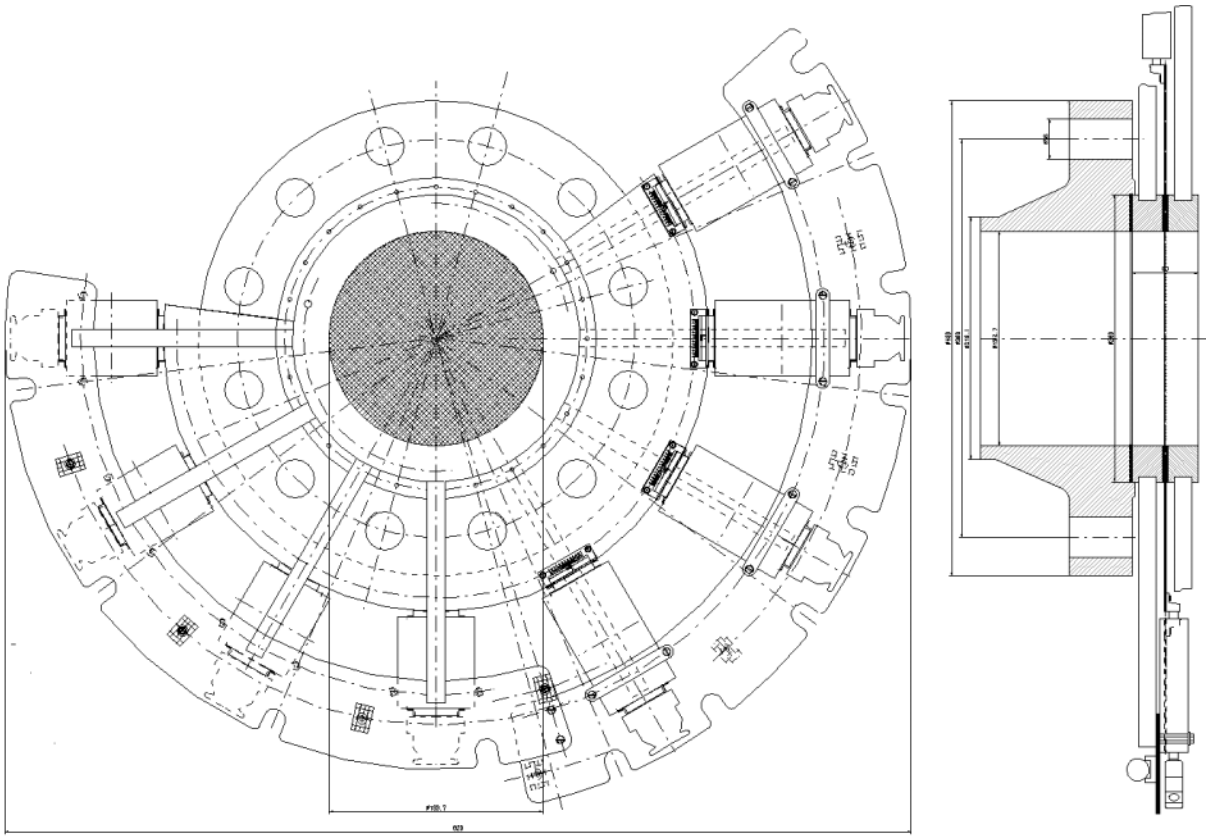

Fig. 3: Wire-mesh sensor for the DN200 test pipe with a measuring matrix of 64x64 points

3. Methods of wire-mesh sensor data visualisation

Conductivity distributions measured by the wire-mesh sensor are transformed into sequences of instantaneous two-dimensional gas fraction distributions by relating the conductivity of the gas-liquid mixture to the conductivity of plain liquid. After this operation (a tomographic image reconstruction is not necessary) the gas fraction distribution can be used for visualisation purposes.

The construction of virtual sectional views is a powerful method [7]: distributions over the pipe diameter are plotted as horizontal bars and a time sequence of such bars is arranged in a vertical order starting from the top of the image. In the result, the plot obtains the character of a sectional view onto the flow structure at a vertical plane situated in the centre of the pipe. The vertical axis is transformed into a virtual z-axis by scaling it according to the velocity of the gaseous phase. If the lateral axis is kept in the same scale as this virtual z-axis, bubbles are displayed without distortion, i.e. with the right length-to-width relation. Since individual bubble velocities are not available, the average phase velocity calculated from the known superficial gas velocity divided by the measured average gas fraction is used as an approximation. This leads to a certain distortion, since the velocity differs from bubble to bubble and shows a characteristic profile with a maximum in the centre of the pipe. The scaling according to the average velocity is nevertheless a helpful procedure to obtain an approximate visualization of the real shape of the bubbles. It is a big advantage of the virtual z-axis, that sectional plots obtained at different air flow rates can be directly compared.

Since virtual sectional views do not show bubbles moving in front or behind the chosen sectional plane, it is useful to complement this method by virtual side projections [5]. They represent the entire information from the measuring cross-section, which is transformed into a virtual side view using a simplified ray-tracing algorithm. To perform this kind of imaging, it is assumed that parallel white light propagates through a three-dimensional column containing the measured gas fraction distribution. The light arriving from aside is partially absorbed and partially scattered towards the observer in front of the column. A simulated image seen by the observer is calculated under the assumption of different absorption and scattering coefficients for each colour component of the light, i.e. a set of individual coefficients for red, green and blue is defined empirically to obtain high contrast between the phases and a plastic impression. Length and width of the image are again scaled considering the average gas velocity. As a result, a life-like image of the flow pattern is created, which is close to the view through a transparent pipe wall.

4. Results

As a result of scaling studies, Ohnuki [8] reported, that the slug flow found in small pipes does not occur in larger pipes (diameters 200 mm and 480 mm). The authors compared their results with those of Leung [9] performed at D = 25.4 mm and Liu et al. [10] at D = 38 mm as well as with the flow maps of Serizawa and Kataoka [11]. Visual observations revealed that in the large pipes an immediate transition from bubbly to churn turbulent flow was found instead of a slug flow. Typical Taylor bubbles that occupy almost the entire cross section occur only in small pipelines. It was assumed that the boundary condition at the pipe walls stabilise the Taylor bubbles in the small pipes.

The plots obtained with the method of virtual side projections confirm the visual observations of Ohnuki [8] (Fig. 4). Large bubbles appear in the flow, the size of which grows rapidly with increasing superficial gas velocity. In the same time, the flow takes a more and more irregular structure, bubble density becomes very inhomogeneous. At high gas flows, the flow pattern becomes churn turbulent, i.e. regular structures disappear completely. Finally, large bubbles are hardly visible anymore since the view is obstructed by the irregular swarms of small bubbles. This gives reason to the conclusion that a transition to churn turbulent flow has taken place.

Virtual sectional side views allow a look into the mid-plane of the pipe without the increasing obstruction of the view by bubbles close to the pipe wall. Such plots reveal that large bubbles are still present, their size and number increases with growing air flow rate (Fig. 5).

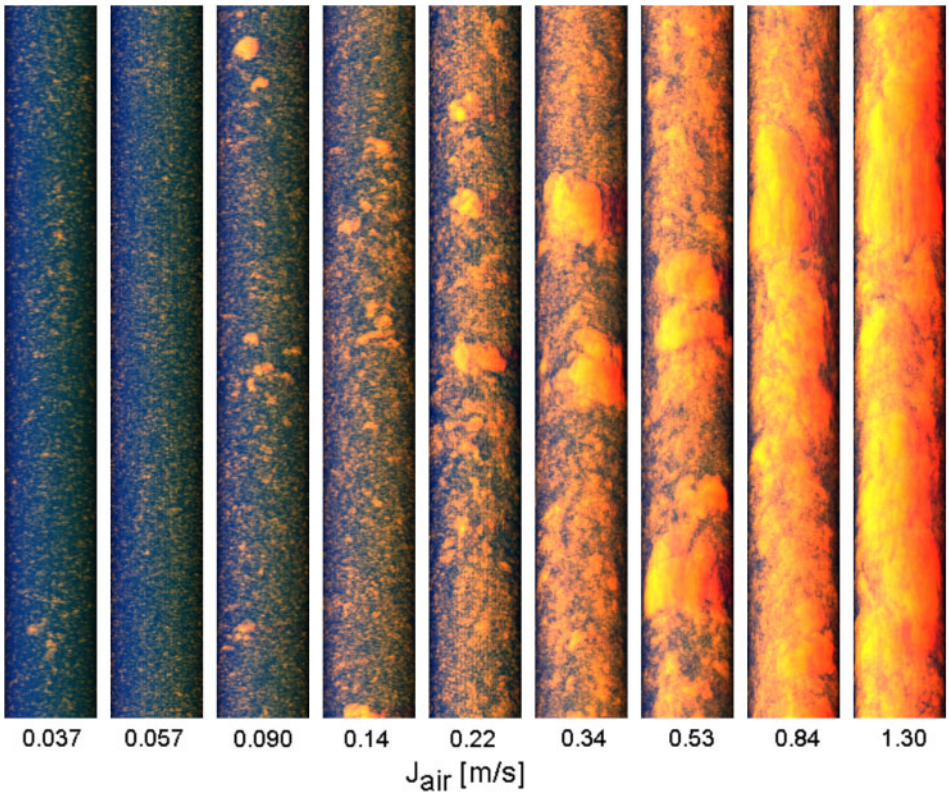

Fig. 4: Virtual side projections of the gas distribution in the DN200 test section, J_{water} = 1 m/s, ratio of vertical to horizontal scale = 1:1, height scaled according to average gas velocity, gas - red to yellow, liquid - blue

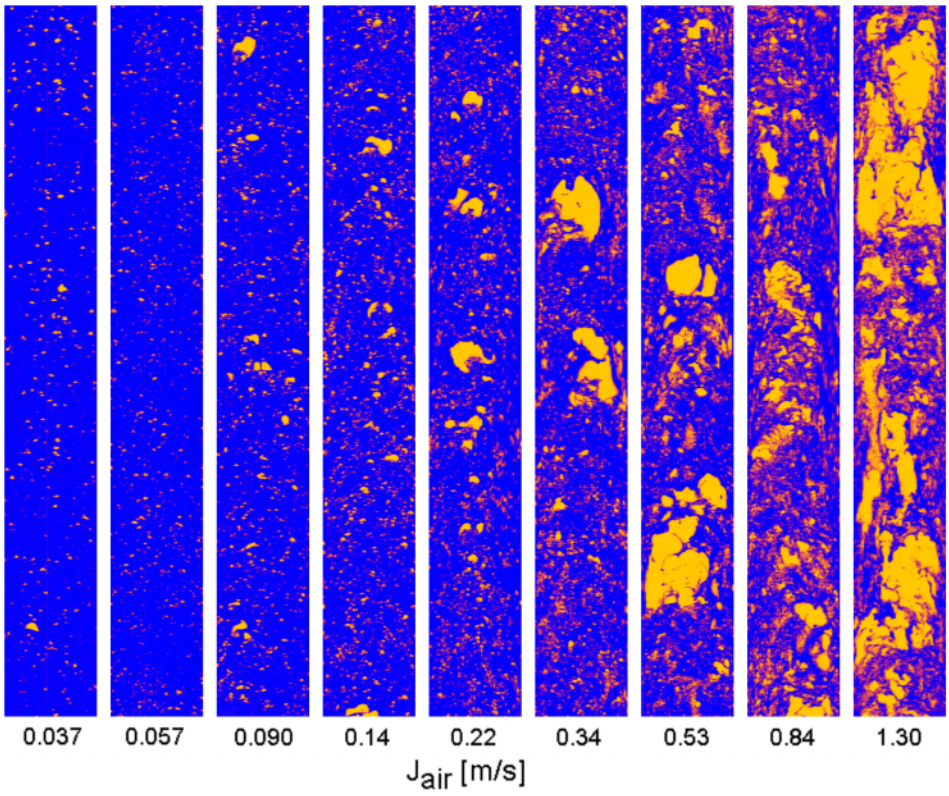

Fig. 5: Virtual sectional views of the void distribution in the DN200 test section, J_{water} = 1 m/s, scaling see Fig. 4, yellow - gas, blue - liquid

Bubble size distributions show the appearance of a bimodal distribution at a superficial gas velocity of about 0.14 m/s. They confirm the observations in Fig. 5, since a further increase of the gas flow leads to a continuous growth of the large-bubble peak in the distribution. The appearing second peak is shifted towards higher diameters, it becomes wider and the amplitude increases.

A direct comparison between bubble size distributions obtained in the two different pipes revealed that the second peak appears at lower superficial gas velocities in the pipe DN50. At a superficial gas velocity that corresponds to the slug flow region in the DN50 pipe the large bubble fraction shows equivalent diameters which are greater than the pipe diameter (see [12]), i.e. the peak is caused by large elongated Taylor bubbles. In the DN200 pipe a bimodal bubble size distribution was found, too (Fig. 6). The bubbles of the large fraction are much larger than in the small pipe, while their contribution to the overall gas fraction (peak height) is smaller. On the other hand, the peaks are much broader.

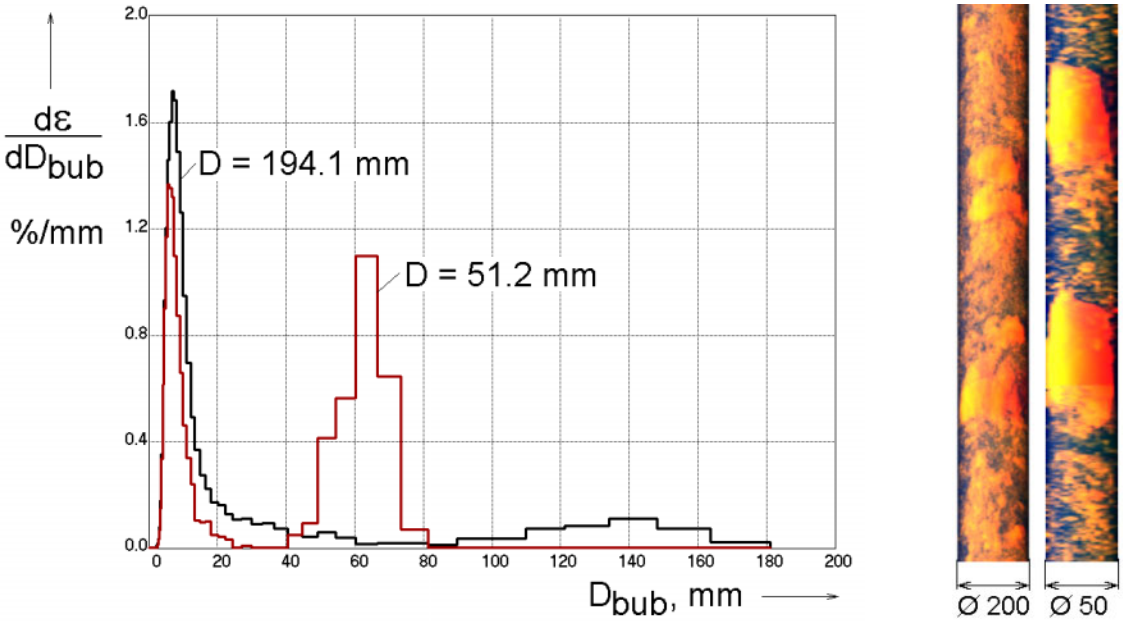

Fig. 6: Comparison of bubble size distributions in DN50 and DN200 test sections for an air flow rate typical for slug flow in pipes of small diameter, superficial velocities: $J_{air} = 0.53$ m/s, $J_{water} = 1$ m/s

In the large pipe, big bubbles can move much more freely, which leads to a higher probability of collisions between them than in the small pipe, where the separating liquid slug has to be drained off, before two Taylor bubbles can coalesce. This hypothesis would explain the observed larger bubble sizes in the bigger pipe.

Additionally to the calculation of bubble size distributions, the bubble identification procedure [6] can be applied to extract individual bubbles from the data array and display them individually. For this purpose the local instantaneous gas fractions in all elements not belonging to the selected bubble are put to zero. When the resulting new distribution is displayed by one of the mentioned visualization techniques, the selected bubble becomes visible without all the other surrounding bubbles, which otherwise may have obstructed the view. In turn it is also possible to eliminate a selected bubble and the display only the surrounding bubbles. For this, the gas fractions of elements labelled by the number of the given bubble have to be set to zero.

This method was applied to extract several large bubbles found in the wire-mesh data at high superficial gas velocities. In Fig. 7 virtual side projections constructed in this way are shown. In the left column, the original data is displayed, the column in the centre presents the virtual projection view of the selected bubble and, finally, the right column shows the flow structure remaining after eliminating the large bubble. It is clearly visible, that the large bubble is heavily deformed as a result of the action of turbulence to the gas-liquid interface. At the given high air flow rate, the bubble was found to be about 660 mm tall.

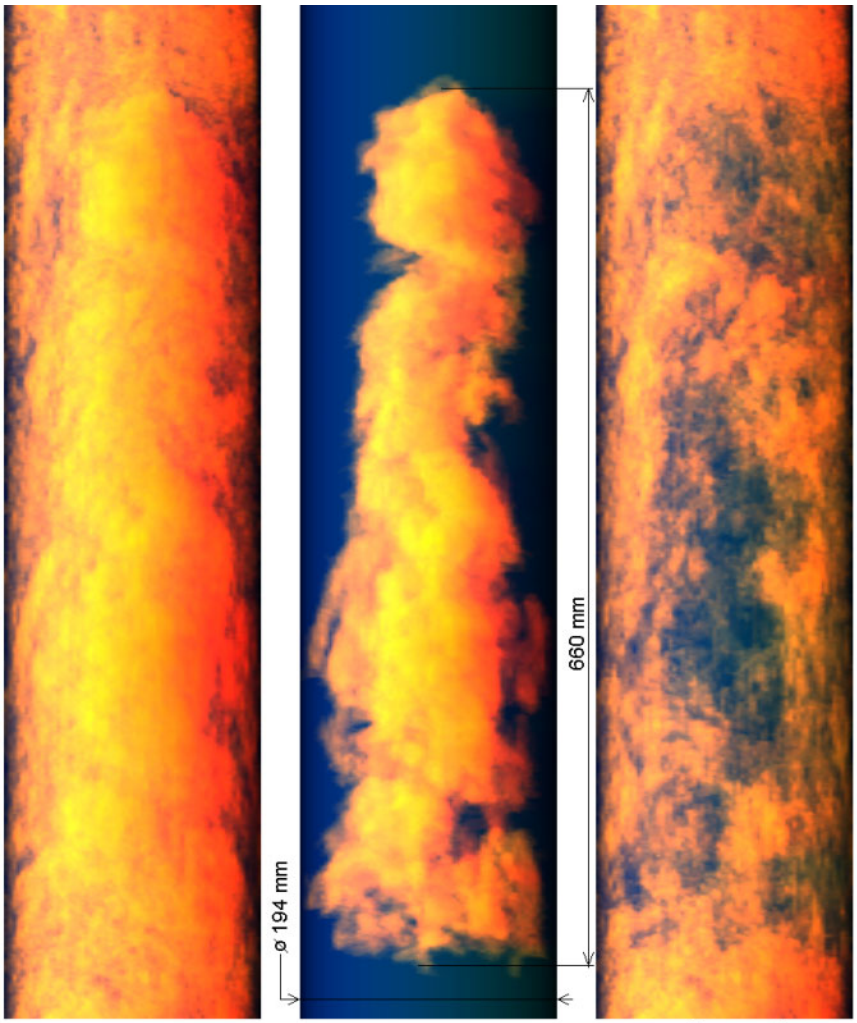

Fig. 7: Example of the extraction of a large bubble from the signal of the wire-mesh sensor (superficial velocities: J_{air} = 1.3 m/s and J_{water} = 1 m/s)

5. Conclusions

Detailed quantitative information about bubble size distributions of a gas-liquid flow in a pipe of DN200 and an advanced visualization of the flow structure are presented for the first time. The results were obtained by a wire-mesh sensor with a measuring matrix of 64x64 points, which delivers 2500 frames per second. They were compared to earlier measurements at a pipe of DN50. Similar to the small pipe it was found also in the large pipe that the monomodal bubble size distribution characteristic for low gas flow rates transits to a bimodal distribution when the superficial gas velocity is increased. This transition was observed earlier in the small pipe. The slug flow

resulting in the small pipe was not found in the large pipe. In this sense, the measurements confirm the findings of Ohnuki [8], though the appearance of the bimodal bubble size distribution points at a certain similarity of the processes.

References

[1] A. Schaffrath, A.-K. Krüssenberg, F.-P. Weiss, E. F. Hicken, M. Beyer, H. Carl, J. Schuster, P. Schuetz, M. Tamme, 2001, TOPFLOW - a new multipurpose thermalhydraulic test facility for the investigation of steady state and transient two-phase flow phenomena, Kerntechnik, **66**(2001)4, pp. 209-212.

[2] A. Schaffrath, A.-K. Krüssenberg, F.-P. Weiss, H.-M. Prasser, 2002, Die Mehrzweck-Thermohydraulikversuchsanlage TOPFLOW des Forschungszentrums Rossendorf e.V. - Aufbau, Ziele und Perspektiven, Atomwirtschaft - Atomtechnik, **47**(2002)6, pp. 383-388.

[3] A. Schaffrath, E. F. Hicken, H. Jaegers, H.-M. Prasser, 1999, Operation conditions of the emergency condenser of the SWR1000, Nuclear Engineering and Design, **188**(1999) pp. 303-318.

[4] H.-M. Prasser, A. Böttger, J. Zschau, 1998, A new electrode-mesh tomograph for gas-liquid flows Flow Measurement and Instrumentation, **9** (1998), 111-119.

[5] H.-M. Prasser, M. Beyer, A. Böttger, H. Carl, D. Lucas, A. Schaffrath, P. Schütz, F.-P. Weiss, J. Zschau, Influence of the pipe diameter on the structure of the gas-liquid interface in a vertical two-phase pipe flow, NURETH-10, Seoul, October 5-9, 2003, paper A00308, submitted.

[6] H.-M. Prasser, D. Scholz, C. Zippe, 2001, Bubble size measurement using wire-mesh sensors, Flow Measurement and Instrumentation, 12/4, pp.299-312, 2001.

[7] H.-M. Prasser, E. Krepper, D. Lucas, 2002, Evolution of the two-phase flow in a vertical tube - decomposition of gas fraction profiles according to bubble size classes using wire-mesh sensors, International Journal of Thermal Sciences, **41** (2002) 17-28.

[8] A. Ohnuki, H. Akimoto, 2000, Experimental study on transition of flow pattern and phase distribution in upward air-water two-phase flow along a large vertical pipe, International Journal of Multiphase Flow, **26**(2000)367-386.

[9] W. H. Leung, C. S. Eberle, Q. Wu, T. Ueno, M. Ishii, 1995, Quantitative characterization of phasic structure developments by local measurement methods in two-phase flow. In: Proc. of the Second Int. Conf. on Multiphase Flow, 1995, Kyoto, IN2-17-IN2-25.

[10] T. J. Liu, S. G. Bankoff, 1993, Structure of air-water bubbly flow in a vertical pipe - II. Void fraction, bubble velocity and bubble size distribution. Int. J. Heat Mass Transfer, **36**(4), pp. 1061 - 1072.

[11] A. Serizawa, I. Kataoka, 1988, Phase distribution in two-phase flow. In: N. H. Afgan (Ed.), Transient Phenomena in Multiphase Flow. Hemisphere, 1988, New York. pp. 179-224.

[12] A.-K. Krüssenberg, H.-M. Prasser, A. Schaffrath, 2000, A new criterion for bubble slug transition in vertical tubes, Kerntechnik, **65/1**(2000), pp. 7-13.

Acknowledgement

The work is carried out in the frame of a current research project funded by the German Federal Ministry of Economics and Labour, project number 150 1265. Electronic equipment for wire-mesh sensors was developed in a close co-operation with TELETRONIC GmbH in Rossendorf (www.tz-rotech.de/teletronic/). The authors express their gratitude to the team of developers of TELETRONIC, in persona: D. Peters, G. Pietzsch, W. Taubert and M. Trepte.

STABILITY OF NATURAL CIRCULATION COOLED BOILING WATER REACTORS DURING START-UP

Annalisa Manera [1], Ulrich Rohde, and Frank Schaefer

1. Introduction

The evolution of boiling water reactors leads to designs with larger cores and to reactors cooled by natural circulation. An item of concern for BWRs was their susceptibility to unstable behavior. Fortunately, the experience collected during the years has reached a level sufficient for eliminating most instability issues. However, two items remain: so called out-of-phase oscillations in large reactor cores and flashing induced flow oscillations in natural circulation. The latter instability mode was suggested to be relevant for natural circulation BWRs by Aritomi et.al. [1]. It is important during the start-up phase of the reactor, when pressure and power are low. In a series of dedicated tests on the Dodewaard reactor, indications for unstable behavior during the start-up phase were found [2]. This confirmation of Aritomi's predictions gave cause for a research campaign in Delft, devoted to analytical modeling of the phenomenon and to experimental research on a dedicated test facility CIRCUS. An overview of the experiments and the modeling of flashing-induced instabilities with the codes FLOCAL and ATHLET is presented in this paper. The research has been carried out within the framework of the EU project NACUSP.

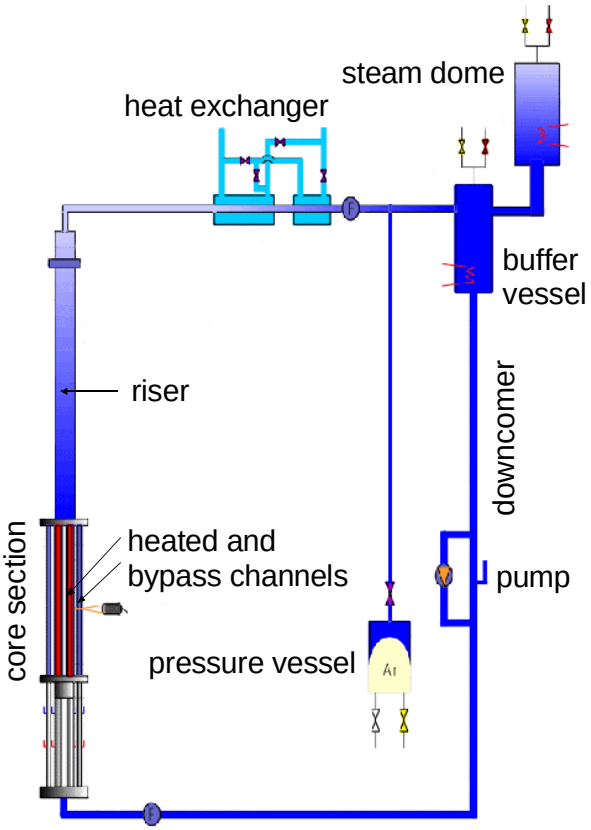

Fig. 1: The CIRCUS test facility

2. The CIRCUS test facility

The CIRCUS facility (Fig. 1) is a natural-circulation water/steam loop. The heated section (1.95 m) consists of four parallel heated channels and four bypass channels. On top of the heated channels a 3 m long adiabatic riser section is present. The steam possibly produced in the heated channels and in the riser section is condensed in heat exchangers. A steam dome, containing a steam-water mixture at saturation conditions, is used to simulate the steam dome of a reactor; here a small heater compensates for heat losses. A buffer vessel is used to damp out temperature oscillations in order to assure a constant temperature at the inlet of the heated section. A detailed description of the test facility is given in [3].

[1] Interfaculty Reactor Institute, Delft University of Technology, The Netherlands

3. The mechanism of flashing induced instabilities

With flashing it is referred to the void production that takes place in a fluid when no external heat source is supplied. In this condition void production occurs due to superheating of the liquid phase (for instance if the local pressure decreases or if hot water is transported from a higher to a lower pressure region). At start-up conditions both system pressure and heating power are low. The low system pressure implies large differences in saturation temperature between the inlet and the outlet of the adiabatic section. At low powers the coolant, which is heated up in the heated section of the natural circulation loop, may not reach saturation conditions in the core itself. However, due to the strong pressure gradient, flashing can occur in the adiabatic section (see Fig. 2), leading to an enhancement of the natural circulation flow rate. In dynamic conditions this phenomenon can cause self-sustained flow oscillations: if only single-phase is present in the system, a low flow rate circulates into the system. If the temperature of the coolant entering the adiabatic section is high enough, flashing takes place. The occurrence of flashing will cause an increase of the loop buoyancy and a decrease of the pressure below the location of bubble formation. The decrease in local pressure will trigger additional void formation, leading to a large variation of the flow rate in the system. The increase of flow rate will cause a subsequent decrease of the coolant temperature entering the adiabatic section, so that the process of flashing may eventually stop and the flow rate will be low again. The coolant temperature entering the adiabatic section will therefore increase leading to a new flashing cycle.

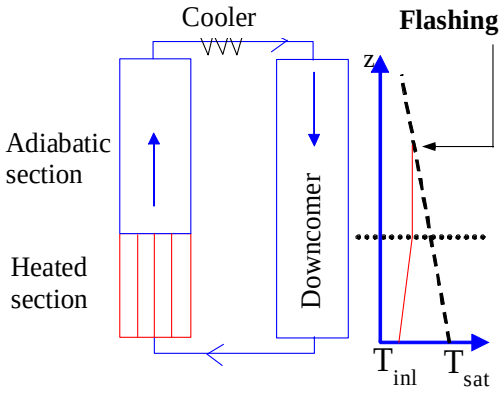

Fig. 2: Flashing in the riser (adiabatic section) of the CIRCUS test facility

4. Experiments and FLOCAL simulations

FLOCAL [4] is a one-dimensional 4-equation two-phase thermal-hydraulic code, originally developed to model the dynamic behavior of the AST-500, a Russian design nuclear reactor. The system of partial differential equations consists of a momentum, energy and mass balance equation for the two-phase mixture and a separate mass balance equation for the vapor phase. An evaporation/condensation model is used to couple the two mass balance equations. The core is modeled as a series of parallel coolant channels associated to one or more fuel assemblies. On top of the core, individual (parallel) risers or a common riser can be modeled. The parallel channels are coupled by a boundary condition of equal pressure drops over their total length. As boundary conditions, the core inlet temperature and the pressure at the riser outlet are kept constant. The boundary condition on the temperature is exact, since the inlet temperature is kept constant also during the experiments. This is not the case for the outlet pressure. At CIRCUS, the loop is connected to a steam dome, where a steam/water mixture is present. During flow instabilities, the production of steam in the adiabatic section causes an equivalent volume of water to enter the steam dome, leading to a compression (and partially condensation) of the steam cushion in the steam dome itself. This leads to a temporary increase of the system pressure, that limits the steam production and expansion in the adiabatic section and therefore the amplitude of the flow oscillations. Since the feedback of the steam dome is not considered in the analysis, one should expect higher amplitude of the flow oscillation in the simulations.

A series of experiments was carried out at the CIRCUS facility to study the characteristics of flashing-induced flow instabilities and to provide a data base on which basis thermal-hydraulic codes can be validated. The experiments were performed at pressures of 1 and 2 bar and for different heights of the steam cushion in the steam dome. During each experiment the power level and the temperature at the inlet of the heated section were kept constant. In Fig. 3 examples are shown of time-traces of the flow rate measured at the CIRCUS facility at a pressure of 1 bar and at a power of 8 kW. The temperature at the inlet of the heated section is reported separately for each case. The results of the FLOCAL simulations are also shown. Four different types of behaviors can be observed both in the experiments and in the simulations: stable single-phase circulation (Fig. 3.a), intermittent natural circulation (Fig. 3.b through 3.f), unstable two-phase circulation (Fig. 3.g) and stable two-phase circulation (Fig. 3.h). At single-phase circulation the liquid temperature always remains below saturation. The intermittent natural circulation occurs as soon as the system passes from single-phase to two-phase operation and is characterized by an alternate presence of liquid and two-phase mixture in the adiabatic section. Within a cycle an incubation period exists before the flow-rate increases, needed to the liquid to reach saturation conditions. The incubation period becomes shorter and shorter with increasing inlet temperature and disappears in the unstable two-phase natural circulation region. In the latter condition, two-phase mixture is always present in the riser section due to flashing, but the location oscillates at which flashing starts (flashing boundary), giving rise to an oscillatory driving force in the system and thus to a flow instability. Finally, when the flashing boundary stabilizes, stable two-phase circulation takes place; in this case a much higher flow rate is achieved with respect to single-phase natural circulation due to the considerable density difference between liquid in the downcomer and two-phase mixture in the heated and adiabatic sections. The same trends are experienced if the inlet temperature is kept constant and the power is increased instead. It is thus clear that to transit from single-phase to two-phase operations an unstable region has to be crossed. The code FLOCAL slightly over-estimates the maximum flow rate achieved during the flow oscillations. As mentioned previously, this is due to the fact that the feedback due to the presence of a steam dome has been neglected. Despite this approximation, the general phenomenology and trends seem to be reproduced very well.

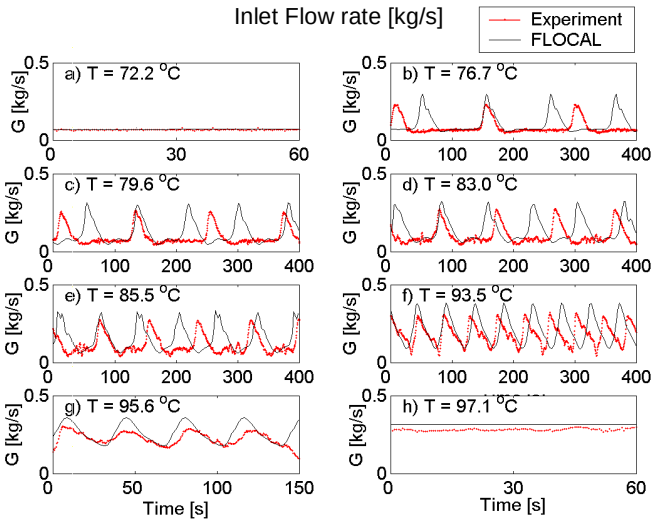

Fig. 3: Typical flow-rate time traces

A better physical insight in the instabilities is achieved if the time evolution of the void fraction in the adiabatic section is also analyzed. This is shown in Fig. 4. Again the time traces were recorded at a total heating power of 8 kW and a system pressure of 1 bar. Different cases are shown corresponding to different temperatures at the inlet of the heated section. The magnitude of the void fraction is represented by means of contour plots. In Fig. 4 both simulated (right picture) and experimental (left picture) time traces are reported. At low inlet temperatures (Fig. 4.a) flashing starts relatively high in the riser and later on the flashing front expands and propagates both in the upward and downward directions. As soon as the inlet temperature

increases, steam bubbles are generated first in the heated section (subcooled boiling) below the riser inlet. These bubbles collapse in the riser (contributing to the heating up of the fluid) before flashing starts (Fig. 4.b and c). Increasing the inlet temperature flashing in the riser is directly triggered by the voids coming from the heated section (Fig. 4.d and Fig. 4.e).

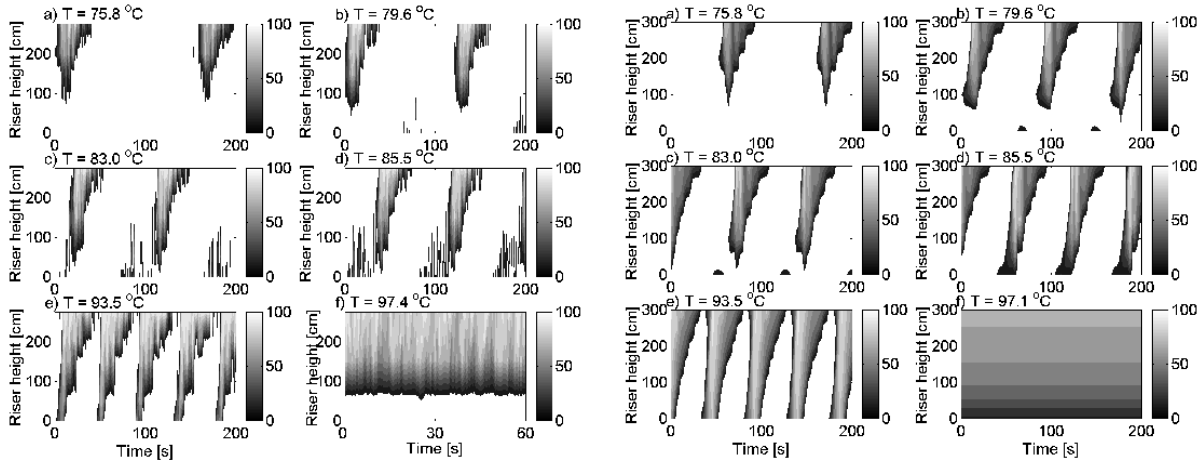

Fig. 4: Void-fraction evolution as measured with needle-probes at the CIRCUS facility (left) and from FLOCAL simulations (right). Vertical bars give the grey-scale coding for the void fraction (in percent)

The physical origin of the instability suggests that the transit time of the mixture through the heated and adiabatic sections is a dominant factor in determining the oscillation period. This transit time is a function of the coolant flow rate and of the void content in the system. Fig. 5 shows that the oscillation period decreases monotonously with increasing average flow rate <G>, although this graph contains cases recorded at different subcooling, heating power and system pressure. Clearly, the relation between oscillation period and average flow rate depends only on the geometrical characteristics of the system. The results of the FLOCAL simulations, also reported in Fig. 5 support this idea. In Fig. 6 the relation between the driving pressure in the loop and the kinetic pressure is shown. All experimental points, both stable and unstable, lie approximately on a straight line passing through the origin. The reason for this behavior is the fact that driving pressure and friction are the major terms in the momentum balance of the loop, while inertia and acceleration pressure drops play a small role in the determination of flow magnitude. This argument has been confirmed by the FLOCAL calculations, since it is found that inertia and acceleration pressure drops are orders of magnitude smaller with respect to frictional and gravitational pressure drops.

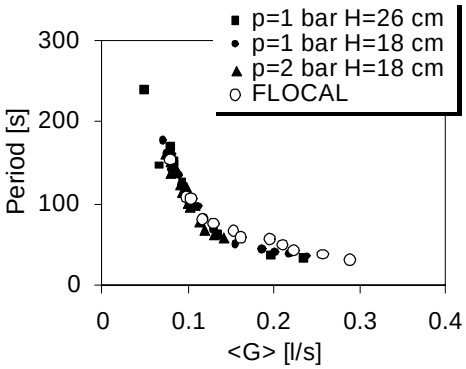

Fig. 5: Oscillations period as function of the average flow rate (H indicates the height of the steam cushion in the steam dome)

The relation between oscillation period and inlet subcooling is presented in Fig. 7 (8 kW, 1 bar), both for experiments and simulations. In many cases the FLOCAL model under-estimates the oscillation period (from Fig. 3 it can be seen that mainly the incubation period is under-estimated rather than the duration of the flow peak caused by the flashing transient). The oscillation period is well predicted at low subcoolings (i.e. high flow rates and absence of

single-phase circulation) and under-estimated at high subcoolings (i.e. at low flow rates and presence of alternate single-phase/two-phase circulation). The reason could lie on both heat losses, neglected in the calculation, and on the smearing of the temperature front during single-phase circulation. Calculations including heat losses have been performed but, though they cause an increased incubation period, they do not justify the extent of under-estimation of the incubation period. The smearing of the temperature front seems to be caused by turbulent diffusion in presence of a negative temperature gradient along the vertical axis of the adiabatic section. It has been shown that indeed this has a strong effect on the incubation period at high inlet subcooling and has no effect at low inlet subcooling. Thus this effect explains the trends observed in Fig. 7. The strong effect of the energy accumulated in the heat structures, namely the walls of riser and heated section, is clearly visible (Fig. 7, "no wall" calculations).

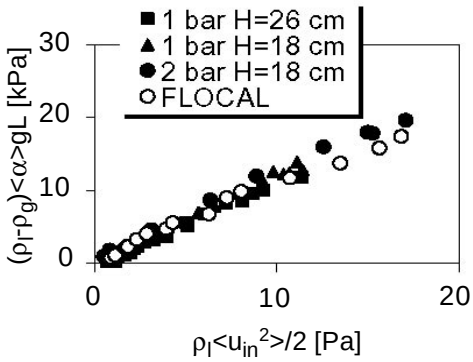

Fig. 6: Driving vs kinetic pressure

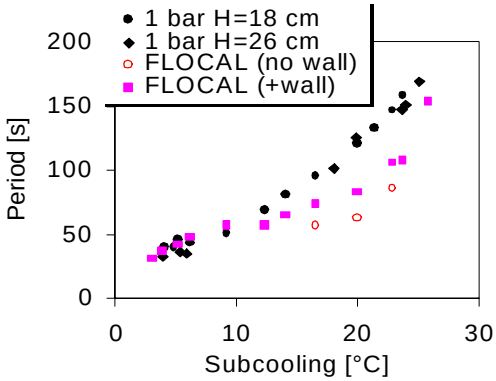

Fig. 7: Oscillation period as function of the inlet subcooling.

Several experiments have been carried out to derive so-called stability maps. These maps are represented in the power-subcooling plane since power and subcooling are the variables directly controlled during the measurements. Examples of stability maps are shown in Fig. 8 at a pressure of 1 bar and two different steam cushion heights in the steam dome. The stability boundaries predicted by FLOCAL are reported in the same figure. In agreement with other experimental results the range of inlet subcoolings for which instabilities occur increases with power. The extension of compressible steam volume in the steam dome does not influence the behavior of the system in steady state conditions since in this case no variation of the compressible volume in the steam dome occurs. In dynamic conditions, however, flashing in the riser will cause a larger pressure increase when a smaller compressible volume is available in the steam dome. The pressure increase will lead to vapor collapse and to an increase of saturation temperature. This feedback limits the amplitude of the flow oscillation. However, the effect on the extension of the unstable two-phase region is not significant, see Fig. 8.

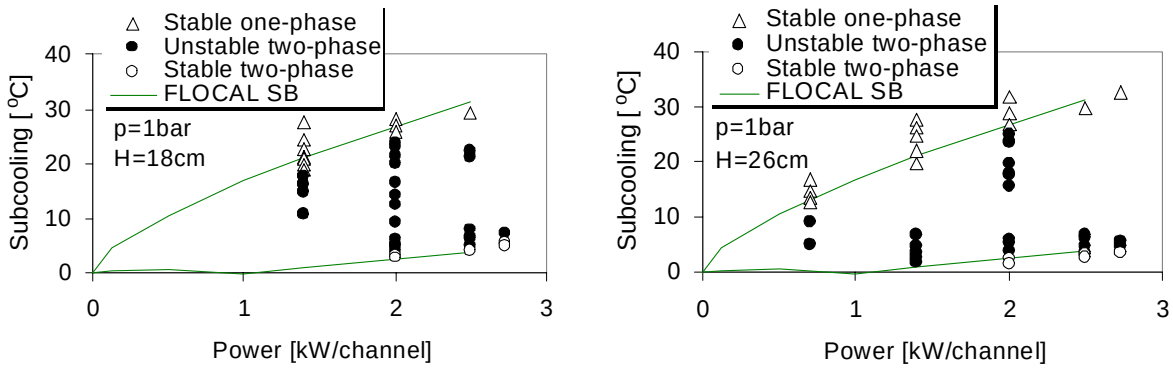

Fig. 8: Comparison between experimental and FLOCAL stability boundaries (H = steam cushion height in the steam dome)

5. Results of the ATHLET calculations

The FLOCAL code described in section 4 has been developed especially to model natural circulation instabilities. The aim of the investigations reported below was to demonstrate whether general thermo-hydraulic system codes like ATHLET are capable of reproducing the relevant phenomena too. For the presented calculations the code version ATHLET Mod 1.2 Cycle B [5] was used. The core section is modeled by 4 parallel channels. Each core channel is simulated as a pipe with an electrical heater. For the riser, downcomer, upper and lower horizontal parts the exact dimensions, heat capacities of glass and copper, heat losses and pressure drops are considered. The riser is modeled as an adiabatic section. The steam dome is connected to a pressure dependent volume to maintain the pressure during a steady state calculation. In the calculations the heat exchanger is not modeled. Therefore a bypass is connected to the downcomer section to keep the core inlet temperature constant. A special amount of water from the loop circulates through the bypass and can be injected with a lower temperature. In all control volumes the 5-equation model (separate conservation equations for liquid and vapour mass and energy, mixture momentum equation) and the full-range drift-flux model were used. With help of a steady state calculation the pressure losses, heat losses and the temperature distribution along the loop were adjusted according to the boundary conditions.

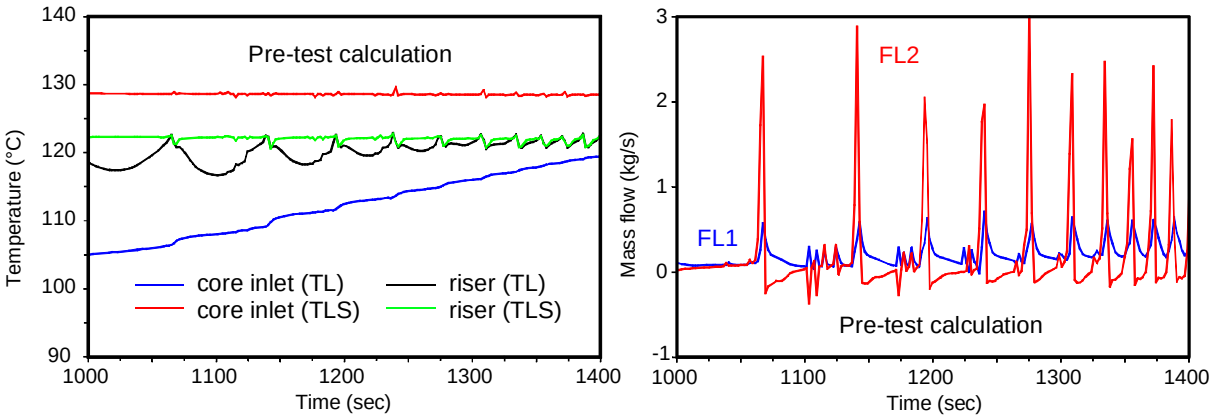

Fig. 9: Liquid (TL) and saturation (TLS) temperature at the core inlet and in the middle of the riser, core inlet mass flow (FL1) and mass flow in the upper horizontal part (FL2)

Within the NACUSP project pre-test calculations for different initial conditions (pressure, mass flow, core inlet temperature and core power) were performed. The pre-test calculations should answer the question, whether the program is able to calculate the flashing induced instabilities or not. The results of one pre-test calculation (pressure 2 bar, 8 kW power) are presented in Fig. 9. In this calculation the heat exchanger was not modelled. Due to the missing heat sink the temperature at the core inlet is rising from appr. 105 °C up to 120 °C. If the temperature in the upper part of the riser reaches saturation conditions, the flashing induced instabilities start. The phenomenology of these instabilities described in the previous section of that paper is well modeled by ATHLET. According to experiments with different core inlet temperatures, the period of the instabilities is shorter for higher temperatures. This effect can be seen in the calculated mass flows.

To consider the behaviour of the heat exchanger, a simplified bypass was modelled for the post-test calculations. The bypass is connected to the top of the downcomer to keep the core inlet temperature nearly constant during the transient calculation. The results for two transient calculations (different core inlet temperatures, pressure of 1 bar, 8 kW reactor power) are pre-

sented in Fig. 10 and 11. The results show, that the period of the instabilities is shorter for higher core inlet temperatures. This corresponds to the experimental findings. In general the calculated mass flows and temperatures show a very good agreement with the experimental data. Especially the period of the flashing induced instabilities can be reproduced very well. However, the magnitude of the mass flow oscillations is slightly overestimated.

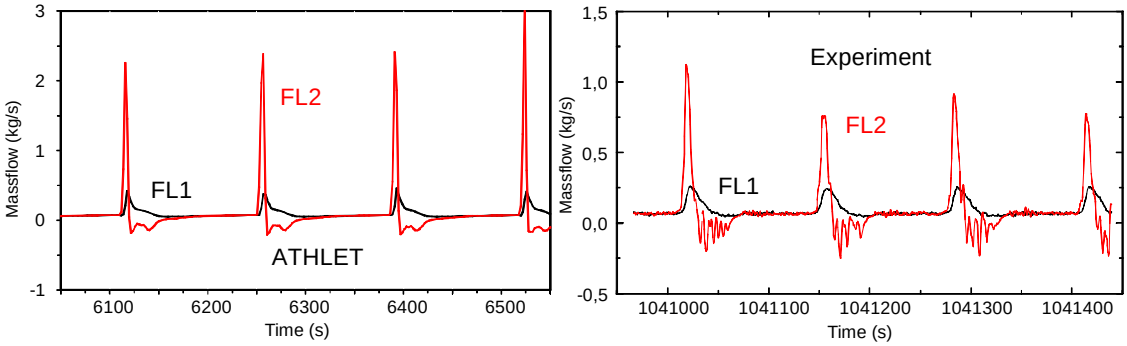

Fig. 10: Core inlet mass flow (FL1) and mass flow in the upper horizontal part (FL2) post-test calculation for 1 bar, 8 kW and T_{inl} = 78 °C

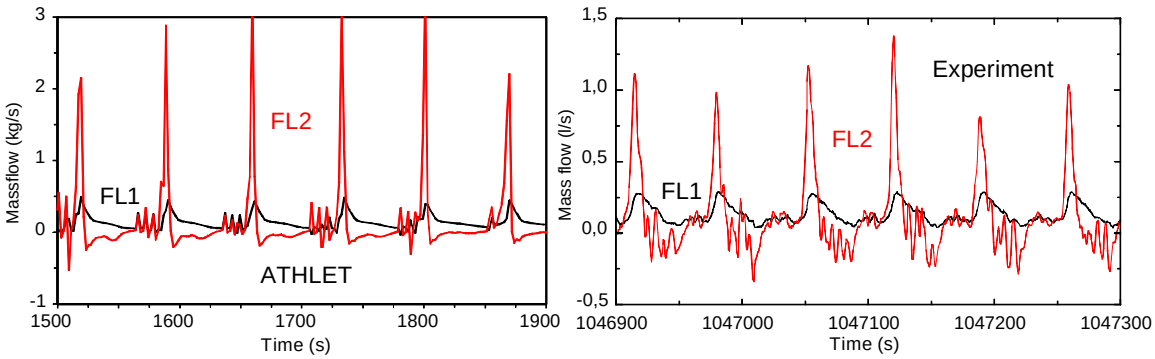

Fig. 11: Core inlet mass flow (FL1) and mass flow in the upper horizontal part (FL2) post-test calculation for 1 bar, 8 kW and T_{inl} = 86 °C

References

[1] M. Aritomi, J. H. Chiang, T. Nakahashi, M. Watarum, M. Mori: "Fundamental Study on Thermohydraulics During Start-up in Natural Circulation Boiling Water Reactors (I)", Nucl. Sci. Technol., 29[7], 631-641, (1992)

[2] T. H. J. J. Van der Hagen, A. J. C. Stekelenburg, S. Kaart, J. C. Schouten: "Investigations on start-up flow oscillations in natural circulation BWRs", ANS proc. of 1996 National Heat Transfer Conference, Houston, USA, August 3-6, 1996, Vol. 9, 188-197, (1996)

[3] W. J. M. de Kruijf, A. Manera, D. W. de Haas, J. G. F. Schut: „Description of CIRCUS“ Delft University of Technology, Netherlands, 2001

[4] U. Rohde: "Theoretische Untersuchung dynamischer Naturumlaufinstabilitäten im Kern-heizreaktor AST-500", Kernenergie 30, 1987

[5] G. Lerchl, H. Austregesilo, 1999, ATHLET Mod 1.2 Cycle B: User’s Manual, Gesellschaft für Anlagen und Reaktorsicherheit (GRS) mbH

CONTROL OF FLOW SEPARATION BY TIME PERIODIC ELECTROMAGNETIC FORCES

Tom Weier, Gerd Mutschke, and Gunter Gerbeth

1. Introduction

Separation is an undesired flow feature in many engineering cases. Usually it implies a loss of lift, an increase of drag, diminished pressure recovery etc. Therefore, a considerable amount of research has been devoted to the control of flow separation and many possibilities to achieve separation control have been investigated. Among the most popular are shaping as a passive means and suction, blowing and wall movement as active control methods. While passive means naturally do not produce any running costs, achievable improvements are modest and performance under off-design conditions is mostly poor. Active control methods may be adjusted to actual operating conditions, but require additional power, i.e. running costs.

If the fluid in question is electrically conductive, an additional active control possibility is given by the application of a Lorentz force **F**. This electromagnetic body force results from the vector product of the magnetic induction **B** and the current density **j**:

$$\mathbf{F} = \mathbf{j} \times \mathbf{B}. \tag{1}$$

The current density is given by Ohm's law

$$\mathbf{j} = \sigma(\mathbf{E} + \mathbf{u} \times \mathbf{B}), \tag{2}$$

where **E** denotes the electric field, **u** the velocity vector and σ the electrical conductivity, respectively. The induced currents due to the motion of a fluid in an imposed magnetic field are given by the $\mathbf{u} \times \mathbf{B}$ term in equ. (2). Under moderate magnetic field strength ($B_0 \approx 1$ T) and in case of low-conducting fluids as electrolytes or sea-water ($\sigma \approx 10$ S/m), conditions considered in the following, these induced currents are too small to generate a perceptible Lorentz force in the flow. In order to influence the flow, an additional electric field has to be applied.

First experimental evidence of separation prevention by Lorentz forces in low-conducting liquids for the flow around a half cylinder has been given by [1] in 1962. However, the general idea seems to be somewhat older [2]. A number of experimental investigations to control the flow around hydrofoils of different types by steady, wall parallel Lorentz forces were carried out by the present authors, for a summary see [3]. The effect of the force on the flow is similar to that reported for flow separation control by blowing. To characterise the action of the Lorentz force, an electro-magneto-hydrodynamic (EMHD) momentum coefficient $C_{\mu EMHD}$ may be defined as

$$C_{\mu EMHD} = \frac{1}{4} \frac{a j_0 M_0}{\rho U_\infty^2} \frac{x_e - x_s}{c}. \tag{3}$$

Here a describes a characteristic penetration depth of the force into the flow, j_0 the applied current density, M_0 the magnetization of the permanent magnets used to generate the applied

magnetic field, ρ the fluids density, U_∞ the flow velocity of the outer flow, x_e-x_s the length of the actuator and c the chord length of the hydrofoil, respectively. In analogy to [4] $C_{\mu EMHD}$ links the total momentum injected into the flow by the Lorentz force to the dynamic pressure. The EMHD momentum coefficient correlates the maximum attainable lift gain under different conditions and allows a first assessment of the practical usability of electromagnetic separation control. A corresponding estimate shows, that power requirements might be a critical point under high speed conditions. In consequence, alternative approaches should be elaborated, which allow to reduce the required input power for a specific lift gain. The approach discussed here is the application of oscillatory Lorentz forces inspired by the use of periodic excitation in aerodynamics.

2. Motivation: oscillatory excitation of separated flows

This section aims to give the reader a very brief and necessarily incomplete introduction to the aerodynamic research on separation control by time periodic forcing, mainly to explain the present authors interest in this method. First investigations on oscillatory excitation of separated flows date back to the 1970s. Now this field is an objective of active research, a thorough review of recent results and previous findings gives [5].
Fig. 1, taken from [6], shows a comparison of separation control by steady blowing and periodic excitation of the separated flow over the flap shoulder of an IAI PR8-40 profile with a constant flap angle of 30°. The uncontrolled airfoil stalls at an angle of attack of approximately 8° reaching a maximum lift coefficient of 1.9. By steady blowing, stall can be delayed up to 14° increasing the maximum lift coefficient to 2.5. Approximately the same effect, even with slightly higher values, may be achieved by oscillatory blowing. Yet this

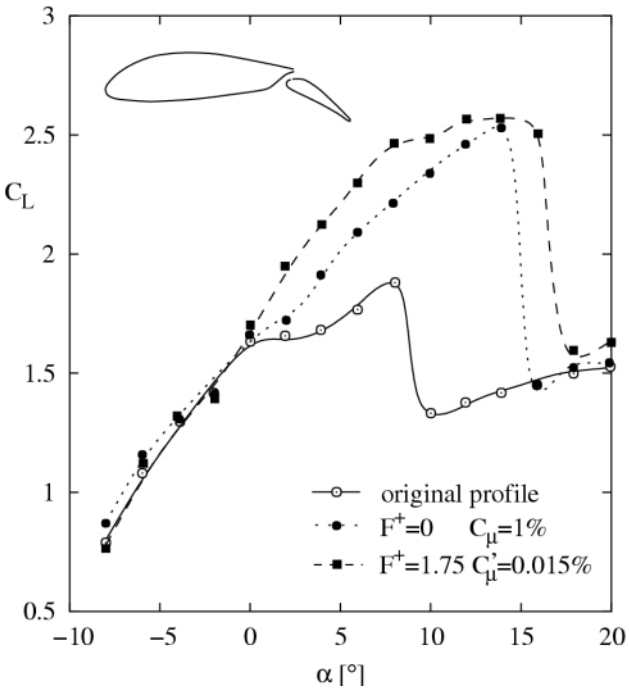

Fig. 1: Lift increase on a IAI PR8-40 profile at Re=1.4×10^5 by means of blowing and oscillatory excitation from the flap shoulder [6].

Fig. 2: Shear layer above a flap excited by an oscillating flaperon [9].

effect has been reached with a momentum coefficient almost two orders of magnitude smaller than with steady blowing.
The dimensionless quantities used in the previous paragraph are the lift coefficient defined in the usual way as

$$C_L = \frac{F_L}{cs\,U_\infty^2 \rho/2}, \tag{4}$$

the forcing Strouhal number

$$F^+ = \frac{f_e x_{te}}{U_\infty}, \tag{5}$$

and the momentum coefficients C_μ and C_μ', where the latter is the rms value of the periodic momentum injection divided by the dynamic pressure and the projected area of the foil. F_L denotes the lifting force, c the chord length and s the span width of the foil, f_e the excitation frequency and x_{te} the distance from the excitation location to the trailing edge, respectively.
A well founded theoretical explanation of the observed phenomena is still missing, although a parallel may be drawn to the behaviour of excited shear layers [5]. A shear layer forms between two fluid streams of different velocity, i.e. the boundary of the separation region and the outer flow can be viewed as a shear or mixing layer. When the shear layer develops in flow direction, it also spreads, thereby entraining fluid from the surrounding flow. Shear layers are known to act as amplifiers of external perturbations [7] and their spreading rate is sensitive to excitation. If, in case of the separation region above a flap, the fluid volume entrained by the excited mixing layer exceeds the volume available in the separated region, the mixing layer will "attach" to the flap, a behaviour similar to the Coanda effect [8]. A visualisation of such a flow from [9] shows Fig. 2. In contrast to the reattachement by steady blowing, where a stationary flow follows the flap contour, the oscillatory excited flow is attached only in an averaged sense. The fluid motion in Fig. 2 is clearly instationary, two vortices move along the flap. Most experimental results show a maximum effect of forcing frequencies with $F^+ = O(1)$.
The dramatically decreased momentum coefficient, necessary to obtain reattachement, is due to the fact, that the shear layer vortices transport high momentum fluid from the outer flow into the recirculation region. The resulting momentum gain of the separated flow is eventually responsible for the reattachement. However, only a small fraction of it has been directly injected by the actuator.

3. Experimental Apparatus

Force measurements at a hydrofoil in a sodium chloride solution with an electrical conductivity of 3.5 S/m have been performed at the Hamburg Ship Model Basin. For a

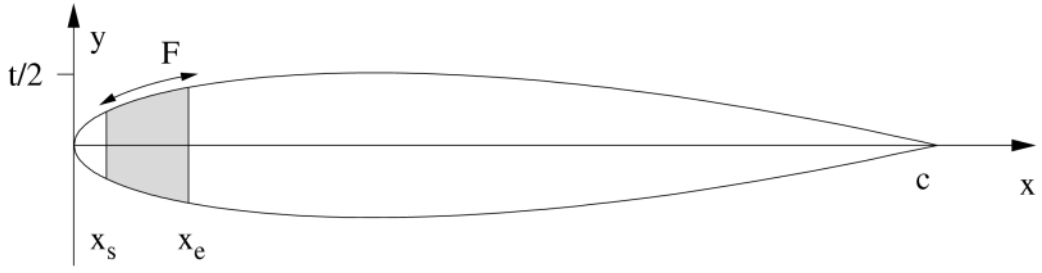

Fig. 3: PTL IV hydrofoil with electromagnetic actuator near the leading edge from x_s to x_e.

detailed description of the force balance, the channel and the general measurement procedure, we refer to [3]. Since time dependent forces have been investigated, the power supply used for the present investigations was a high power amplifier FM 1295 from FM Elektronik, driven by a Hameg HM 8130 frequency generator.
The electrodes of an existing PTL IV hydrofoil, described as PTL IV_S in [3], were isolated and only a small portion near the leading edge, shaded grey in Fig. 3, remained in contact with the flow. Thereby the force was concentrated near the origin of separation. The chord length of the foil was c=158 mm, the electrode/magnet area extended from x_s=6 mm to x_e=21 mm. At both ends of the foil, endplates made from Perspex have been mounted, leaving a spanwidth of s=345 mm between them. Both, magnets and electrodes, had a width of a=5 mm.

4. Results

Hydrogen bubble flow visualisations in Fig. 4 show the action of a time periodic Lorentz force on the separated flow at an 15° inclined flat plate. Directly behind the leading edge of the 130 mm long plate, an actuator region 10 mm long and consisting of a=10 mm wide magnets and electrodes was placed.
The unforced flow at a chord length Reynolds number $Re=1.4\times10^4$ is completely separated, the shear layer at the border between separation region and outer flow shows the typical Kelvin-Helmholtz vortices. A periodic forcing with $F^+=1.36$ and $C'_\mu=8.9\%$ reattaches the flow to the plate. Two vortices move along the plate contour, quite similar to these visible in Fig. 2. Since the Reynolds number is very small, the oscillatory momentum coefficient necessary to reattach the flow is relatively large, an effect observed previously also in [10].

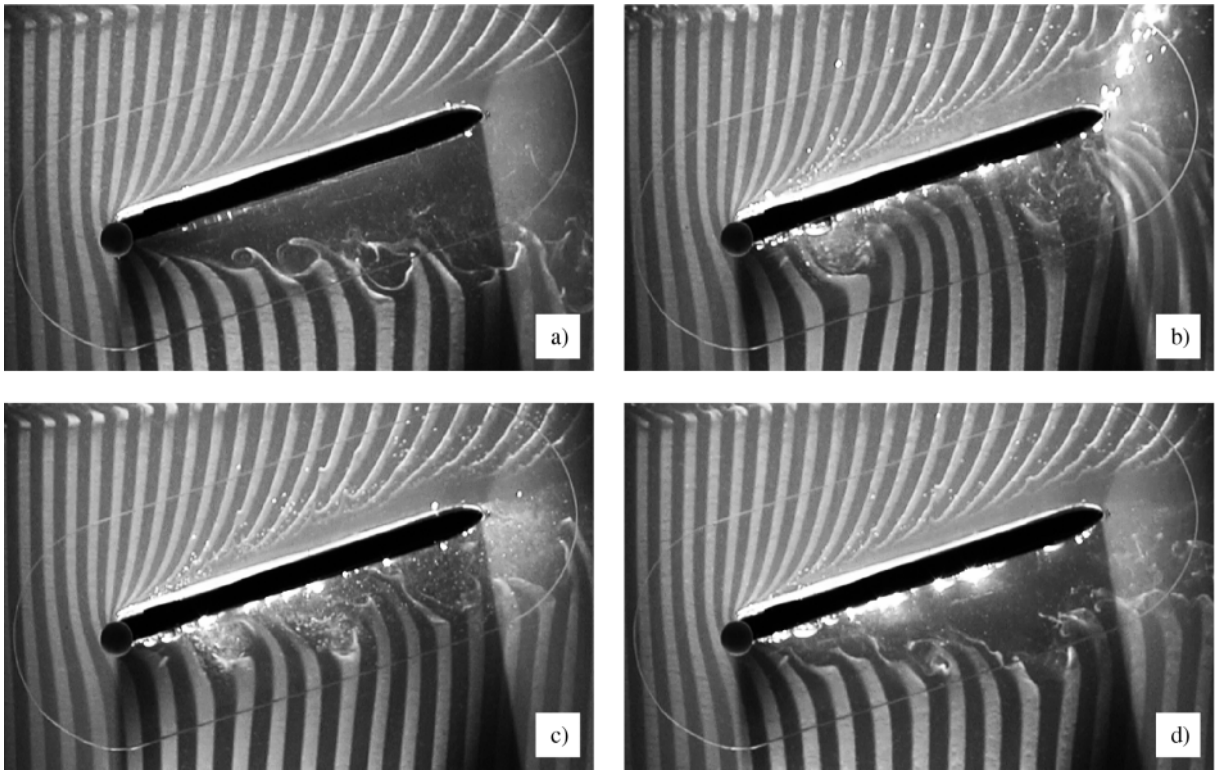

Fig. 4: Excitation of the shear layer at a 15° inclined flat plate at $Re=1.4\times10^4$: a) uncontrolled flow; b) $C_\mu'=8.9\%$, $F^+=1.36$; c) $C_\mu'=8.9\%$, $F^+=2.95$; $C_\mu'=8.9\%$, $F^+=11.8$.

Here, the oscillatory momentum coefficient is defined as

$$C_\mu' = \frac{1}{4}\frac{aM_0}{\rho U_\infty^2}\frac{x_e - x_s}{c}\sqrt{\frac{1}{T}\int_0^T j_0^2 dt}, \tag{6}$$

where j_0 is the time dependent current density, t denotes the time and T is the cycle duration of oscillation.

An increase of the forcing frequency to F^+=2.95 results in an increase of the number of vortices moving along the plate at the same time. The flow is still mainly attached to the plate. Finally, at a forcing frequency of F^+=11.8, the flow is no longer attached to the plate. While the shear layer is influenced by the forcing, its spreading rate is not much larger than in the unforced case.

The lift coefficient versus forcing frequency measured at the PTL IV hydrofoil at different angles of attack and different C_μ' at a chord length Reynolds number of 4.9×10^4 is given in the diagrams of Fig. 5. The flow around the foil is still attached at an inclination angle of α=13°. Consequently, no reattachement is possible, and forcing, regardless of its frequency, does not increase the lift coefficient. In the contrary, a slight decrease of C_L can be observed. An increase of the angle of attack to 15° leads to a separated flow on the suction side. The lift coefficient, C_L=0.66, is smaller than the value of C_L=0.8 for α=13°. Periodic excitation with a sinusoidal varying Lorentz force, a configuration used throughout the experiments in Fig 5, leads to a reattachement of the flow. The lift coefficient is increased to C_L=0.9. However, this increase seems independent of the forcing frequency. Since the angle of attack is still not to large and the state of the boundary layer almost certainly laminar, a forced boundary

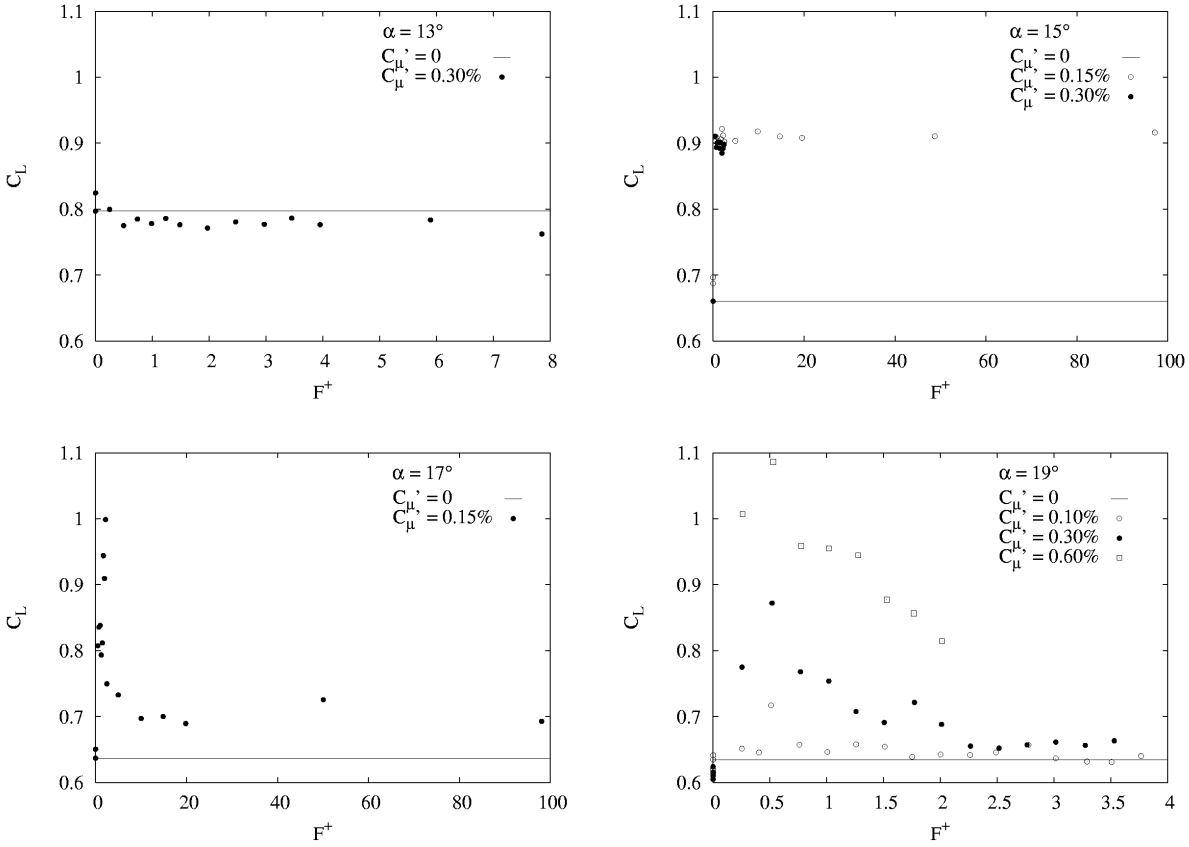

Fig. 5: Lift coefficient of the PTL IV versus forcing frequency for different angles of attack and different oscillatory momentum coefficients at Re=4.9×10^4.

layer transition should be the very likely cause of the observed behaviour. As generally known, a turbulent boundary layer is able to resist larger adverse pressure gradients, than that, a laminar boundary layer may overcome. A similar effect could be accomplished using a passive trip. At α=17° reattachement, i.e. a considerable lift increase of ΔC_L=0.35, can be observed only for a very small band of excitation frequencies around $F^+ \approx 1$. This observation is consistent with the findings in oscillatory blowing experiments [5].For higher excitation frequencies, lift is still increased, but only by a small amount of ΔC_L=0.05. The reason might be again forced transition of the boundary layer. Whereas at this inclination angle, even the turbulent boundary layer is not any more able to stay attached to the whole suction side, but merely separates a little further away from the leading edge. The largest inclination angle shown in Fig. 5 is α=19°. A small momentum coefficient, C_μ'=0.1%, results only in a small lift increase. This increase of ΔC_L=0.05 is very sensitive to the excitation frequency and can be observed only for F^+=0.5. Higher momentum coefficients of C_μ'=0.3% and C_μ'=0.6% lead to larger lift increases, ΔC_L=0.2 and ΔC_L=0.45, and broader effective frequency bands. However, the maximum lift increase is always obtained for F^+=0.5.
Fig. 6 shows a comparison of the momentum coefficient necessary to establish a certain lift gain by a steady and by an oscillatory Lorentz force. The corresponding definitions of the momentum coefficient, denoted simply by C_μ, in the figure, are those given in equ. (3) and equ. (6). To increase the lift coefficient by ΔC_L=0.37 the oscillatory excitation requires only 7% of the momentum input necessary in case of steady forcing.

5. Conclusions

First experimental results on separation control by oscillatory Lorentz forces have been presented. These results show striking similarities to the findings reported for periodic excitation by other means. Essential features as characteristic excitation frequency, excitation amplitude and resulting lift gain are reproduced in an almost quantitative sense.

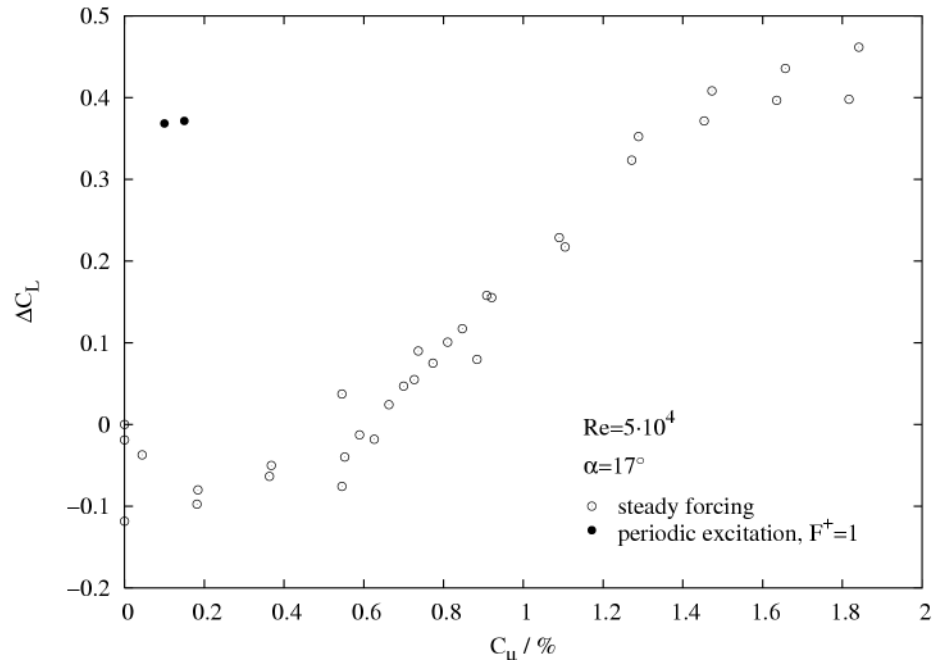

Fig. 6: Comparison of steady forcing and periodic excitation at the PTL IV hydrofoil

As expected, the momentum input required for a specific lift gain can be reduced considerable by using oscillating Lorentz forces instead of steady ones.
Further research is aimed at optimising the oscillatory momentum input by studying additional hydrofoil and actuator geometries as well as forcing by different wave forms different from the sinusoidal shape.

References

[1] R. Dukure, O. Lielausis (1962), Experimental investigation of the effect of electromagnetical forces upon flow around bodies in electrolyte. In: Problems of Magnetohydrodynamics and Plasmadynamics (Voprosi Magnitnoi Gidrodinamiki i Dinamiki Plazmi), Riga, pp.647-650

[2] E. L. Resler, W. R. Sears (1958), The Prospects for Magneto-Aerodynamics, J. Aero. Sci., 25, 235-245

[3] T. Weier, G. Gerbeth, G. Mutschke, O. Lielausis, G. Lammers (2002), Control of Flow Separation Using Electromagnetic Forces. IUTAM Symposium on Unsteady Separated Flows, Toulouse, France (invited)

[4] P. H. Poisson-Quinton (1956), Einige physikalische Betrachtungen über das Ausblasen an Tragflügeln, Jahrbuch der WGL, 29-51

[5] D. Greenblatt, I. J. Wygnanski (2000), The control of flow separation by periodic excitation, Prog. Aero. Sci., 36, 487-545

[6] A. Seifert, A. Darabi, I.J. Wygnanski (1996), Delay of Airfoil Stall by Periodic Excitation, Journal of Aircraft, 33, 691-698

[7] P. Huerre, (2000), Open Shear Flow Instabilities, in G. K. Batchelor, H. K. Moffatt, M. G. Worster (Eds.): Perspectives in Fluid Dynamics, Cambridge University Press, Cambridge, 159-229

[8] D. J. Tritton, (1988), Physical Fluid Dynamics, Clarendon Press, Oxford

[9] I.J. Wygnanski, A. Seifert, (1994), The Control of Separation by Periodic Oscillations. AIAA Paper 2608-94

[10] D. Greenblatt, I. J. Wygnanski (2001), Use of periodic excitation to enhance airfoil performance at low Reynolds numbers, J. Aircraft, 38, 190-192

Acknowledgements

Financial support from VDI under Grant NLD-FKZ 13N7134/1 is gratefully acknowledged. Thanks are due to Gerd Lammers and Lutz Hoffmann from HSVA for the pleasant cooperation and their help and advice throughout the force measurements.

ULTRASONIC VELOCITY MEASUREMENTS IN LIQUID METALS USING ACOUSTIC WAVE GUIDES

Sven Eckert, Gunter Gerbeth, and Vladimir I. Melnikov[1]

1. Introduction

The ultrasound Doppler velocimetry (UDV) is an innovative and non-invasive method to determine the velocity in liquid flows. Main advantages are the ability to investigate flows of opaque liquids and to deliver complete velocity profiles in real-time [1,2]. Therefore, the intention to apply this measuring technique to liquid metal flows is obvious with respect to the situation that until today no velocity measuring technique for liquid metal flows is available commercially.
The feasibility of velocity profile measurements by UDV has already been reported for low temperature liquid metals as mercury [2,3] and gallium [4]. Recently, successful measurements for liquid sodium at a temperature of 150°C were published [5]. The wetting of the sensor by the liquid metal to achieve a sufficient acoustic coupling or the allocation of suitable tracer particles have to be considered as relevant problems for the application of UDV in liquid metal flows.
However, the today's available ultrasonic technology reveals considerable limitations with respect to the practicability of measurements at high temperatures above 200°C. The conventional piezoelectric transducers using PZT based materials are usually restricted to temperatures of 150°C. A way to develop transducers for higher temperatures is to use piezoelectric materials with a higher Curie temperature, for instance $GaPO_4$ or $LiNbO_3$. Ultrasonic transducers based on $LiNbO_3$ piezoelectric elements were used, for instance, as detector for the fluid level of liquid sodium in Liquid Metal Fast Breeder Reactors (LMFBR) [6]. Such measuring systems work up to temperatures of about 700°C, but, there is a significant loss in the piezoelectric properties at high temperatures. Such transducers show a low coupling factor resulting in a poor signal-to-noise ratio. The sensitivity of a sensor required for UDV cannot be achieved.
Another approach is described here. An integrated ultrasonic sensor is designed consisting of the piezoelectric element and an acoustic wave guide made of stainless steel. The effect of the wave guide is the thermal and the chemical decoupling between the active transducer and the fluid. Therefore, the wave guide allows to extend the range of UDV applications to higher temperatures and measurements in chemically reactive fluids.

2. Wave guide concept

The goal of our activities is to develop an ultrasonic sensor which can work up to maximum temperatures of about 800°C. Stainless steel was selected as wave guide material. Steel resists against a number of metallic melts at these high temperatures. Moreover, there are several technologies available to achieve wetting between the metallic melt and the wave guide material.
To meet these requirements an integrated ultrasonic probe consisting of a wave guide and a piezoelectric transducer equipped with electronic components and a stainless steel housing was developed. A scheme and a photograph of this probe is shown in Figure 1. The wave

[1] University Nishni-Novgorod, 603 600 Nishni-Novgorod, Russia

guide is fabricated from a stainless steel foil with a thickness of 0.1 mm which is wrapped axially around a capillary tube. The wave guide is closed at the front end by means of laser beam melting resulting in a flat stainless steel surface. This surface has to be prepared for the measurements to obtain a sufficient wetting with the liquid metal.
The working frequency f of the ultrasonic transducer is 4 MHz. For measurements of the Doppler shift in the signal a dispersion-less propagation of the ultrasonic wave inside the wave guide has to be required resulting in a restriction of the thickness d of the wave guide according to the following relation [7]:

$$\frac{d \cdot f}{c} < 0.1 \tag{1}$$

The sound velocity c for longitudinal waves propagating in steel is about 5000 m/s. Therefore, in our case the thickness d has to be limited to a maximum of 0.125 mm to provide a mono-mode behaviour of the wave guide.
The wave guide has an outer diameter of 7.5 mm and a length of 200 mm. The half angle δ of the divergence of the ultrasonic beam depends on the diameter of the emitter D and the wavelength λ:

$$\delta = \arcsin\left(\frac{1.22 \cdot \lambda}{D}\right) \tag{2}$$

From relation (2) we obtain an angle δ of 3.5° in water and 4.2° in PbBi, respectively.

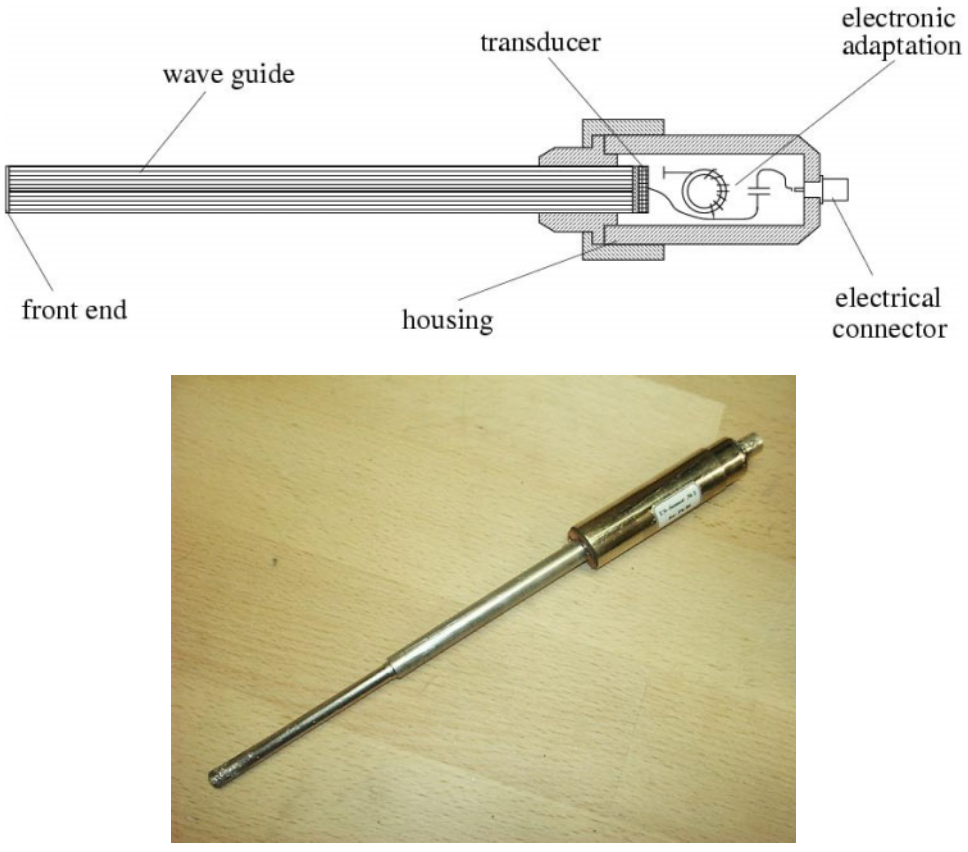

Fig. 1: Schematic view and photograph of the integrated ultrasonic probe

3. Velocity measurements in liquid metal alloys

To prove the capability of the integrated ultrasonic sensor for applications at high temperatures velocity measurements were performed in metallic melts. Here, we report about experiments made in PbBi at temperatures between 180°C and 300°C and in CuSn at temperatures of about 620°C.
The detected flows were driven by a swarm of rising N_2 gas bubbles in PbBi and by means of a mechanical stirrer in CuSn, respectively. The DOP2000 ultrasonic velocimeter manufactured by Signal-Processing SA (Lausanne, Switzerland) has been used to carry out the velocity measurements.

3.1 PbBi bubbly flow

The UDV method has already been used for measurements of bubbly flows in water [8].
We have carried out similar experiments in the eutectic alloy PbBi (Pb44Bi56, melting point 125°C). The experimental facility with the sensor position is shown in Figure 2. A cylindrical container made of stainless steel with a diameter of 125 mm and a height of 250 mm contains about 2.5 l of the liquid metal. The container is provided with an electrical heater. Isolated thermocouples (chromel-alumel) are used to determine the temperature of the fluid. The measurements were performed at fluid temperatures between 180°C and 300°C. Nitrogen bubbles were injected into the stagnant liquid metal by means of a single orifice with an inner diameter of 0.5 mm. The orifice is located in the centre of the cross-sectional area of the fluid container 160 mm below the free surface of the melt. The gas flow rate was controlled by means of a mass flow controller (MKS 1359C). The ultrasonic probe was installed through the free surface at a vertical distance of 150 mm and a radial distance of 30 mm with respect to the position of the orifice. The Doppler angle θ was chosen as 20°. The velocities presented below represent the velocity components v_z in vertical direction.

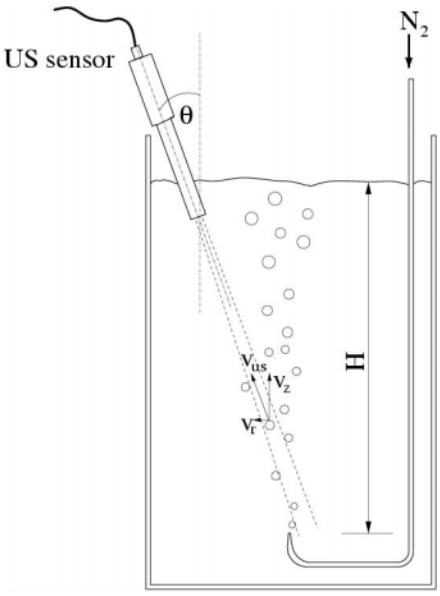

Fig. 2: Experimental scheme of the PbBi bubbly flow facility

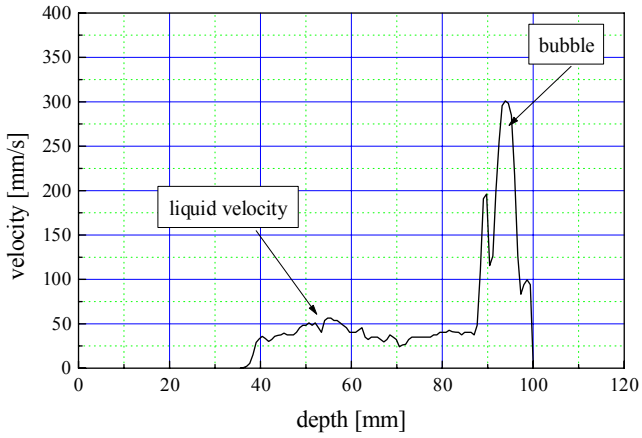

Fig. 3: Typical velocity profile of a singular bubble case

The measurements were restricted to a single bubbly flow regime at small gas flow rates. The maximum gas flow rate was chosen as 3 cm^3/s.
An example for a typical velocity profile obtained from the bubbly flow is shown in Figure 3. The lower velocity at the small measuring depths corresponds to the flow of the liquid metal which is driven by the rising bubbles. Since the ultrasonic pulse is reflected at the bubble interface, the velocity measured can be interpreted as an interfacial velocity. If the entire ultrasonic energy is reflected by the bubble as demonstrated in this example, no information can be received from measuring depths behind the bubble position (shadow effect).

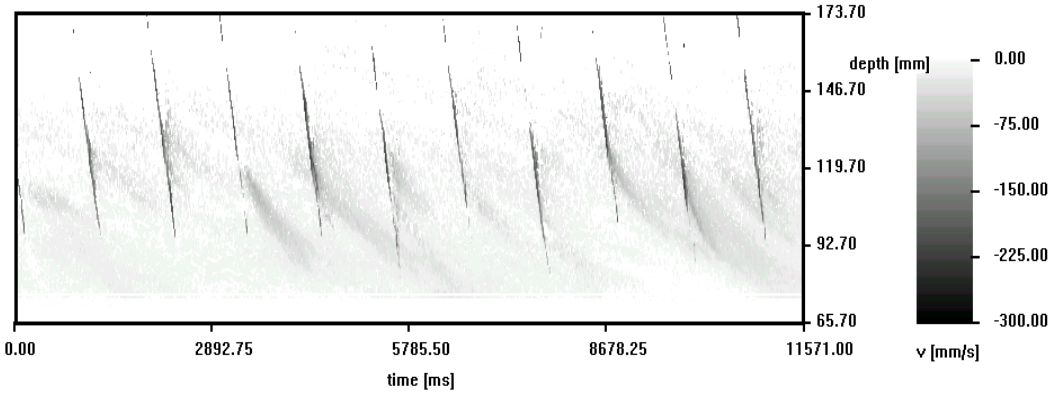

a) $Q_{gas} = 0.034\ cm^3/s$

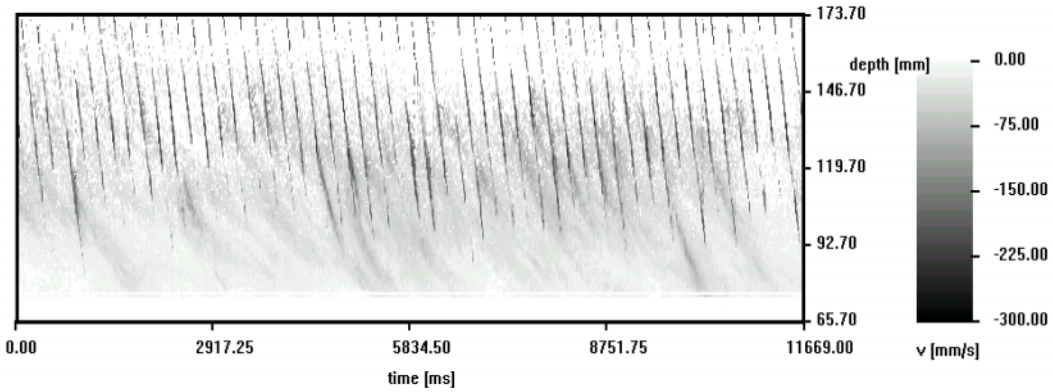

b) $Q_{gas} = 0.224\ cm^3/s$

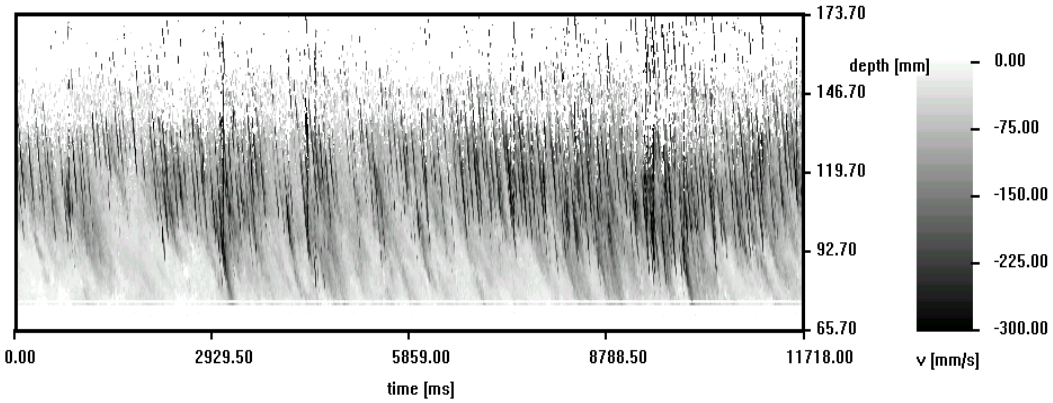

c) $Q_{gas} = 1.119\ cm^3/s$

Fig. 4: Sequences of velocity profiles obtained from the PbBi bubbly flow experiment at different gas flow rates

Measurements of the phase velocities and the bubble frequency were performed for variations of the gas flow rate between 0.034 cm^3/s and 1.119 cm^3/s. The spatio-temporal structure of the bubbly flow becomes obvious in Figure 4 where density plots of the velocity are displayed for gas flow rates of 0.034, 0.224 and 1.119 cm^3/s. The measurement depth of the particular velocity profiles along the ultrasonic beam are drawn on the vertical axis. The x-axis represents the temporal co-ordinate resulting from a line up of 700 velocity profiles measured sequentially. The velocity values are represented by the gray-scale axis on the right hand side of each figure. The sharp signals with the high velocity values coincide with the echoes received from the bubbles passing the measuring volume. A regular chain of single gas bubbles can be observed in the case of the lowest gas flow rate. The bubble frequency is about 1 Hz and increases with growing gas flow rate. The regular structure of the flow is lost if the gas flow rate reaches a value of 1.119 cm^3/s.
A phase separation of the measured velocities was carried out by a calculation of the corresponding probability density functions (PDF). Here, the assumption is made that the PDF of both phases can be expressed by a normal distribution.
Figure 5 shows the averaged mean phase velocities increasing slightly with growing gas flow rate. Corresponding values for the determined bubble frequency and the equivalent bubble diameter, assuming a spherical bubble shape are displayed in Figure 6. Further results and a detailed discussion can be found in [9].

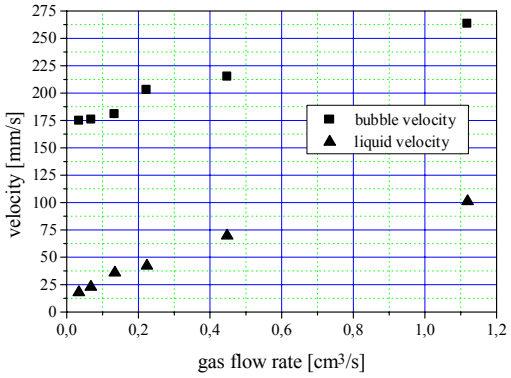

Fig. 5: Averaged phase velocities vs. gas flow rate

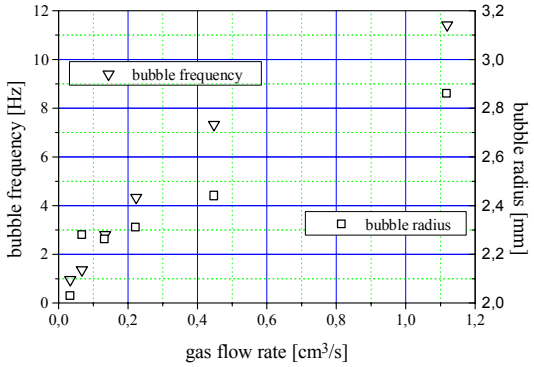

Fig. 6: Bubble frequency and equivalent bubble diameter v.s gas flow rate

3.2 CuSn flow

A demonstration experiment was done in a flow of CuSn alloy (Cu35Sn65, melting point 550°C) at
a temperature of 650°C. The experimental configuration can be seen in Figure 7. The liquid metal was molten inside a rectangular alumina crucible (130 × 80 mm^2) by means of a high frequency inductive heating system (ELDEC, 150-350 kHz, 20 kW). The depth of the melt was about 40 mm. The melt temperature was controlled using a bolometer.
The sensor was dipped into the metallic alloy through the free surface. A clear velocity signal could be obtained by an up and down movement of the sensor inside the melt volume. As a next step a mechanical stirrer was used to generate a flow. The ultrasonic probe was installed at two positions on both sides of the stirrer (see Figure 7) with a Doppler angle of 35°. The inductive heating system was switched off during the velocity measurements. Results obtained from this experiment are displayed in Figure 8. The mean velocity profiles determined at both measuring positions are similar with respect to the shape and the

amplitude, but show different signs in accordance with the chosen rotation direction of the mechanical stirrer. Several repetitions of the measurements showed the reproducibility of the results of the mean velocity.
After an exposing time of about 30 minutes the ultrasonic sensor was still working, however, the quality of the signal starts slightly to deteriorate because the wave guide and the stirrer started to be dissolved by the metallic melt. The removal of the probe from the liquid metal revealed a destruction of the outer layer of the stainless steel foil. At the same exposing time the stirrer was almost dissolved. In order to improve the stability of the sensor for the next experiments a new variant of the integrated probe will be designed where the acoustic wave guide is covered by an additional protective shield. The temperature near the piezoelectric element was controlled during the experiments. The values observed were always significantly below 100°C. Therefore, we can expect a reliable function of the integrated sensor also at higher temperatures of about 800°C.

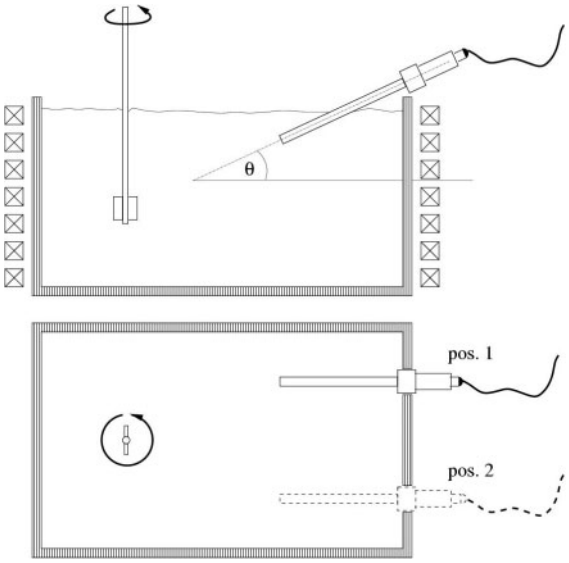

Fig. 7: Schematic view of the CuSn experiment

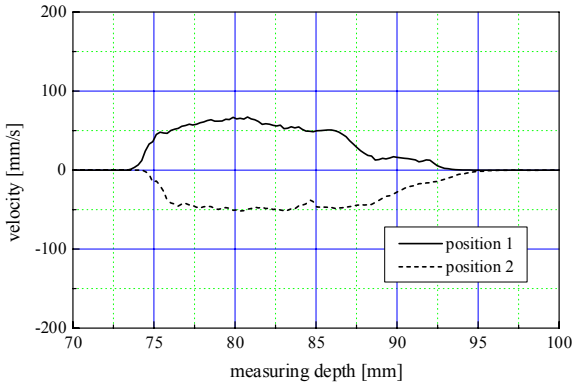

Fig. 8: Mean velocity profiles obtained at two different positions in the CuSn melt

4. Conclusions

A new type of an integrated ultrasonic probe for measurements with the ultrasound Doppler velocimetry (UDV) has been developed. The use of this integrated sensor enables the possibility to apply the UDV for velocity measurements in hot, metallic melts up to about 600 – 800°C. This approach may open a new field for applications of UDV. It represents a powerful measuring technique for investigations of the velocity structure in liquid metals, thus improving the poor measuring situation for such kind of opaque fluids.
The reliability of the sensor has been demonstrated with successful measurements in PbBi at 300°C and CuSn at 650°C. The sensor delivered clear signals leading to reproducible results of velocity profiles. We expect that an application of this measuring technique should also be possible at temperatures of about 800°C. In a next step we will focus our activities on a further development of the sensor design. Protective layers will be used to enhance the chemical stability of the wave guide material in copper alloys and pure copper. Furthermore, we will work on an application of our integrated probe in liquid aluminium. Here, besides the

temperature some other serious problems will occur with respect to the wetting, the handling of the oxide layers or the chemical action of the aluminium on the wave guide material.

References

[1] Takeda Y. (1991) Development of an ultrasound velocity profile monitor, Nucl. Eng. and Design Vol. 126, (pp. 277-284)

[2] Takeda Y. (1987) Measurement of velocity profile of mercury flow by ultrasound Doppler shift method, Nucl. Techn. Vol. 79, (pp. 120-124)

[3] Takeda Y., Kikura H. and Bauer G. (1998) Flow Measurement in a SINQ Mockup Target using Mercury. Proc. of ASME FED Summer Meeting, Washington DC

[4] Brito D., Nataf H.-C., Cardin P., Aubert J., Masson J.P. (2001) Ultrasonic Doppler Velocimetry in liquid gallium, Exp. Fluids Vol. 31, (pp. 653-663)

[5] Eckert S., Gerbeth G. (2002) Velocity measurements in liquid sodium by means of ultrasound Doppler velocimetry, Exp. Fluids Vol. 32, (pp. 542-546)

[6] Boehmer L.S., Smith R.W. (1976) Ultrasonic instrument for continuous measurement of sodium levels in fast breeder reactors. IEEE Trans. Nucl. Sci. Vol. 23, (pp. 359-362)

[7] Melnikov V.I., Usynin G.B. (1987) Acoustic diagnostic methods for two-phase coolants of a nuclear energy station. Energia Atomizdat, Moscow (in Russian)

[8] Suzuki Y., Aritomi M., Kikura H. (2000), Measurement of the flow around bubbles using the ultrasonic velocity profile monitor. Bulletin of the Research Laboratory for Nuclear Reactors (Tokyo Institute of Technology) 3: 93-99

[9] Eckert S., Gerbeth G., Melnikov V.I. (2002), Velocity measurements at high temperatures by ultrasound Doppler velocimetry using an acoustic wave guide, submitted to Exp. Fluids

Acknowledgement

This work was supported by Deutsche Forschungsgemeinschaft in form of the DFG-Innovationskolleg "Magnetofluiddynamics of Electrically Conducting Fluids" (INK18/B1-1), by the Saxonian Ministry of Research under grant No. 4-7531.50-02-844-01/1 and by the European Community in frame of the Growth Programme under grant No. G6RD-CT-1999-00045 (project "HITUV"). The financial support is gratefully acknowledged.

GAMMA TOMOGRAPHIC VISUALIZATION OF THE FLUID DISTRIBUTION IN A HYDRODYNAMIC COUPLING

Dietrich Hoppe, Juergen Fietz, Uwe Hampel, Horst-Michael Prasser, Cornelius Zippe, Karl-Heinz Diele[1], and Reinhard Kernchen[1]

1. Introduction

Gamma tomography is a useful tool for the investigation of single and multiphase flow phenomena. In particular, when phase distributions and flow patterns are to be assessed non-invasively in opaque containments, it is often the only applicable and most reliable method [1], [2]. In the past few years, a gamma tomography apparatus has been developed at the Institute of Safety Research at Research Center Rossendorf which can be used to visualize quasi-stationary fluid distributions in rotating hydromachines, such as axial pumps, mixers, turbines or hydrodynamic couplings [3]. The characteristic principle of the system is the acquisition of tomographic projections in synchronization with the rotation cycle of the investigated object [4]. Furthermore, the approach is based on a difference imaging principle where the distribution of the radiologically less absorptive fluid is reconstructed from a difference measurement of the empty machine and the machine at load. In that way, the absorption contribution of the radiologically dense material of the machine body itself is eliminated before reconstruction resulting in clean slice images of the interesting fluid distribution.

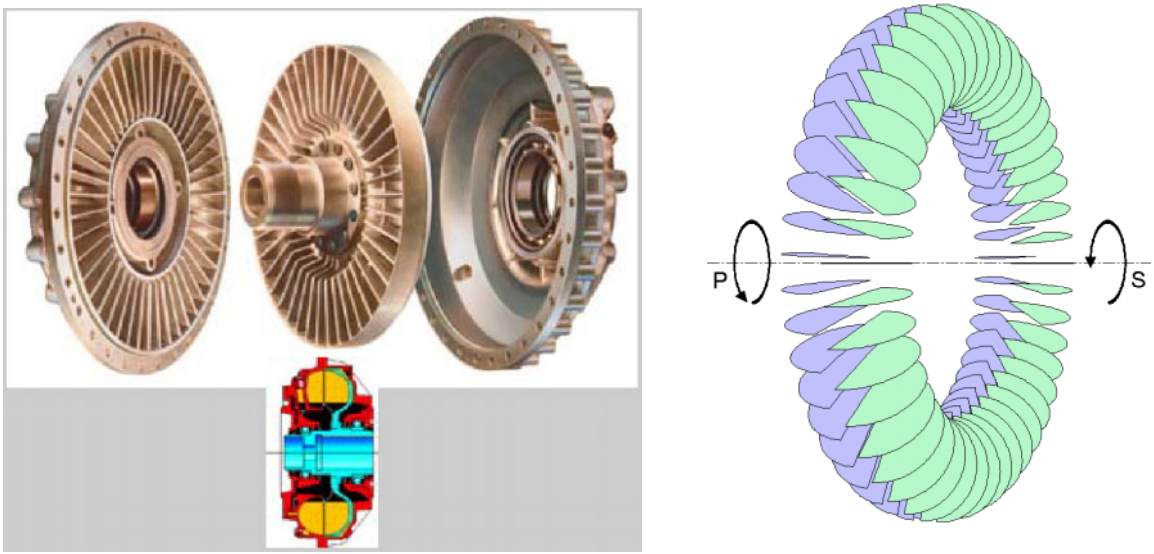

Fig. 1: Assembly and functional principle of a hydrodynamic coupling.

[1] Voith Turbo GmbH Crailsheim

2. Hydrodynamic couplings

Hydrodynamic couplings serve as torque conversion elements in heavy load rotating drive systems and can be found in numerous technical systems such as power plants, naval vessels, railed vehicles, busses and trucks. [5]. They use the principle of torque conversion by means of a fluid – a principle that is superior to other coupling mechanisms in terms of conversion efficiency, smooth transient behavior, low material deterioration and thus long durability.

The functional principle of a hydrodynamic coupling is described in Fig. 1. The coupling comprises a metal housing and two axially supported bladed wheels which oppose each other. In the presence of a coupling fluid, which is oil in most cases but may also be water, a torque is transferred from the rotating primary wheel (P) to the secondary wheel (S). Thereby, the rotational speed n_S is lower than the rotational speed n_P, which is referred to as the slip $S = 1 - n_S / n_P$. The conversion of power in a hydrodynamic coupling depends on the geometry and design of the coupling elements (distance of the bladed wheels, number, shape, and arrangement of the blades) and on the filling level F. The latter may be used to realize the coupling function, i. e., the smooth coupling and decoupling of engine and load by varying F with a filling control system.

An optimization of the static and transient behavior of a hydrodynamic coupling in operation is mainly achieved by thorough design of the coupling elements. However, to assess the interrelation of flow patterns, torque conversion characteristics and coupling design it is required to look inside the coupling during operation. One way to achieve this is to build test couplings with optically clear housing parts for visual inspection. However, optical methods such as stroboscopic video imaging give poor information on the fluid volume distribution due to multiple reflection and refraction of light at the phase boundaries. They also require larger manufacturing effort and provide less flexibility to the experimenter since the design of the test coupling and its surroundings must be accommodated to the needs of visual inspection. One aim of the reported work was thus to initially prove the applicability of gamma tomography to the diagnostics of flow phenomena in hydrodynamic couplings.

3. Tomographic measurement system

The Rossendorf gamma tomograph is shown in Fig. 2 as it was installed at the hydrodynamic coupling test facility at Voith Turbo GmbH in Crailsheim. The system consists of a Cs-137 source with an overall activity of $1{,}85 \cdot 10^{11}$ Bq, a detector arc, a tomograph gantry, a control and data acquisition unit, and a measurement PC. The gamma source is a cylindrically shaped capsule with a diameter of 5,8 mm and a length of 11,9 mm contained in a double-welded stainless steel envelope which in turn resides in a shielded working container. The source can be manually driven to the working position by means of a bowden cable. A collimator that is mounted in front of the source container provides a spatial limitation of the gamma radiation to an angle of 60° within the measurement plane and 10° axial. The detector arc is mounted on the gantry in a distance of 1200 mm away from the source. It consists of 64 consecutively arranged BGO crystals with 1 cm x 1 cm active area and 3 cm depth. The scintillation light is converted to electrical pulses by photomultipliers (one per crystal) which are further processed by proper analog electronics, comprising a pulse forming amplifier and an energy discrimination stage which excludes the scattered events from the data. A subsequent digital electronics counts the valid events of each detector in hardware. Additionally, the measurement PC acquires the signals from two zero-angle transmitters at the primary and the

secondary coupling shaft. The source container and the detector arc are mounted in horizontal position on the tomograph gantry which itself resides on sliding rails such that the whole system can be manually moved to a desired axial scanning plane. The test coupling itself is in the center of this arrangement.

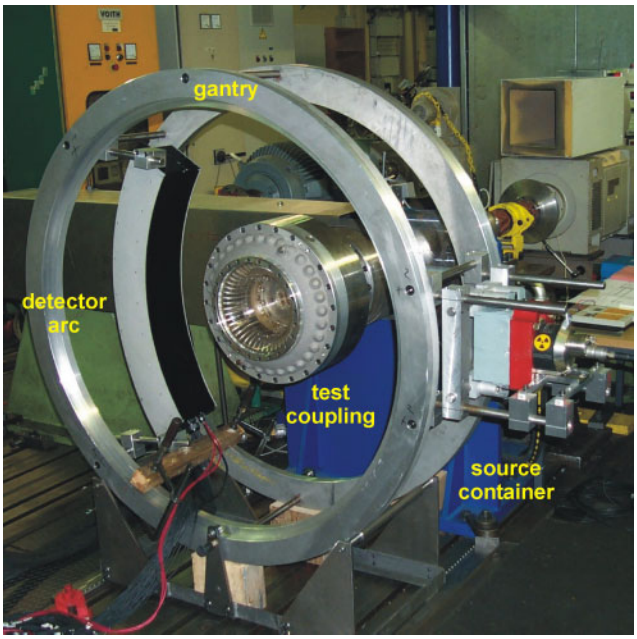

Fig 2: Gamma tomograph at the coupling test facility.

The tomographic reconstruction principle requires the measurement of the integral radiological density for the 64 spatial channels defined by the source and the detector elements and for a number of equally spaced rotation angles. To achieve the angular resolution the counting of valid detector events is limited to intervals of approximately $T = 100$ µs. From the counter values obtained at these intervals a sinogram is built whose number of projection angles is defined by the time per rotation, obtained from the zero-angle transmitter, devided by T. The resulting count number sinogram is further processed to a data set suitable for image reconstruction. From the linear relationship

$$N = N_0 \exp\left(- \int_{source}^{detector} \mu_{Fluid}(s)\, ds \right) \tag{1}$$

with N_0 denoting the count number at a given detector and angular interval for an empty coupling, N the corresponding count number for a coupling partly filled with fluid, and μ_{Fluid} the mass extinction coefficient distribution of the fluid along the ray path parameterized by s it follows, that the integral extinction value E, which is the input data for image reconstruction, is calculated as

$$E = \ln N_0 - \ln N\,. \tag{2}$$

The overall spatial resolution of system is mainly limited by the size of the source and the detector elements. From experiments we have determined the resolution to be about 5 - 6 mm in the vicinity of the object's center.

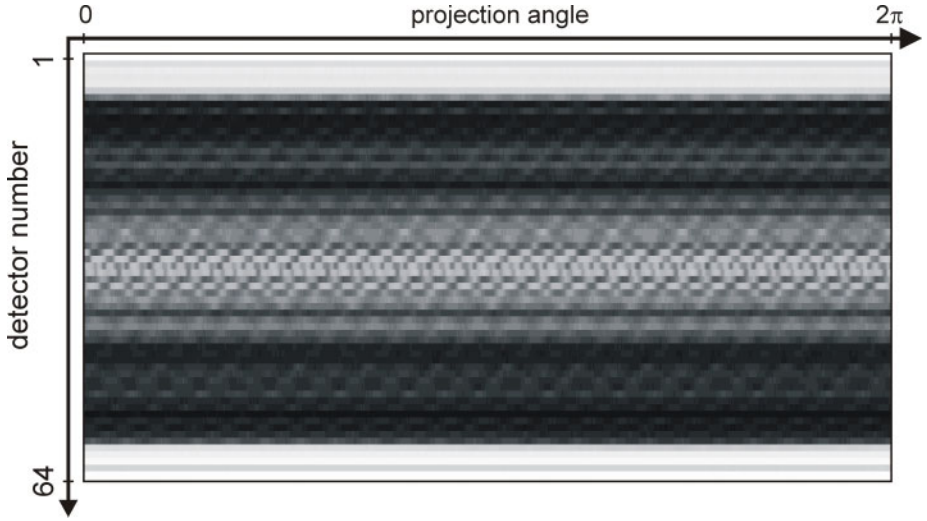

Fig. 3: Normalized gray value represenation of a count number sinogram.

4. Image reconstruction

For image reconstruction, we applied the method of filtered backprojection [6] which we will only briefly sketch in the following. The two-dimensional object space in the tomographic plane has been divided into 491 x 491 square pixels with 1.1 mm edge length. With this discrete representation the image reconstruction process can be formally described as an algebraic operation that reconstructs the fluid mass extinction coefficient μ_{ij} in each pixel *(i,j)*. With the μ_{ij} lumped together in the object vector $\boldsymbol{\mu}$ and the sinogram data in the data vector $\mathbf{m}$ and furthermore introducing the projection matrix $\mathbf{A}$ which contains the geometric area contributions of each pixel to each projection channel, the discrete backprojection is defined by the transformation

$$\mathbf{b} = \mathbf{A}^T \mathbf{m} \tag{3}$$

giving the backprojection image $\mathbf{b}$. This backprojection image is processed to the original object distribution by application of the reconstructing filter matrix $\mathbf{H}$ with

$$\boldsymbol{\mu} = \mathbf{H}\,\mathbf{b} = \mathbf{H}\,\mathbf{A}^T \mathbf{m}\,. \tag{4}$$

The ideal reconstruction operator is given by the discrete Fourier inverse of the two-dimensional ramp filter [6]. However, to avoid image degradation by the present data noise this filter is modified with an apodising cosine window. To increase computational efficiency the deconvolution in equ. 4 is realized by a matrix multiplication in the Fourier domain.

5. Results

A complex experimental program has been carried out to acquire data from different axial planes and operating points of the test coupling. Performing a single scan thereby comprised the following experimental steps:

- selection of the axial plane by manual positioning of the tomograph;
- driving the hydrodynamic test coupling into its operational state (filling level, primary angular speed, secondary angular speed);
- acquisition of projection data over 300 seconds.

This procedure has been repeated for an overall number of 179 tomographic scans. The region of most interest within the hydrodynamic coupling are the chambers formed by the blades of the primary and secondary wheel. Within this region a number of six axial measurement planes has been selected for experimental investigation (Fig. 4). The reconstruction of the cross-sectional image of one such plane (plane no. 3) is illustrated in Fig. 5. The two top images are the reconstruction results for the test coupling with no water (a) and for a water level of F=0.3 (b) at S=0. In both images the material structures of the coupling elements, such as blades and mounting holes, are clearly shown. The water phase is recognized as a dim ring at the outer bladed region. The reconstruction from the difference sinogram is shown in Fig. 5c. Here all invariant image details are cancelled out and the annular water phase is clearly displayed. In Fig. 5d the same reconstruction result is displayed in color for clarity and a scale is provided which indicates the calculated water content of each pixel. Although the fluid distribution is clearly reconstructed, there are also some image distortions to be recognized. Thus, the granularity of actually homogeneous object regions results from statistical noise and background scattering. Partial volume effects combined with the low-pass filtering at the reconstruction stage lead to smooth fluid distribution gradients at the far radius of the fluid annulus where sharp gradients would be expected. Another resolution-related artifact is the appearance of “continuation of the blades and chambers” into the inner section where the test coupling is actually hollow.

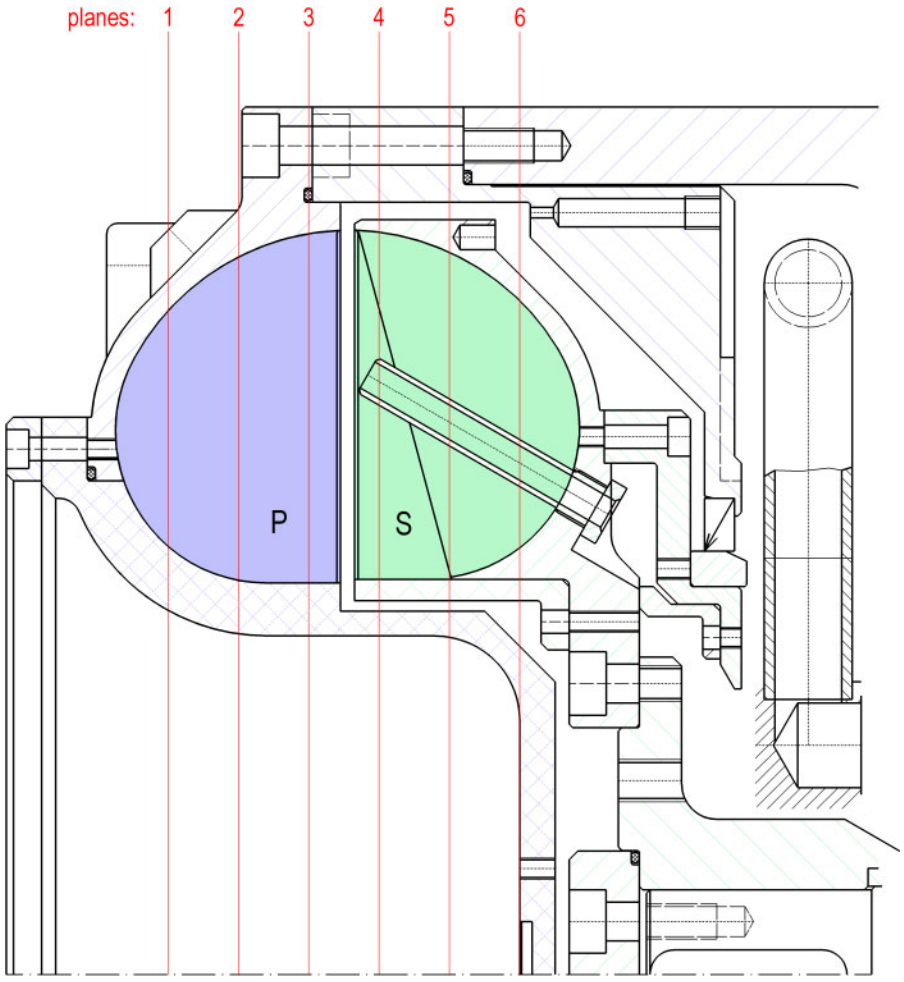

Fig. 4: Axial cross-section of the blades with position of the tomographic planes.

Fig. 6 shows the image stack for all reconstructed slices. From a set of such 2D images taken for the test coupling at F=0.3 and S=0.75 a three-dimensional fluid distribution has been fused, showing the mean volume distribution of the coupling fluid for both primary and secondary side, each reconstructed according to its own angular speed. It should be noted, that only fluid dynamic processes with the angular speed equal to the that of the blades are sharply mapped. Other quasi-stationary components of the flow, which may for example extend from one side into the other are to some degree blurred. Furthermore, it should be mentioned, that the varying mass fraction of the material within the tomographic planes currently limits the absolute accuracy of the fluid mass coefficient reconstructed with the filtered backprojection method which brings about some problems when fusing images of different slices together.

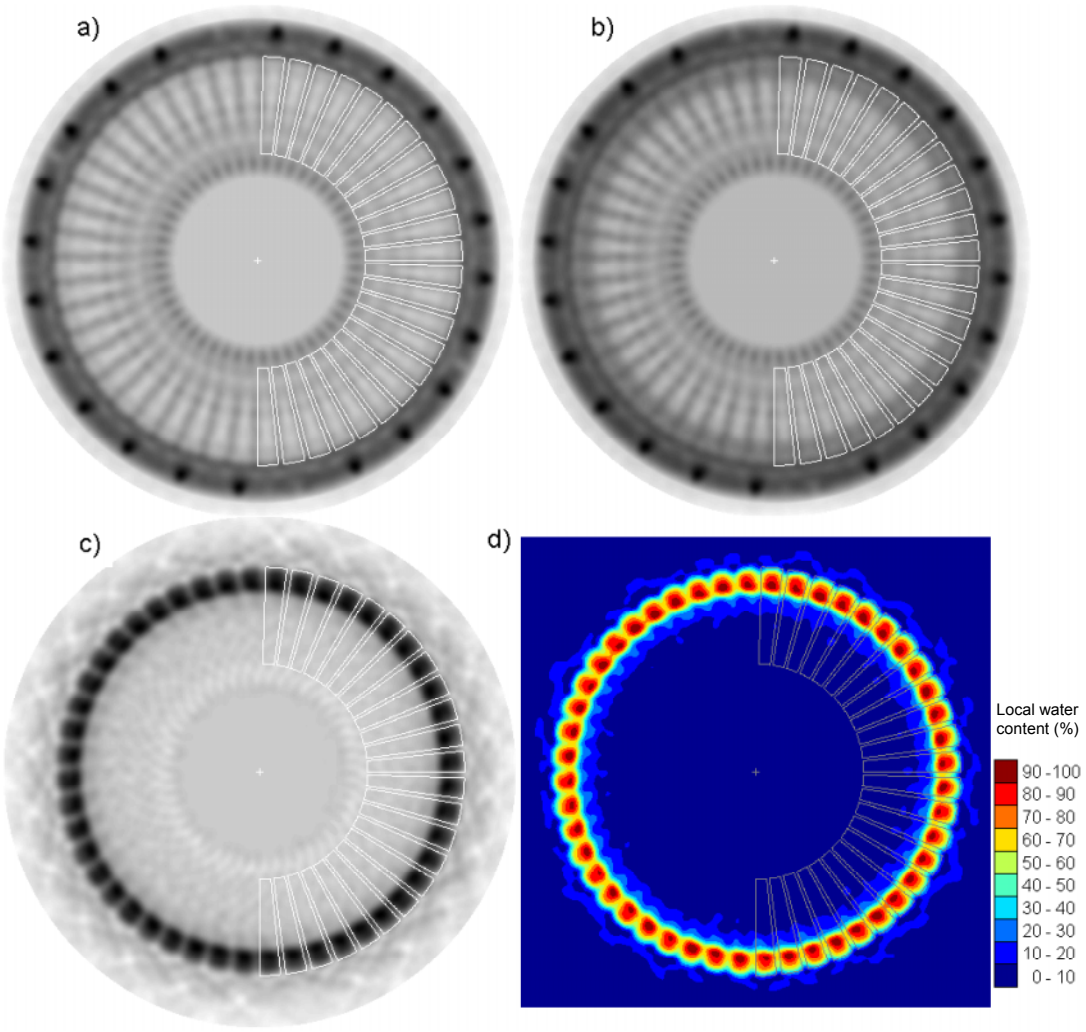

Fig. 5: Reconstructed images of slice no. 3 for the test coupling at S=0. a) Empty coupling (F=0.0), b) filled coupling with F=0.3, c) difference image showing the water distribution, d) color image of c).

6. Discussion

The method of gamma tomography has been used to visualize quasi-stationary fluid distributions in the primary and secondary chamber system of a hydrodynamic coupling in different modes of operation. The reconstructed images give a considerable amount of

information on the interrelation of the coupling design and the local transfer of kinetic energy between the bladed wheels, which may by useful to optimize the design and layout of the coupling elements for specific applications. Though gamma tomography proved to be highly successful for this application remaining problems to be solved in the future are the improvement of spatial resolution and an increase of accuracy in the reconstructed absolute extinction values which may be achieved by iterative image reconstruction algorithms.

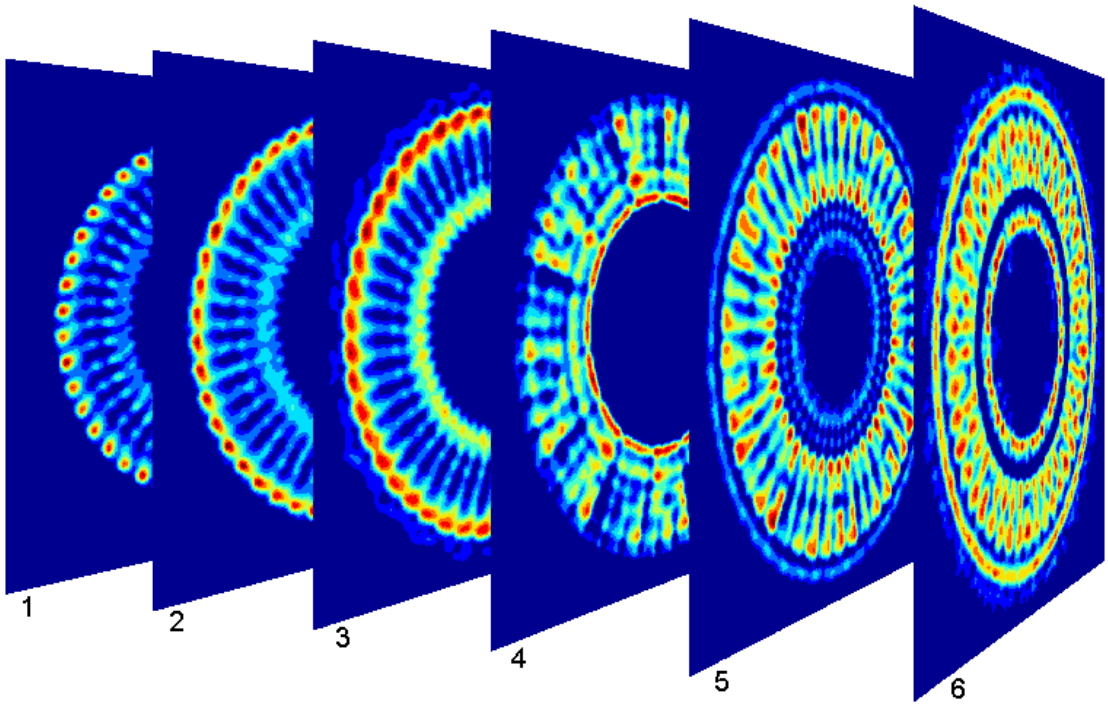

Fig. 6: Series of reconstructed images for the six consecutive axial planes shown in Fig. 4.

References

[1] A. C. Devuono, P. A. Schlosser, F. A. Kulacki, P. Munshi, "Design of an isotopic CT scanner for two-phase flow measurements", IEEE Trans. Nuclear Science, **NS-27,** 1980.

[2] T. Frøystein, "Flow imaging by gamma-ray tomography: data processing and reconstruction techniques, systems", in *Frontiers in Industrial Process Tomography II*, 8–12.4.97, Delft (NL), pp. 185–187, 1997

[3] H.-M. Prasser, D. Baldauf, J. Fietz, U. Hampel, D. Hoppe, C. Zippe, J. Zschau, M. Christen, G. Will, "Time resolving gamma-tomography for periodically changing gas fraction fields and its application to an axial pump", to be published in Flow Meas. and Instrument., 2003.

[4] H.-M. Prasser, J. Zschau, "Anordnung zur messtechnischen Erfassung einer Projektion des Strahlabsorptionsvermögens eines periodisch veränderlichen Messobjektes", Erfindungsanmeldung Az. 101 17 569.8, 1999.

[5] H. Höller, „Hydrodynamische Kupplungen mit konstanter Füllung", Publikation der Voith Turbo GmbH & Co. KG, Crailsheim.

[6] A. C. Kak and M. Slaney. *Principles of Computerized Tomographic Imaging*. IEEE Press, New York, 1987.

ANALYSIS OF THE BOILING WATER REACTOR TURBINE TRIP BENCHMARK WITH THE CODES DYN3D AND ATHLET/DYN3D

Ulrich Grundmann, Soeren Kliem, and Ulrich Rohde

1. Introduction

The three-dimensional core model DYN3D was developed for steady-state and transient analysis of thermal reactors of western type with square fuel assemblies and Russian VVER type with hexagonal fuel assemblies [1]. It was coupled with the thermal-hydraulic system code ATHLET [2] of the German Gesellschaft fuer Anlagen- und Reaktorsicherheit (GRS) for best-estimate analyses of the reactor systems. DYN3D consists of three-dimensional neutron kinetic models coupled with one-dimensional thermal hydraulics in parallel core channels. The ATHLET code has its own neutron models which consists in point kinetics or one-dimensional kinetics. The codes DYN3D and ATHLET can be used coupled or as stand alone. In accomplishing the coupling of ATHLET and DYN3D two basically different ways, the so-called internal and external couplings were used [3].

For the calculation of the benchmark, the codes have been coupled using a modified version of the external coupling, the so-called 'parallel coupling'. Contrary to the pure external coupling, where the core is cut off from the system model and the DYN3D-core model is directly coupled to the system model through two interfaces in the lower and upper plenum, in the new coupling both core models are running in parallel. ATHLET containing its own core model calculates the behaviour of the whole plant and provides pressure boundary conditions at the core inlet and outlet and the core inlet coolant enthalpy. Using these boundary conditions, the whole core behaviour is calculated by DYN3D and the total core power is transferred to the ATHLET-core. This parallel coupling shows a more stable performance at low time step sizes necessary for a proper description of the feedback in the calculation of the current boiling water reactor benchmark problem.

The OECD/NRC (Organisation for Economic Co-operation and Development/Nuclear Regulatory Commission) Boiling Water Reactor (BWR) Turbine Trip (TT) Benchmark based on the turbine trip test 2 (TT2) in the American Peach Bottom 2 reactor [4] was analysed to validate the code DYN3D and the coupled system DYN3D/ATHLET for BWR's. Moreover, groups from several countries around the world participate in the benchmark for the validation of the code systems.

The transient was initiated by the closure of the turbine stop valve. The resulting pressure wave propagates to the core. It is attenuated by opening the bypass valve. When the wave reaches the core the void in the core is reduced, which results in an increase of the reactivity and power. The power peak is limited by the Doppler effect and the reactor scram. The scram was initiated at t = 0.63 s. The control rod motion starts with a delay of 0.12 s at t = 0.75 s. It has a significant influence on the power after the power peak. The transient was investigated in the time interval from t = 0 to 5 s.

The benchmark consists of three different exercises:

- Exercise 1 - Simulation of the transient by means of an advanced thermal-hydraulic system code using a fixed power curve based on the experimental data.
- Exercise 2 - Calculation of the core response on given time-dependent thermal-hydraulic boundary conditions.
- Exercise 3 - Best-estimate coupled 3D neutron kinetic core/thermal-hydraulic system calculation.

The modelling of the Peach Bottom reactor is described in Sec. 2. Concerning the modelling of the BWR core several simplifications and their influence on the results are investigated for the Exercise 2 with the core model DYN3D. DYN3D allows calculations with and without assembly discontinuity factors (ADF) to study their influence on this transient. The calculations with DYN3D are performed with 764 coolant channels (1 channel per fuel assembly). Depending on the used codes several participants of the benchmark performed calculations with only 33 thermal-hydraulic channels. The influence of the number of coolant channels was studied by different calculations with DYN3D. The phase slip model of MOLOCHNIKOV [5] is the standard model of DYN3D for void fraction calculation. A comparison was made with the ZUBER-FINDLAY model [6]. The results of the different modifications are compared in Sec. 3 with the results of the standard model based on 764 coolant channels, the consideration of the ADF, and the phase slip model of MOLOCHNIKOV.

The Exercise 3 was calculated with the parallel coupling ATHLET/DYN3D. The core model in these calculations is the standard DYN3D model applied for the calculations for Exercise 2. The thermal-hydraulic model of ATHLET was used as applied for the calculations of Exercise 1. Key results are compared with the measurements in Sec. 4.

2. Modelling of the Peach Bottom 2 reactor

The BWR Peach Bottom 2 reactor core consists of 764 fuel assemblies [4], each of them is modelled by one thermal-hydraulic channel in the standard case. The core was divided into 24 axial layers. Each of them has a height of 15.24 cm. The assemblies and their water gap have a width of 15.24 x 15.24 cm which determines the radial size of the nodes. The density of the bypass coolant flowing between the fuel assemblies (fuel assembly bypass) is different to the two-phase flow density inside the channels. About 1.7% of the generated power is released in the bypass. Performing the cell calculations with the CASMO code [4] the coolant density was assumed at saturation temperature in the bypass. Due to the specification, a density correction has to be taken into account in the nodal two-group cross section calculation, if the density in the bypass deviates from the saturation value. As a sufficient approximation all fuel assembly bypasses are lumped to one bypass channel in DYN3D. The DYN3D calculations are based on the given total mass flow rate through the core. Applying the thermal-hydraulic model FLOCAL of the DYN3D code the flows through the individual channels are calculated using

Table 1: Key parameters of the initial state of the turbine trip test 2

thermal power	2030 MW
pressure (core outlet)	6.798 MPa
inlet temperature	274 °C
total core mass flow	10445 kg/s
inchannel mass flow	9603 kg/s
Core average void fraction	30.4 %

the resistance coefficients of the channels according to the specification [4]. In the case of given total mass flow rate, the individual flows through the channels are determined by the condition of equal pressure drop over the core. The decay heat is calculated by the model implemented in DYN3D assuming an infinite operation at the power level of the initial state of the TT2. It is based on the German standard [7]. In DYN3D, each coolant channel is described by one average fuel rod. The power of a coolant channel is obtained by averaging the nodal powers of the fuel assemblies belonging to it. The main parameters of the initial state of TT2 are given in Table 1. The transient calculations for the Exercise 2 were performed with given transient thermal-hydraulic boundary conditions, i.e. pressure, at the core exit, the total mass flow rate and the core inlet temperature.

For the calculations of Exercise 3, the ATHLET-input deck developed and used by the Gesellschaft fuer Anlagen- und Reaktorsicherheit (GRS) for Exercise 1 has been used. This input deck consists of the lower plenum, the core region with one single thermal-hydraulic core channel and one bypass channel, the upper plenum, stand pipes, and the separator. Fig. 1 shows a node scheme of the Peach Bottom 2 plant developed for the code RETRAN [4]. The downcomer section is splitted into several parts, to include the jet pumps and the diffusors. Two symmetric recirculation loops, one steam line up to the turbine stop valves and the turbine bypass line are modelled For the Exercise 3 calculations, the above described standard core model with 764 thermal-hydraulic channels was applied in DYN3D. The core boundary conditions were transferred from the ATHLET code to DYN3D. Instead of the total mass flow rate (Exercise 2) the pressure drop over the core calculated by the ATHLET-model was used as boundary condition.

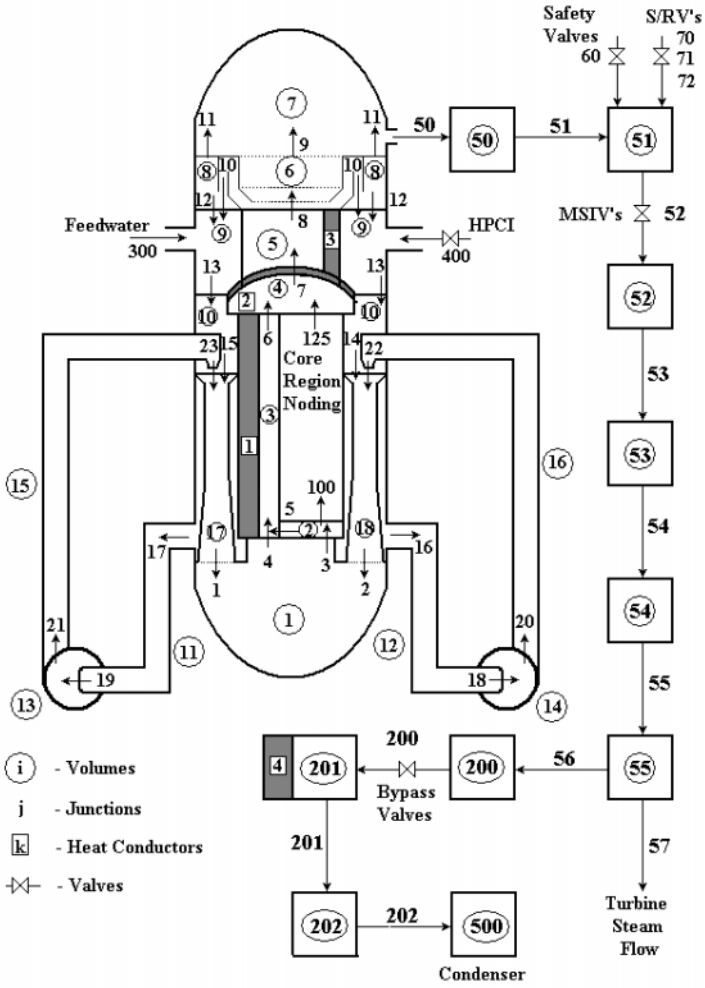

Fig. 1: RETRAN node scheme of the Peach Bottom 2 plant [4]

3. Steady-state and transient results for Exercise 2 using DYN3D

A hot zero power (HZP) state was defined with equal thermal-hydraulic parameters in all nodes for a first comparison of the codes. It was calculated with and without the ADF to investigate their influence. Table 2 gives the results for the eigenvalue k_{eff}, the 3D nodal power

Table 2: Influence of the ADF on k_{eff} and power peak factors at HZP and the initial state of the turbine test 2.

	HZP Without ADF	HZP With ADF	HZP Diff. (%)	TT2 Without ADF	TT2 With ADF	TT2 Diff. (%)
k_{eff}	0.99133	0.99654	0.53	1.00270	1.00410	0.14
F_Q	5.056	5.364	6.1	2.260	2.235	1.0
F_{xy}	1.884	1.998	6.1	1.448	1.448	-
F_z	2.692	2.698	0.2	1.494	1.459	2.4
Max. ass. 75	2.257	2.137	5.6	1.207	1.102	9.5
Max. ass. 367	3.584	3.293	8.8	1.766	1.716	2.9

peak factor F_Q, the assembly power peak factor F_{xy}, the axial power peak F_z of the radially averaged distribution and of the assemblies 75 (peripheral) and 367 (central). It is demonstrated that the ADF's influence the eigenvalue and the radial distribution (F_Q, F_{xy}). Therefore, the maximum values of the axial distribution in single fuel assemblies (for example assembly 75 and 367) show larger differences, while the influence on the averaged axial distribution is small. The power of the initial state of the TT2 is 2030 MW_{th}. Table 2 proves that the influence of the ADF on k_{eff}, F_Q and F_{xy} is smaller at that power level than in the HZP case. However, considering the single assemblies 75 and 367, the influence of the ADF is not negligible.

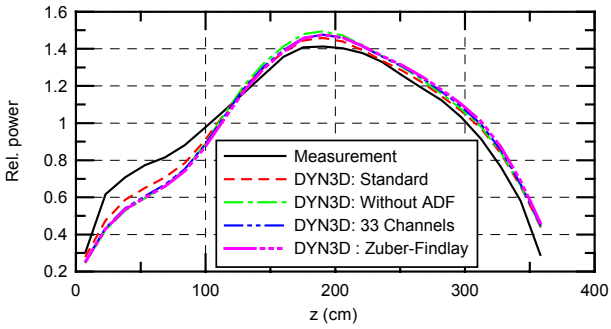

Fig. 2 : Averaged axial power distribution.

The averaged axial power distributions of the TT2 initial state are compared with the measured distribution in Fig. 2 for all different DYN3D calculations described in the introduction. The Figure shows that the differences of the calculations are rather small. The deviations from the measurement are in the range of the results of the other participants taking part in the benchmark. Nevertheless, the standard calculation is closer to the measurement than the other cases. The boiling model of ZUBER-FINDLAY yields only small changes in comparison to the standard model. The changes are caused by the different void fractions obtained with the models. The standard model of DYN3D provides 29.2 % average core void and the ZUBER-

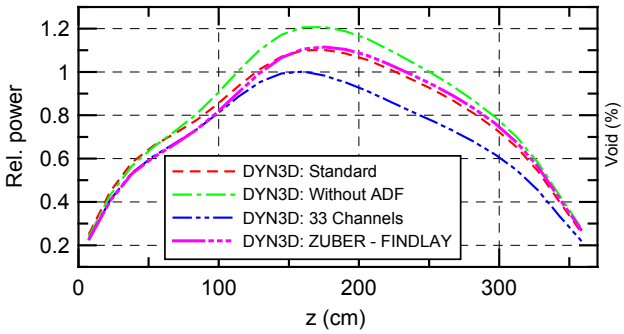

Fig. 3: Axial power distribution in the assembly 75.

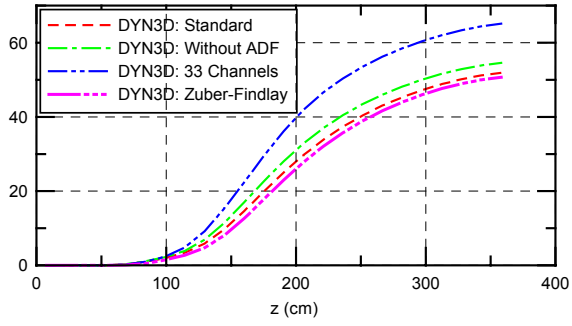

Fig. 4: Void distribution in the assembly 75.

FINDLAY 28.1%, which results in a higher neutron flux in the upper core region when using the ZUBER-FINDLAY model. The results for the peripheral fuel assembly 75 show larger deviations (see Fig. 3). The effect of the ADF depends on the control rod positions. If an assembly is rodded, the deviation of the ADF from unity is larger than for unrodded assemblies. In case of the initial state of TT2, the assembly 75 is rodded. Therefore the consideration of the ADF has a considerable effect on the power generation in this assembly. The higher power in assembly 75 of the calculation without the ADF leads to higher void in the coolant channel (see. Fig. 4). The lumping of the thermal-hydraulic channels of the fuel assemblies to 33 channels also leads to larger differences of power generation in single elements. The model with 33 channels produces a higher void (Fig. 4), because the fuel assembly 75 is linked together with fuel assemblies of higher power. The application of the ZUBER-FINDLAY slip model instead of the standard model provides only small differences in the power and the void distribution, which are in the same order of magnitude as for the radial averaged power distribution (Fig. 2).

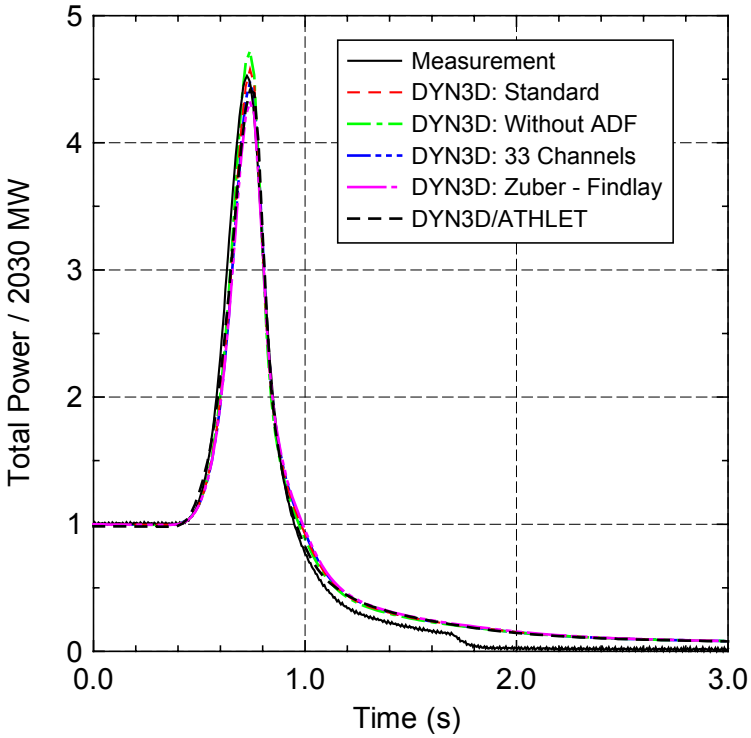

Fig. 6: Total power versus time of the different DYN3D calculations and the DYN3D/ATHLET calculation compared with measurement

In the first phase of the transient up to t = 0.65 s, the core void decreases mainly as a result of the pressure increase. The reactivity change is determined by the change of the coolant density in the core as long as the fuel temperature is unchanged and the shut down is not activated. Fig. 5 shows the power versus time. The reactivity increase by the reduced core void leads to a power excursion. All calculations including the standard simulation provide a relative power peak close to the measured value of 4.5.

4. Calculation of Exercise 3 with the coupled code DYN3D/ATHLET

Fig. 6 shows the calculated steam dome pressure and the pressure at the core exit compared with the measured value in the steam dome and the specified value at core exit which was provided from a TRAC-BF1/NEM calculation [4]. The DYN3D/ATHLET pressures are slightly lower in the initial state than the measured and the specified one. Nevertheless, the time, when the pressures starts to increase is well reproduced by the ATHLET plant model. The calculated absolute pressure increase during the first 0.8 s (the most important time interval in the calculation) is in full agreement with the measurement. This excellent description of the thermal-hydraulic aspects of the transient together with the appropriate DYN3D core model are the basis for the good agreement of the time course of the core power between cal-

culation and measurement which can be seen in Fig. 5. The shape of power increase, the time of the maximum and the maximum value itself agree very well with the measurement. In the later phase of the transient (after t = 2 s) , the calculation slightly overpredicts the system pressure. But this is of no influence on the core power behaviour, because at that time, the core is already in a subcritical state. Fig. 7 shows the comparison of calculations with the measurements of the local power range monitors (LPRMs). The values A, B, C, and D are the radial averaged values of 42 micro fission chambers at four axial levels, which are located at 45.72, 137.16, 228.6 and 304.8 cm above the core bottom. The agreement between calculated and measured time behavior is similar to the power in Fig. 5.

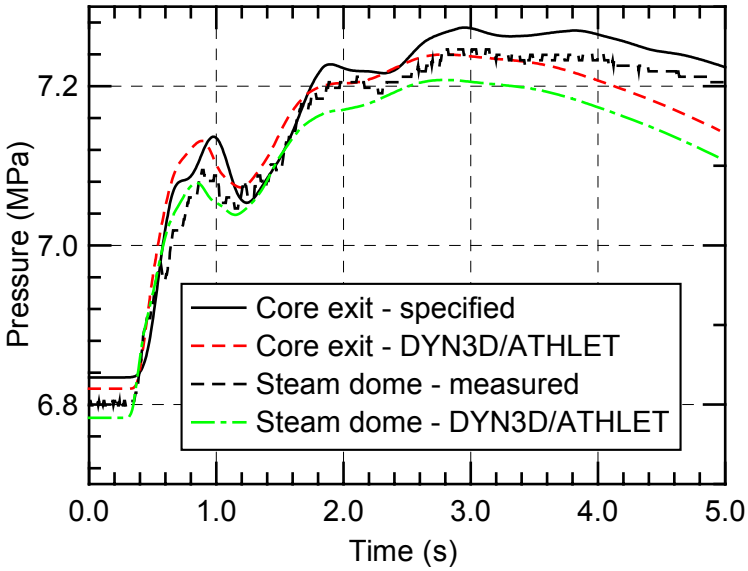

Fig. 6: Transient behaviour of the calculated pressure in the steam dome and at the core exit with measured or specified values.

5. Summary

The Exercise 2 of the OECD/NRC BWR TT Benchmark was analysed with the core model DYN3D using different model options. The results of the standard case that includes the consideration of 764 thermal-hydraulic channels (one channel/passembly), the ADF and the standard phase slip model of MOLOCHNIKOV show a good agreement with the measurements. The results without ADF, with 33 thermal-hydraulic channels or with the ZUBER-FINDLAY slip model yields only small differences, when core-averaged values are compared. However, the calculations without the ADF or with 33 thermal-hydraulic channels provide deviations to the standard case in single fuel assemblies. The available computer allows transient calculations with such detailed models as in the standard case which is in agreement with the models used for design and fuel cycle calculations. For the calculations of Exercise 3, the parallel coupling of DYN3D and ATHLET has been used. The results of the calculation were com-

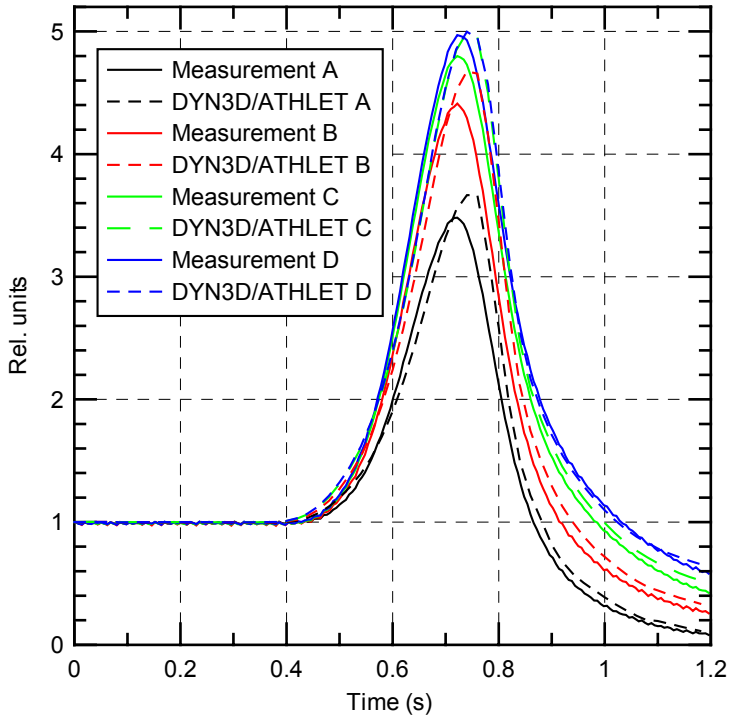

Fig. 7: Comparison of DYN3D results with the LPRM signals at the four axial levels A, B, C, D.

pared with measuring data. Only small deviations are found between the calculated and measured core power and the LPRM signals.

The calculations of Exercise 2 and 3 prove the applicability of the codes DYN3D and ATHLET/DYN3D to the simulation of such boiling water reactor transients with a strong feedback and are a substantial contribution to the validation of DYN3D and ATHLET/DYN3D.

References

[1] U. Grundmann, U. Rohde, and S. Mittag (2000), DYN3D – three-dimensional core model for steady-state and transient analysis of thermal reactors, Proc. of Int. Topl. Mtg. on Advances in Reactor Physics and Mathematics and Computation into the Next Millennium (PHYSOR2000), Pittsburgh (USA), May, 7- 11, 2000.

[2] V. Teschendorff, H. Austregesilo, and G. Lerchl (1996), Methodology, status and plans for development and assessment of the code ATHLET, Proc. OECD/CSNI Workshop on Transient Thermal-Hydraulic and Neutronic Codes Requirements, Annapolis, USA, Nov. 5-8, 1996, p. 112, NUREG/CP-0159, NEA/CSNI/R(97)4.

[3] S. Kliem, U. Grundmann, and U. Rohde (1997), The coupled code complex DYN3D/ATHLET - application to main steam line break analysis, Proc. Joint International Conference on Mathematical Methods and Supercomputing for Nuclear Applications, pp.1358-1366, ANS, La Grange Park, IL (1997).

[4] J. Solis, K.N. Ivanov, B. Sarikaya, A. M. Olson, and K.W. Hunt (2001), Boiling water reactor turbine trip (TT) benchmark", Volume 1: Final Specifications, NEA/NSC/DOC (2001) 1, Paris, June 2001.

[5] Yu. S. Molochnikov (1982), Generalisation of experimental data on volumetric void fraction for sub-cooled boiling of water (in Russian). Teploehnergetika No.7, p. 47.

[6] N. Zuber and J. A. Findlay (1965), Average volumetric concentration in two phase flow systems, Journal of Heat Transfer, 87c, p.453.

[7] DIN Norm 25463, Part 1 (1990), Berechnung der Nachzerfallsleistung der Kernbrennstoffe von Leichtwasserreaktoren.

Acknowledgements

The participation in the OECD/NRC BWR TT Benchmark was funded by the German Federal Ministry of Economics and Labour (BMWA).

ROCOM EXPERIMENTS ON THE COOLANT MIXING IN THE UPPER PLENUM OF A PWR

Gerhard Grunwald, Thomas Hoehne, Soeren Kliem, Horst-Michael Prasser, and Ulrich Rohde

1. Introduction

The reactor core of light water reactors consists of fuel elements with different enrichment and exposure. This circumstance is responsible for differences in the heat release of the single fuel elements [1]. As a consequence, the fuel element outlet temperatures differ, too. Differences of more than 30 K are reached in the stationary state at full power [2]. It is known, that these differences in the outlet temperatures do not fully disappear during the travelling of the coolant through the upper plenum. Thus, a certain temperature profile is still existing over the cross section of the hot leg nozzles.

In order to study the coolant mixing inside the upper plenum, special tests have been carried out at the test facility ROCOM (Rossendorf Coolant Mixing Model). This facility represents a KONVOI type PWR (1300 MW_{el}) in a linear scale of 1:5 and has been used during the last four years for the investigation of coolant mixing inside the reactor pressure vessel in a wide range of flow conditions [3, 4, 5].

2. Methodology of the experiments

The core simulator in the ROCOM test facility consists of 193 pipes (one for each fuel assembly) with an inner diameter of 30 mm. The pipes are a direct connection between core inlet and outlet. This construction allows to carry out experiments, where the distribution of the coolant in the upper plenum from one certain fuel element could be measured. For that purpose, eight lockable penetrations have been introduced into the vessel head. An injection lance can be inserted through these penetrations into each fuel assembly of a 90°-sector of the core. The outer diameter of the lance is 4 mm. Salted tracer solution is injected into the fuel assembly. The tracer volume flow rate of 1.7 l/min enhances the flow rate through the pipe by only 2.7 % on the average at nominal conditions. Thus, the disturbance of the flow in the pipe is negligible. The lower end of the injection lance with the outlet for the tracer is located about 20 cm above the core support plate. At running pumps, tracer is injected into the pipe. When flowing upwards, the tracer is completely mixed with the surrounding coolant in the pipe. The mixture enters into the upper plenum and leaves the vessel through the outlet nozzles. In all four outlet nozzles, wire-mesh sensors with a space resolution of 8.9 mm are installed for measuring the time dependent conductivity of the coolant (Fig. 1). These conductivity values $\sigma_{t,x,y,z}$ can be transferred into a dimensionless mixing scalar θ, representing the share of the coolant from the pipe with injection at the given position x,y,z,

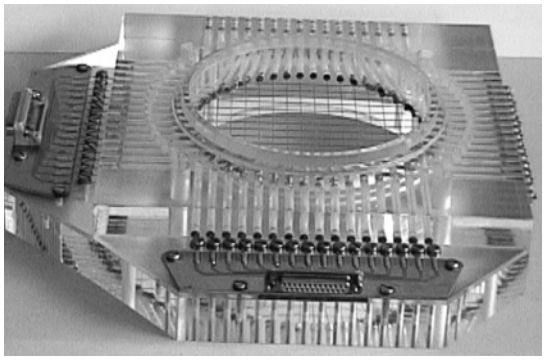

Fig. 1: Sensor in the outlet nozzle

relating the local conductivity to the conductivity at the outlet of the pipe σ_1 according to:

$$\theta_{t,x,y,z} = \frac{\sigma_{t,x,y,z} - \sigma_0}{\sigma_1 - \sigma_0} \quad (1),$$

where σ_0 is the conductivity of the coolant before the experiment.

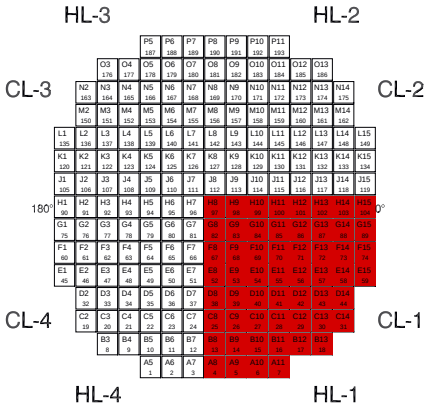

Fig. 2: Scheme of the carried out experiments

It was the goal of the experiments presented here to obtain stationary mixing coefficients, representing the time-averaged mixing scalars according to eq. (1) on a stationary concentration level at each grid point in the cross section of the outlet nozzles and for each fuel element in the 90° core sector. For that purpose, tracer has been injected into the fuel assembly during quasi-stationary flow conditions at scaled nominal state conditions (all pumps are delivering 185.0 m^3/h) until a quasi-stationary concentration profile established.

Partly, the experiments are of generic character, because the plain vessel head of the ROCOM test facility does not correspond to the original and no internals are installed in the upper plenum of the test facility. The construction of the outlet of the fuel assemblies also deviates from the original.

3. Experimental results

In the experiments tracer was injected into all 56 fuel assemblies of a 90°-sector of the reactor core (Fig. 2). Information about the other sectors can be derived due to symmetry conditions. For the enhancement of the statistical confidence, each experiment was repeated five times. Fig. 3 shows the experimental results of tracer injection into fuel assembly A08 (middle element of lowest row in Fig. 2). In the upper part of the figure, the average over all 864 measuring points of all four outlet plans is shown, the two others show the time course of the tracer at a certain measurement position in the outlet nozzle 1. 2 s after start of injection, the tracer reaches the measuring cross section. The average value increases quickly to a quasi-stationary level and then remains nearly constant. The already well known oscillations of the whole flow field [3] are accompanied by high-frequent fluctuations of the mixing scalar, as can be observed in the behaviour of the average as well as in the signal of the single measurement point, shown in the middle and lower part (as zoom over 1 s) of Fig. 3. Due to these fluctuations, all measurements have been recorded with a measurement frequency of 200 Hz. Within several ten of milliseconds, the instantaneous mixing scalar at the selected position changes by a factor of about 6, what can be resolved by the measurement technique. The instantaneous maximum value at that position is 18 % from the coolant leaving the assembly.

To cope with the oscillations, all measured instantaneous values of the mixing scalar at the quasi-stationary plateau (comp. Fig. 3) are averaged over all realisations of the experiment. This has been done for each of the 864 measurement positions. Due to the different flow paths, the time interval for the averaging differs in the single experiments, but about 5000

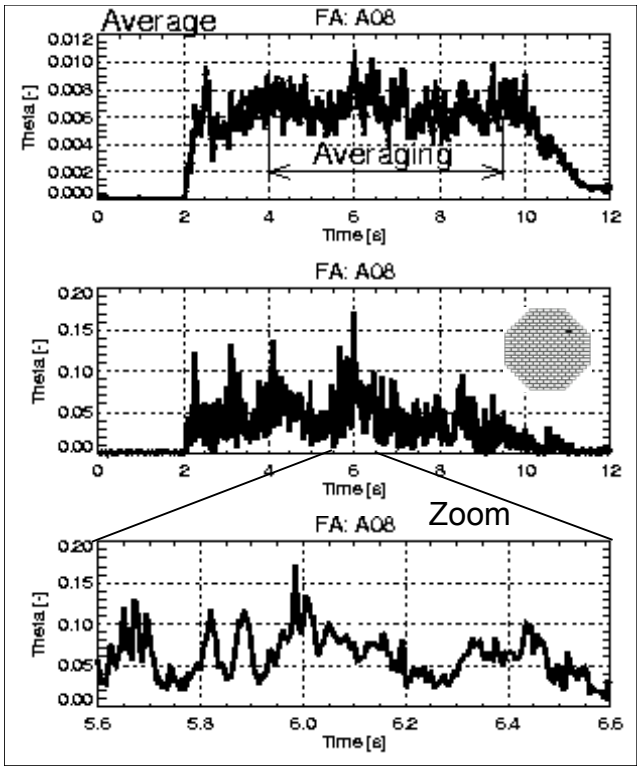

Fig. 3: Time course of the average of the mixing scalar over all positions and the mixing scalar at a certain measurement position

instantaneous values have usually been included in the average. Fig. 4 shows the results of this averaging for two typical experiments. In the left part, the results for fuel assembly A08, located at the symmetry line between outlet nozzle 1 and 4, are shown. The tracer is distributed nearly symmetrically between these two nozzles. The sensors in the outlet nozzles on the opposite side of the vessel did not register any tracer at all. The maximum of the tracer concentration has been found in the lower part of the outlet nozzle. The results for fuel assembly F11 on the right of Fig. 4, show a complete different behaviour.

Nearly the whole tracer passes the measuring plane in outlet nozzle 1, only small amounts are registered in outlet nozzle 2. Contrary to the fuel assembly A08, the maximum tracer concentration is found in the upper part of the outlet nozzle cross section.

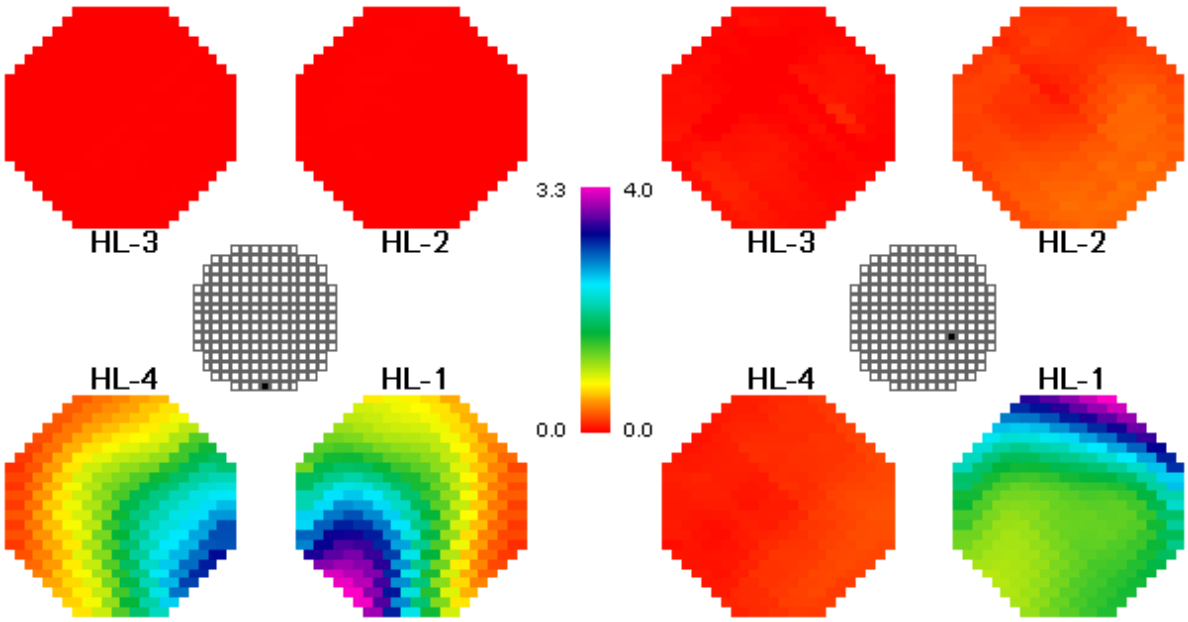

Fig. 4: Averaged concentration profile in the outlet nozzles in the experiments for fuel assembly A08 (left) and fuel assembly F11 (right)

4. Conclusions and outlook

Based on all the experiments at nominal flow conditions, the following conclusions concerning the flow field and the coolant mixing in the upper plenum can be drawn:

- High-frequent fluctuations of the mixing scalar are found in the upper plenum of the ROCOM test facility. They were fully resolved by the installed measuring technique with a time resolution of 5 ms.
- On the way through the upper plenum, the coolant mixing obeys certain patterns. Preferably, the coolant flows from the fuel assembly outlet to the nearest outlet nozzle.
- In the corresponding outlet nozzle, the coolant from fuel assemblies located at the periphery of the core passes the measuring plane preferably at positions in the lower part, from fuel assemblies in the inner zone of the core preferably at positions in the upper part of the nozzle.

The goal of future work should be the experimental and analytical investigation of the nature of the high-frequent fluctuations. The experimentally obtained mixing coefficients should be used for the reconstruction of the temperature profile in the outlet nozzles based on calculated core outlet temperature or assembly power values.

References

[1] S. Mittag, U. Grundmann, R. Koch and J. Semmrich (2002), Creation and use of 2-group diffusion parameters libraries for the calculation of a KWU-KONVOI reactor by means of the reactor dynamics code DYN3D, Report FZR-346, ISSN 1437-322X, Rossendorf (in German)

[2] H. Kantee (1998), Power degradation of one turbine to house load level – experiment on Loviisa-1 NPP, PHARE Programme SRR1/95, Technical report IVO/SRR195/LOV1.1

[3] G. Grunwald, Th. Höhne, H.-M. Prasser, F.-P. Weiß (2000), Coolant mixing in PWR at constant coolant flow in the primary circuit, Proc. Ann. Meeting on Nucl. Technology ‘00, pp. 109–114, INFORUM GmbH, Bonn

[4] S. Kliem, H.-M. Prasser (2001), A semi-analytical model for the description of coolant mixing inside the KONVOI reactor pressure vessel during pump start-up, Proc. Ann. Meeting on Nucl. Technology ‘01, pp. 107–112, INFORUM GmbH, Bonn

[5] S. Kliem, H.-M. Prasser, G. Grunwald, U. Rohde, Th. Höhne, F.-P. Weiß (2002), ROCOM experiments on the influence of density differences on the coolant mixing inside the reactor pressure vessel of a PWR, Proc. Ann. Meeting on Nucl. Technology ‘02, pp. 65–69, INFORUM GmbH, Bonn

Acknowledgement

The project this paper is based on is funded by the BMWi (Bundesministerium für Wirtschaft) and is registered with No. 150 1216.

DEVELOPMENT AND VERIFICATION OF A 1D DYNAMICS CODE FOR MOLTEN SALT REACTORS

Jiri Krepel, Ulrich Grundmann, and Ulrich Rohde

1. Introduction

The three-dimensional code DYN3D [1] for calculation of steady states and transients in light water reactors (LWR) has been developed at FZR. The neutron kinetics of DYN3D is based on the nodal expansion method applied to Cartesian or hexagonal fuel assembly geometry. It is coupled with a two-phase thermo-hydraulic model and a fuel rod model. The subject of this report is the description of the DYN1D-MSR (Molten Salt Reactor) version development.

The MSR is a project [2], which is presently revisited, because of its safety advantages, the possibility to use the uranium-thorium fuel cycle, and the potential to transmute actinides. The fuel of this reactor is liquid in the form of a molten salt mixture, which also acts as a coolant. The thermo-hydraulic and neutron kinetic characteristics of MSR differ significantly from that of a classical LWR.

The MSR modification of the DYN3D code is designed to calculate steady states and transients of Molten Salt Reactors. The first step in the DYN3D-MSR development is a 1D version, which is based on a numerical method for hexagonal fuel element geometry and includes new models for describing fuel flow. For the code development, a MSR design with fuel flowing in cylindrical channels inside a hexagonal graphite structure is considered (Fig 2).

2. Delayed neutrons model

For neutron kinetics, the DYN3D nodal expansion method [5] is used. However, it is a special feature of the MSR kinetics that the precursors of delayed neutrons are partly drifted out of the core with the fuel. For this reason, a part of delayed neutrons are released in the primary circuit. The ratio of delayed neutrons contributing to criticality is a function of the fuel velocity and of the fuel salt fraction in the core. The equations describing the distribution of the *i*-th group of precursors are:

$$\frac{\partial}{\partial t}C_i(z,t)+\frac{\partial}{\partial z}\left(\mathrm{v}C_i(z,t)\right)=\frac{1}{k_{eff}}\sum_g \beta_i \nu\Sigma_{f,g}\Phi_g(z,t)-\lambda_i C_i(z,t) \quad \text{in the core and} \tag{1}$$

$$\frac{\partial}{\partial t}C_i(z,t)+\frac{\partial}{\partial z}\left(\mathrm{v}C_i(z,t)\right)=-\lambda_i C_i(z,t) \quad \text{in other parts of primary circuit.} \tag{2}$$

Standard notation is used. The equations contain a convective term accounting for the movement of precursors with the flowing fluid fuel. To find the solution of these equations, the entire primary circuit and core are divided into nodes. The source term on the right hand side of eq. 1 is described by DYN3D with a polynomial character in space and an exponential character in time. Assuming an average fuel velocity within each node and time step, the solution within one node is found analytically. Using these nodal solutions, the overall distribution of the precursors can be found. Fig. 1 shows the distributions of the nuclear power and the precursors for a steady state condition with given fuel mass flow.

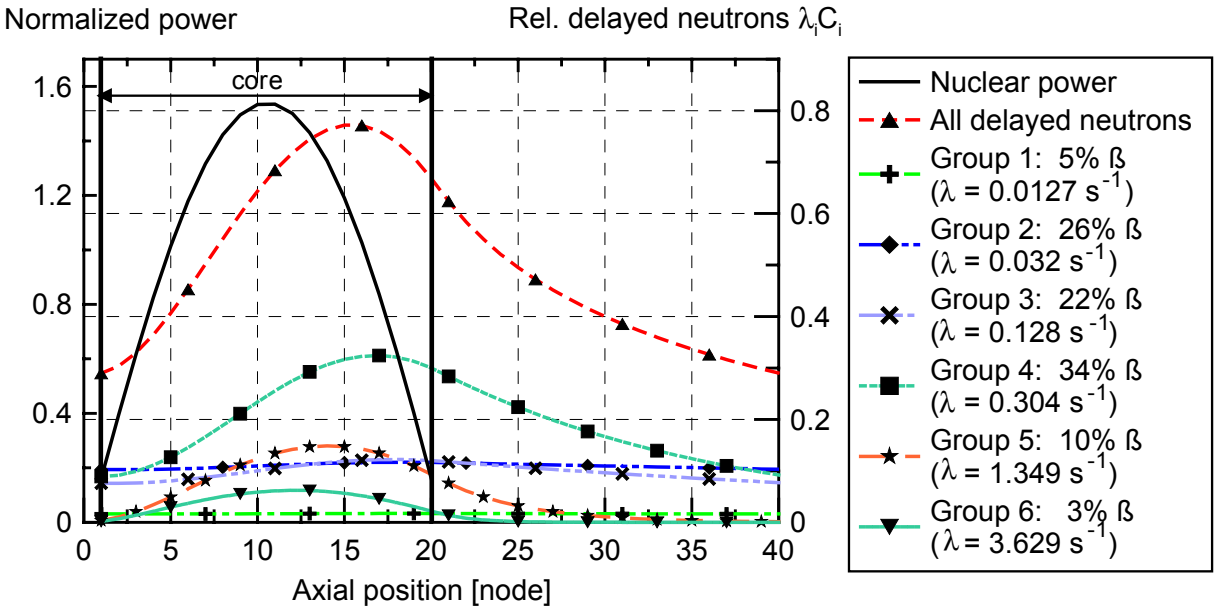

Fig. 1: Distribution of 6 groups of delayed neutrons for flowing fuel (v ≈1m/s) reactor.

3. Thermo-hydraulic (TH) model

The TH model is determined by the fact that the energy from fission is predominantly released into the fuel salt and is directly drifted out of the core. However, there is a small fraction of energy, which is released through the gamma radiation in the surrounding graphite and an additional part is released with delay as decay heat. Assuming the absence of either boiling or solidification of fuel salt, a single phase TH model can be used. The energy equation in this case will have the following form:

$$\frac{\partial}{\partial t}(\rho h(z,t))+\frac{\partial}{\partial z}(\mathrm{v}\rho h(z,t))=Q_{fission}+Q_{decay}+Q_{graphit} \tag{3}$$

The first of the three source terms is heat released from fission directly to the fuel and is proportional to the neutron flux. The second source term is the decay heat, which is assumed to be constant during a transient, and the third term accounts for the heat exchange with graphite [3]. In the present model, it is assumed that the pressure remains constant, the fuel density is dependent on temperature and the velocity for each node is obtained from the continuity equation. The temperature distribution for this reactor can be obtained from the energy balance equation using the method of characteristics [4]. The method of characteristics involves integrating the energy balance equation along the path of a fictitious particle moving with the flow.

In the TH model the hexagonal graphite block of Fig 2 is approximated by a cylinder with an inner channel of flowing fuel. The radial heat conduction equation is solved in the graphite. No heat transfer to the next graphite block is assumed at the outer boundary. The method of effective heat transfer coefficients is used for solving the heat conduction equation. For the numerical solution of the heat conduction equation in each node, the cylinder is divided into an arbitrary number of coaxial segments. Effective heat transfer coefficients are derived from the analytical solution of a steady state system.

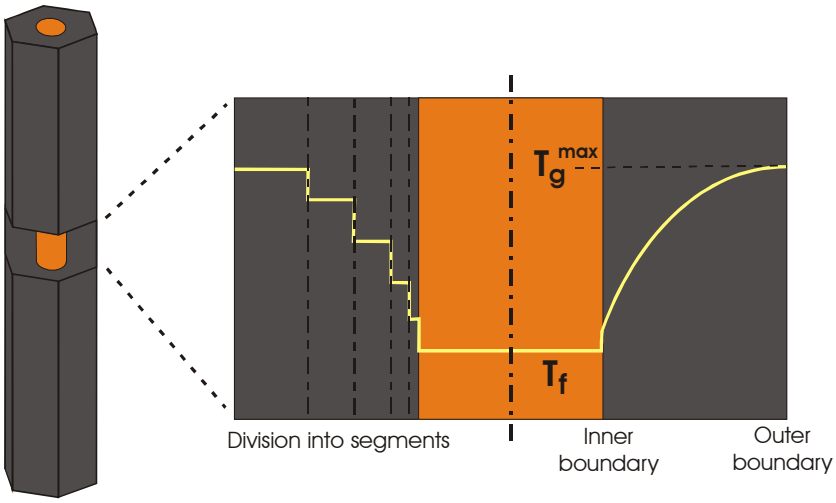

Fig. 2: Modeling of the temperature distribution in a graphite channel by 5 segments with effective heat transfers coefficients. The comparison of the calculated steady state distribution (on the left) with analytical solution (on the right) is shown.

Using the heat transfer coefficients thus obtained, the temperature distribution in the graphite channel is calculated at every time step from a system of linear algebraic equations. The axial temperature distributions in a hexagonal fuel element divided into 20 axial nodes can be seen in Fig 3. The core inlet temperature of the molten fuel is 550°C. Flowing through the core, it is heated up by 150°C approximately.

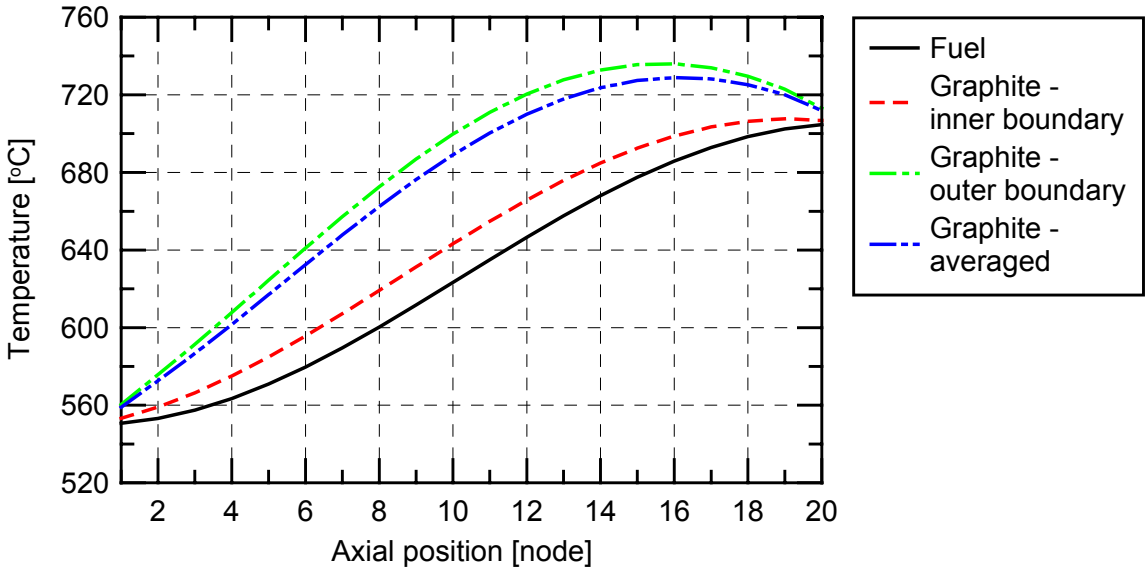

Fig. 3: Axial distributions of temperature in the MSR fuel channel.

4. Validation of 1D code kinetics

The data measured during the Molten Salt Reactor Experiment (MSRE) in the Oak Ridge National Laboratory (ORNL) were used to validate the DYN1D-MSR kinetics, especially the delayed neutrons model. MSRE was based on a 10 MW_{th} thermal reactor, moderated by graphite and with liquid molten salt fuel. It was constructed for the verification of molten salt reactor technology.

From the above ORNL MSRE data, only three zero-power experiments are considered and used for the validation calculations. The first of them was focused on the leakage of delayed neutrons due to the fuel flow. Measuring results are represented in terms of reactivity loss.

The MSRE reactivity loss for U235 fuel was found to be 212 pcm and for the U233/U235/Pu239 fuel mixture 100±15 pcm. The reactivity loss values calculated by DYN1D-MSR are 242.8 pcm and 119.5 pcm for the U235 fuel and the U233/U235/Pu239 fuel mixture respectively. The agreement with results obtained by the other codes is excellent. However, the results of all numerical codes differ from the experiment. The differences between experiment and calculations can be caused by inaccuracies of the cross-section input data. The accuracy of this data has recently been questioned by researchers and efforts are underway to calculate more reliable data. Considering also the 1D nature of the code, the elliptical upper plena of reactor core can be modeled only as a flat area with constant height. This limitation was used also in SIMMER 3D calculation to get comparable results.

Table 1: Loss of reactivity by fuel flow (Static benchmark calculated by MOST project).

Code used	ORNL Experiment	NILO	DYN1D-MSR	APOLLO2	SIMMER 3D
Reactivity loss (pcm) ^{235}U fuel	212	243	243	240	263 244 (long plena)
Reactivity loss (pcm) ^{233}U/^{235}U/^{239}Pu	100	122	120	-	131 122 (long plena)

The second and the third experiment were focused on protected fuel pump start-up and coast-down transients. During these two transients a constant power was maintained. The change in the delayed neutron production was compensated by the use of control rods.

During the fuel pump start-up, the delayed neutron precursors are drifted out of the core. However, there is a small fraction of them, which can return to the core and cause the oscillations of the delayed neutrons production. It depends on the physical size of the primary circuit and on the velocity of the fuel flow. In case of the fuel pump start-up transient the velocity is changing from zero to the nominal value in 10 seconds and so the number of productively released delayed neutrons (delayed neutrons released in the core) changes rapidly from 1 (all delayed neutrons are released in core) to 0.77 (only 77% of delayed neutrons are released in the core) as seen in Fig 4.

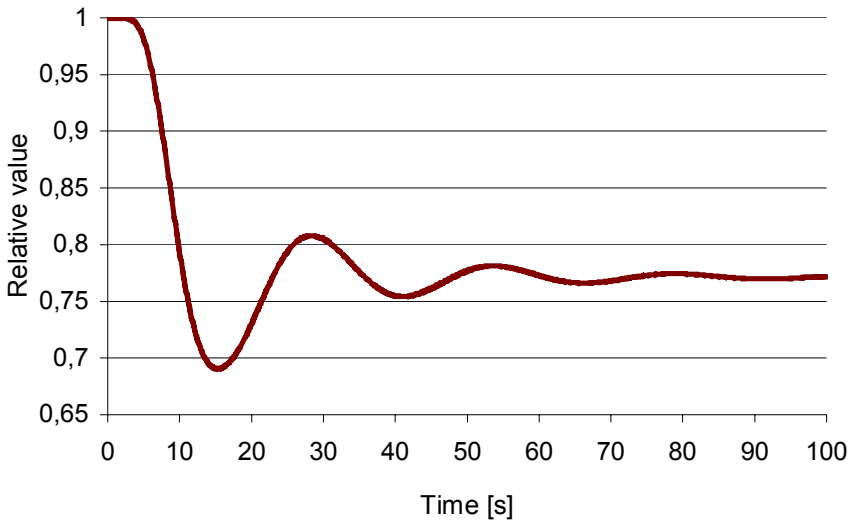

Fig. 4: Ratio of delayed neutrons released in core during fuel pump start-up transient calculated by DYN1D-MSR.

To compensate the changes in the distribution of delayed neutrons and maintain a constant power, the motion of control rods is necessary. However the withdraw velocity of the control rods was limited during the MSRE. Owing to this limitation, the power can be lower than nominal during the first 20 seconds of the fuel pump start-up. This limitation was not accounted for in the DYN1D-MSR calculation (Fig 5).

The discrepancy between the transient profiles of inserted reactivity obtained from DYN1D-MSR calculations and the ORNL experiment, seen in Fig 5, is primarily caused by two phenomena. Firstly, the limitation associated with control rod motion has not been accounted for and secondly, the stabilized delayed neutron loss to be compensated in both cases differ (Tab.1), in the ORNL case it is 212 pcm and in the DYN1D-MSR case it is 243 pcm.

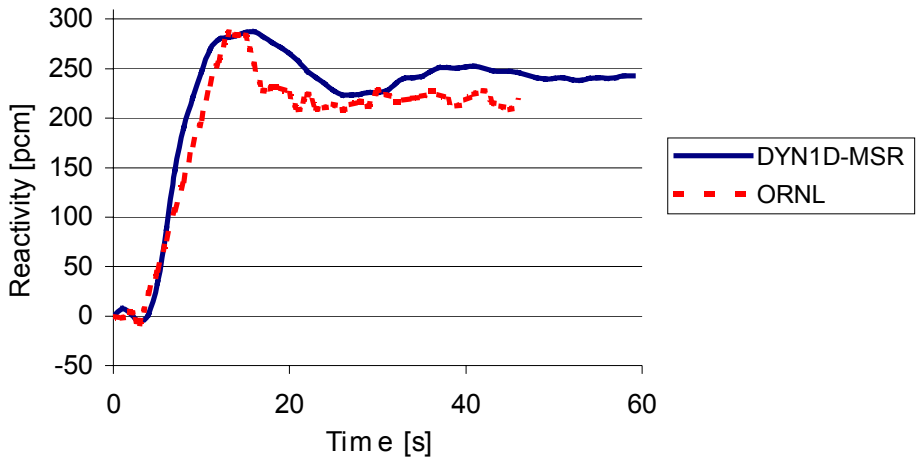

Fig. 5: Reactivity inserted to compensate the loss of delayed neutrons during the fuel pump start-up transient.

5. Transient calculation with thermal feedback

The fuel slowdown under constant deceleration (linear decrease of velocity from the nominal value to 1% of the nominal value) in 30 seconds, was the first full power transient calculated for the MSR model described in paragraph 3. Temperature dependent cross-sections were used in this calculation. The transient response was calculated for a given inlet temperature that remained constant during the transient. (see Fig 6).

Two antagonistic effects mostly influence reactor power during this type of a transient. The increasing fuel temperature results in a negative reactivity insertion by virtue of the thermal feedback coefficient being negative. At the same time, the change of the delayed neutron distribution introduces a positive reactivity. In long-term view, a third effect will appear due to the delayed increase of graphite temperature, which can introduce positive or negative reactivity dependent on the core size and geometry. An example of MSR response to this transient is shown in Fig. 6. The graphite thermal feedback is negative in this case.

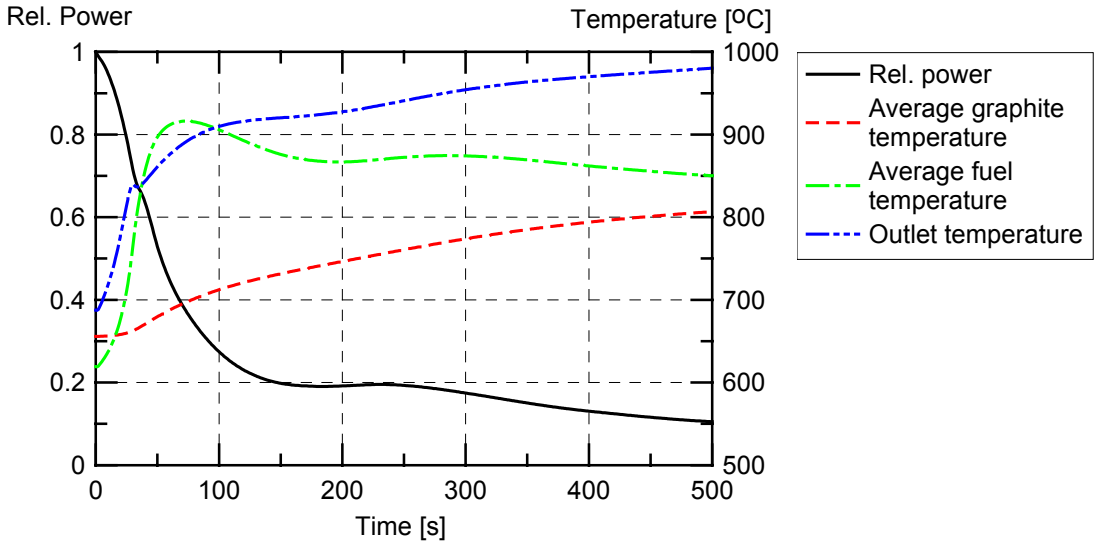

Fig. 6: MSR response to fuel pump coast-down for constant inlet temperature 650°C.

6. Conclusion

DYN1D-MSR, the first step in a 3D version development has been shown to be an effective tool for MSR transient analysis. The new delayed neutrons model, together with the TH model, is integrated into the node expansion method of DYN3D neutron kinetics. Preliminary results for zero-power benchmark and for a fuel flow slowdown scenario have shown DYN1D-MSR's ability to perform space dynamics calculations. The future development of DYN3D-MSR will include:

- Consideration of other transients and benchmarks.
- Heat exchanger model.
- Extension to 3D version.

References

[1] U. Grundmann, U. Rohde, S. Mittag: "DYN3D - Three-Dimensional Core Model for Steady-State and Transient Analysis of Thermal Reactors," Proc. of Int. Topl. Mtg. on Advances in Reactor Physics and Mathematics and Computation into the Next Millennium (PHYSOR2000), Pittsburgh (USA), May, 7- 11, 2000.

[2] Rosenthal, M.V., et al.: "Advances in the development of MSBR." Proceedings of the Fourth International Conference on the Peaceful Uses of Atomic Energy, A/Conf.49/P/048, Geneva, 1971

[3] Kasten, P.R., et al.: "Graphite behavior and its effects on MSBRE performance." ORNL, USA, 1968

[4] U. Rohde: " Ein theoretisches Model für Zweiphasenströmung in wassergekühlten Kernreaktoren und seine Anwendung zur Analyse des Naturumlaufs im Heizreaktor AST-500. "Dissertation, Zentralinstitut für Kernforschung Rossendorf bei Dresden, Juli 1986

[5] U. Grundmann: "HEXNEM – A Nodal Method for the Solution of the Neutron Diffusion Equation in Hexagonal Geometry", Proceedings of the M&C'99 Conference on Mathematics and Computations in Nuclear Applications, pp. 1086-1095, Madrid, September, 27 – 30, 1999

INCINERATION OF TRANSURANIC WASTE IN A MOLTEN SALT REACTOR BASED ON THE THORIUM-URANIUM-233 FUEL CYCLE

Reinhard Koch and Andrey Myasnikov[1]

1. Introduction

The Molten Salt Reactor (MSR) is suitable for the removal of actinides, accumulated in light water reactors, of dismantled nuclear weapons, and for the efficient and economical energy production. It has a simpler design as a reactor with solid fuel. The neutron economy is much better, because mainly non-fissile materials with very low neutron absorption cross section are present and no artificial absorbers in the coolant and control rods are necessary. MSR-fuel can consist of all three major fissile fuels, U 233, U 235, and plutonium. At FZR, the MSR-effort is focused to minimize the stock of plutonium and minor actinides by spent fuel transmutation. Stimulated by the MOST-project, first preliminary calculations on MSR were carried out.

2. Molten Salt Reactor

The U. S. Nuclear Energy Research Advisory Committee and the Generation IV International Forum rank the MSR among the six most promising nuclear reactor-systems [1]. In a MSR fission power will be produced in a circulating molten salt fuel mixture. MSRs are fueled with uranium or plutonium fluorides dissolved in a mixture of molten fluorides, with Li 7 and Be 9 fluorides as the primary option. Molten fluoride salts have a very low vapor pressure. This reduces stresses on the vessel and piping and hazards associated with high pressures, such as ruptures or depressurizations. Potentially, MSRs have a high availability - refueling, processing, and fission product removal can be performed on-line. High temperature, ranging from 500 to 800 °C, offers the potential for thermochemical hydrogen production.

Four fuel cycle options are under discussion: (1) Maximum conversion ratio using a Th-U-233 fuel cycle, (2) denatured Th-U-233 converter with minimum inventory of weapons grade material, (3) denatured once-through actinide burning (Pu and minor actinides) fuel cycle with minimum chemical processing, and (4) actinide burning with continuous recycling.

Two liquid fuel reactors have been designed, built, and operated by Oak Ridge National Laboratory (ORNL): the Aircraft Reactor Experiment (ARE) and the Molten Salt Reactor Experiments (MSRE). The operation of the Molten Salt Reactor Experiment (MSRE) with various fuels from 1964 to 1969 was very successful [2]. Based on these experiences the concept of the molten salt breeder reactor (MSBR) was developed [3]. The present investigations in Europe are based mainly on the papers of the latter program. The original program was finally closed in 1976. It stimulated molten salt reactor studies in many other places, for example in the Soviet Union [4]. One program was conducted at KFA Jülich with the Molten Salt Epithermal (MOSEL) Reactor in the sixties [5].

[1] KIAE Moscow, andm@nsi.kiae.ru

3. Safety and waste

The safety properties of the MSRs are much more favorable than those of the solid fuel reactors. The fuel is critical only if the moderator - the graphite - is present. If the fuel escapes from the core, it will become subcritical. A meltdown is impossible. Because of the expansion of the fluid the fluid fuel has a negative temperature coefficient. The continuous removal of Xe 135 by Helium and of other fission gases reduces significantly the radioactivity within the core. The fission products with short half-lifes can be removed by on-line processing, those with a long half-life can be retained in the salt, for example I 129, as long as they are transmuted into stable nuclides. The salts are chemically stable and nonflammable, and there are no dangerous chemical interactions between the salts and water.

In case of fluid fuel it is possible to shutdown the reactor by dumping the salt into outer containers from which the decay heat can be removed by thermal conduction and natural convection. If no Pa 233 is removed from the fuel, which decays with a half-life of 27 days into the fissile U 233, the MSR is proliferation resistant, as proposed in the Denatured Molten Salt Reactor concept [6]. It was summarized that MSRs can be designed in an extremely safe and economical manner.

The safety and the handling of nuclear waste mainly determine the acceptability of nuclear reactors. The continuous processing of the waste, the separation of short-lived nuclides and the potential transmutation of long-lived fission products and actinides minimizes the waste problem. This reduces the need for very long controlled storage time of the waste.

4. Project MOST

Under the headline “Review of MOlten Salt reactor Technology (MOST)” a EURATOM-project was initiated in 2001, coordinated by the French Commissariat à l'Energie Atomique. The goal of the project is to summarize the state of the art on molten salt reactor. This review analyses different scenarios in which MSRs can be used, and it focuses on the best available data and methods to define the weak points and advantages. Sixteen institutes of nine countries take part in this project with duration of two years. The project work plan is subdivided into nine work packages, and the Institute of Safety Research of the Forschungszentrum Rossendorf (FZR) is involved in the work package 2 “Reactor physics study and non-proliferation issues” and in the work package 3 “Design review on nominal operating conditions”. MOST reviews the concepts of MSRE [2], MSBR [3], and the concept Actinides Molten Salt TransmutER (AMSTER) of Electricité de France [7].

5. MSR model

In co-operation of the FZR and the KIAE Moscow a code system for MSR consideration was developed linking the well-known codes MCNP-4C and ORIGEN 2.1. Our calculations of the Denatured Molten Salt Reactor [6] for a time period of three operating years showed the internal consistency between our calculations with the codes MCNP-ORIGEN and the Russian calculations with the codes MCU-ORIGEN-S. In the framework of the MOST project, preliminary studies were performed to examine the fuel cycle characteristics of a MSR of the AMSTER-type.

The studied AMSTER-model of the MSR has a cylindrical core with removable blocks of graphite, a fixed graphite reflector, and a vessel of the Ni-Mo-Cr-Fe-alloy, Hastelloy N. The removable blocks with a hexagonal shaped cross section have vertical holes in which the molten salt flows. The graphite moderates the neutrons. Usually the reactor model has two regions without graphite, the lower and the upper plenum. These parts were disregarded in the present calculations. In contrast to solid fuel reactors the fuel in liquid fuel reactors is heat carrier and coolant as well.

Our calculations were done with a salt composition of 70 % LiF (Li 7 only), 15 % BeF_2 and 15 % ThF_4 (mole percent), a graphite density of 1.68 g/cm^3, a salt density of 3.328 g/cm^3, a temperature of salt and graphite of 900 K and a thermal power 2250 MW. The system contains 168 metric tons of salt and 400 tons of graphite. The main geometrical and physical parameters are summarized in Table 1.

Table 1: The calculational model geometry and the main physical parameters

Radius of the MSR (cm)	411.1571
Height of active core (cm)	500
Thickness of radial reflector (cm)	50
Thickness of axial reflector (cm)	50
The side of the hexagon (cm)	13
The radius of hole in the hexagon (cm)	4
Total salt volume in primary circuit (m^3)	48.4
Salt volume in active core (m^3)	30.4
Thermal power of reactor (MW)	2250
Electrical power of reactor (MW)	1000

As fuel feeding strategy of the MSR burner, the inventory of Th 232 was kept constant in the core. The criticality was assured by feeding TRU-nuclides (Np, Pu, Am, and Cm).

Table 2: Composition of the feed in transuranic (TRU) nuclides in percent

Np 237	6.419
Pu 238	3.179
Pu 239	43.940
Pu 240	21.272
Pu 241	13.516
Pu 242	7.875
Am 241	0.545
Am 243	2.328
Cm 244	0.926

Under startup conditions, all fissions occur in these TRU-nuclides. Then more and more U 233 contributes to the fission process. The TRU-feeding is continued until the end of life (EOL) of the reactor with constant percentage of the TRU-nuclides, typically from spent fuel of light water reactors (LWRs) after reprocessing. The amount of feeded TRU varies and must be recalculate in each time step in order to fulfill the criticality condition.

A main reprocessing time of the MSR-salt of 300 equivalent full power days (efpd) was used with the assumption of a loss rate of 10^{-3} for the transuranic nuclides (TRU). The Table 3 lists the recycling characteristics of our calculations.

Table 3: Recycling characteristics for the present calculations

Component	**Removal time**	**Removal operation**
Kr, Xe (noble gases)	50 s	Sparging with He
Zn, Ga, Ge, As, Se, Nb, Mo, Ru, Rh, Pd, Ag, Tc, Cd, In, Sn, Sb, Te	2.4 h	Plating out on surfaces and escape to off gas system
U 233, U 234, U 235, U 236, U 237, Np (tetravalent)	300 efpd	Volatilization in primary fluorinator
Br, I (halogens)	300 efpd	
Zr	300 efpd	Reductive extraction
Ni, Fe, Cr (corrosion products)	300 efpd	
Pa 233 (tetravalent)	No	
Pu, Am, Cm (trivalent TRU)	300 efpd	
Y, La, Ce, Pr, Nd, Pm, Gd, Tb, Dy, Ho, Er (trivalent lanthanides)	300 efpd	
Sm, Eu, (divalent lanthanides)	300 efpd	

6. Numerical results

From the calculations we get nuclide number densities of all components of the salt as a function of time. So we can calculate the inventory of all nuclides. Fig. 1 shows the inventory of the heavy nuclei and the fission products (FP) versus depletion time for a life of 80 years. The scale is logarithmic in order to present such different inventories as those of Th 232 with 79 tons and Pa 233 with 61 kg (at the EOL). As we can see, after a certain time the inventory of most of the nuclides is almost constant. The TRU-nuclides and the U 233 follow the Th 232 in the mass fraction. For the fission products and U 236 an equilibrium cannot be really achieved. At EOL an amount of 100 kg of fission products still exists. But the radiotoxic waste remains in the system in contrast to LWRs. At EOL the fraction of neutrons generated by fission is 99.5 %, those generated by (n,2n)- and (n,3n)-reactions is 0.5 %. The neutron (and energy) production by fission can be subdivided as follows: 57 % from U 233, 6 % from U 235, 12 % from Pu 239, 17 % from Pu 241, and 6 % from Cm 245. A small contribution of 1.5 % comes from the more than 15 other TRU-nuclides.

In Fig. 1 the sum of TRU-nuclides was plotted. Fig. 2 shows the transuranic inventory in more detail. The mass fraction of Pu 239 is the highest in a short period after startup only. Then the non-fissile nuclides Pu 240 and Pu 242 are the dominating TRU-nuclides, later Am 243 too. The shown TRU-distribution strongly depends on the neutron spectrum of the system. A harder spectrum than in the present AMSTER-model, attained, for example, by reducing the mass-fraction of the graphite moderator with “larger holes”, can drastically change the distribution of TRU-nuclides.

It should be mentioned that the MSR-system could also be used in an undercritical system in connection with a proton accelerator, called in an Accelerator Driven System (ADS). As mentioned above, in our critical system we feed the system continuously with TRU-nuclides and incinerate some of the radiotoxic waste of LWRs.

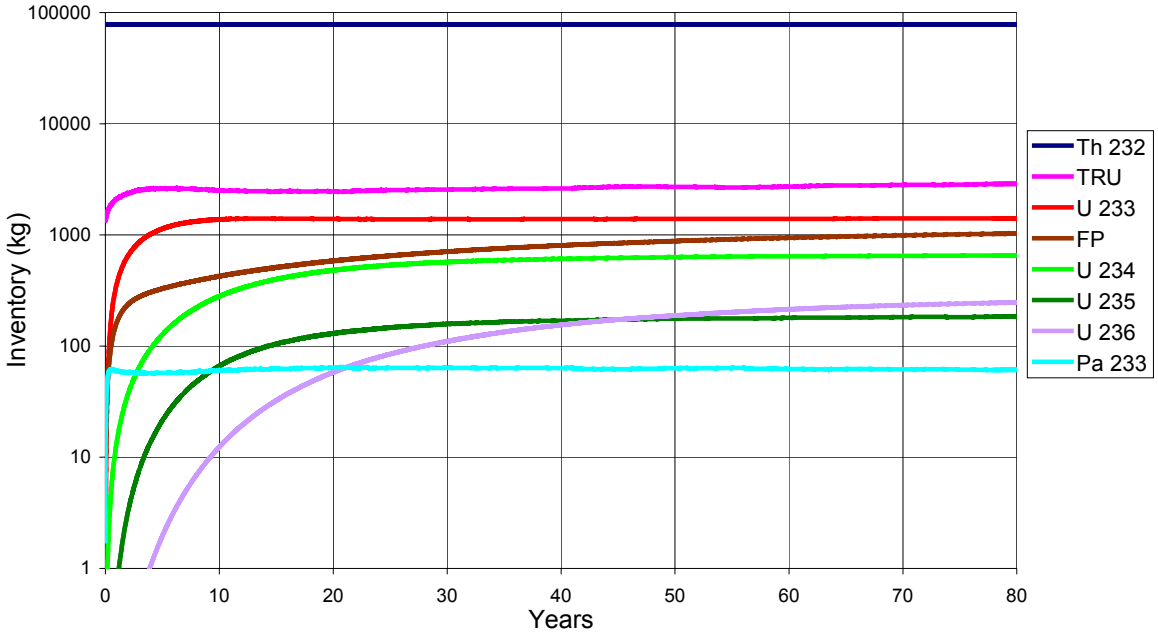

Fig. 1: Inventory of heavy nuclides and fission products (FP) versus depletion time for the AMSTER-system

Simultaneously with an energy-production of 80 GWa a surplus of almost 20 metric tons TRU-waste of the LWRs could be burned with this AMSTER-system, as shown in Fig. 3, and (almost) no new radiotoxic waste would be extracted from the system.

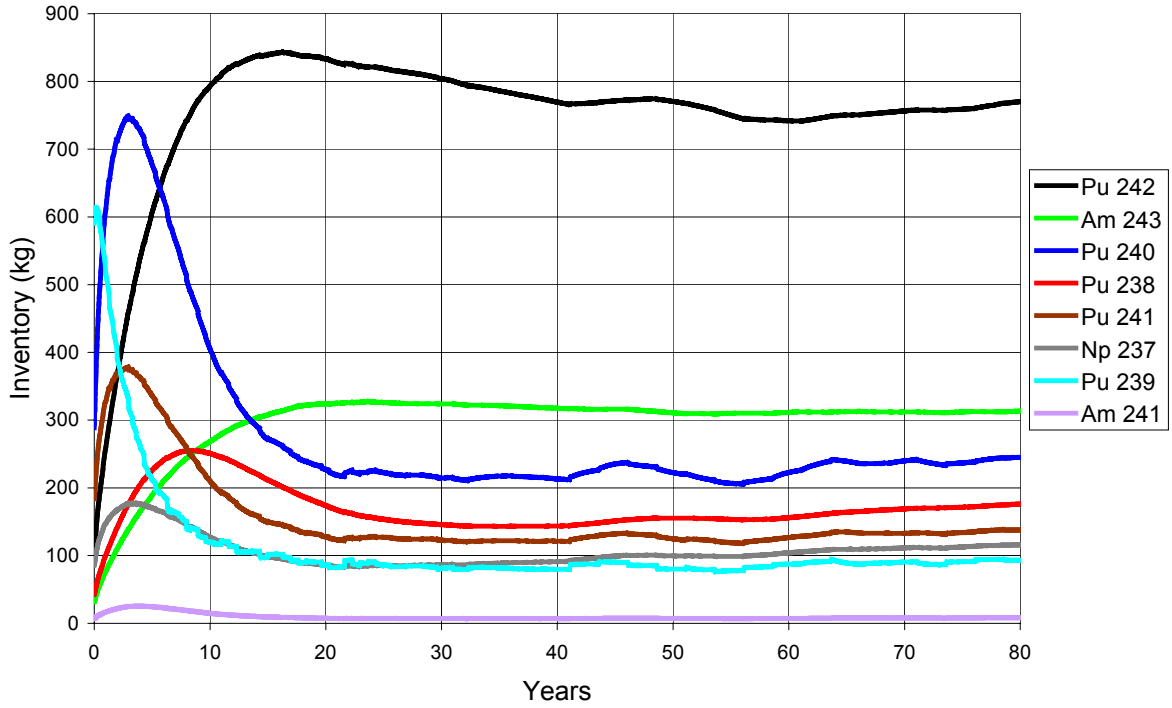

Fig. 2: Detailed transuranic (TRU) inventory versus depletion time

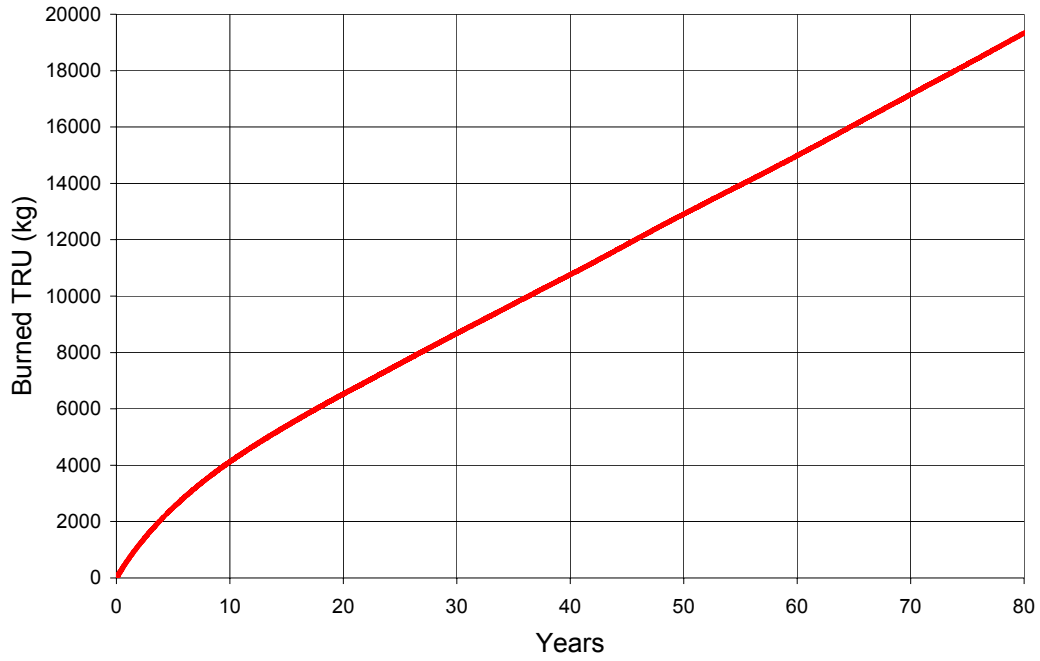

Fig. 3: The burned ("consumed") TRU-mass in the Molten Salt Reactor of the AMSTER-type

7. Summary and prospects

Our results, obtained for the AMSTER-model of the burner type, which was not completely defined at the date of our calculations, demonstrate the physical feasibility of MSR. There are small differences with the results of other groups due to various approaches in the fuel policy: Somewhere the total heavy nuclei inventory was kept constant during transition to the equilibrium. In our calculations the Th 232 inventory is constant. Moreover different salt and graphite densities were used and different uranium losses in the thorium- uranium cycle, too.

The Monte-Carlo calculations with the code MCNP are very time consuming. Therefore, applications of faster deterministic codes like the well-known collision probability cell-code HELIOS and discrete ordinates transport codes as well as diffusion codes are planned. Many of these codes have never been used for calculations of reactors with fluid fuel, so the data libraries must be provided with supplemental nuclides. Since the geometry of the MSRs differs from those of LWRs, some other changes will be necessary on these deterministic codes. Moreover, fundamental research will be necessary, for example to determine kinetic and thermodynamic data, to determine the optimum process for separating fission products, including lanthanides without removal of minor actinides. Data of the solubility of minor actinides and lanthanides will be needed to design MSRs capable of burning minor actinides with minimum inventories in the reactor.

References

[1] A Technology Roadmap for Generation IV Nuclear Energy Systems, December 2002, Issued by the U. S. DOE Nuclear Energy Research Advisory Committee and the Generation IV International Forum, GIF-002-00, http://gif.inel.gov/roadmap/

[2] P. N. Haubenreich and J. R. Engel, Experience with the Molten Salt Reactor Experiment, Nucl. Appl. Technol., 8, 118-136 (1970)

[3] L. E. McNeese and Staff of the Molten-Salt Reactor Program, Program Plan for Development of Molten-Salt Breeder Reactors, ORNL-5018, December 1974

[4] W. L. Blinkin and W. M. Novikov, Fluid Salt Nuclear Reactors (in Russian), Atomistdat, 1978

[5] P. R. Kasten, U. Gat, S. Schulze Horn, and H. W. Vorhusen, Design Concepts for the Core Structure of a MOSEL (Molten Salt Experimental) Reactor, Nucl. Struct. Eng., 2, 224 (1965).

[6] J. R. Engel, W. R. Grimes, H. F. Bauman, H. E. McCoy, J. F. Dearing, & W. A. Rhoades, Conceptual Design Characteristics of a Denatured Molten-Salt Reactor With Once-Through Fueling, (1980), ORNL/TM-7207 , 156 pages

[7] David Lecarpentier, Le Concept AMSTER, Aspects Physiques et Surete, Thèse, Juin 2001

PARTICLE FLUX CALCULATIONS FOR A PULSED PHOTONEUTRON SOURCE AT THE RADIATION SOURCE ELBE

Carsten Beckert, Hartwig Freiesleben[1], Eckart Grosse[2], Baerbel Naumann[1], and Frank-Peter Weiss for the NToF@ELBE collaboration

1. Introduction

The main beam parameters of the new radiation source ELBE of Research Center Rossendorf lead to the idea to convert the very short and intense electron pulses into short neutron pulses in order to measure energy resolved cross sections of neutron reactions in a time-of-flight (TOF) arrangement with a very short flight path of only a few meters. The ELBE facility for research with various kinds of radiation is centered around a superconducting Electron Linac. The beam energy of ELBE can be varied between 12 and 40 MeV. Beam intensities of about 1mA can be delivered with a wide variability in the pulse structure. The maximum frequency of the beam is 13 MHz. This frequency can be lowered by a factor of 2^n. The pulse width is less than 10 ps. Pico second electron pulses are used for the production of sub-ns neutron pulses. The small emittance of the ELBE beam permits the irradiation of very small radiator volumes.

The project aims at measuring neutron cross sections like (n,p), (n,α) and (n,f) at a time-of-flight spectrometer. It is the primary objective to determine neutron cross sections firstly for construction materials of fusion and fission reactors, which is important to select materials as irradiation resistant as possible, and secondly for the waste from such reactors, especially in order to find processes which transmute long-lived radioactive waste into short-lived and finally stable isotopes. In addition the distribution of fragments can be analysed, which are produced by the neutron induced transmutation of long-lived radioactive nuclides. The range of usable neutron energies reaches from 600 keV up to 6 MeV.

At present time-of-flight measurements are done at linear electron accelerators (Oak Ridge, Geel, Dubna) and at proton accelerators (LANSCE, CERN-PS). All facilities offer neutron pulse widths of some ns and therefore need longer flight paths. For example the CERN-PS has a 200 m flight path and a big lead radiator and it aims at a wide energy range from thermal up to GeV. Now at the ELBE radiation source we pursue the idea to make available a pulsed neutron source that allows very short time-of-flight paths.

In the following presentation main attention is directed towards the calculation of the particle fluxes at the neutron radiator and at the measuring place. The calculations are performed with the Monte Carlo codes MCNP [1] and FLUKA [2].

A principle layout of the TOF-experiment with the main components is shown in Fig. 1a. The electrons are stopped in a heavy target providing bremsstrahlung photons, which produce by (γ,n)-reactions the so-called photoneutrons. The electron pulse structure is mapped into a similar pulse structure of the neutrons allowing time-of-flight experiments.

[1] Institute for Nuclear and Particle Physics, Technical University Dresden
[2] Institute of Nuclear and Hadron Physics, Research Center Rossendorf

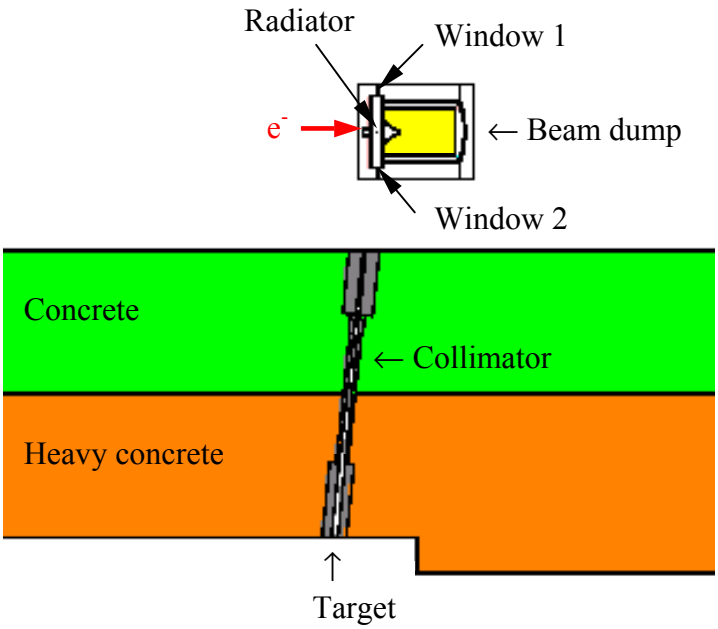

Fig. 1a: Sketch of the time-of-flight experiment

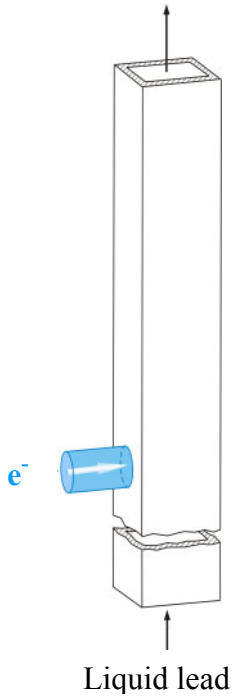

Fig. 1b: Neutron radiator tube

2. Design of the photoneutron radiator

The electron beam will be directed to the photoneutron radiator as shown in Fig. 1a and 1b. Neutrons, which are emitted under an angle of about 90 degrees, will be directed to the target place through a collimator (Fig. 1a). A flight path of about 3.6 meters makes it possible to separate the neutrons from the bremsstrahlung and the secondary electrons. In the primary beam direction a beam dump will be placed behind the neutron radiator (Fig. 1a) to absorb the unused particles and so to reduce the dose rate.

The development of a technologically feasible neutron radiator is a challenging task in itself. The material selection has to satisfy physical and thermo-mechanical criteria. On the one hand the neutron production has to be as large as possible. This can be reached using a material with a high atomic number. However working with a beam current of about 1 mA this results in a power deposition in the radiator material of about 10 kW. On the other hand the neutron pulses have to be as short as possible to enable a short flight path, what requires a small volume neutron radiator avoiding multiple neutron scattering deforming the sharp neutron pulse structure. It turned out that it is impossible to use a solid, e.g. a tungsten target, because that would result in melting due to the high energy deposition. An optimum cooling is expected for liquid metals and therefore we selected lead as the radiator material. The lead circulates in a cooling loop.

The time resolution of the TOF-experiment depends on the spread of the neutron tracking time inside the radiator volume. Therefore short neutron path lengths inside the active volume have to be realised. The material depth seen by the electron beam was chosen in the order of one radiation length (X_0(Pb) = 5.6 mm). Selecting the channel wall material properties like a high melting point, a high heat conductivity, a high fracture strain (larger than 2 %) and a low thermal expansion are requested. Finally beryllium and molybdenum turned out to be feasible

wall materials. For thermo-mechanical reasons the wall thickness has to be in the range of 500 μm. The power distributions in the wall and in the liquid lead were calculated using the Monte-Carlo Code FLUKA. For that an electron beam of E = 30 MeV, a current of I = 1mA and a beam radius of 1.5 mm had been assumed. The liquid lead is exposed to the electron beam when it passes a radiator section with a cross sectional area of 5.6 mm x 5.6 mm (see Fig. 1b). Thermo-mechanical calculations for the target section predict a maximum temperature of 530 °C in the lead and the wall respectively for a mean lead velocity of about 5 m/s and a temperature of 400 °C at the inlet of the radiator section. The numerical flow and heat transfer simulation were done using the multi-purpose finite elements code FIDAP [3]. The temperature distribution provides mechanical loads in the wall. The stresses and strains were evaluated using a finite element model based on the code ANSYS [4]. The nodal temperatures were taken from the FIDAP calculations. The obtained plastic equivalent strains for beryllium and for molybdenum are far below the respective fracture strains even at room temperature.

3. Particle fluxes at the radiator and at the target position

Results of detailed calculations of the energy angle distribution of the neutrons, photons and electrons leaving the lead-molybdenum radiator show, that photons and electrons prefer forward scattering in beam direction and the neutrons are scattered isotropically. To reduce photon and electron background at the measuring place the neutrons are decoupled at about 90 degrees. The photons and electrons are stopped in a beam dump with large acceptance.

The particle spectra at the radiator surface in front of the collimator are shown in Fig. 2. The

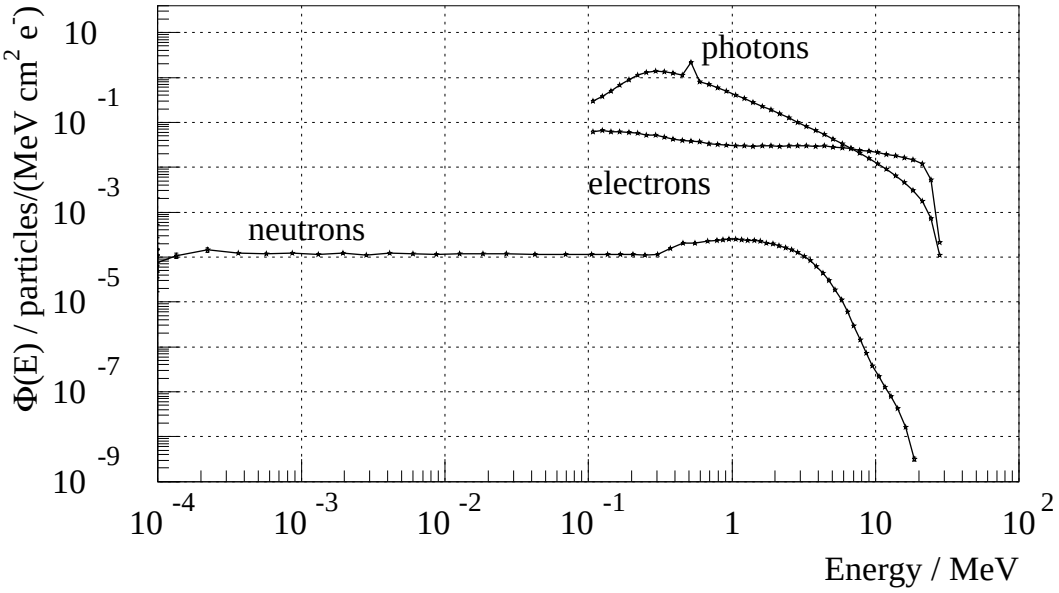

Fig. 2: Particle spectra at the radiator surface

calculation was carried out using MCNP for an incident electron energy of 30 MeV.
A first rough MCNP calculation of the neutron flux only with the lead-beryllium radiator neglecting all other constructional components yields a neutron fluence of $7.94 \cdot 10^{-10}$ n/cm^2 per starting electron (E_{e^-} = 30 MeV) at a distance of 3.6 m. With an electron current of 1 mA this gives a total flux of about $5 \cdot 10^6$ n/(cm^2 s) at the target position.

Further MCNP calculations of the background and flux at the target considered all necessary geometric details (see Fig. 1a). Two principles were applied for these calculations, first: remove material, especially near the radiator, out of the range of vision of the collimator and second: reduce the background of thermal neutrons from the collimator what can be achieved with boric polyethylene as cladding material of the collimator. Fig. 3 shows the neutron fluence spectra at the target position ($E_{e^-} = 30$ MeV). Almost all neutrons come directly from the lead and the channel wall without further collisions. The background is low and stems from windows 1 and 2 of the radiator vacuum housing, which are in the range of vision of the col-

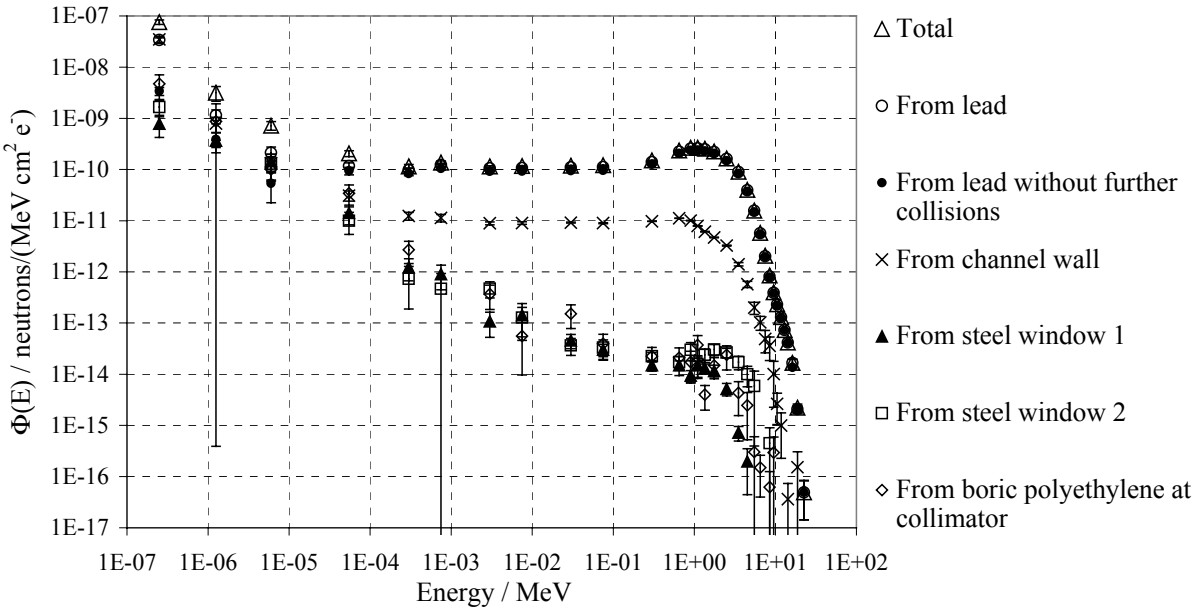

Fig. 3: Neutron spectra at the target position

limator (see Fig. 1a), and from the collimator itself.
In Fig. 4, the neutron flux due to a δ-shaped electron pulse is shown at the target position over the time. At t = 0 the electron pulse hits the radiator and at 12 ns the prompt photons reach the target position. The energy range of the measurement determines the maximum number of usable electron pulses. For example if only each fourth electron pulse is taken, the next bunch of photons arrives at $2^2 \cdot 77\text{ns} + 12\text{ns} = 320\text{ns}$. This determines the lowest usable neutron energy, which is in this constellation about 660 keV ($t < 320$ ns corresponds to $E_n > 660$ keV). It is clear that skipping electron pulses reduces the neutron yield at the target. Quantitatively in this case it means that a fourth of the electron current yields a fourth of the neutron flux. So for starting electrons with an energy of 30 MeV instead of the first estimated neutron flux of about $5 \cdot 10^6$ n/(cm^2 s) we get only $1.25 \cdot 10^6$ n/(cm^2 s).

A rough estimation of the energy resolution at the target position due to the radiator provides values of about 0.16% and 0.19% for a radiator depth of $X_0 = 5.6$ mm and $2X_0 = 11.2$ mm, respectively. The total energy resolution also depends on the electron pulse width and on the detector resolution. An assumed detector time resolution of 300 ps provides an energy resolution of $\Delta E/E \approx 0.4\%$ for a neutron energy of $E_n \approx 3$ MeV for a radiator depth of $X_0 = 5.6$ mm.

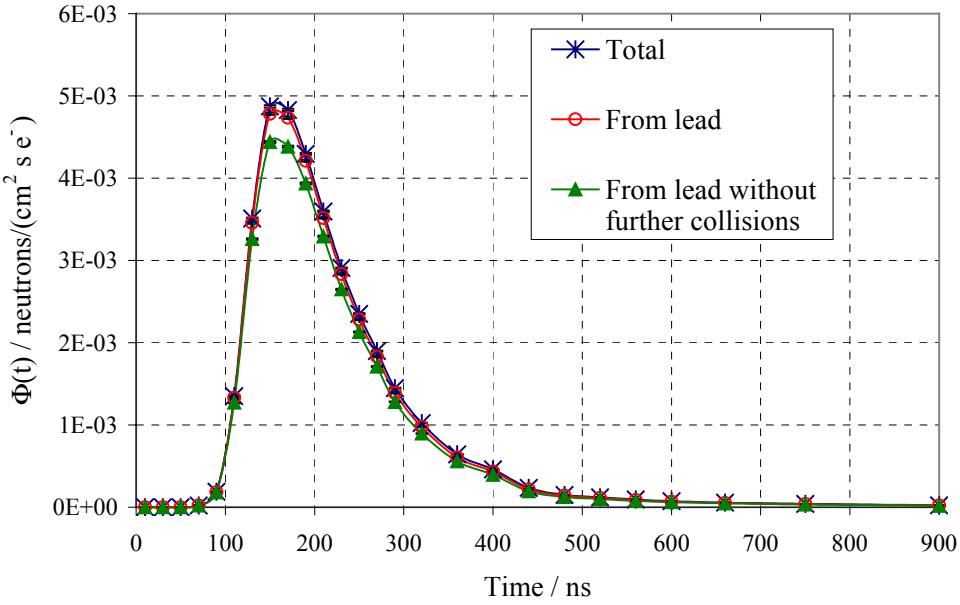

Fig. 4: Neutron flux at the target position over the time for one e^--δ-pulse

4. Conclusions

The radiator is technologically feasible with the selected materials, lead as fluid, beryllium or molybdenum for the channel wall.

The calculated neutron intensities at the measuring place show, that there is a usable energy range of about 600 keV up to 6 MeV. In this energy range the total neutron flux at the measuring place is about $4.2 \cdot 10^6$ n/(cm^2 s) for an electron current of 1 mA and an incident electron energy of 30 MeV.

It is planned to install an electron source with a lower pulse frequency and the same average current of 1 mA. This would decrease the lowest usable neutron energy.

Moreover a lead radiator with a depth of two electron radiation lengths (11.2 mm) has about a 2.3 times higher neutron intensity than one with a depth of one radiation length. However this yields a worse energy resolution, here roughly estimated with 0.19% compared to 0.16%, what is practically an insignificant deterioration.

References

[1] J. F. Briesmeister, editor, *MCNP a general Monte Carlo n-particle transport code*, version 4A, LA 12625 M, November 1993.
[2] A. Fasso, A. Ferrari and P. R. Sala, *Proc. of the Monte Carlo 2000 conference*, Lisbon, 23-26 October 2000, Springer-Verlag Berlin Heidelberg New York.
[3] Fluent Inc.: *FIDAP 8 theory manual*, Lebanon, NH, USA, 1998.
[4] ANSYS *User's manual for rev. 5.6*, Swansons analysis systems, Inc., 1999.

Acknowledgement

The project is supported by the DFG.

NEUTRON AND GAMMA FLUENCE AND RADIATION DAMAGE PARAMETERS OF EX-CORE COMPONENTS OF RUSSIAN AND GERMAN LIGHT WATER REACTORS

Bertram Boehmer, Joerg Konheiser, Klaus Noack, Anatolij Rogov, Gennady Borodkin[1], Eckhard Polke[2], and Pavel Vladimirov

1. Introduction

Radiation embrittlement of pressure vessel steel in mixed neutron-gamma fields is mostly determined by neutrons, but in some cases also by gamma-radiation. This was the clear outcome of the surveillance specimen story at HFIR [1]. Depending on reactor type, gamma radiation can influence evaluations of lead factors of surveillance specimens, affect the interpretation of results of irradiation experiments and finally, it can result in changed pressure vessel lifetime evaluations. The paper presents some results of work which has been done in this respect. Absolute neutron and gamma flux spectra had been calculated for two core loading variants of the Russian PWR type VVER-1000, for a German 1300 MW PWR and for a German 900 MW BWR. The present investigations extend a similar work done before for VVER-440 and VVER-1000 reactors [2]. Based on the calculated spectra, several fluence integrals and radiation damage parameters were derived for the region around the azimuthal flux maximum in the mid-plane at different radial positions between core and biological shield. The relative contributions of gamma radiation to the sum of gamma and neutron contributions are of special interest. As damage parameters the displacements per atom of iron are given separately for neutrons and gammas as well as estimations of the numbers of freely migrating defects (FMD). To get some notion about the uncertainties of the obtained dpa, the calculations were performed using different dpa cross section evaluations. Additionally, gamma produced dpa were calculated by means of the Monte Carlo code EGS4. Another parameter of practical interest for pressure vessel dosimetry and which depends on the gamma flux spectra is the contribution of photo-fissions to the activation of fission detector materials. Therefore, neutron and photo-fission rates were calculated for the fission detector reactions ^{237}Np(n,f) and ^{238}U(n,f). Most of the calculations were performed using a 3D synthesis of 2D/1D-flux distributions. To increase the reliability of the evaluations some of the calculations were repeated by another laboratory. To verify the accuracy of the results additional calculations with the continuous energy Monte Carlo code MCNP were performed for two reactors.

This work was supported by the German Federal Ministry for Economy and Technology.

2. Calculations of absolute neutron and gamma flux spectra

2.1. Calculation methods

Most of the calculations were done according to the 3D flux synthesis method but in two versions. In the first, the 3D flux of an energy group g is synthesized using

$$\Phi_g(R,\Theta,Z) = \Phi_g(R,\Theta)\cdot\frac{\Phi_g(R,Z)}{\Phi_g^{1D}(R,\Theta)},$$

[1] Scientific and Engineering Centre for Nuclear and Radiation Safety of GOSATOMNADZOR of Russia
[2] Framatome ANP GmbH, 91058 Erlangen, Germany

where $\Phi_g(R,\Theta)$, $\Phi_g(R,Z)$ and $\Phi_g^{1D}(R,\Theta)$ are 2D flux density distributions obtained by the DORT code [3]. $\Phi_g^{1D}(R,\Theta)$ was calculated using the same (R,Θ) space grid, as for the calculation of $\Phi_g(R,\Theta)$, but for a 1D cylindrical model. The advantage of this procedure is a reduction in non-physical Θ-oscillations. Neutron and gamma data for the transport calculations were taken from the ENDF/B-VI based 47-neutron/20-gamma group data library BUGLE-96T [4]. The traditional synthesis scheme, as e. g. described in [5] was applied in the calculations which were independently performed at FRAMATOME-ANP using the library BUGLE-96 and the codes DORT and ANISN [3]. In the calculations rather fine meshes were used to describe the geometries of the reactors and the fission source distributions in detail. So, deviations between deterministic and Monte Carlo results should be mainly caused by the multi-group approach of the synthesis method.

The Monte Carlo code MCNP [5] with continuous energy data based on ENDF/B-VI Rev.3 was applied to validate the deterministic results for the VVER-1000 with standard loading and for the 1300 MW PWR. Geometric and fission source details were described to a maximum possible degree. The weight window method was used to reduce the statistical errors.

2.2. Reactor models

VVER-1000 with standard fuel loading:
The VVER-1000/320 type reactor with hexagonal assemblies and a 60° rotational symmetry was modeled in all details including the complex baffle construction and pin-to-pin power distributions [6].
VVER-1000 with low leakage fuel loading:
This reactor differs from that described above only in the fuel loading scheme. In the outer rows of fuel assemblies such assemblies with the highest burn-up were situated warranting in that way a lower leakage of neutrons out of the core and consequently a lower radiation load on the RPV.
German 1300 MW PWR:
The reactor - in the following called PWR-1300 - has a 45° symmetry and quadratic assemblies. The neutron source was given pin-wise and for different height layers. Surveillance specimens were positioned at the outer wall of the barrel.
German 900 MW BWR:
The reactor - in the following called BWR-900 - has quadratic assemblies with 49 fuel pins in each. The neutron source was given assembly-wise for 24 axial layers. For these layers also the water densities were given, changing considerably over the height in this reactor type. Surveillance specimens were affixed with some distance to the inner wall of the pressure vessel.

2.3. Absolute neutron and gamma flux spectra and flux integrals

Absolute neutron and gamma flux spectra and flux integrals were calculated for the azimuthal flux maxima in the mid-planes of four reactors at nominal powers for different radial positions between core and the biological shield, particularly, at surveillance positions, as well at inner and outer surfaces of RPV walls as at the 1/4 RPV thickness positions. Table 1 gives the flux integrals which are important for the RPV embrittlement evaluations. These results base on the neutron and gamma fluxes calculated by the synthesis method (1).

Table 1: Flux integrals in 1/cm^2/s calculated by the synthesis method for the azimuthal maxima in the mid-planes of several reactors.

Reactor	Position	$\Phi_{n\text{-total}}$	$\Phi_{n\text{-thermal}}$	$\Phi_{n,E>0.1\ MeV}$	$\Phi_{n,E>0.5\ MeV}$	$\Phi_{n,E>1\ MeV}$	$\Phi_{\gamma,total}$	$\Phi_{\gamma,\ E>1\ MeV}$
VVER-1000	Inner wall	2.65E+11	1.34E+11	7.00E+10	4.70E+10	3.08E+10	3.03E+12	1.20E+12
Standard	¼ T	1.03E+11	8.15E+09	5.85E+10	3.41E+10	1.83E+10	7.25E+11	2.76E+11
	Outer wall	2.23E+10	1.41E+09	1.24E+10	5.45E+09	1.82E+09	1.62E+10	7.08E+09
VVER-1000	Inner wall	1.98E+11	9.92E+10	5.30E+10	3.56E+10	2.33E+10	2.31E+12	9.15E+11
Low-leakage	¼ T	7.85E+10	6.05E+09	4.48E+10	2.60E+10	1.40E+10	5.54E+11	2.12E+11
	Outer wall	1.81E+10	1.16E+09	9.91E+09	4.31E+09	1.44E+09	1.28E+10	5.58E+09
PWR-1300	Surv. pos.	2.43E+11	1.30E+11	5.37E+10	3.72E+10	2.49E+10	1.40E+12	4.04E+11
	Inner wall	1.95E+10	7.79E+09	6.68E+09	4.74E+09	3.33E+09	7.16E+11	2.43E+11
	¼ T	8.13E+09	8.51E+07	5.38E+09	3.03E+09	1.58E+09	9.78E+10	3.68E+10
	Outer wall	1.71E+09	7.83E+07	9.29E+08	3.45E+08	9.31E+07	8.74E+08	3.95E+08
BWR-900	Surv. pos.	1.70E+10	1.32E+10	2.24E+09	1.88E+09	1.59E+09	2.12E+12	3.43E+11
	Inner wall	3.63E+09	9.80E+08	1.66E+09	1.23E+09	8.74E+08	6.27E+11	2.12E+11
	¼ T	2.26E+09	1.21E+08	1.46E+09	9.82E+08	6.12E+08	2.22E+11	7.95E+10
	Outer wall	7.99E+08	3.63E+07	4.71E+08	2.61E+08	1.24E+08	1.26E+10	5.14E+09

As example, neutron and gamma spectra at inner RPV surfaces at nominal power are presented in figures 1 and 2. We see that the standard VVER-1000 has more than one order of magnitude higher and the BWR-900 about four times lower neutron fluxes than the PWR-1300. The differences between the gamma fluxes of these reactors are considerably smaller as can be seen in Fig. 2. The reason is that the water gaps between core and RPV are growing in the order: VVER-1000, PWR-1300, BWR-900 and that the neutrons are much more attenuated in water than the photons. The spectrum of the low leakage VVER-1000 variant, not shown here, is very similar to that of the standard variant differing by a factor of about 0.75 only.

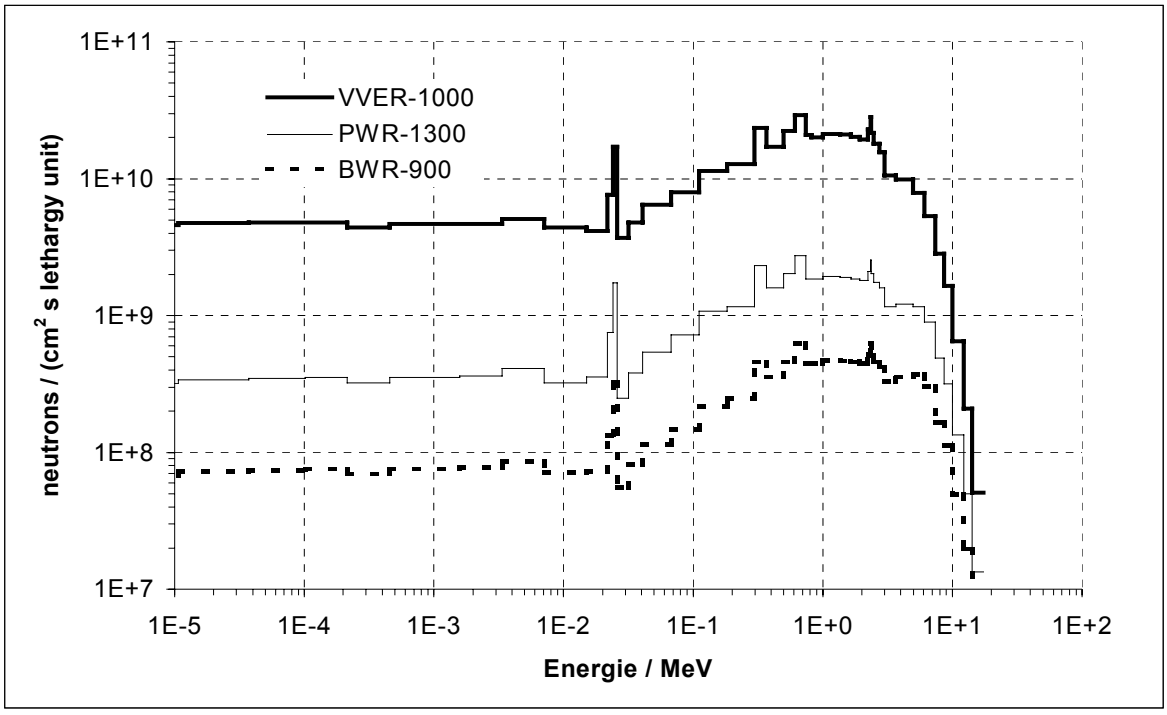

Fig. 1: Neutron flux spectra for nominal power at the inner RPV surfaces.

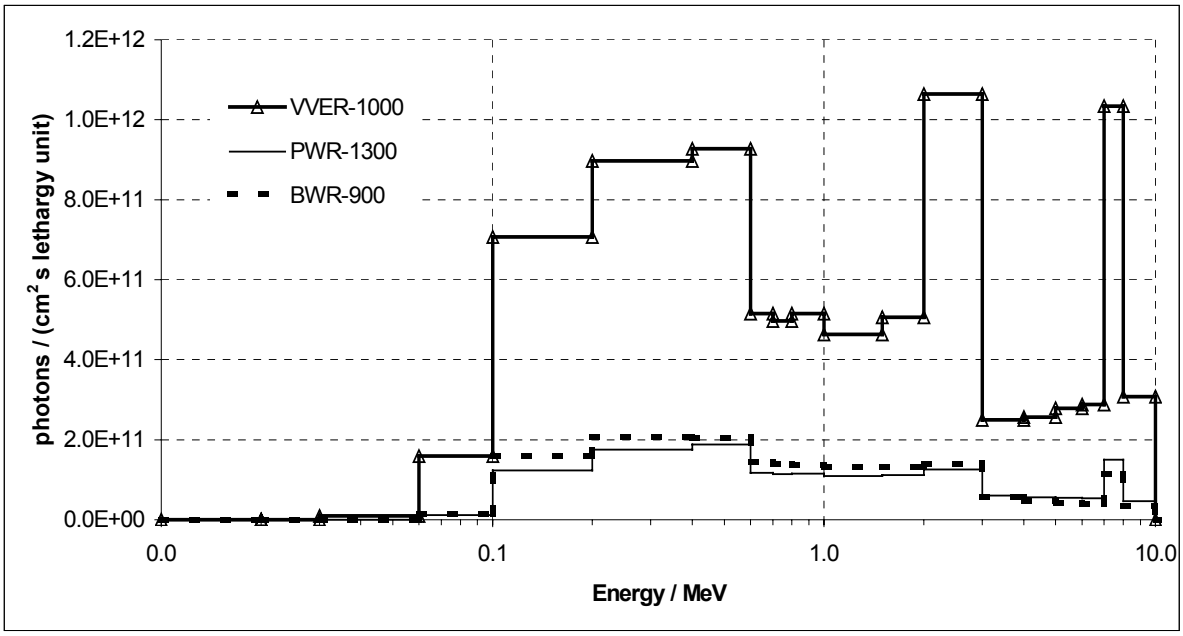

Fig. 2: Gamma flux spectra for nominal power at the inner RPV surfaces

3. Calculation of neutron and gamma damage parameters

3.1. Definition of radiation damage parameters

Although the theoretical aspects of the effect of radiation on materials are well elaborated, there is still no proved theory allowing to predict the deterioration of pressure vessel steel properties from first principles. While the effect of gamma radiation is usually completely neglected, the effect of neutron radiation on the RPV is mainly considered to be characterized by the fast fluence above 1 MeV (Western standard) or above 0.5 MeV (Russian standard). According to the regulation guides the material property parameter most important for the RPV safety, the ductile-to-brittle transition temperature, is supposed to be proportional to the cubic root of the fast neutron fluence. The proportionality factor is obtained by experiments with sets of Charpy specimens. Obviously, this procedure cannot take into account effects of low energy neutrons, of the neutron spectrum, of gamma radiation and of the fluence rate (flux) while all these factors can be of different importance to steel embrittlement in various irradiation conditions.

Another widely used irradiation exposure parameter depending on the radiation spectra is the number of displacements per atom (dpa) caused by the radiation. Fast reactor neutrons transfer up to some tens of keV recoil energy to a primary knocked-on atom (PKA) that through multiple collisions initiates an atomic displacement cascade. During this process lasting about 0.1 ps and called collision stage, a large number of atoms (NNRT), which can be estimated using the Lindhard approach, are displaced from their lattice sites producing point defects: vacancies and interstitials. As the displacements are located very closely and the temperature in the cascade region is high, point defect motion, recombination and defect clustering will occur. After the cascade cooling time of the order of tens of ps only about one third of the primary defects NNRT survive. After much longer time, diffusion and recombination result in a further reduction of the number of defects. Only about 1 – 5% of the defects escape the cascade region and become freely migrating defects (FMD). FMD will contribute to long range diffusion over the bulk of the irradiated material. Unfortunately, up to now, recombination effects have not yet been taken into account in dpa standards. Nevertheless, FMD have been

proposed as an additional exposure parameter for radiation damage [7,8]. Further theoretical and experimental investigations are needed to explore their role in RPV embrittlement. The displacements induced by photons due to small PKA energies cannot produce cascades and no recombination occurs. Therefore, the efficiency of producing FMD by fast gammas is about 20 to 100 times higher than that of neutrons. A similar enhancement could be possible for the displacements caused by the recoil of gammas from the capture of thermal neutrons. However, in our calculations this effect has been found to be negligibly small. These arguments support the use of FMD as tentative exposure parameter for comparison of the neutron and gamma irradiation effects.

3.2. Calculated damage parameters

For the calculations of neutron dpa rates the displacement cross section of iron recommended by the ASTM had been used. Gamma displacements have been calculated as well using cross sections obtained by other authors (Baumann-[9], Alexander-[10], Kwon-[11]) as the cross sections which have been newly calculated by us with the help of the electron-gamma transport code EGS4. The Monte Carlo simulation allows to take into account the generation of secondary particles and avoids the continuous slowing down approximation used in other cross section calculations. However, test calculations showed that the influence of these effects is very small. The FMD rates were calculated using the methodology described in [12]. The needed PKA spectra were calculated on the base of the code package NJOY [13]. Table 2 shows the calculated gamma and neutron dpa and FMD rates.

Table 2: Neutron and gamma dpa and FMD rates at azimuthal maximums in the mid-planes of several reactors.

Reactor	Position	dpa_n/s	dpa_γ/s	$\gamma/(n+\gamma)$ %	FMD_n	FMD_γ	$\gamma/(n+\gamma)$ %
VVER-1000 Standard	Inner wall	4.70E-11	1.72E-12	3.5	1.60E-12	1.72E-12	51.9
	1/4T	3.05E-11	4.01E-13	1.3	1.04E-12	4.01E-13	27.9
	Outer wall	4.65E-12	1.06E-14	0.2	1.58E-13	1.06E-14	6.3
VVER-1000 Low leakage	Inner wall	3.58E-11	1.32E-12	3.6	1.22E-12	1.32E-12	52.0
	1/4T	2.34E-11	3.09E-13	1.3	7.95E-13	3.09E-13	28.0
	Outer wall	3.71E-12	8.44E-15	0.2	1.26E-13	8.44E-15	6.3
PWR-1300	Surveill.	3.90E-11	4.62E-13	1.2	1.21E-12	4.62E-13	27.6
	Inner wall	5.14E-12	3.26E-13	6.0	1.59E-13	3.26E-13	67.2
	1/4T	2.81E-12	4.90E-14	1.7	8.72E-14	4.90E-14	36.0
	Outer wall	3.23E-13	5.60E-16	0.2	1.00E-14	5.60E-16	5.3
BWR-900	Surveill.	2.52E-12	2.95E-13	10.5	7.05E-14	2.95E-13	80.7
	Inner wall	1.34E-12	2.37E-13	15.0	3.76E-14	2.37E-13	86.3
	1/4T	9.69E-13	8.96E-14	8.5	2.71E-14	8.96E-14	76.8
	Outer wall	2.37E-13	6.12E-15	2.5	6.64E-15	6.12E-15	48.0

To generate Table 2, the gamma displacement cross section of Ref. [11] was used. Fig. 3 presents the calculated radial dependence of the dpa_γ/dpa_n ratio for the BWR-900 in the direction of the azimuthal flux maximum for the four considered gamma dpa cross section evaluations. The comparison of results obtained with different cross sections gives some impression of the magnitude of uncertainty caused by these cross sections. The data of Kwon result in the highest gamma-dpa rates. Another increase by about a factor 2 could be obtained by lowering the displacement threshold energy in supposable limits and by considering secondary displacements [11]. The presented radial dependencies show that the relative gamma dpa contribution

reaches its maximum at the inner surface of the RPV wall. The curves for the other reactors are quite similar but with remarkably lower maxima, see Table 2. The highest relative gamma-contribution is the consequence of the largest water gap between core and RPV in case of the BWR-900. The differences in the gamma contributions at surveillance positions and RPV inner wall is of special interest to the RPV surveillance programs.

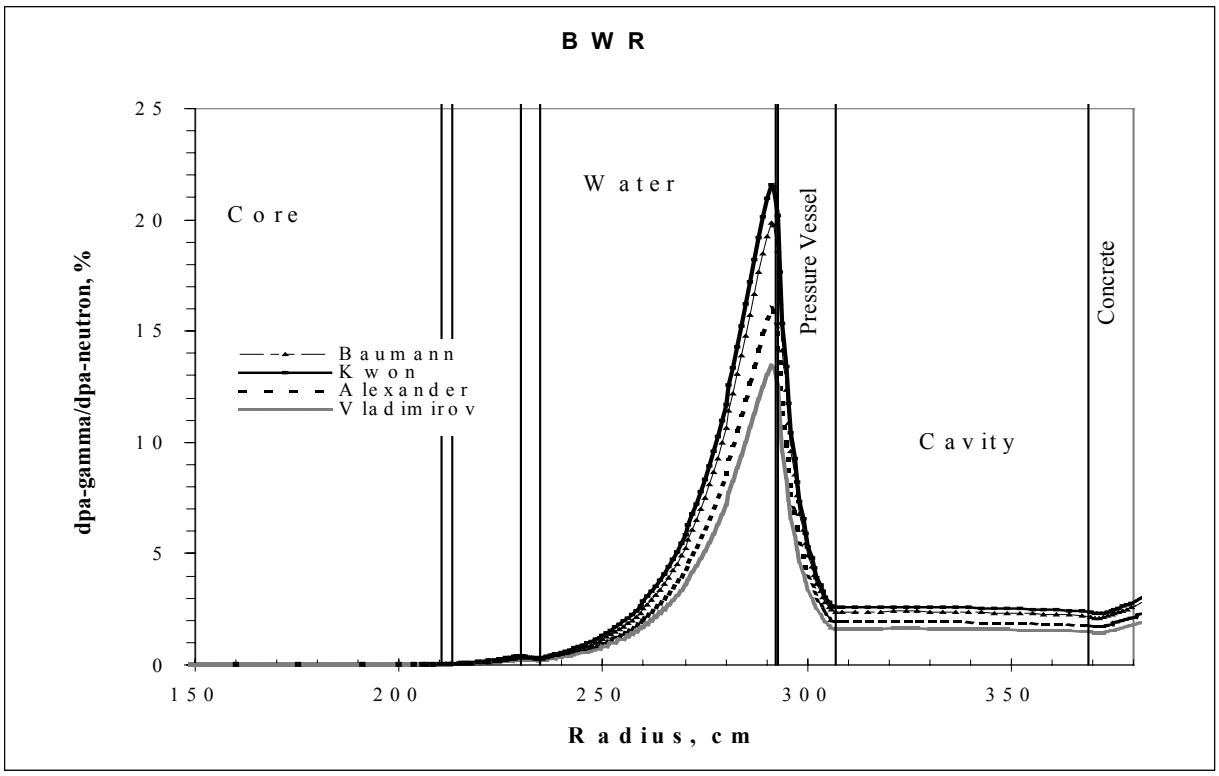

Fig. 3: Ratio of gamma-dpa to neutron-dpa as function of radius for the BWR-900.

4. Impact of gamma radiation on neutron fission detector measurements

Fission detectors based on threshold fission reactions are very well suited to cover the lower energy region of the fast neutron spectrum in pressure vessel neutron fluence measurements. Unfortunately, they are sensitive to some degree also to gamma radiation due to the gamma fission reactions caused by high energy photons. Therefore, they can be used in reactor environments as neutron detectors only then, if the contribution of gamma fissions can be separated. In cases of high gamma contributions these detectors can be even used to deliver information on both components. In Table 3 the relations between the calculated gamma and neutron fission rates are given at different positions in the four considered reactors. One can realize that the use of these detectors in some cases demands a correction for gamma-induced fissions. The highest gamma/neutron fission ratio was found for the BWR-900.

Table 3: Ratios of gamma-fission to neutron-fission rates for ^{237}Np and ^{238}U in per cent.

Reactor	VVER-1000 standard		VVER-1000 low leakage		PWR-1300		BWR-900	
Position	^{237}Np	^{238}U	^{237}Np	^{238}U	^{237}Np	^{238}U	^{237}Np	^{238}U
Surv. Pos.	-	-	-	-	3.25	8.22	22.09	34.05
Inner wall	10.72	24.82	10.78	24.76	17.60	33.04	35.07	54.06
Outer wall	0.67	3.98	0.67	4.00	0.50	3.62	6.17	19.01

5. Comparison of results obtained by different laboratories and by Monte Carlo and deterministic methods

Results produced by means of the Monte Carlo code MCNP with continuous energy data based on ENDF/B-VI Rev.3 data were applied to validate the deterministic results. Calculations at different laboratories with the same method and slightly different nuclear data libraries were compared to evaluate uncertainties caused by different discretisation schemes, the influence of taking into account up-scattering in the thermal region etc.. Fig. 4 compares obtained gamma spectra and Table 4 compares several neutron and gamma flux integrals.

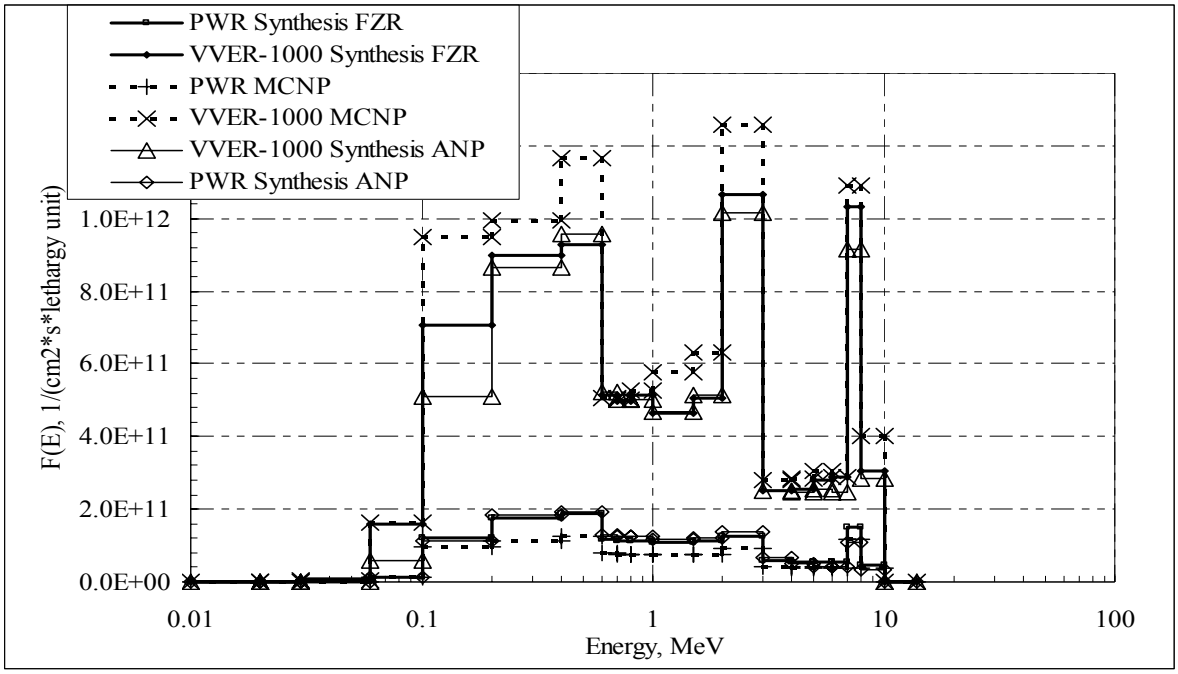

Fig. 4: Gamma flux spectra at the flux maximum position of the inner RPV surface obtained by different numerical methods and users.

Table 4: Comparison of neutron and gamma flux integrals for VVER-1000 and PWR-1300 discrete ordinate synthesis calculations at FZR and Framatome-ANP (ANP) with MCNP results.

VVER-1000:	Position	$\Phi_{n\text{-total}}$	$\Phi_{n\text{-therm}}$	$\Phi_{n,E>.1MeV}$	$\Phi_{n,E>.5\ MeV}$	$\Phi_{n,E>1MeV}$	$\Phi_{\gamma,total}$	$\Phi_{\gamma,\ E>1MeV}$
Synth. FZR / MCNP	Inn. wall	0.94	1.44	1.13	1.18	1.21	0.85	0.85
	¼ T	1.24	2.64	1.24	1.25	1.25	0.86	0.92
	Out. wall	2.03		1.37	1.30	1.28	1.08	1.03
Synth. ANP / MCNP	Inn. wall	0.70	0.71	1.13	1.16	1.21	0.78	0.82
	¼ T	1.23	0.75	1.27	1.20	1.25	0.81	0.90
	Out. wall	2.33		1.45	1.28	1.41	1.28	1.22
PWR-1300:								
Synth. FZR / MCNP	Surv. Pos.	0.76	0.74	0.79	0.80	0.81	0.95	0.93
	Inn. wall	0.87	0.77	0.91	0.92	0.94	1.23	1.10
	¼ T	0.90	0.25	0.92	0.88	0.84	0.77	0.80
	Out. wall	0.71	0.39	0.75	0.78	0.81	0.50	0.65
Synth. ANP / MCNP	Surv. Pos.	-	-	-	-	-	-	-
	Inn. wall	0.67	0.37	0.89	0.88	0.91	0.96	0.92
	¼ T	0.97	0.16	0.95	0.86	0.87	0.79	0.83
	Out. wall	0.91	0.93	0.72	0.67	0.84	0.62	0.73

As expected, the FZR and ANP deterministic results show very good agreement for the fast neutron fluxes. Discrepancies in the thermal region are caused by neglecting upscattering in the ANP calculations. In the average, the MCNP results agree within limits of 20% as well for fast neutrons as for photons with the deterministic calculation. However, for thermal neutrons much greater discrepancies are observed.

6. Conclusions

The calculated gamma and neutron spectra, flux integrals and damage parameters are recommended for evaluations of the influence of gamma radiation on steel embrittlement and fission detector dosimetry for the Russian reactor type VVER-1000 and two typical German reactors, a 1300 PWR and a 900 MW BWR.

The contributions of gamma radiation to the displacement rates at the inner PV wall are about 4% , 6% and 15% for the VVER-1000, PWR-1300 and the BWR-900, respectively. The relative uncertainty of these values can exceed 50%, to a large extent due to the uncertainty of the gamma dpa cross sections. That was concluded from the comparison of dpa rates calculated by means of different gamma-dpa cross section evaluations, showing considerable discrepancies. A new evaluation of gamma-dpa cross sections seems to be necessary.

Considerations about the role of defect recombination in cascades and of freely migrating effects make the FMD a candidate for a new or additional damage parameter. The FMD formation is even dominated by gamma-radiation at the inner RPV wall, amounting to 52% for the VVER-1000 and 86% for the BWR-900.

Gamma-fission can contribute up to 35% to the measured values obtained with fission neutron detectors at potential detector positions, for a ^{238}U-detector at BWR surveillance position 25%.

Comparison of results obtained with BUGLE-96 with and without upscattering in the thermal region and with the continuous energy code MCNP show a relatively good agreement for the gamma flux results, within 20%, as the gamma flux apparently, is not dominated by thermal neutrons showing much greater discrepancies. As all used libraries are based on the same gamma production data, gamma flux spectrum measurements are needed to validate the accuracy of the calculations.

References

[1] K. Farell, et al., J. Nucl. Mat. **210** (1994) 268.
[2] E. Brodkin, B. Böhmer, A. Egorov, S. Zaritsky, ,Proc. JT KT 2000, Bonn, p. 597-600
[3] DOORS3.2, RSIC CODE PACKAGE CCC-650.
[4] J.E. White et al., BUGLE-96, ANS RP&S Topical Meeting,Falmouth MA, 1996.
[5] J.F. Briesmeister, MCNP-Manual, LA-12625-M, 1993.
[6] B. Borodkin, B. Böhmer, Trans. American Nuclear Society, 2000, **Vol. 82**, p. 223-225.
[7] D.E. Alexander, L.E. Rehn, J. Nucl. Mat. **209** (1994) 212.
[8] D.E. Alexander, L.E. Rehn, Proc. 9th Int. Reactor Dosimetry Symp., Prague 1996, p.508.
[9] N.P. Baumann, Proc. 7th ASTM-EURATOM Symp. on Reactor Dosimetry, Strasbourg, 27-31 Aug. 1990, p.689.
[10] D.E. Alexander, J. Nucl. Mat. **240** (1997) 196
[11] J. Kwon and A.T. Motta, Ann. Nucl. Energy **27** (2000) 1627.
[12] B.Petrovic, et al., Proc.ANS RP&S Conference, 1998, Nashville, Vol.2.pp.25-32
[13] R.E. MacFarlane and D.W. Muir, LA-12740-M, 1994.

THE SHIP EXPERIMENT AT THE GDT FACILITY : CONCEPT AND RESULTS OF CALCULATIONS

Andrey V. Anikeev[1], Petr A. Bagryansky[1], Alexandre A. Ivanov[1], and Klaus Noack

1. Introduction

The Gas Dynamic Trap (GDT) experimental facility of the Budker Institute Novosibirsk is a long axisymmetric mirror system with a high mirror ratio to confine a two-component plasma [1]. The mirror ratio can be varied in the range of 12.5-100. One component is a collisional "background" or “target” plasma with ion and electron temperatures up to 130 eV and a density up to 1.8×10^{14} cm^{-3}. Its ion mean free path of scattering into the loss cone is much less than the mirror-to-mirror distance what results in the gas dynamic regime of confinement. The second component is the population of fast ions with energies of 2-17 keV and a density up to 10^{13} cm^{-3}. They are produced by a 45° neutral beam (NB) injection into the central cell. The fast ions are confined in the mirror regime having their turning points at the mirror ratio of 2. To provide MHD stability of the entire plasma axisymmetric min-B cells are attached to both ends of the central cell.

At present, the GDT facility is being upgraded. The first stage of the upgrade is the SHIP (Synthesised Hot Ion Plasmoid) experiment [2]. It aims, on the one hand, at the investigation of plasmas which are expected to appear in the region of high neutron production in a GDT based fusion neutron source proposed by the Budker Institute [3] and, on the other hand, at the investigation of plasmas the parameters of which have never been achieved before in magnetic mirrors. The expected record values of plasma parameters and several peculiarities of the plasma, like the composition of two energetically very different ion components where the high-energetic part represents the majority, strong non-isotropic angular distribution of the high-energetic ions and non-linear effects as non-paraxial effective magnetic field and high value of plasma-β offer a great field for interesting investigations.

In order to simulate the particle fields inside the GDT device and later in a GDT based neutron source an Integrated Transport Code System (ITCS) is being developed in collaboration between Forschungszentrum Rossendorf and Budker Institute [4]. It consists of modules which allow the calculations of neutral gas, background plasma and of the fast ion component considering their mutual interactions.

This contribution explains the concept of the SHIP experiment and presents results of first calculations by means of the ITCS modules.

2. Technical description

The experiments will be performed in a small, additional mirror section which is installed at the end of one side of the GDT. Figure 1 shows a schematic view of this arrangement. The magnetic field on the axis will be in the range of 0.5-5 Tesla and the mirror ratio will amount to 1.2-1.4. The magnetic field strength may be varied by extending/shortening the distance between the coils. The SHIP mirror is filled with a hydrogen background plasma streaming in from the central cell of the GDT. This plasma component is maxwellised and will have an

[1] Budker Institute of Nuclear Physics, Novosibirsk, Russia

electron temperature of about 100 eV. It is pre-heated up by the standard neutral beam injection system of the GDT. Two neutral beam injectors, which have been newly developed, will perpendicularly inject into the SHIP mirror a total current up to 120 eq. Amperes of hydrogen atoms with an energy up to 25 keV as a ramp-like pulse with a duration of at least 1 ms. So, the injection power will be variable in the range of 1-3 MW. Ionisation of the beams generates the high-energetic ion component. The density of the resulting hot ion plasmoid is expected to be substantially higher than that of the target plasma. For the given experimental conditions, the lifetime of the synthesised plasma is essentially determined by the target plasma cooling rate and might be of the order of one millisecond. Since the energy loss of the fast ions by a background plasma with high electron temperature is negligible in the millisecond time-scale the averaged energy of the trapped ions is expected to be not much lower than the injection energy, i.e. in the range 15-20 keV. It was estimated that their density should reach 10^{14} cm^{-3} in a volume of about 500 cm^3 even in the case of low magnetic field what will result in high β-values between 20-40 per cent. The SHIP device will be equipped with several diagnostic methods which are successfully used in GDT experiments. The construction of the SHIP experimental cell will soon have been finished.

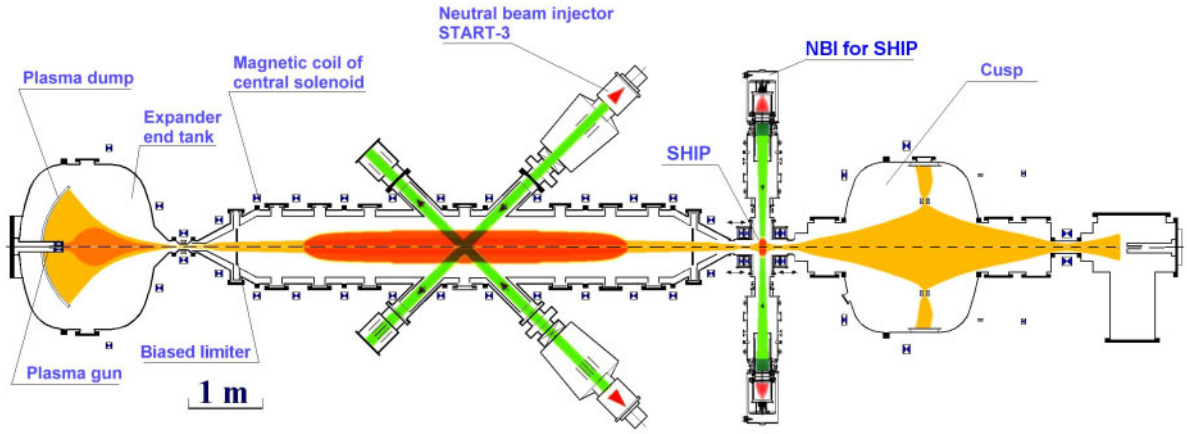

Fig. 1: GDT facility with the SHIP experiment.

3. Scientific objectives

The SHIP plasma will have some peculiarities which are of particular interest from the point of view of plasma physics:

- The ions will be divided into two energetically very different components of which the high-energetic one has the majority.
- The distribution of the flight directions of the fast ions will be highly non-isotropic.
- The non-isotropic movements of the fast ions will result in azimuthal currents which will distort the paraxial external magnetic field so that the effective magnetic field will become non-paraxial.
- Because of their high energy the fast ions will move on relatively large gyro-radii.
- In the case of a high-power injection (3 MW) and of low magnetic field a high value of β is expected for the whole plasma to which the fast ions contribute by far the greatest part.

These peculiarities and the envisaged record parameters of the SHIP plasma offer the opportunity to investigate the following objectives which are of interest from the point of view of fundamental plasma physics and at the same time of high importance regarding the neutron source project:

- To study equilibrium states of two-component plasmas with high parameters under the condition that the high-energetic ion component represents the majority.
- To study the contribution to MHD-instability and to explore the influence of non-paraxial effective magnetic field on this issue.
- To investigate the level of micro-fluctuations in the high-energetic ion component and its dependence on the background plasma.
- To determine high-β threshold to instability of any kind in the attainable parameter range.
- To explore the influence of non-paraxiality of the effective magnetic field on the equilibrium density distribution of high-energetic ions. Regarding the neutron source the question whether a longitudinal quenching will appear or not is of special interest because this effect could remarkably raise the maximum of the neutron production density.

4. Physical considerations

Several physical facts, which are of importance when comparing GDT and SHIP experiments, are to be briefly discussed. Considering target plasma and neutral gas as known distribution functions, in GDT experiments hitherto performed, the transport of the fast ions could be considered as a linear transport process. Substantial effects resulting from the interaction of a fast ion test particle with the population of the other fast ions were not observed. Results of measurements and of calculations which were done just in the frame of this approximation well agreed [5]. This is a result of the fact that the fast ion density is too low to produce non-linear effects. In the SHIP experiments the situation will be substantially different from that in the GDT. Here, the fast ion density is expected to be remarkably higher than that of the target plasma ions and will reach such values leading to several non-linear phenomena. This is because the fast ion population itself now considerable contributes to various interaction processes of a fast particle. Those are: the ionisation of the neutral beams, the angular scattering and the high-β effect which can result in a spatial redistribution of the fast ions as consequence of magnetic field deformations by strong azimuthal fast ion currents.

The question of main interest is whether the desired high parameters of the fast ions, which have been estimated on the basis of classical plasma theory, may be actually achieved with two injectors of the new type. These results are to check by means of more accurate numerical methods. The main resistance against high fast ion parameters comes from the fact that a strong fast ion density will produce a high electrostatic potential which will lower the ion density of the target plasma. The lowering of the warm ion density then results in a reduction of the ionisation rate of the neutral beams. This is because the charge-exchange (CX) with warm ions gives the highest ionisation rate for the injection energy in the range of 20-25 keV. The loss of this rate might not be compensated by an increase of the electron or ion impact ionisation. So, this feedback strongly acts against the built-up of the fast ion population. In an approximate model the relation

$$n_w = (\sqrt{n_f^2 + 4 \cdot n_0^2} - n_f)/2 \qquad (1)$$

may be derived, where:
n_w - density of the so called "warm" ions of the target plasma,
n_f - density of the fast ions,
n_e - electron density, $n_e = n_w + n_f$.
In equation (1) all densities are in their radial (r), axial (z) and time (t) dependencies and $n_0(r,t)$ is a fixed radial profile of the target plasma at the entrance into the SHIP chamber. The assumptions of the model are: the fixed profile n_0 for electrons and warm ions at the entrance,

their distribution according to the law of Boltzmann with the same temperatures T_w and T_e in the region of sloshing fast ions and the neutrality condition.

Another feedback effect connected with the densities of warm and fast ions is caused by the neutral gas. For SHIP one may expect a strong interaction between fast ions and the gas. The charge-exchange ionisation of the neutral beams with the warm ions of the target plasma produces a strong source of neutral gas just in the vicinity of the centre. Other possible source terms should be negligible. Since the central gas source is proportional to the warm ion density an increase of the fast ions will be supported by a thinner gas, which will reduce their charge-exchange losses.

5. Pre-Calculation

5.1. Calculation model

It was the main interest of the first calculations to get to know about the time behaviour of the fast ion density considering the feedback by the target plasma ions via equation (1) and by the neutral gas. This was done by means of an iteration cycle. The iteration was terminated when the changes of the fast ion density between subsequent calculations were in the range of the statistical error, i.e. about a few per cent. Unfortunately, the effect of the neutral gas could be taken into account by a rough approximation only.

Magnetic Field:

In the calculations the time independent, standard magnetic field was used, i.e. both coils produce 5.1 Tesla on the axis which gives 2.4 Tesla in the centre of the SHIP chamber. The field did not vary in time.

Target Plasma:

As boundary condition for the densities of electrons and of warm ions (protons) a time independent Gauss-like distribution $n_0(r)$ with a maximum of 5×10^{13} cm^{-3} and a half-width of 3.25 cm was chosen, see Fig. 2. For the first iteration both densities were constructed along the magnetic field without an electrostatic potential, i.e. assuming n_f as zero. The temperatures were fixed to be $T_w=T_e=100$ eV and were not changed in the iteration. After calculating a fast ion density distribution by means of MCFIT new densities n_w and n_e were determined according to equation (1) for the next fast ion simulation.

Neutral Gas Calculations:

The neutral gas calculations were done by means of the Monte Carlo code TUBE [4]. The distributions of warm and fast hydrogen atoms and of molecules were calculated inside the SHIP chamber. It was modelled as cylinder with height and radius both equal to 25 cm. The inner surface was assumed to be coated by titanium as it is in the central cell of the GDT. Unfortunately, TUBE has not yet been extended to be able to consider the interaction of the neutral gas with the fast ions what in case of SHIP will be a serious approximation. But, it acts into the direction that just in the volume occupied by the fast ions too much gas appears and consequently the fast ion density will be calculated too low. Furthermore, the space dependent gas distribution was calculated only once at the beginning of the iteration. For a next iteration step the amplitude of the gas field was multiplied with a factor that has been determined as relation of the neutral beam ionisation rates of both steps.

Neutral Beam Injection:

Up to now only the calculations of a “minimum” variant were performed and have been analysed. The target plasma was that as described above. For the neutral beam injection system only modest parameters were assumed: injection energy of the hydrogen atoms 20 keV and a ramp-like injection power of 1 MW with a duration up to 1 or 2 ms.

Fast Ion Calculations:
The calculations of the fast ion field in each iteration step were done by means of the Monte Carlo code MCFIT [4]. The code simulates test particles starting as high-energetic neutrals from the injectors, being ionised by several interaction partners and moving as fast ions in the magnetic field and interacting with reaction partners in various processes. Recently, the code was modified to be able to consider the interactions between fast particles too. Especially:

- MCFIT now considers the three densities n_w, n_f and n_e and the corresponding particles as interaction partners, see section 4.
- Now, the fast ion density n_f gives a contribution to the angular scattering of a fast ion test particle too.
- Moreover, n_f also contributes to the ionisation of the neutral beam particles. The ionisation by charge-exchange has not yet been implemented. This process would not have a direct effect on the particle balance of the fast ions.

Special MCFIT calculations were performed to determine fast ion energy and particle confinement times τ_E and τ_n, respectively. In the final iteration step, after reaching the steady state (in about 1 ms) the injection was switched off, gas, target plasma and the background fast ions were hold in their current states. Fitting the drops of the energy and particle contents by exponential time functions gave the time constants.

5.2. Results

Up to now, only the calculations for the "minimum" regime could be finished and analysed in detail. It turned out, that the fast ion population reached its steady state very quickly, already in about 1 ms. After four iteration steps the maximum of the fast ion density distribution remained in the range of the statistical error of a few percent. Figures 2 and 3 show the steady state radial (in the mid-plane) and axial distributions (on the axis) of the various densities. The density will reach the maximum value of 8×10^{13} cm^{-3}. The volume in which the density of the fast ions is greater than that of the warm ions is about 400 cm^3.

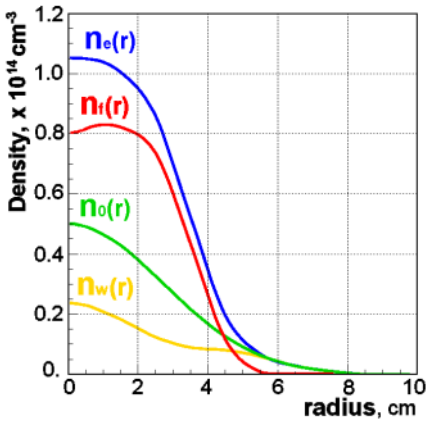

Fig. 2: Radial distributions of densities.

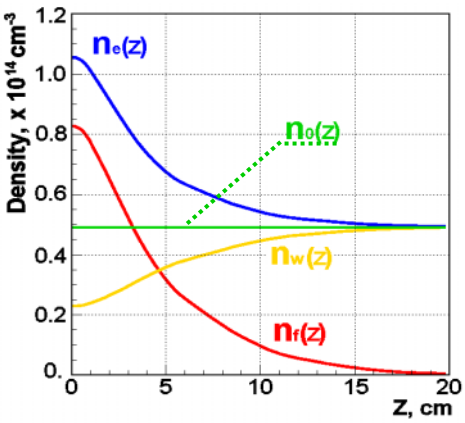

Fig. 3: Axial distributions of densities.

Figure 4 shows the power balance for the fast ions in the case of a 1 ms injection. The remarkable low CX-loss power is a consequence of the decrease of the warm ion density forced by the fast ion potential, see Figs. 2 and 3. Figure 5 shows the energy distribution of the fast ions for several time intervals in the case of a 2 ms NB injection. One can see that the energy spectrum practically does not change after 1 ms. The resulting mean energy is about 9 keV only. The soft steady state spectrum is the consequence of the increased electron density, see Figs. 2 and 3. Since the soft energy spectrum and the strong magnetic field the maximum β-value of the fast ions is merely 8%.

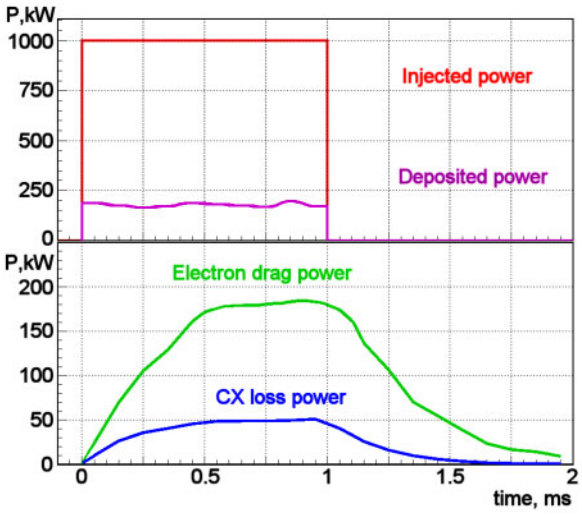

Fig. 4: Power balance of fast ions.

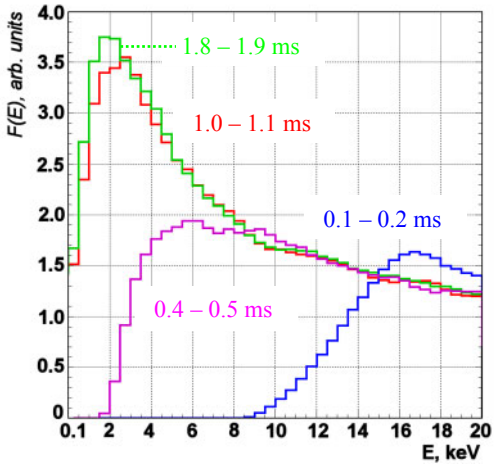

Fig. 5: Fast ion energy distributions for several time intervals.

Figure 6 shows the fast ion energy and particle content as calculated by the special calculation for energy and particle confinement times. The fitting of the drop after 1 ms gave the energy confinement time τ_E=225 µs. The corresponding fitting of the particle content resulted in two exponential functions: up to 1.6 ms with τ_n=550 µs and with τ_n=270 µs afterwards.

6. Conclusions

From the work that hitherto has been done the following conclusions may be drawn:

- The construction of the SHIP experimental cell and of the new injectors will soon have been finished.
- The fast ion transport code MCFIT has been extended to be able to consider non-linear processes too.
- The neutral gas code TUBE has to be extended to include the interactions of the neutral gas particles with fast ions.

The pre-calculations of a "minimum" regime were performed and analysed. The fast ion density will be substantially greater than that of the warm target plasma ions, it will reach 8×10^{13} cm^{-3}. The mean energy in the steady state will be about 9 keV and the maximum of the fast ion β-value will amount to 8%.

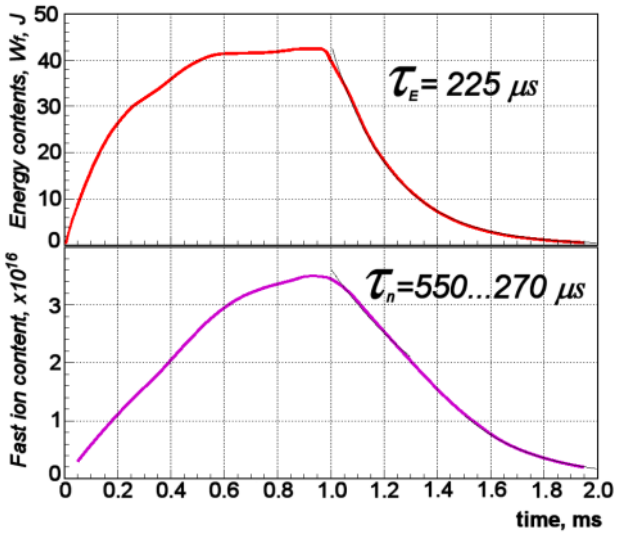

Fig. 6: Results of fast ion energy and particle contents from model calculation.

References

[1] P. A. Bagryansky, et al., Recent results of experiments at the gas dynamic trap, *Trans. Fusion Technol*, **35**, 79 (1999)

[2] A. A. Ivanov, et al., Gas-dynamic trap experiment: Status and perspectives, *Trans. Fusion Technol.*, **35**, 107 (1999)

[3] A. A. Ivanov, et al., Mirror-based neutron sources for fusion technology studies, *Nucl. Sci. Eng.,* **106**, 235 (1990)

[4] A. V. Anikeev, et al., An integrated transport code system for the calculation of multi-component, high-β plasmas in the gas dynamic trap, *Trans. Fusion Technol.,* **39**, 183 (2001)

[5] A. V. Anikeev, et al., Fast ion relaxation and confinement in the gas dynamic trap, *Nuclear Fusion*, **40**, 753 (2000)

FEM SIMULATION OF CRACK PROPAGATION IN 3PB AND CT SPECIMENS

Eberhard Altstadt, Matthias Werner and Jan Dzugan

1. Introduction

The single specimen test technique (unloading compliance technique) is widely used for the measurement of the fracture toughness of metals. In this technique the crack length extension is estimated from the compliance at certain deflections of the three point bending (3PB) specimen or compact tension (CT) specimen respectively. Therefore several steps of partial unloading are included in the test sequence. The compliance is determined from the elastic slopes of the load-deformation-curve, which occur during the partial unloading. The deformation can be described by the crack opening displacement (COD). The COD is mainly affected by the material properties of the sample and its geometry (including the initial and current crack depth), but to some extent also by the test arrangement (in particular the kinematics of the roller support). The practical experience shows, that the standardized relation between compliance and crack extension [6] leads to some inaccuracy for large deflections of the 3PB samples (i.e. for highly ductile materials). Therefore efforts are made to find corrections for this relation [5]. Finite element (FE) models have been developed for the simulation of the single specimen test technique to support the experiments. A key issue of the FE-simulation is the model for the crack propagation. For the simulation described in this paper, a strain based damage criterion is used considering the constraint (triaxiality).

2. Strain based damage model for crack propagation

Several FEM techniques have been established to simulate crack propagation. The most simple one is the debonding method, where the crack extension is realized by a gradual release of node constraints if a critical stress or strain is exceeded. In this method the crack path must be known before the simulation. Moreover, numerical instabilities may occur due to the sudden modifications of the model boundary conditions. Another possibility is the substructure technique, where the crack tip region is modeled with special elements (wedge shaped or triangular). When the crack propagates the substructure is displaced accordingly followed by re-meshing of the structure. However, these mesh-manipulating algorithms are rather time consuming and therefore restricted to relatively small models. A reasonable compromise seems to be the damage controlled deactivation of elements. In this technique (as used in this paper) the stiffness matrix of an element is reduced by a factor of 10^{-6} when its damage exceeds the value of 1.

For all these techniques a criterion is needed that controls the crack extension (i.e. node debonding, mesh manipulation or element deactivation). A damage model that can be used in connection with ductile (plastic) material behavior was developed by Gurson [1] and modified by Tvergaard and Needleman [2]. In this model (established as GTN-model) the material damage is associated with a void fraction (corresponding to the volume of micro cracks and cavities). The influence of triaxiality is well described by the GTN-model since the hydrostatic stress contributes to the plastic flow condition. However, six independent parameters are needed for the GTN-model (3 within the flow condition and 3 for the void evolution model [2]). Thus the formulation of the GTN- model for a certain material is an expensive task. Therefore a more simple damage accumulation concept is used in this paper. It is based

on a strain based damage measure, which does not influence the material properties. For plastic and viscoplastic deformation the damage increment is:

$$\Delta D = \left[\frac{\Delta \varepsilon^{cr}_{eqv}}{\varepsilon^{cr}_{frac}(\sigma, T)} + \frac{\Delta \varepsilon^{pl}_{eqv}}{\varepsilon^{pl}_{frac}(T)} \right] \cdot R_\nu \tag{1}$$

with $\varepsilon^{cr}_{frac}(\sigma, T)$ being the creep fracture strain of the uniaxial creep test at constant stress and temperature and $\varepsilon^{pl}_{frac}(\sigma, T)$ the plastic fracture strain (true strain) of the tensile test. R_ν is a function that considers the damage behavior in dependence on the triaxiality of the stress tensor [3]:

$$R_\nu = \frac{2}{3} \cdot (1+\nu) + 3 \cdot (1-2\nu) \cdot \left(\frac{\sigma_h}{\sigma_{eqv}} \right)^2 \tag{2}$$

where σ_h is the hydrostatic stress and σ_{eqv} is the von-Mises equivalent stress. The damage increment is calculated for each element by averaging its nodal equivalent creep and plastic strains. The accumulated damage is:

$$D = \sum_{i=1}^{ldstep} \Delta D_i \tag{3}$$

If the element damage reaches the value of D = 1, the element is deactivated. Thus within this accumulation concept the there is no feedback onto the material behaviour but a “binary” feedback onto the structural behaviour. This damage model is integrated into the ANSYS code via FORTRAN subroutines linked to the original code [4].

3. Simulation of the compliance function of a three point bending (3PB) specimen

The FE-code ANSYS® is used for modelling. The model covers as well the sample with the roller support as a part of the support of the bending device (Fig. 1). For symmetry reasons it is sufficient to model a quarter of the specimen. The model consists of several parts:

- the central section of the sample containing the structure of the initial crack front and the side groove; this section is meshed with 3D elements (alternatively SOLID45 or SOLID95) using elastic-plastic material behaviour with multi-linear kinematic hardening (MKIN)
- within the remaining range of the sample there is no plastic strain, therefore a 2D mesh (PLANE42) with elastic material behaviour is sufficient
- the roller support on the sloping plane is also meshed with 2D elements (PLANE42) considering contact and friction (CONTAC48); in this way the influence of the kinematics of the rollers onto the bending of the sample is correctly considered

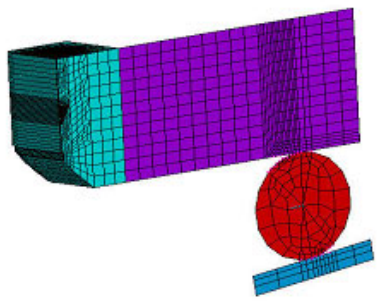

Fig. 1: FE-model of the 3PB sample

Table 1: Composition of steel 10 CrMo 9 10 (weight %)

C	Si	P	S	Mn	Cr	Ni	Cu	Mo
0.14	0.32	0.007	0.021	0.504	2.31	0.106	0.155	0.99

The simulation of the unloading compliance technique is applied to a highly ductile steel with an elastic modulus $E = 208\,961$ N mm^{-2} and a true fracture strain of 135 %. Table 1 gives the chemical composition. The considered heat was tempered at 640°C for 2 hours in order to obtain desired strength - toughness ratio. Figure 2 shows the damage and the corresponding crack extension for increasing load at a Charpy specimen with an initial crack of 5 mm. At a deflection of $\Delta d = 0.2$ mm no critical damage value is reached. At $\Delta d = 0.67$ mm the first element is deactivated (D = 1) and the crack starts to open in the region of the side notch. At deflections of $\Delta d = 1.55$ mm and $\Delta d = 3.75$mm the crack growth reaches 0.5 mm and 2.0 mm respectively. Figure 3 shows the applied load versus the COD for this simulation. The partial unloading is realized at nine deflection levels in order to calculate the sample compliance C_i at several crack extensions.

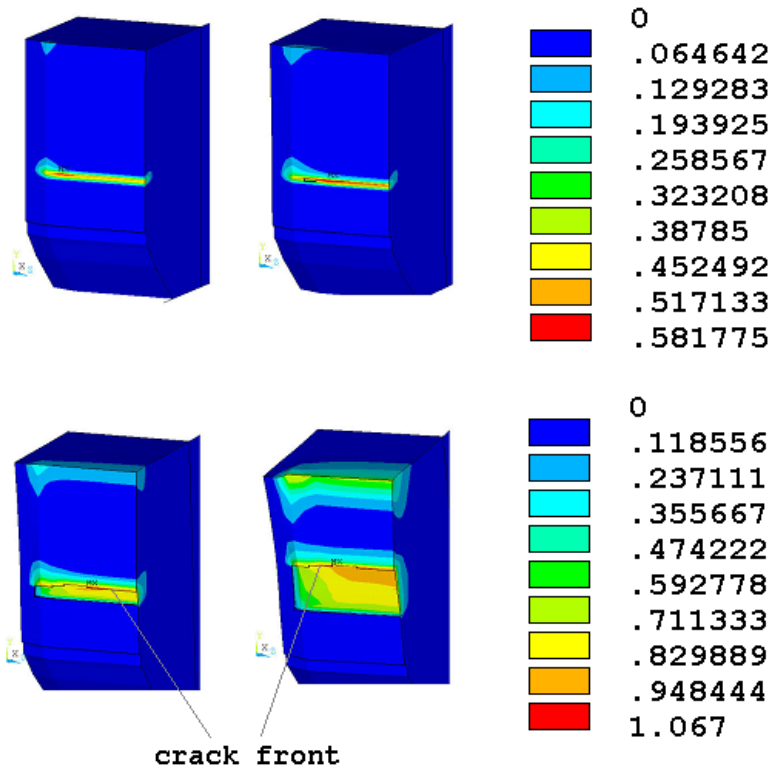

Fig. 2: Damage and crack extension at a Charpy specimen at 4 load steps; the colour refers to the damage D

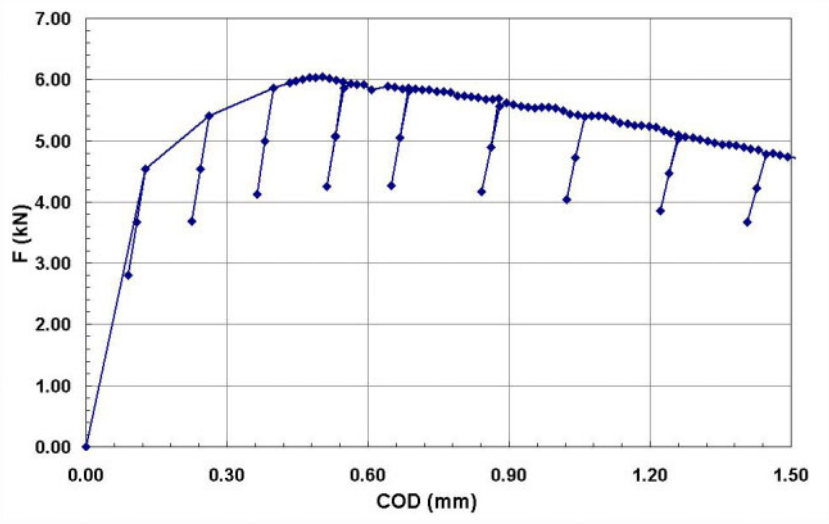

Fig. 3: Load-COD curve of the 3PB sample calculated by the FE-model

In the experimental case the compliance is also determined from the load-COD-curve. The ASTM standard [6] gives a rule, how the total crack extension a_i has to be calculated from the compliance at various load levels (C_i):

$$a_i = W \cdot \left(0.999748 - 3.9503 \cdot u + 2.9821 \cdot u^2 - 3.21408 \cdot u^3 + 51.5156 \cdot u^4 - 113.031 \cdot u^5\right)$$

$$\text{with} \quad u = \frac{1}{\left[\frac{B_e \cdot W \cdot E \cdot C_i}{S/4}\right]^{1/2} + 1} \tag{4}$$

B_e is the effective thickness of the specimen, E the Young's modulus, S the span of the sample support and W the width (height) of the specimen.

Figure 4 shows the curves of the experimentally and theoretically obtained crack growth (load versus crack extension). The deviations within the lower range are due to the circumstance that in the FE-model the blunting effect (plastic deformation of the crack tip) is not interpreted as crack growth. At deflections above 1 mm the crack growth calculated with the FE-model agrees well with the crack growth based on the experimental data.

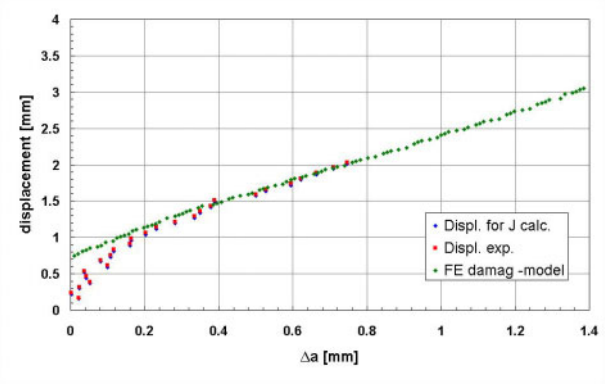

Fig. 4: Experimental (blue and red points) and theoretical crack extension in dependence on the load line displacement of the Charpy specimen.

In Fig. 5 the dependence of the crack depth on the deflection is represented. Two methods are compared for the calculation of crack extension: 1) the direct estimation by the FE model (based on the number of killed elements) and 2) according to equation 4 but with the compliance taken from the FE-simulation. An increasing deviation can be observed for increasing deflection. The correction of the compliance method according to Steenkamp [5] leads to a better agreement between the direct method and the compliance based method for the crack extension.

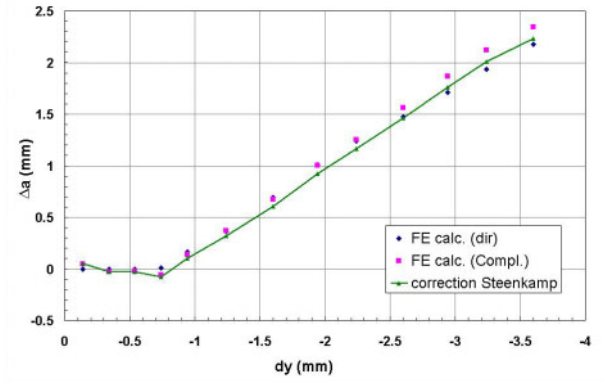

Fig. 5: Comparison of crack extension calculation methods and the effect of the correction by Steenkamp

4. FE-model of CT specimens

Figure 6 shows the 3D-mesh of a one inch CT specimen. Double symmetry is used in this model (planes y = 0 and z = 0 are symmetry planes). This model is used to investigate the compliance during the blunting process. Like for 3PB specimens the ASTM standard [6] gives a rule for the calculation of the crack extension depending on the current compliance:

$$a_i = W \cdot \left(1.000196 - 4.06319 \cdot u + 11.242 \cdot u^2 - 106.043 \cdot u^3 + 464.335 \cdot u^4 - 650.677 \cdot u^5\right)$$

$$\text{with} \quad u = \frac{1}{\left[B_e \cdot E \cdot C_i\right]^{1/2} + 1} \tag{5}$$

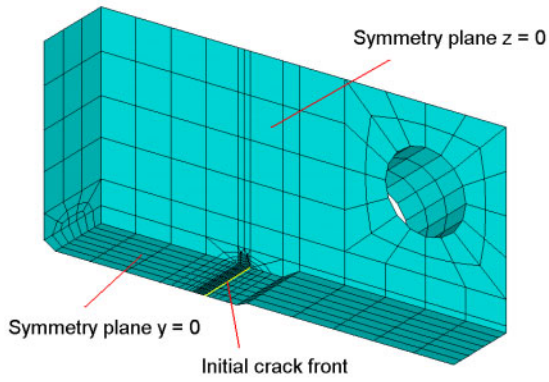

Fig. 6: FE-Model of a 1T-CT specimen

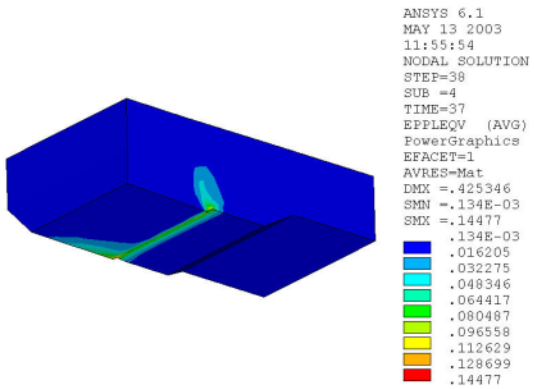

Fig. 7: Plastic equivalent strain in the crack region at the end of the compliance test

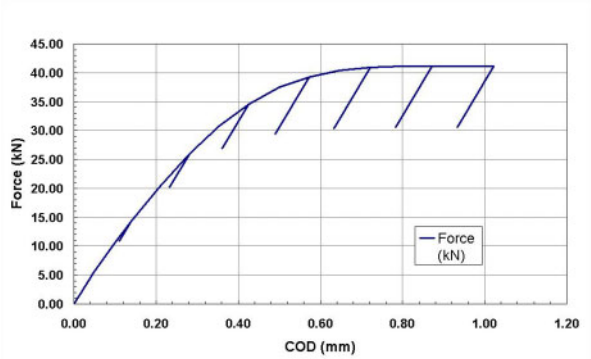

Fig. 8: Load versus crack opening displacement (COD)

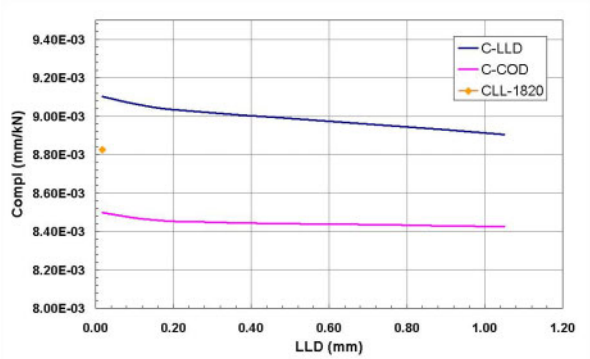

Fig. 9: Compliance versus load line displacement (LLD)

This equation can also be used to calculate the compliance for a given crack extension. In the FE simulation the plastic deformation of the crack front region is considered, however, no crack extension is allowed to get only the influence of the blunting effect to the compliance. Figure 7 shows the plastic equivalent strain at the end of the test simulation and Figure 8 the load-displacement-curve of the simulated compliance test. In Figure 9 the compliance is shown in dependence of the load line displacement (LLD, displacement of the point of attack). The LLD is measured at the bolt hole (Fig. 6). The upper curve is the load line compliance ($\Delta LLD / \Delta F$), the lower curve is the COD-compliance ($\Delta COD / \Delta F$) with F being the loading force. The load line compliance is higher than the COD compliance since the elasticity of the holes for the loading bolts is included in the latter one. It can be seen that the elastic compliance is slightly decreasing during the blunting process (as long as no crack extension occurs).

5. Conclusions

Fracture tests with 3PB and CT specimens are simulated by FE-models with elastic-plastic material behaviour and damage controlled crack propagation. The results can be summarized as follows:

- A strain based damage criterion can be used to simulate crack extension
- For small loads there is a deviation between the crack extensions calculated by FEM simulation and those calculated by ASTM equations based on test results
- During the blunting process the elastic compliance is slightly decreasing

References

[1] Gurson, A.L. Continuum Theory of Ductile Rupture by Void Nucleation and Growth: Part 1 - Yield Criteria and Flow Rules for Porous Ductile Media. Transaction of ASME, Journal of Engineering Materials and Technology, 1977, 3

[2] Needleman, A.; Tvergaard, V.: An analysis of Ductile Rupture in Notched Bars. Journal of Mechanics and Physics of Solids, Vol. 32, 1984, pp 461-490

[3] Lemaitre, J.: A Course on Damage Mechanics. ISBN 3-540-60980-6, 2nd edition Springer-Verlag Berlin, Heidelberg, New York, 1996

[4] Altstadt, E., Mössner, T.: Extension of the ANSYS creep and damage simulation capabilities. FZR-Report Nr. 296, ISSN 1437-322X, Juli 2000

[5] P.A.J.M. Steenkamp, Fracture Mechanics 18th Symposium, ASTM STP 945, Philadelphia, 1988, p.583-610

[6] ASTM Standard E1820-01: Standard Test Method for Measurement of Fracture Toughness, ASTM 2001

THERMO-MECHANICAL ANALYSIS OF A PWR CORE BAFFLE CONSIDERING THE IRRADIATION INDUCED CREEP OF THE BOLTS

Eberhard Altstadt, Erwin Fischer[1], Herrmann Kumpf, Gerhard Nagel[1], Georg Sgarz[1], and Frank-Peter Weiss

1. Introduction

In some PWRs the core baffle (Fig. 1) consists of sheets (light blue) and formers (red). The sheets are separated by small gaps (0.2 mm to 0.4 mm). The connection between the core baffle sheets and the formers and between formers and core barrel (blue) respectively is realized by a large number of bolts (about 900). During the manufacturing process of the core baffle the bolts are tightened with well defined pre-stress to guarantee the geometrical and mechanical stability of the structure. During operation the pre-stress of the bolts is reduced as a consequence of thermal and mechanical loads and promoted by neutron irradiation possibly leading to expanding gaps and affecting the flow induced vibrations of fuel rods in outer fuel elements. These effects were investigated by an extensive structural analysis.

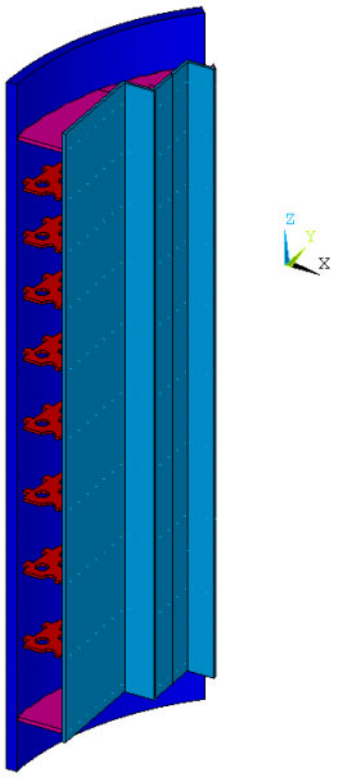

Fig. 1: Core baffle (45° section)

The core baffle of a PWR is loaded by the axial gradients of differential pressures in the bypass and the core and by temperature profiles originating from gamma heating and heat transfer into the coolant. Strain, deformation and gaps are assessed considering the effect of neutron irradiation induced creep of the core baffle bolts. The complete analysis requires three major steps:

- Evaluation of the three dimensional distributions of the neutron and gamma fluxes
- Calculation of the temperature distribution in the core baffle
- Calculation of time dependent deformations, stresses and strains

2. Neutron and gamma induced heating

The 3-dimensional distributions of the neutron and gamma fluxes and of the resulting heat deposition is calculated with the Monte Carlo code MCNP®. This program simulates the destiny of fission neutrons, fission gammas and of generated secondary particles from their birth in the pins until their absorption. The calculations are based on pin wise power distributions at the core edge for typical loading patterns. A 45°-symmetry is assumed. The neutron flux is calculated for neutrons with energies higher than 1 MeV. For the evaluation of the heat deposition two calculations are superimposed: 1) the transport of the prompt fission gammas and 2) the transport of neutrons and gammas from neutron capture and inelastic scattering. Fig-

[1] E.ON Nuclear Power

ure 2 shows the neutron flux and the energy deposition over the circumference of the core baffle sheets (averaged over the height) for the so called low-leakage core load pattern.

Two typical core loading patterns are investigated: In the early fuel cycles the fresh fuel elements (low burn-up) were placed into the outer regions of the core (classical core). In the mid nineties the strategy was changed to reduce neutron leakage from the core. The fuel elements with low burn-up were now placed in the central core region (low-leakage core).

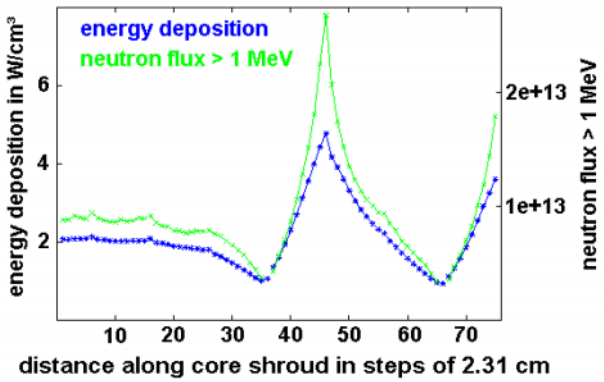

Fig. 2: Neutron flux [n/cm² s] for E > 1MeV and energy deposition [W/cm³] in the core baffle sheets over the circumference with 0 = principal axis (0°); 75 = secondary axis (45°)

3. Thermal finite element analysis

The finite element code ANSYS® is applied for the thermal and mechanical analyses. The FE-model comprises a complete 45° sector of the core baffle structure including the core barrel, the formers, the core baffle sheets. The thermal analysis is done for different operational conditions and core loading patterns. The following effects are considered: heat conduction in the components, internal heat sources (neutron and gamma heating) and convectional boundary conditions (heat transfer coefficients and bulk temperature of the coolant). Based on the coolant temperature and mass flow at different positions the heat transfer coefficients for the convectional boundary condition are calculated by:

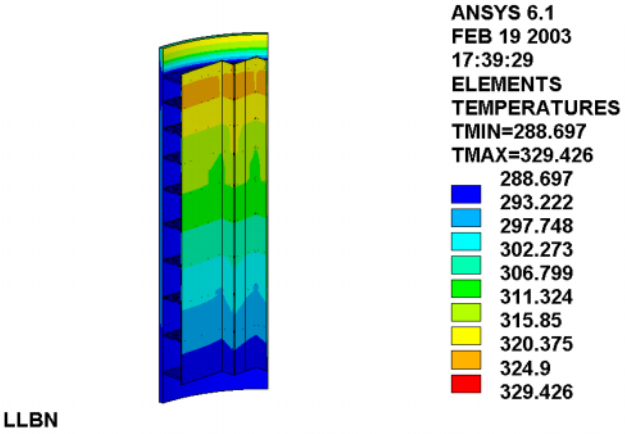

Fig. 3: Temperature distribution [°C] in the core baffle for normal operation with a low-leakage core

$$\alpha = \frac{Nu \cdot \lambda_{water}}{D_H} \tag{1}$$

The Nusselt number follows from the empirical correlation [1]:

$$Nu = 0.0214 \cdot \left[Re^{0.8} - 100\right] \cdot Pr^{0.4} \cdot \left[1 + \left(\frac{D_H}{L}\right)^{0.667}\right] \tag{2}$$

$$\text{with:} \quad Pr = \frac{\mu_{water} \cdot c_{water}}{\lambda_{water}}; \quad Re = \frac{\rho_{water}}{\mu_{water}} \cdot D_H \cdot v$$

where μ is the coolant viscosity, λ the heat conduction coefficient, ρ the density, v the mean velocity, D_H and L the equivalent hydraulic diameter and length respectively. Figure 3 shows the typical temperature distribution for the low-leakage core during normal operation. It can be seen that the region of the highest temperature is the edge of the core baffle that is located closest to the core center. The maximum temperature exists inside the sheet. The heating up of

the bypass water (the coolant streaming through the core baffle formers) is also calculated, but it is negligible (about 1 K). The bolts are not modelled in the global thermal model. Instead of this, the bolt temperatures were evaluated with a local model of a single bolt with a variable heat power input according to the individual bolt position. The local model calculates the temperature difference in the bolt shaft relative to the temperature of the sheets at the bolt's head and thread.

4. Mechanical finite element analysis

The mechanical finite element model for the sheets, the formers and the core barrel is based on the same mesh as the thermal model. It considers additionally about 230 bolt connections, the non-linear contact between the single components, the effect of friction, and the creeping of the bolts. The load follows from the weight, the coolant pressure, the temperature fields for different operational situations and from the prestressing of the bolt connections. The pre-stress of the bolts is realized by a modified reference temperature $T_{B,ref}$ (where the thermal strain is zero):

$$T_{B,ref} = T_{ref} + \frac{\sigma_V}{E \cdot \alpha} \tag{3}$$

with T_{ref} – analysis reference temperature of the components (except bolts), σ_V pre-stress of the bolt, E – elasticity modulus of the bolt material, α – thermal expansion coefficient of the bolt material. The irradiation induced creep of the bolts is correlated to the neutron flux ϕ and to the axial stress σ_{ax} as follows:

$$\dot{\varepsilon}_{ax}^{cr} = K_1 \cdot \phi^n \cdot \sigma_{ax}^p \tag{4}$$

The parameters K_1, n and p were determined from results of relaxation experiments.

The viscoplastic analysis comprises a time frame of 30 full power years, which can roughly be subdivided into four large periods:

- Commissioning until bolt replacement (period 1)
- Bolt replacement until change of core loading pattern (period 2)
- Change of core loading pattern until core baffle modification (period 3)
- Core baffle modification until 30 full power years (period 4)

The end of period 1 is marked by the replacement of the bolts in 2 former planes (Fig. 1). After the replacement the new bolts receive the nominal pre-stress of 250 MPa whereas the remaining bolts exhibit already some relaxation due to creep. As a consequence of the change of the core loading pattern (end of period 2) the creep rate of the bolts is reduced (lower neutron flux, equation 4), likewise the average temperature level is slightly decreased (lower gamma heating). The core baffle modification is a hydraulic change in the upper former, which leads to a lower pressure in the bypass (between the core barrel and the core baffle sheets) during normal operation. For each of the four periods a heat-up and a cool-down load step has additionally been analyzed. The replacement of bolts required two more load steps in the cold state, so the mechanical analysis comprises 14 load steps in total. Each of the periods is characterized by a specific temperature-, pressure- and neutron flux field.

5. Results

The time dependent results of the mechanical analysis are: elastic deformation, stresses and strains in all core baffle components, creep strain in the bolts, self controlled and equalizing

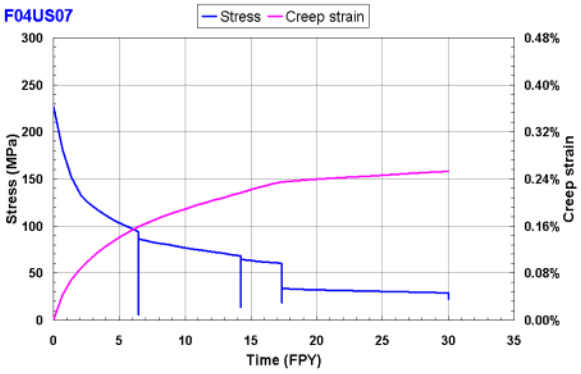

Fig. 4: Creep strain (red) and axial stress (blue) versus time (baffle bolt number 7 plane 4)

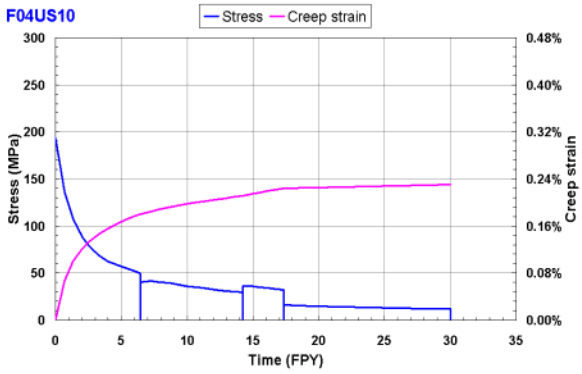

Fig. 5: Creep strain (red) and axial stress (blue) versus time (baffle bolt number 10 plane 4)

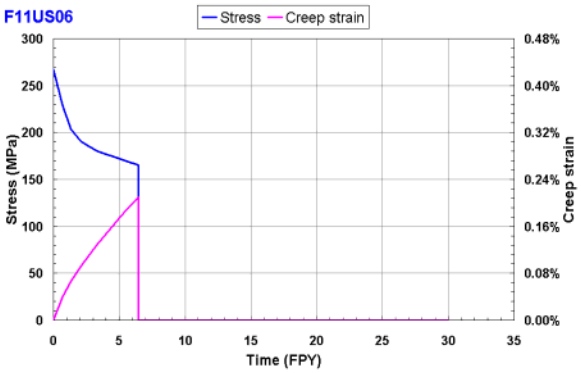

Fig. 6: Creep strain (red) and axial stress (blue) versus time (bolt number 4 plane 2); old bolt

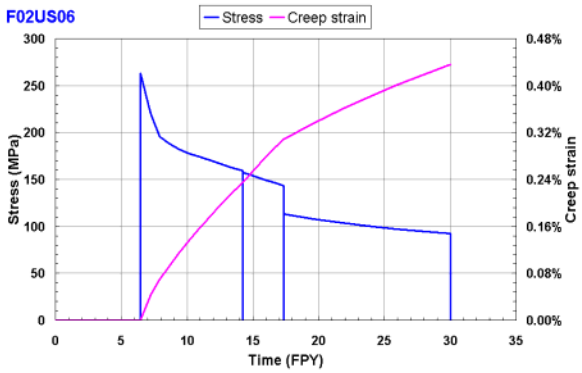

Fig. 7: Creep strain (red) and axial stress (blue) versus time (bolt number 4 plane 2); new bolt

redistribution of bolt loads, gap widths between adjacent core baffle sheets, contact status between former and core barrel and between former and core baffle sheets. Figures 4 and 5 show axial stress and creep strain versus time for two different bolts. It can be seen that the heat-ups and cool-downs, which are connected with large thermal strains and therefore with sliding processes, can lead to significant changes in the axial bolt stresses and to a redistribution of the loads amongst the bolts. The Figures 6 and 7 show the stress and strain curves for bolts of the former plane 2, where a bolt replacement took place. The results can be summarized as follows:

- The bolt pre-stresses in the sheet bolts of the former planes 2 to 4 are significantly reduced over the load history
- The calculated maximum creep strain is 0.44% (former plane 2)
- The gaps are not affected by creep and reduced pre-stress of the bolts
- The bending stresses in the bolts are abolished by the neutron induced creep

The results show the equalizing effect of redistribution of bolt loads from high flux to lower flux exposure locations in a self controlled process, keeping the mechanical and geometrical stability of the core baffle structure and leaving the gaps between sheet edges unaffected.

References

[1] VDI-Wärmeatlas, 7. Auflage, VDI-Verlag, 1994

USE OF THE MASTER CURVE APPROACH FOR THE DYNAMIC TOUGHNESS CHARACTERIZATION OF PRESSURE VESSEL STEELS

Hans-Werner Viehrig, Juergen Boehmert, and Alekzander Gokhman

1. Introduction

The master curve approach developed by Wallin [1] is a new fracture mechanics based tool for brittle fracture safety assessment of structural components. The master curve describes the temperature dependence of the J-integral related fracture toughness, K_{Jc}, on the base of a statistical brittle fracture model und using a reference temperature, T_0, for temperature scaling.
The procedure of the determination of T_0 has already been established in the international standard regulation, e.g. in ASTM E1921. In this application, the determination is so confined that T_0 is conservative in every case. Furthermore, the method is only valid for quasi-static loading.
Recently, there is effort to qualify the method for dynamic loading conditions and to use it for a sensitive characterization of the toughness behaviour of materials or materials conditions. A step towards this goal is described in the following.

2. Master curve approach

The master curve approach postulates the following assumptions:

- The fracture toughness, K_{Jc}, can be described by a 3 parametric Weibull distribution

$$P[K_{Jc} < K_I] = 1 - \exp\left(\frac{K_{Jc} - K_{min}}{K_o - K_{min}}\right)^n \quad (1)$$

  with the parameters n = 4 and K_{min} = 20 MPa √m.
  P ($K_{Jc} < K_I$) is the cumulative failure probability, K_{Jc} is the J-integral-related fracture toughness, K_o is a temperature and specimen size dependent normalisation fracture toughness corresponding to the 63.2 % cumulative failure probability.

- K_{Jc} values can be transferred to different specimen sizes by means of the Weibull distribution

$$K_{B2} = K_{min} + [K_{B1} - K_{min}]\left(\frac{B_1}{B_2}\right)^{1/4} \quad (2)$$

  B_1 and B_2 are the thickness of the specimens and K_{B2} and K_{B1} the corresponding values of the fracture toughness.

- The temperature dependence of K_o, related to B = 25 mm follows an exponential law

$$K_o = 31 + 77 \cdot \exp[0{,}019\,(T - T_0)] \quad (3)$$

  The reference temperature, T_0, is the temperature (in °C) at which the mean fracture toughness is 100 MPa√m.

- The fracture behaviour is J integral related. This includes the maintenance of the constraint and it defines an upper limit of the validity of K_{Jc}

$$K_{Jc} \leq \sqrt{\frac{E \cdot b \cdot \sigma_y}{M\ (1-\upsilon^2)}} \tag{4}$$

with the Young's modulus E, the thickness of the initial ligament b, the Poisson ratio ν, the yield strength σ_y and the size criterion constant M = 30.

Based on the above-mentioned assumption, ASTM E 1921 adjusts the measuring conditions, censors specimens outside the validity limit and defines the sample size needed. The tests are carried out at one single temperature (single temperature method) or at different test temperatures (multi-temperature method).

3. Experimental

The material used is a rolled plate of the IAEA reference material JRQ of the type ASTM A533B cl. 1. The material has been extensively characterized [2,3]. The plate of the thickness of 225 mm was cut into 20 layers over the thickness using an electro-erosive cutting machine. A total of 15 precracked and side grooved (20 %) specimens were machined from each layer in LT-orientation. The microstructure of the plate varies through the thickness. In the middle region, heterogeneously composed upper bainite with segregation zones is characteristic.
The specimens were tested on an instrumented 300 J pendulum-type impact machine at a potential energy of 78 J and an impact velocity of 2.8 m/s.
The measurement of dynamic fracture toughness by means of Charpy impact tests is more complicated and recently has not yet been fixed by a standard. However, there are code recommendations [4-6], which were used for the test evaluation. The details are described in [7]. The further evaluation was performed according to ASTM E1921-97 but is based on the multi-temperature method as established by the last code version of ASTM E 1921-02.
For comparing the results with the toughness parameters obtained by already proven methods, similar series of tests were carried out using quasi-static 3-point bending tests and Charpy V-notch impact tests [8].

4. Results

The scatter of the K_{Jc} values measured at specimens from the same depth position and at identical temperatures is large. Nevertheless, the dynamic reference temperature, T_0^{dyn}, shows a clear course through the thickness position as depicted in Fig. 1 together with the results of the quasi-static reference temperature, T_0^{stat}, and the Charpy-V transition temperature related to an impact energy of 41 J, TT_{41J}. T_0^{dyn} increases from the plate surfaces till about 1/4 thickness and is nearly constant in the range of 1/4 to 3/4 thickness. This trend could be expected due to the depth dependence of the microstructure and is found in the same manner for TT_{41J} or T_0^{stat}. However, the level of the transition temperatures is clearly different: T_0^{dyn} exceeds approximately TT_{41J} by 25 K and T_0^{stat} by 75 K. This proves that the crack initiation for cleavage depends significantly on the loading rate. As well the quasi-statically well as the dynamically measured reference temperatures correlate with the Charpy-V transition temperature and so reveal a relationship between the fracture mechanics based master curve parameters and the not-physically defined transition temperatures from the Charpy test. The correlations are presented in Fig. 2.

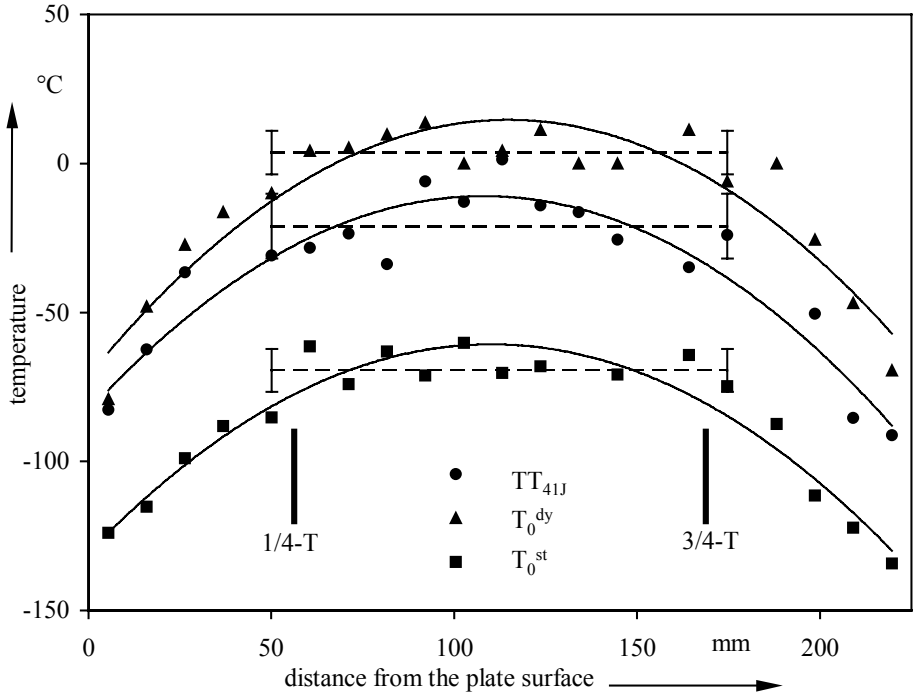

Fig. 1: Effect of specimen location on the ductile-brittle transition temperature determined by the dynamic (T_0^{dyn}) and static (T_0^{stat}) master curve procedures and by Charpy-V impact tests (TT_{41J})

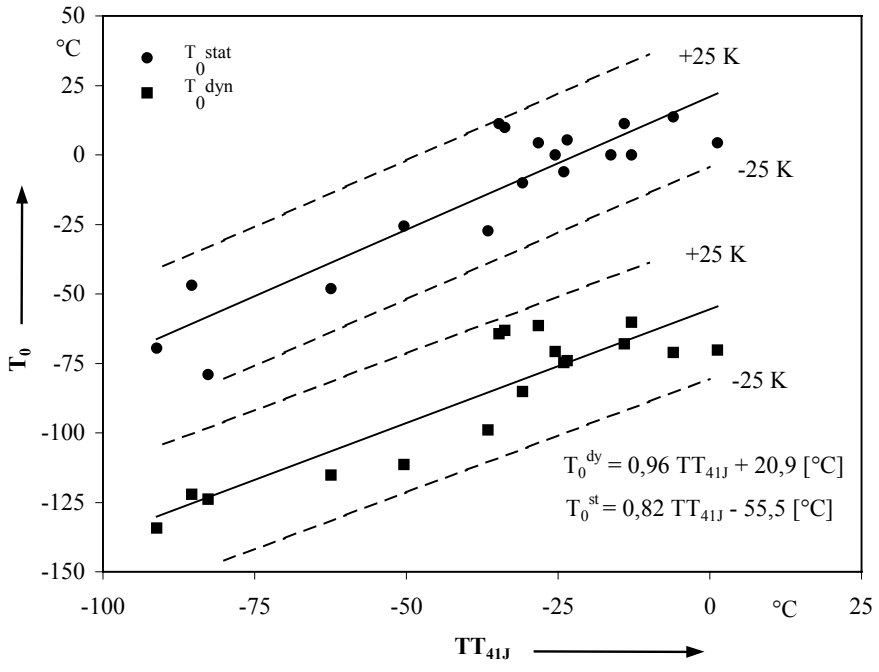

Fig. 2: Correlation between Charpy-V transition temperature, TT_{41J}, and the quasi-static (T_0^{stat}) or dynamic (T_0^{dyn}) reference temperature

From Fig. 1, it can be seen that the transition temperature parameters remain constant for depth positions between ¼ and ¾ thickness within a scatter band. This implies that all data come from a material with identical but strongly scattering toughness and can be evaluated as one data set with about 150 observations. Thus, the results can be evaluated by statistical tests. Fig. 3 shows the course of the master curve determined from the data set of the middle layers (median value and 5 % and 95 % quantiles resp.) and the measured and thickness corrected K_{Jc} values. In principle, the results lie preferentially within the 90 % scatter range and follow the master curve. A large number of data lies beyond the measuring capacity ($K_{Jc(limit)}$).

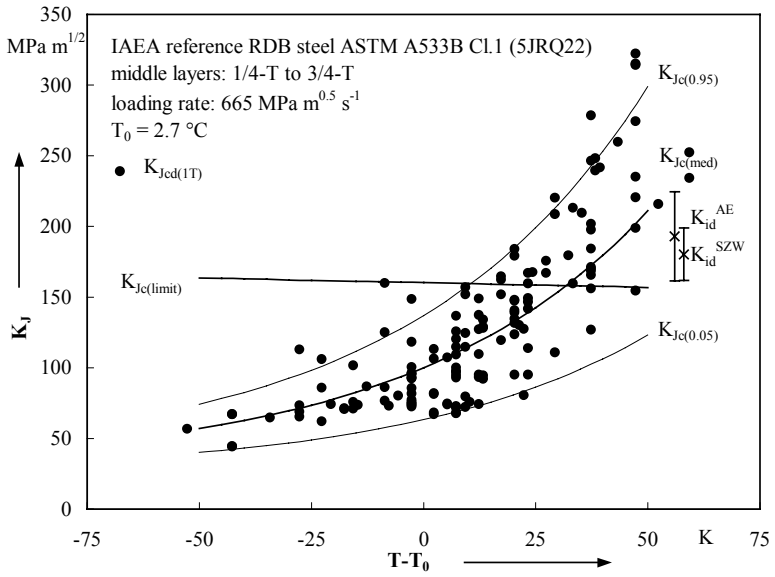

Fig. 3: Dynamic fracture toughness: measured K_J values and master curve for the JRQ steel plate

For the purpose of a statistical analysis the data set was newly arranged in 10 subsets with 8 to 22 observations. Every subset was tested at the same test temperature and evaluated by the single-temperature method.
In this way the influence of the test temperature on the determined T_0 values could be estimated. The result is presented in Fig. 4 and indicates that T_0 increases if the test temperature increases. This finding is causing concern because at higher test temperatures the measuring capacity is soon exceeded and lower test temperatures yield too low and, thus, non-conservative values.
The Kolmogorov-Smirnov test [9] was used to test the hypothesis that the isothermally determined K_{Jc} values of each subset follow the Wallin-Weibull distribution according to Equ. (1). For a large part of the subsets the hypothesis must be rejected on the 5 % error probability. On the other hand, fitting of the results to a Weibull distribution with other parameters by means of the maximum-likelihood method [9] provides weighted mean values for K_{min} = 28 MPa$\sqrt{m}$ and m = 4.8 which are sufficiently close to the parameter of the Wallin-Weibull distribution.
Finally, the influence of the sample size was investigated. For that, sub-samples of different sample size (n = 6 to 18) were randomly selected from each isothermal test series, T_0 was determined and compared with the T_0 value determined from the whole sample. The standard deviation of the T_0 determination for all sub-samples is presented in Fig. 5 as a function of the sample size. The expected theoretical standard deviation for the minimum sample size according to the ASTM E1921 (n =6) is $\sigma_{To} = 17/\sqrt{n} = 6{,}9$ K.

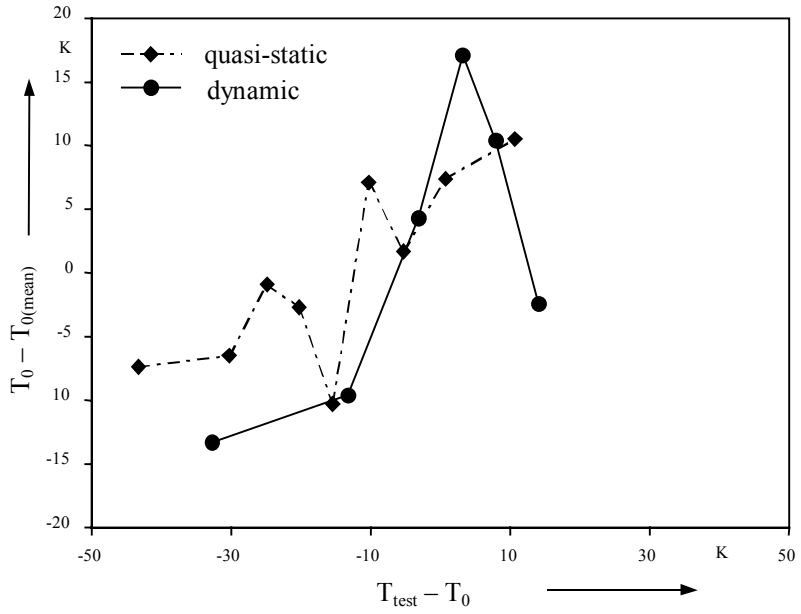

Fig. 4: Effect of the test temperature, T_{test}, on the dynamic and static reference temperatures

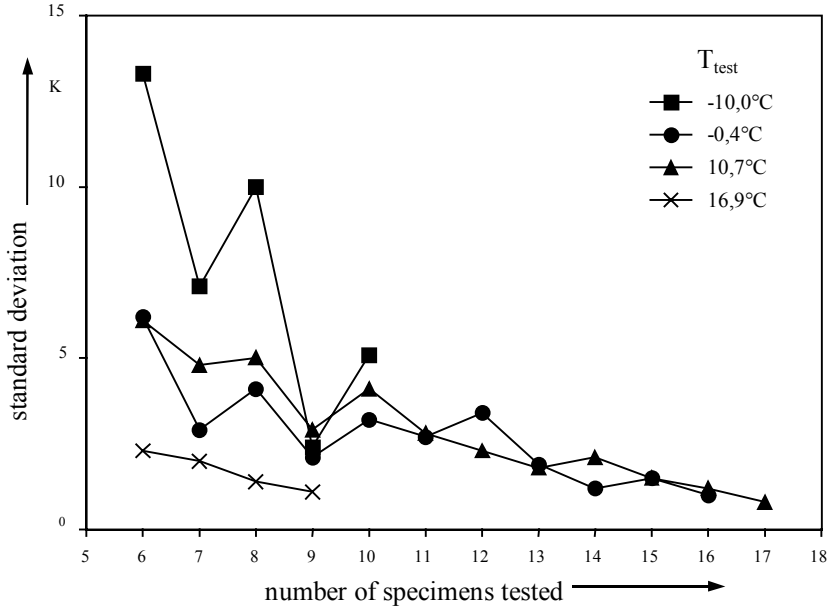

Fig. 5: Dependence of the standard deviation on the number of the tested specimens under impact loading

Thus, a minimum of 8-9 valid tests meets the standard requirement. A similar result is obtained for quasi-static tests on the same material.
For impact tests an additional problem arises from initial oscillations. In the case of low K_{Jc}, (corresponding to low absorbed energy and, thus, requiring low test temperature) the cleavage failure occurs within the inertial oscillation and the measurement of the absorbed energy is inaccurate. At higher test temperatures, the measurement of the absorbed energy is more precise but the K_{Jc} values often lie above the validity criterion. Thus, the temperature window for the T_0 determination is very small for impact tests with Charpy-size specimens.

5. Conclusions

The examination of the toughness dependence on the depth position of the thick-walled rolled plate from A533 B cl.1 shows that the T_0 values determined by impact tests on Charpy-size specimens sensitively characterize the toughness changes through the thickness in a sensitive manner. The through-the-thickness dependence is comparable to those for Charpy V-notch transition temperatures or quasi-static T_0. However, the number of specimens which must be tested is smaller than for the Charpy transition temperature and the effort for testing is lower than in the case of quasi-static tests.
Fracture mechanics impact tests with Charpy-size specimens can be performed and evaluated according to ASTM E 1921. The results follow the master curve approach within a sufficient approximation.
Dynamic T_0^{dyn} values are significantly higher than the quasi-static ones. That implies that brittle failure assessment on the base of quasi-static T_0^{stat} values does not provide conservative results for dynamically loaded components.
The temperature range which can be used for testing is small. Too low temperatures result in inaccurate K_{Jc} values and/or too low and, thus, non-conservative T_0 values. Too high temperatures yield too high K_{Jc} values which exceed the validity limit. Therefore, it is strongly recommended to use the multi-temperature method.
Further work is needed to adopt the procedure of quasi-static T_0 determination to dynamic loading conditions.

References

[1] Wallin, K. (1999) Int. J. of Material and Product Technology **14** 342

[2] Ando, Y. (1986 Manufacturing History and Mechanical Properties of Japanese Materials provided for the International Atomic Energy Agency, Atomic Energy Research Committee, Japan Welding Energy Society, CRP Subcommittee report.

[3] Wallin, K., M. Valo, R. Rintamaa, K. Törrönen, R. Ahlstrand (1989) Research Report 739, Technical Research Centre of Finland, Espoo

[4] Mc. Cornell, P., W. I. Server (1980) EPRI Instrumented Impact Test Procedures, in: Proc. C. S. N. I. Specialist's Meeting on Instrumented Precracked Charpy Testing, EPRI-NP-2102-LD, R. A. Wullaert (Ed.), Palo Alto, USA, 1980, pp. 1-1

[5] Ireland, D. R., A Review of the Proposed Standard Method of Test for Impact Testing Precracked Charpy Specimen of Metallic Materials, in: Proc. C. S. N. I. Specialist's Meeting on Instrumented Precracked Charpy Testing, EPRI-NP-2102-LD, R. A. Wullaert (Ed.), Palo Alto, USA, 1980, pp. 1-23

[6] "Proposed Standard Methods for Instrumented Pre-cracked Charpy Impact Testing of Steels – Combined K_{Id}, J_{Id}, and CTOD Tests Methods", Draft International Standard: ESIS, European Structure Integrity Society

[7] Viehrig, H.-W., J. Böhmert, Use of Instrumented Charpy Impact Tests for the Determination of Dynamic Fracture Toughness Values, ESIS-Publication 30, D. Francois, A. Pineau, Eds., Charpy Centenary Conference, 2-5 October 2001, Poitiers, France, Elsevier Science Ltd. and ESIS, 2002, p. 245

[8] Viehrig, H.-W., J. Böhmert, J. Some Issues Using the Master Curve Concept (1999), Nucl. Engn. Des. 212 (2002) 115

[9] Bolshev, L., N. Smirnov, Statistical Handbook, Nauka, Moscow, 1983, pp. 416

CORRELATION BETWEEN RADIATION-INDUCED CHANGES OF MICROSTRUCTURAL PARAMETERS AND MECHANICAL PROPERTIES

Juergen Boehmert, Hans-Werner Viehrig, and Andreas Ulbricht

1. Introduction

The pressure vessels of nuclear reactors (RPV) are constructed from thick section forgings rings or rolled plates of high grade low alloy ferritic steel. The area of the RPV surrounding the core is subjected significant neutron dose during the lifetime of a nuclear power plant. Neutron irradiation influences the mechanical properties by increasing the strength (neutron hardening) and decreasing the toughness (neutron embrittlement). The last one is affected by an increase of the ductile-brittle transition temperature and a reduction in the upper shelf energy. This is relevant for the safety and, thus, has been an object of manifold research activities for long time. Whereas the work has been preferentially addressed the mechanical properties, the microstructural changes due to neutron radiation have been hardly investigated. One of the main reasons for that is, not at least, because the microstructural radiation effects are hardly detectable by the established microstructural analysis methods. In the consequence, the mechanism of the phenomenon has not yet completely understood up to now.
The Institute of Safety Research has extensively investigated the neutron-effected degradation of the mechanical properties of RPV steels, above all, but not only, on the base of the specimens sets irradiated in the irradiation programme Rheinsberg I and II. The programme was focussed on VVER-type RPV steels. For this steel group the phenomenon is specially safety relevant. Simultaneously with the mechanical testing, the microstructure was examined by small angle neutron scattering (SANS) on the same specimen sets. SANS is a modern structure analysis method which is suitable for the detection of microstructural radiation effects.
The relations found between the radiation-induced changes of the microstructure and the neutron hardening and embrittlement are presented by this paper. They are a contribution to a data base for the neutron embrittlement modelling.

2. Experimental background

The material base of the investigation is a broad variation of irradiation probes taken from the irradiation programme Rheinsberg I and II, surveillance programmes of Russian, Ukranian and Hungarian NPPs or special irradiation experiments in VVER reactors. It comprises both base metal and weld metal, steels according to manufacturer's specification, outside the specification or model alloys, VVER-type steels and ASTM-related types. Manufacturers, fabrication procedures, heat treatment and chemical composition varied in a very broad range. The materials investigated are listed in Table 1. More details are given in [1].
Irradiations were performed at temperatures of 255 °C to 290 °C and neutron fluxes of 2 to $54 \cdot 10^{11}$ n/cm^{2}s [E > 0.5 MeV], the neutron exposure reached values between 2.6 and $630 \cdot 10^{18}$ n/cm^2 [E > 0.5 MeV].
The mechanical test programme included HV 10 hardness measurement, tensile tests, Charpy V-notch impact tests and fracture mechanics three-point-bend tests for T_0 determination. They were conducted in the hot cells of the Institute of Safety Research of FZR and the RRC Kurchatov Institute Moscow, respectively.

Table 1: Investigated materials

Type		Designation	Heat/ Code	Producer/ Supplier	Comment
1.1 Irradiation programme Rheinsberg I					
VVER-440	BM	15Kh2MFA	R1 R2 R3 D25	Prometey RRC-KI	Russian fabrication line
VVER-1000	BM	15Kh2NMFAA	R16 R17	VNIIAES	Novovoronesh NPP, unit 5 South Ukrainian NPP, unit 1
VVER-1000	W	10KhGMFAA	R19	VNIIAES	South Ukrainian NPP, unit 1
1.2 Irradiation programme Rheinsberg II					
VVER-440	BM	15Kh2MFA	KAB-B	Greifswald	Prototype RPV steel for
VVER-440	W	Sv10KhMFT(u)	KAB-W	NPP	VVER-440/230
VVER-440	BM	15Kh2MFA	ESW-A ESW-B ESW-C ESW-D	ESW	test heats
ASTM-steel	BM	A533B cl. 1 A508 cl. 3	JRQ JFL	Japan	IAEA reference material IAEA-CRP-programme
2. Surveillance programme					
VVER-440	BM	15Kh2MFAA	PA1-B	Skoda	NPP Paks, unit 1
	W	Sv10KhMFT	PA1-W		NPP Paks, unit 1
	BM	15Kh2MFA	RO-B KO-B	RRC KI	NPP Rovno, unit 1 NPP Kola, unit 3
VVER-440	W	Sv10KhMFT	RO-W AR-W	RRC KI	NPP Rovno, unit 1 NPP Armenia, unit 3
3. Model alloys					
Fe base alloy (FeMnSi)			ML-A ML-B ML-C ML-D ML-F ML-G ML-H	RRC-KI	variation of content of P, Cu and Ni
4. Special irradiation					
VVER-1000	W	10KhGMFAA	TA-1 TA-2	RRC-KI	Novovoronesh NPP, unit 5, surveillance position

BM – base metal; W – weld metal

3. Microstructural analysis by SANS

SANS has proved to be one of the most appropriate methods to detect and to characterize the nano-scaled microstructural features produced by neutron radiation. SANS is an indirect structural analysis method. It does not provide a real space image but only the Fourier transform of the averaged spatial scattering density distribution. From that, the real microstructure cannot be reconstructed. However, some microstructural parameters can be extracted from the scattering intensity distribution, at least by assuming a simplified structural

model and by assuring of suitable measuring conditions. For the analyses of this paper, the following conditions and assumptions were selected:

- The SANS intensity is measured over a large range of the scattering vector.
- A saturating magnetic field is applied during the experiment in order to separate the nuclear and magnetic contribution of the SANS intensity.
- The device-caused and the incoherent scattering effects are carefully eliminated.
- The structural model is based on the two-phase approach: isolated scattering particles of low concentration in homogeneous matrix
- The particles are spherical, polydisperse and non-ferromagnetic.
- The particle-size distribution function is computed by the indirect transformation method developed by Glatter [2].

Under these circumstances the microstructure is characterized by

- size distribution function of the radiation defects related to the volume fraction or the number density (parameters are given in relative units from the total or the nuclear scattering cross section and in absolute units from the magnetic scattering cross section)
- the volume fraction and the total number density of microstructural defects within a selected size range
- the defect radius at the maximum of the size distribution (mode)
- the A-ratio as ratio between total scattering cross section and nuclear scattering cross section.

The last parameter includes information about the composition and structure of the defects.

SANS measurements were conducted at different European SANS facilities using 10 mm x 10 mm x 0.8 mm discs cut from the halves of broken Charpy specimens. For the different instruments nearly the same experimental conditions were chosen. The SANS facilities used and the measuring parameters are summarized in Table 2.

Table 2: SANS instruments used and measuring parameters

Instrument	SANS-V4	PAXE	D11	KWS-II	Yellow Submarine
Site	HMI Berlin (BER II)	LLB Saclay (Orphee RR)	ILL Grenoble (HFR)	FZ Jülich (DIDO)	KFKI Budapest
Size/mm	7.5	7.5	7.5	8.0	8.0
wave length/ nm	0.5 / 0.6	0.5 / 0.6	0.5	0.715	0.47
distance probe – detector/m	1.086; 4.0	1.5; 5.0	1.1; 4.0; 16.5	1.5; 4.1	5.5
Q-range/ nm^{-1}	0.2 – 3.2	0.2 – 2.6	0.2 – 4.0	0.12 – 1.25	0.2 – 0.8
detector type	2d position-sensitive He detector, 64 cm x 64 cm				
magnetic field/T	1.3	1.4	1.5	1.5	< 1.0
calibration standard	water	-	water	polyethylene	-
comments	very quali-fied infra-structure		high flux, short meas-uring time	test operation	to low flux

4. Results

The qualitative course of the size distribution is similar for all materials investigated. The distribution is bimodal with a steep peak near 1 nm and a broad second relative maximum of low height between 8 and 16 nm. The first peak appears in the irradiated condition and is reduced partly or almost completely by annealing. Material composition and irradiation conditions do not change the position and shape but clearly affect the height of the peak. Only the very highly irradiated surveillance specimens show a broader first peak. The low second peak is hardly influenced by irradiation. Fig. 1 shows the volume-fraction related size distribution function for the material KAB as an example.

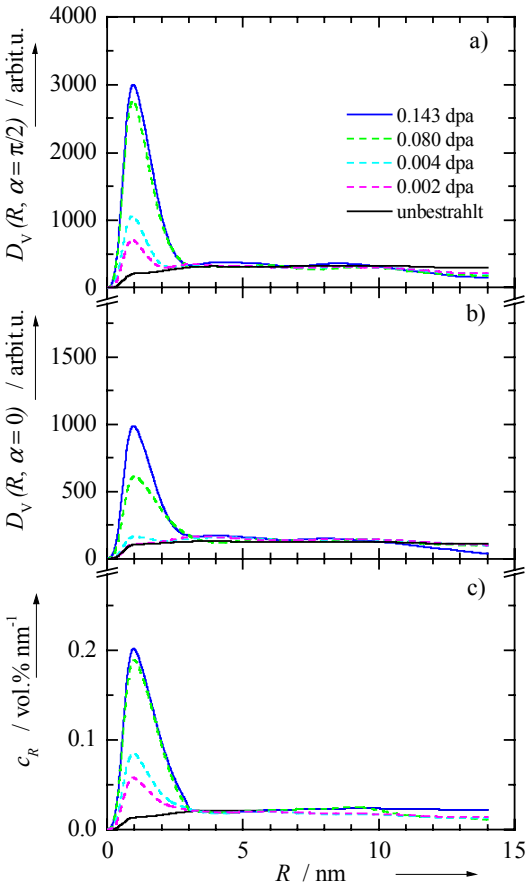

Fig. 1: Relative volume-related size distribution function D_v (a,b) and volume fraction c_R versus radius R of the scattering defects (c) obtained from SANS measurements at the VVER 440-type RDB steel 15Xh2MFA, heat KAB-B

The result emphasizes that the first peak characterizes the radiation-induced defects and the difference of the integral under the peak for the irradiated condition and unirradiated initial state is considered to be the volume fraction or number density respectively of the radiation defects. Because the changes of the size mode values are marginal, the parameter "volume fraction" is selected as correlation parameter. Typical variations of the A-ratio with the chemical composition point to the fact that the type of the defect can be also modified.

The correlations between the radiation-induced increase of the yield stress, or the shift of the Charpy transition temperature respectively and the volume fraction of the radiation defects are depicted in Figs. 2 and 3.
The measuring points represent different types of RPV steels, manufacturer, irradiation temperatures, neutron fluxes and neutron fluences. Considering that, the broad scattering range is not surprising. However, the data trend is clear:
Provided that the results of the model alloys are excluded, yield stress and transition temperature increase roughly with a linear or, better, a square root relationship with the volume fraction of the defects. The fit lines are included in the figures.

5. Discussion

In the bainitic RPV steels irradiation produces nano-scaled microstructural defects that are causally connected with the radiation-induced increase of the strength and the shift of the transition temperature. The relation is specially evident if the scope of the parameter of influence is reduced. The causality between these phenomena is also proved by the similarity of their thermally activated recovery [3]. Obviously, the fine scale radiation defects act as

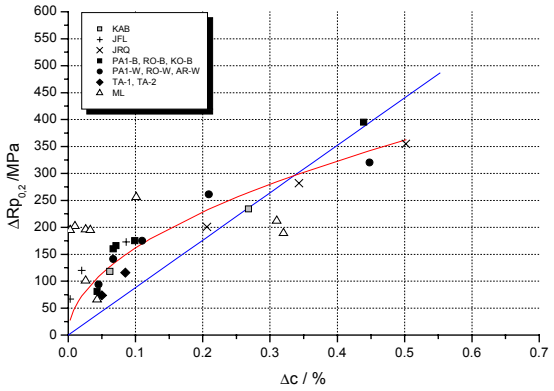

Fig. 2: Correlation between the radiation-caused increase of the yield stress $\Delta R_{p0.2}$ and the volume fraction of radiation defects Δc

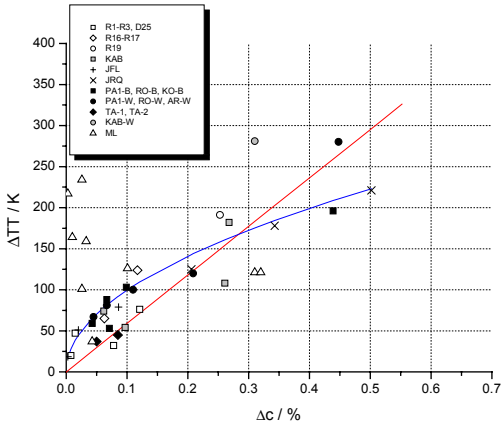

Fig. 3: Correlation between the radiation-caused shift of the transition temperature ΔTT and the volume fraction of the radiation defects Δc
(ΔTT is related to a Charpy energy of 48 J)

dispersed obstacles to the motion of the dislocation. A detailed analysis [3] using well-known theoretical approaches to the dislocation-particle-interaction mechanism shows:

a) the measured increase of the yield stress does not represent the unbiased contribution of the radiation defects.
b) There are no generally valid correlation between the increase of the yield stress and the square root of the volume fraction of the radiation defects.
c) Assuming the same content of volume fraction the radiation hardening effect decreases with increasing strength in the initial condition.
d) The transition temperature shift can be put down to the radiation hardening effect when the mode of the fracture is not changed.

6. Conclusions

A series of commercial RPV steels and model alloys was irradiated to fluences between 2.5 and 630 · 10^{18}/cm^2 [E > 0.5 MeV] in a neutron spectrum and under thermal condition representative for VVER reactors. The bainitic VVER-type and ASTM-related RPV steels and the ferritic Fe-base model alloys exhibit nano-scaled microstructural features which can be definitely detected by SANS. Types and compositions of materials as well as the neutron fluences hardly affect the characteristics of the features but change the volume fraction of the defects. There is a clear trend, the bigger the volume fraction the higher the irradiation-induced increase of hardness and strength and the larger the shift of the transition temperature. The correlations approximately follow a square root dependence. However, the proportionality is also influenced by the type of material and, thus, it is not possible to predict the changes in strength and toughness on the base of microstructural analyses using a generally valid correlation. The neutron embrittlement as identified by the transition temperature shift is a consequence solely of the irradiation hardening. In the first approximation there is no evidence that additional microstructural phenomena which are not detectable by SANS are of essential influence on the mechanical properties of the material investigated.

References

[1] J. Boehmert, M. Große, A. Ulbricht, Nachweis, Interpretation und Bewertung neutroneninduzierter Defektstrukturen bei WWER-Reaktor-Druckbehälterstählen, Forschungszentrum Rossendorf, Wissenschaftlich-technische Berichte, FZR-381, 2003

[2] O. Glatter, Determination of Particle-Size Distribution Functions from Small Angle Scattering Data by Means of the Indirect Transformation Method, J. Appl. Cryst. 13 (1980) 7

[3] J. Boehmert, H.-W. Viehrig, A. Ulbricht, Correlation between radiation-induced changes of microstructural parameters and mechanical properties, J. nucl. mat., publication in preparation

Summaries of research activities

Accident analysis of nuclear reactors

U. Grundmann, S. Kliem, J. Krepel, S. Mittag, U. Rohde, F. Schäfer

Development, validation and application of the code complex DYN3D - ATHLET

The validation of the code complex DYN3D - ATHLET for boiling water reactors (BWR) was performed by participating in an OECD benchmark task on a turbine trip transient in the NPP Peach Bottom 2 (USA). The DYN3D-ATHLET calculations show good agreement with the measured data and the results of other codes. A new method of coupling the reactor core model DYN3D to the thermo-hydraulic system code ATHLET, the so called parallel coupling, has been developed. This type of coupling ensures numerical stability even in cases with very strong feedback of thermo-hydraulics to neutron kinetics and was applied to analyse ATWS scenarios. Further, using ATHLET, experiments have been analysed on natural circulation instabilities at low pressure, which were performed at the CIRCUS test facility at TU Delft.

Generic analyses on hypothetical boron dilution accidents have been performed by using the code complex DYN3D-SAPR. SAPR is a semi-analytical model developed in the institute for the description of coolant mixing inside the reactor pressure vessel (RPV). Sensitivity studies were done for reactivity parameters, obtained by different macroscopic cross section libraries. It was shown, that the differences in the neutronic data lead to significant differences in the height of the power peak, but safety relevant parameter limits are not exceeded even for a pump start-up scenario with the maximum possible diluted slug in the cold leg.

The 1D version of a reactor dynamics code for molten salt rectors (MSR) was developed. In MSR kinetics, the effect of the transport of delayed neutron precursors with the flowing fuel has to be considered. The code has been verified with a series of benchmark tasks considered within the European research project MOST. In the next step, a 3D version of the code based on DYN3D will be developed.

supported by BMWA

G. Grunwald, T. Höhne, M. Kliem S. Kliem H.-M. Prasser U.Rohde

Coolant mixing in pressurised water reactors

Experiments aiming at the measurement of temperature and boron concentration distributions in a pressurised water reactor were carried out at the mixing test facility ROCOM (1:5 scaled model of a PWR Konvoi). The disturbance is modelled by injecting salt water as a tracer into the affected loop. A new quality of tests is achieved by using mesh-sensors with high resolution in time and space.

In the reported period, the mixing of slugs of deborated condensate accumulated during boiler-condenser mode in the course of a small-break LOCA was investigated, when the slugs are displaced into the reactor due to the onset of natural circulation. Density differences between the slugs and the inventory of the reactor were modelled by

funded by BMWA, EC and industries

adding ethanol. It was shown that the lower the density in the slugs is, the lower the amplitude will be of the deboration at the core entrance.

H.-G. Willschütz, E. Altstadt

In-vessel retention in LWRs

The FOREVER-experiments, currently underway at the KTH Stockholm (Sweden), are simulating the thermal and pressure loads on the lower RPV head for a corium melt pool with internal heat sources. A 2D Finite Element model has been developed for the numerical simulation of this in-vessel scenario. The temperature field in the melt and in the vessel wall was evaluated using a CFD model considering turbulent convection, heat conduction, crust formation and heat radiation. The Effective Conduction-Convection Model (ECCM) has also successfully been applied to calculate the transient temperature fields for other experiments. The implementation of the dynamic coupling between the thermal and mechanical FE-model was started. The creep data base was improved and validated for temperatures up to 1300 °C. The REVISA tests were used for validation concerning the creep behaviour of the 16MND5 steel. The creep data base was applied to simulate the RUPTHER-14 test (2D, small scale, 16MND5) and the MPA-Meppen test (2D, large scale, 20MnMoNi55). The creep behaviour of the chemically equivalent steels 16MND5 and 20MnMoNi5.5 exhibits some differences. However, the scattering of the results of different tests with the same material (uniaxial creep tests) is in the same order of magnitude like the differences between 16MND5 and 20MnMoNi5.5. Therefore, it seems to be justified to use one creep data base for the FEM simulation, which conservatively covers the creep behavior of 16MND5 und 20MnMoNi5.5. The comparison of pre-test calculations of the EC-2 experiment with the measured data shows a good agreement of the outer surface temperatures and of the vessel failure time and location. Metallographic investigations of specimens of the broken vessel yield a good qualitative correspondence of the local material damage distribution (represented by creep cavities) with the damage predicted by the calculation. The damage model also causes that the fracture of the vessel starts at its outer surface – as confirmed in the experiment. After analysing the calculations, it seems to be advantageous to introduce a vessel support, which can unburden the vessel from a part of the mechanical load and, therefore, avoid the vessel failure or at least extend the time to failure.

supported by BMWA

Safety and effectiveness of chemical processes

G. Hessel, R. Hilpert, H.-M. Prasser H. Kryk, M. Roth, W. Schmitt, F.-P. Weiß

Safe and economical process control and state monitoring in chemical plants

The efficiency of the on-line monitoring system MoSys, based on an energy and mass-balance approach with adaptive functions, could be proven during two hydrogenation campaigns in a 4 m³-stirred tank reactor (Degussa, Inc.). Operational experiences showed that MoSys reliably monitors exothermic chemical processes and its concentration estimations were in good agreement with off-line chemical analyses (HPLC). Pop-up windows at all operator stations indicate the occurrence of undesired operational states and the corresponding operator hints for countermeasures. Moreover, archived process data and MoSys-outputs (e.g. conversion rates, concentration profiles) allow to optimise complex chemical batch processes.

supported by BMBF

The monitoring system MoSys was handed over to Degussa, Inc. for further routine application.

G. Hessel, H. Kryk, W. Schmitt, F.-P. Weiß,

Experiments and numerical simulations of exothermic chemical reactions

The concentration profiles of the reactants, the intermediates, and of the product in the catalytic hydrogenation of aromatic nitro compounds to the corresponding amino compounds were measured both by on-line (in situ) Fourier-Transform-Infrared (FTIR) spectroscopy and by off-line High-Performance-Liquid Chromatography(HPLC). As an alternative optical technique to the FTIR spectroscopy, the Raman spectroscopy was tested.

In aqueous reaction mixtures the FT-Raman analysis provides advantages compared to FTIR spectroscopy because interference from the aqueous phase is minimal. By using HPLC, FTIR- and Raman analysis, the mechanism and pathways of complex heterogeneous reactions could be investigated in more detail.

supported by industry

T. Weier, G. Mutschke, J. Hüller, G. Gerbeth

Boundary layer control in electrolytes

A significant control of lift- and drag-coefficients is possible by application of stationary electromagnetic forces. However, the energetic effort for this flow control turned out to be too high for velocities above 10 m/s. Therefore, the idea of using alternating electromagnetic forces has been tested which resulted in a reduction of the energetical effort by up to two orders of magnitude, but for the same effect on the lift. Application in electrochemical processes seems possible.

supported by BMBF-VDI, DFG

Thermo-fluiddynamics

M. Beyer
H. Carl
U. Hampel
K. Lindner
H. Pietruske
H.-M. Prasser
H. Rußig
P. Schütz
M. Tamme
D. Walter
S. Weichelt
C. Zippe

Thermal hydraulic test facility TOPFLOW

TOPFLOW is a large-scale high-temperature and high-pressure test facility for generic research in the field of transient two-phase flow and for studies of safety relevant fluid-dynamic problems in components of nuclear power plants and chemical installations. The new facility has a heating power of 4 MW. The parameters allow experiments with steam-water mixture at saturation pressures of up to 7 MPa. The facility was put into operation in October 2002 reaching nominal pressure and temperature at a power level of 1.8 MW. Commissioning is continued. It is being prepared for the acceptance procedure by the TÜV, which is planned for the first half of 2003.

Parallel to the commissioning activities, experiments were started with an air-water flow in the vertical test sections. The tests are part of a project (Construction and execution of experiments at the multi-purpose thermal hydraulic test facility TOPFLOW for generic investigations of two-phase flows and the development and validation of CFD codes) in the framework of the German reactor safety research and the embedded CFD initiative. In the test section DN200, flow pattern studies were performed using a wire-mesh sensor of 64x64 measuring points for the first time. The data acquisition rate of 2,5 kHz allows as well the visualisation of the phase boundary as void profile and bubble size measurements. First results allow to quantify scaling effects. Special attention is given to the transition from bubble to churn-turbulent flow. At large pipe diameters, this transition does not lead via slug flow. Detailed information about the effect of scaling to flow structure was obtained.

funded by BMWA

A. Böttger
G. Grunwald
T. Höhne
S. Kliem
H.-M. Prasser
U. Rohde
M. Tamme
J. Zschau

Coolant mixing studies

In the framework of the project funded by BMWA, the mixing was studied in the upper plenum. For this purpose, all four coolant outlet nozzles of the ROCOM reactor model were equipped with wire-mesh sensors. Salt tracer solution was injected into individual fuel element positions. The data were used to interpret characteristic temperature distributions in the hot legs. The results can be taken for the more accurate hot leg temperature measurement, which is important for the efficiency of the plant operation.

Additional experiments on slug mixing during the start-up of the first main circulation pump were carried out in the framework of European FLOMIX project. The results of these experiments will be made available to the project partners for CFD code validation. While CFD codes well describe the high turbulent, momentum forced mixing, the simulation of mixing driven by small density differences has still to be improved.

funded by EC

At the CCEF test facility, experiments on cross flow in rod bundles were performed. CCEF is a plexiglass test section with asymmetric water flow through the rod bundle (inlet at the bottom and outlet at the side). Detailed velocity distributions measured by means of laser Doppler

anemometry (LDA) have been compared with the results of CFD calculations performed with rod-wise modelling of the geometry and applying standard turbulence models, on the one hand, and CFD simulations in the porous body approximation, on the other hand. The simulation with applying turbulence models in detailed geometry shows good agreement with the measurements. The porous body approach is able to reproduce the global velocity fields, but larger local deviations occur. However, the much lower computing time in the porous body approximation makes feasible the CFD simulation of the whole reactor core.

funded by BMWA and VGB

A. Böttger
J. Fietz
H. Futterschneider
U. Hampel
D. Hoppe
H.-M. Prasser
J. Zschau
W. Zimmermann
C. Zippe

Development and calibration of two-phase flow measurement techniques

The development of electrode-mesh sensors for high temperature and pressure conditions was continued. A sensor with a measuring matrix of 12x12 points and a nominal diameter of DN80 was constructed and successfully applied during water hammer experiments in the main steam line of the integral test facility PMK-2 in Budapest. A vacuum soldering technology was used for the first time to built the sensor body with its hidden cooling channels and blind holes for the fixing of the electrodes. This sensor plays the role of a prototype of the main manufacturing techniques necessary to construct wire-mesh sensors for the planned high-temperature tests at TOPFLOW. Other sensors for tests at the Pilot Plant Pipework of UMSICHT Oberhausen were equipped with a set of micro-thermocouples to perform synchronised gas fraction and temperature measurements to study the heat exchange at the water-steam interface during void collapses. Additionally to these novel advanced sensors, needle probes were applied with integrated thermocouple.

funded by EC

funded by VGB

The diversified level indication system for boiling water reactors developed by FZR is qualified according to the German reactor safety regulations. The qualification procedure is accomplished by Framatome ANP. FZR contributes as a scientific consultant. The completion of the qualification is expected for the first half of 2003.

funded by Voith Turbo, Crailsheim

The gamma-tomography to visualise periodically changing void fraction fields, which was originally developed for an axial pump at TU Dresden, was used to measure the phase distribution inside a hydraulic coupling. The main challenge of this application is to handle the different rotation speeds of the pump and turbine wheels of the coupling. The measurements aimed at clarifying the reasons for momentum jumps in the characteristics of the clutch, which are caused by flow regime transitions in the cells between the pump respectively turbine blades.

funded by DFG

The construction of the PET detector was completed for measuring the distribution of a tracer marked by a positron emitting nuclide in a bubble column. The scanner consists of 8 axial layers with 16 BGO detectors each. The spatial resolution is in the range of a centimetre. Tests were performed with a solution of the sodium salt of capronic acid ($C_4H_{13}COONa$), which is a weak surfactant that leads to the production of wet, unstable foam on top of the column. In separate experiments

either the liquid phase or the surfactant was labelled with a positron emitting nuclide ($Na^{18}F$ for the liquid, ^{11}C for the sodium capronate). The redistribution of the tracer after a sudden start of the gas supply has shown a rapid enrichment of the surfactant in the foam layer, while the counter-test with the fluoride has not shown such an effect, i.e. the measured concentration distribution of ^{18}F corresponds to the local liquid fraction in the column. In this way, the effect of the molecular floatation of the weak surfactant was demonstrated in-situ for the first time.

Significant progress was made in the field of ultra-fast scanned electron-beam X-ray tomography. Preliminary tests were performed in co-operation with IKE Stuttgart, using an electron beam welding device as flexible strong X-ray source. It was demonstrated that a linearly scanned electron beam can be used to create a travelling X-ray focus, which allows high-speed tomography with about 1000 frames per second.

D. Lucas
E. Krepper
H.-M. Prasser
C. Zippe

Transient two-phase flows in pipelines

In the framework of a project sponsored by BMWA flow patterns and their evolution in a vertical tube were investigated. The last series of experiments was dedicated to transient flow after a sudden change of the liquid superficial velocity during constant air injection. Fast transitions between different flow regimes were recorded and analysed by calculating time dependent radial gas fraction profiles and bubble size distributions from wire-mesh sensor data. Theoretical efforts were focussed on transient flow maps. A novel correlation was proposed for bubble-to-slug flow transition taking into account the inlet length. The theoretical models of the partial bubble size resolved radial gas fraction profiles allow to predict the transition from a wall-peaked to a central-peaked gas fraction profile as well as the onset of slug flow with a unified set of closure relations. The model equations can be implemented into CFD codes for two-phase flows.

funded by BMWA

Liquid metal magnetohydrodynamics

I. Grants, J. Priede, G. Gerbeth

Crystal growth

The analysis of the GaAs crystals grown at the Vertical Gradient Freeze facility of Bergakademie Freiberg, and the comparison with numerical simulations revealed that a significant influence on the solid-liquid phase boundary is possible by the application of a rotating magnetic field. For an even stronger control of the radial-meridional flow fields, the use of a travelling magnetic field has been studied numerically. Besides the influence on the shape of the phase boundary, the possibility of higher growth velocities has been derived from the simulations.

For the floating zone growth of intermetallic compounds at IFW Dresden, a strong control of the flow field has been developed using a second induction coil in addition to the primary one. Based on a vast of numerical simulations for an optimisation of this approach, the technical realization has been done at IFW. First growth experiments demonstrated convincingly the strong influence of the double inductor on the shape of the solid-liquid phase boundary and on the stability of the overall growth process.

supported by SMWK, DFG

V. Galindo, W. Witke, S. Eckert, A. Cramer, B. Willers, G. Gerbeth

Metallurgy

Based on numerical simulations and low-temperature model experiments, a steady magnetic field has been designed and built for the investment casting process of aluminium alloys. During a first test of this magnet at the industrial partner TITAL Bestwig, this magnet showed promising results for the reduction of the melt flow, particularly at the beginning of the filling process. The strong reduction of the velocity peaks lead to a reduction of the oxid entrapment and thus to the improvement of the quality of the casted aluminium alloys.

In order to influence the microstructure of solidified metals, basic studies on the role of convection during the solidification process have been performed. Various compositions of a Pb-Sn-alloy have been solidified under the influence of a rotating magnetic field. The microstructure changed, from a columnar dendritic one without magnetic field to an equiaxed one in case of an additional stirring of the liquid phase due to the magnetic field action.

supported by BMBF, DFG

S. Eckert, W. Witke, Th. Gundrum, F. Stefani, G. Gerbeth

Measuring techniques

The ultrasonic Doppler velocimetry (UDV) provides a full profile of the velocity field. Applications to liquid metals, however, are limited by the maximum temperature of about 100°C of the ultrasonic transducers. Therefore, ultrasonic wave-guides have been developed and tested in order to overcome the temperature limitations. Successful tests have been performed for flows of sodium, lead-bismuth, copper-tin and aluminium up to temperatures of 700°C. The integrated system of wave-guides, transducers and the Doppler system worked stable and robust. The wetting between the wave-guide and the melt turned out to be of crucial importance for the system. Due to the wetting problem, first tests in molten copper and in molten steel have not been successful yet.

For the idea of a magnetic tomografy, i.e. reconstruction of the flow

field out of external magnetic field measurements, a demonstration experiment has been set-up. The tests showed convincingly that the induced magnetic field as well as the surface electic potential follow the flow structure changes.

supported by
EU, DFG

I. Grants,
A. Cramer,
Ch. Heinzelmann,
S. Eckert,
G. Gerbeth

Basics of MHD flows

The stability of flows in rotating or steady magnetic fields has been analysed theoretically. An irregular, intermittent behaviour of the flow field occurs already far below the threshold of linear instability. It is caused by non-linear non-normal transitions. A theoretical approach has been developed to predict the global flow stability, and it agreed very well with experiments for the flow in a rotating magnetic field.

Velocity measurements in rotating and travelling magnetic fields have been performed in the highly turbulent regime. Though these measurements are very sensitive and difficult, they revealed a strong mixing effect if two types of flow symmetries are coupled.

supported by
DFG

F. Stefani,
Th. Gundrum,
U. Günther,
M. Xu,
G. Gerbeth

Dynamo effect

A further measuring campaign at the Riga dynamo delivered much more data on the distribution of the self-excited magnetic field. The maximum field strength measured at the inner wall of the dynamo module reached values of up to 170 mT. The saturation of the flow induced magnetic field has been shown to take place via a weak-field back-reaction, mainly leading to a modification of the azimuthal velocity component in the vertical direction. Basic studies have been started on the integral equation approach for the dynamo and the spectral properties of the dynamo operator.

supported by
EU, DFG

Materials and components safety

I. Stephan, B. Böhmer, F. Prokert

Neutron dosimetry

The gamma-spectrometry based neutron-dosimetric analysis of the Irradiation Programme Rheinsberg II was finished and adjusted neutron fluences were determined for all eight experiments. The experiments were equipped with a fluence monitor set comprising different activation detectors which cover various spectral responses. The measured reaction rates were used for spectrum adjustment by the spectrum adjustment code COSA. The adjustment results were compared with the results of Monte Carlo neutron fluence calculations. Calculated and experimental fluences show a good agreement. This allowed to remove errors in the experimental neutron dosimetry and to extrapolate the fluence values to all positions of interest. On this base, well-proved data of the neutron exposure are available for the materials irradiated in the irradiation programme Rheinsberg II.

Furthermore, the monitoring of the irradiation temperature was evaluated. For that pre-irradiated diamond powder was used. The powder is isochronically annealed and the lattice constant is measured using an X-ray diffractometer. The lattice parameter is constant in the lower annealing range and is linearly reduced for higher annealing temperatures. The point of intersection of both lines is the irradiation temperature. The measurements show large scatters and provide irradiation temperatures that lie above the expected values. The results suggest that an additional neutron flux effect is of influence on the point of intersection. The effect cannot be quantified from the available data.

co-operation with IIM

B. Böhmer, J. Konheiser, K. Noack,

Neutron and gamma dosimetry of reactor pressure vessels

A new project in the framework of the Scientific and Technical Cooperation Agreement with Russia aims at investigations of material specimens from reactor pressure vessels of the shut down NPP Greifswald. Calculations of neutron and gamma fluences needed for these investigations are being prepared. Necessary input data for these calculations – construction specifications, neutron source characteristics and reactor operation data - were obtained from NIS Rheinsberg and verified.

supported by BMWi

H.-W. Viehrig, W.-D. Leonhardt, S. Schneider

Radioisotope laboratory for machining of test specimens

For the safety assessment, for the evaluation of aged material conditions, or for failure analyses of nuclear components that are radioactive, appropriate hot cells must be available in order to machine test specimens or to prepare probes from the material pieces. A radioisotope laboratory is being erected for this purpose. The core of the setup is a CNC-controlled electric discharge machine. The machine bases on a commercial machine, but the design and operational function must be changed to a substantial extent. As an example, the filter technique and the water purification equipment are newly designed and, in the consequence, the whole water circuit changed. The working room of the machine is capsuled and the wire waste treatment is reconstructed. Furthermore an additional assembly setup is constructed next to the

machine where the raw material or the prefabricated pieces are fitted on special self-constructed chucks.

co-operation with ZA Forschungs-technik

The setup must ensure the function of the complicated machining procedure by remote handling and maintenance must not lead to significant exposure of the staff. The general function of the setup has been proved, and the extensive test phase is started.

J. Boehmert, G. Mueller, A. Ulbricht, M. Uhlemann

Effect of hydrogen on the toughness of reactor pressure vessel steels

The BMWA-supported project "Effect of hydrogen on the toughness of reactor pressure vessels" dealt with the investigation of unirradiated pressure vessel steels under typical LWR condition. In this case hydrogen is of only marginal influence on the toughness behaviour. Continuing the research, a further project is to investigate the hydrogen effect on irradiated steels. Therefore, the mechanical tests already performed at the unirradiated specimens have to be repeated with irradiated specimens from the irradiation programme Rheinsberg. For this purpose a hydrogen charging device was constructed and installed into the radioisotope laboratory. Probes for small angle neutron scattering (SANS) experiments were already hydrogen loaded and tested at the SANS facility of the BENC at HMI Berlin. SANS experiments are expected to show interrelation between microstructural radiation defects and hydrogen. The first experiment using Cu-rich steel with high radiation effect did not show a difference between the unloaded probes and the hydrogen loaded ones.

supported by BMWA

J. Boehmert, H.-W. Viehrig, A. Ulbricht

Final evaluation of the results of the irradiation programme Rheinsberg

The irradiation programme Rheinsberg made available nearly 2000 specimens from 18 different heats of both base metal and weld metal of reactor pressure vessel (RPV) steels. The material variety was focussed on VVER 440-type steel but comprises steel for VVER 1000 or ASTM-related RPV steels, too. The specimens were exposed to neutron doses between 2.6 to $128 \cdot 10^{18}$ n/cm^2 [E > 0.5 MeV]. Hardness, tensile properties, Charpy V-notch transition temperatures and reference temperatures according to the Master Curve approach were measured in the initial, irradiated and, partly, the annealed condition. Additionally, for each specimen set and state the microstructure was analysed by small angle neutron scattering (SANS). For that, a procedure was developed to measure the mean diameter, the size distribution and the volume fraction of the radiation-induced structural inhomogeneities (radiation defects).

The VVER-type RPV steels showed good toughness properties in the unirradiated condition. In the post-irradiation condition, the typical neutron hardening and embrittlement were detected in every case. The effect increases with increasing neutron fluence and strongly depends on the steel type or heat. The content of copper or phosphorus is the most important parameter of influence. However, this parameter cannot always explain the different sensitivity against neutron embrittlement. In principle, the nickel-poor VVER 440-type steel exhibits very low radiation sensitivity if the purity of the steel is high. The comparison of the results with the prediction according to the Russian codes shows that

the prediction is conservative as a rule, but not in every case. The radiation defects detected by SANS correlate with the radiation hardening and embrittlement.

E. Altstadt ,
H. Carl,
R. Weiss

Water hammers in pipelines

Water hammers can occur in case of an inflow of sub-cooled water into pipes filled with steam or steam-water mixture. They also may appear as the consequence of valve closing or opening actions. In the latter case, shock waves in two-phase flow must be expected. The influence of the fluid-structure interaction on the magnitude of the loads on pipe walls is investigated by experiments and finite element simulation. Therefore, at FZR a cold water hammer test facility (CWHTF) was designed and built up in 2000. An experimental programme covering pressure amplitudes up to 106 bars was realised. The dependence of the maximum pressure on the residual air, the bouncing velocity and on the valve opening time was investigated. The results of the finite element simulations support the understanding of the FSI after the bouncing. For example it could be shown that the high frequent pressure oscillations superimposing the basic pressure course are not due to wave reflections at the pipe bend but that they are the result of the coupling between stress wave in the pipe wall and pressure wave in the fluid. This work is done in the frame of a project sponsored by the European Community. The deliverables (measurement data, measurement evaluation reports) were forwarded to the EC.

supported by EC

M. Werner,
E. Altstadt

Finite Element-modelling of crack propagation

A 3-dimensional FE-model of a Charpy specimen was developed to simulate the crack propagation. This model as well includes the kinematics of the roll bearings as the crack opening mechanism. The plastic material behaviour is considered. The crack propagation is controlled by a strain based damage criterion which was integrated into the finite element code ANSYS. The numerical stability could be improved in this way. The unloading compliance method is simulated using this model and results are compared with experiments. A 3-dimensional FE-model is being developed for CT specimens.

Particle and radiation transport

C. Beckert, K. Noack

Photoneutron source at ELBE

Within this network-project of the FZR, which is partly supported by the DFG, calculations were made for the design of a photoneutron source at ELBE. Monte-Carlo calculations of the neutron beam and background at the measuring place provided information about the construction and the material selection of the neutron radiator including the vacuum housing, the beam dump and the collimator.

For different radial Gaussian distributions of the primary electron beam, its widening behind the beryllium windows was calculated and the time resolution at the measuring place was investigated. Other calculations were done to search for possibilities to increase the neutron intensity. It turned out that it is possible by means of a bigger radiator. Even a radiator with a twice as large cross section does not significantly worsen the energy resolution. Furthermore calculations were carried out concerning radiation protection problems. Based on these results, the additional shielding was specified which has to be installed.

supported by DFG

R. Kuechler, K. Noack, T. Zorn

Transport of radio-nuclides in the water unsaturated zone

By means of batch and column experiments the dissolution behaviour of pyrite and calcite mixtures was investigated in water and in water-unsaturated sand columns. To determine optimum conditions for the experiments, appropriate numerical models and codes have been developed and applied. Finally, the computation results were compared with the corresponding results of the measurements and conclusions were drawn concerning the dissolution of the mineral mixture. With a further column experiment investigations were started for the pyrite dissolution catalysed by bacteria. As expected, it turned out that the bacteria strongly accelerate the pyrite dissolution. Detailled information is needed about the growth and distribution of the bacteria in the column for the numerical modelling of the complex bio-chemical processes. Furthermore, a spectrometer of the *SpectraWin* type has been installed at the column stand. It will allow the height-dependent measurement of the oxygen consumption inside the column.

B. Böhmer, J. Konheiser, K. Noack, I. Stephan

Increasing the accuracy of neutron and gamma fluence assessment

The upgrading of the Monte Carlo code TRAMO to facilitate coupled neutron-gamma transport calculations was essentially completed. The prepared extensions include codes for processing of nuclear data, the improved simulation of thermal neutron transport, and models for the production and transport of gamma radiation. First test calculations were compared for simple models with results of the code MCNP/4C2. Thereby, unexpected deficiencies of MCNP in modelling thermal neutron transport were found and confirmed by an author of this code. Another deficiency found in MCNP concerns the gamma production and is caused by insufficiencies in the available nuclear data libraries. This gap was closed in TRAMO by suitable extrapolations of the nuclear data. Good agreements were obtained between TRAMO results and results obtained with the codes MCNP/4C2, DORT and HELIOS in

supported by DFG and EU

calculations of neutron and gamma spectra for different positions in a simple reactor model,

In the framework of a DFG-project, criticality calculations were performed with MCNP for the training reactors AKR (TU Dresden) and ZLFR (Hochschule Zittau/Görlitz). A comparison of calculated and measured activation rates allowed the absolute power calibration of both reactors. The calibrations are needed for the evaluation of neutron-gamma transmission experiments used for the validation of TRAMO and related neutron-gamma cross section libraries.

supported by DFG

R. Koch, A. Myasnikov

Neutronic calculations of Molten Salt Reactors

The Molten Salt Reactor (MSR) can be an appropriate means for the disposal of spent fuel that was accumulated in the years of operation of light water reactors with solid fuel, of dismantled nuclear weapons and for the efficient and economical energy production. The design of such a reactor can be rather simple. The neutron economy of an MSR is much better than that of a traditional LWR, because mainly non-fissile materials with very low neutron absorption cross section are present and no artificial absorbers are necessary in the coolant and control rods. MSR-fuel can consist of all three major fissile fuels, U 233, U 235, and the Pu isotopes.

The MSR-effort at Rossendorf is focused to the transmutation of plutonium and minor actinides. Stimulated by the MOST-project (Review of Molten Salt Reactor Technology) first preliminary calculations on the MSR were carried out. In co-operation with the KIAE Moscow a fully automated code for MSR burn-up calculations was developed by linking the well-known codes MCNP-4C and ORIGEN 2.1. The calculations of the model "Denatured Molten Salt Reactor" for an operating time period of three years proved the consistency between calculations using MCNP-ORIGEN on the one hand and the Russian calculations with the codes MCU-ORIGEN-S on the other hand. In the framework of the MOST project, preliminary studies were made to examine the fuel cycle characteristics of a MSR of the AMSTER-type.

Co-operation with KIAE Moscow

Publications

Publications in scientific and technical journals and in conference proceedings, monographs

Altstadt, E.; Carl, H.; Weiß, R.
Fluid-Structure Interaction Experiments at the Cold Water Hammer Test Facility (CWHTF) of the FZ-Rossendorf
Jahrestagung Kerntechnik 2002, Stuttgart, Tagungsband S. 59-64, May 14-16, 2002

Altstadt, E.; Willschütz, H.-G.
Nachrechnung von mittelskaligen Experimenten zum Kriechbruchversagen von Druckbehältern
2. Workshop "Kompetenzverbund Kerntechnik" vom 18. - 19. 09. 2002 in Köln, Tagungsband, Vortrag Nr. 13

Anikeev, A.; Bagryansky, P.; Ivanov, A.; Noack, K.
The SHIP Experiment at GDT: Physical Concept and Pre-Calculations
29th EPS Conference on Plasma Physics and Controlled Fusion, 17-21 June 2002, Montreux, Switzerland, Proceedings: ECA Vol. 26B, P-4.098 (2002)

Böhmer, B.; Borodkin, G.; Konheiser, J.; Manturov, G.
Testing of Neutron Data Libraries in Application to Reactor Pressure Vessel Dosimetry
International Conference on Nuclear Data for Science and Technology, 7-12th Oct. 2001, Tsukuba, Japan, Proceedings in the Journal of Nuclear Science and Technology, Supplement 2, p. 1006-1009 (August 2002)

Böhmer, B.; Grantz, M.; Hansen, W.; Hinke, D.; Konheiser, J.; Mehner, H.-C.; Noack, K.; Schneider, R.; Stephan, I.; Unholzer, S.
Gamma and Neutron Spectra Investigations in Iron-Water Benchmark Configurations for the Verification of Monte Carlo Calculations in Reactor Material Dosimetry
Jahrestagung Kerntechnik 2002, Stuttgart, 14.-16. Mai 2002, Proceedings pp. 511-514

Böhmer, B.; Grantz, M.; Hansen, W.; Hinke, D.; Konheiser, J.; Mehner, H.-christoph; Noack, K.; Schneider, R.; Stephan, I.; Unholzer, S.
Investigation of Gamma and Neutron Energy Fluences in Iron-Water Benchmark Configurations for the Verification of Monte Carlo Calculations and their Application in Reactor Material Dosimetry
International Conference on Nuclear Data for Science and Technology, 7-12th Oct. 2001, Tsukuba, Japan, Proceedings in the Journal of Nuclear Science and Technology, Supplement 2, p. 947-950 (August 2002)

Böhmert, J.; Müller, G.
Thermally activated deformation of irradiated reactor pressure vessel steel
Journal of Nuclear Materials 301 (2002) 227-232

Böhmert, J.; Müller, G.; Willschütz, H.-G.
Analyse von Simulationsexperimenten zu nuklearen Kernschmelzunfällen - Beitrag der Metallographie -
Fortschritte in der Metallographie, Sonderbände der Praktischen Metallographie, G. Petzov (Hrsg.), Vortragstexte der 35. Metallographie-Tagung 2001, Neu-Ulm, 19.-21. September, S. 69

Böhmert, J.; Viehrig, H.-W.; Gokhman, A.
Application of the Master Curve Approach for Dynamically Loaded Pressure Vessel Steels
ECF 14: Fracture Mechanics Beyond 2000, Volume I/III, Editors: A. Neimitz, I.V. Rokach, D. Kocanda, K. Golos, Proceedings of the 14th Bienniel Conference on Fracture ECF 14, 8.-13.09.2002, Cracow, Poland, p. 281

Böhmert, J.; Viehrig, H.-W.; Ulbricht, A.
Bewertung der Neutronenversprödung russischer Druckbehälterstähle anhand der Ergebnisse der Bestrahlungsexperimente Rheinsberg
2. Workshop "Kompetenzverbund Kerntechnik" vom 18. - 19. 09. 2002 in Köln, Tagungsband, Vortrag Nr. 17

Böhmert, J.; Viehrig, H.-W.; Ulbricht, A.
Einfluss des Gefüges auf die Neutronenversprödung von Reaktordruckbehälterstählen
7. Tagung "Gefüge und Bruch", Tagungsband, Leoben (Österreich), April 2002, S. 129

Dudlik, A.; Schönfeld, S. B. H.; Schlüter, S.; Fahlenkamp, H.; Prasser, H.-M.
Prevention of Water Hammer and Cavitational Hammer in Pipeline Systems
Chemical Engineering and Technology, 2 (2002) Sept., pp. 888-890.

Eckert, S.; Gerbeth, G.
Velocity measurements in liquid sodium by means of Ultrasound Doppler Velocimetry
Experiments in Fluids 32(2002)5, 542-546

Eckert, S.; Gerbeth, G.; Melnikov, V.
Determination of velocity profiles in liquid metal flows by means of Ultrasound Doppler Velocimetry
5th International Conference on Fundamental and Applied MHD (PAMIR), September 16-20, 2002, Ramatuelle, France, Proceedings I 119-124

Eckert, S.; Gerbeth, G.; Melnikov, V.; Lefhalm, C.-H.; Knebel, J.
Application of Ultrasound Doppler Velocimetry to flows of hot metallic melts
3rd International Symposium on Ultrasonic Doppler Methods for Fluid Mechanics and Fluid Engineering, September 9-11, 2002, Lausanne, Switzerland PSI-Proceedings 02-01, 77-82, ISSN 1019-6447

Gailitis, A.; Lielausis, O.; Platacis, E.; Dement'ev, S.; Cifersons, A.; Gerbeth, G.; Gundrum, T.; Stefani, F.; Christen, M.; Will, G.
Dynamo experiments at the Riga sodium facility
Magnetohydrodynamics, Vol. 38, No. 1/2 (2002), pp. 5-14

Gailitis, A.; Lielausis, O.; Platacis, E.; Gerbeth, G.; Gundrum, Th.; Stefani, F.
New results from the Riga dynamo experiment
5th International Conference on Fundamental and Applied MHD, Ramatuelle (France), Sept.16-20, 2002, Proceedings V17-12

Gailitis, A.; Lielausis, O.; Platacis, E.; Gerbeth, G.; Stefani, F.
Laboratory Experiments on Hydromagnetic Dynamos
Reviews of Modern Physics 74 (2002), 973-990

Gailitis, A.; Lieleausis, O.; Platacis, E.; Gerbeth, G.; Stefani, F.
On back-reaction effects in the Riga dynamo experiment
Magnetohydrodynamics, Vol. 38, No. 1/2 (2002), pp. 15-26

Galindo, V.; Gerbeth, G.; Ammon, W. von; Tomzig, E.; Virbulis, J.
Crystal growth melt flow control by means of magnetic fields
Energy Conversion and Management 43 (2002) 309-316

Gokhman, A.; Böhmert, J.; Ulbricht, A.
A Kinetic Study of Clusters Evolution under VVER-type Reactor Condition
Nucleation Theory and Applications, J. W. P. Schmelzer, G. Röpke, Y. B. Priezzhev (Eds.), Dubna, April 14-21, 2002, pp. 81-107

Grahn, A.
Doppeldiffusive Instabilität beim Flüssig-Flüssig-Stoffübergang: Simulation und Experiment
GVC/DECHEMA-Jahrestagungen 2002, Wiesbaden, 11.-13.6.2002 Chemie-Ingenieur-Technik 74 (2002), S. 570

Grahn, A.
Double-diffusive instability during liquid-liquid mass transfer---simulation and experiment
HEAT 2002: Third International Conference Transport Phenomena in Multiphase Systems, Baranow Sandomierski, Poland, June 24-27, 2002, pp. 293-300

Grants, I.; Gerbeth, G.
Intermittency route to turbulence in a rotating magnetic field driven flow
5th International Conference on Fundamental and Applied MHD, Ramatuelle (France), Sept.16-20, 2002, Proceedings I 179-183

Grants, I.; Gerbeth, G.
Linear three-dimensional instability of a magnetically driven flow
Journal of Fluid Mechanics (2002), vol. 463, pp. 229-239

Grundmann, U.; Rohde, U. (Editors)
Analysis of the Boiling Water Reactor Turbine Trip Benchmark with the Code DYN3D
PHYSOR 2002 International Conference on the New Frontiers of Nuclear Technology: Reactor Physics, Safety and High-Performance Computing, October 7-10, 2002, Seoul, Korea

Hämäläinen, A.; Kyrki-Rajamäki, R.; Mittag, S.; Kliem, S.; Weiss, F.-P.; Langenbuch, S.; Danilin, S.; Hadek, J.; Hegyi, G.
Validation of coupled neutron kinetic / thermal-hydraulic codes Part 2: Analysis of a VVER-440 transient (Loviisa-1)
Annals of Nuclear Energy 29 (2002) 255-269

Hessel, G.; Hilpert, R.; Kryk, H.; Roth, M.; Schmitt, W.; Seiler, T.
Monitoring-System mit adaptiven Wärmebilanzen für Batch-Reaktoren
GVC/DECHEMA-Jahrestagungen 2002, 11.-13. Juni 2002, Wiesbaden
Chemie Ingenieur Technik 74, 5 (2002) 596

Hessel, G.; Hilpert, R.; Kryk, H.; Roth, M.; Schmitt, W.; Seiler, T.; Deerberg, G.
MoSys - ein Online-Zustandserkennungssystem für exotherme chemische Reaktionen
Tagungsband der 6. GVC·VDI-Fachtagung "Anlagen-, Arbeits- und Umweltsicherheit", Köthen, 7./8. November 2002, Herausgeber: GVC·VDI-Gesellschaft Verfahrenstechnik und Chemieingenieurwesen, Düsseldorf, 2002, Vortrag E-05

Hessel, G.; Hulzer, G.; Kryk, H.; Schmitt, W.
Calorimetric and FTIR Spectrometric Investigation of a Grignard Reaction
5th Workshop and Exhibition on Reaction Calorimetry, DECHEMA-House, Frankfurt am Main, 17. April 2002

Hessel, G.; Kryk, H.; Schmitt, W.; Seiler, T.; Hilpert, R.; Roth, M.; Deerberg, G.
Monitoring-System mit adaptiven Wärmebilanzen für Batch-Reaktoren
Chemie Ingenieur Technik 74, 12 (2002) S. 1692-1698

Hicken, Enno F.; Schaffrath, A.; Fethke, M.; Jaegers, H.
Der NOKO-Versuchsstand der Forschungszentrum Jülich (FZR) GmbH - Rückblick auf 7 Jahre experimentelle Untersuchungen zur Erhöhung der Sicherheit von Leichtwasserreaktoren
Atomwirtschaft-Atomtechnik 47 (2002), Nr. 5, S. 343-348

Höhne, T.
Numerical Simulation of ISP-43 Test A with CFX-4
ANS/ASME Student Conference, Penn State University, USA, April 10-13, 2002, CD-ROM

Höhne, T.
Post Test Calculation with CFX-4 of the OECD/CSNI International Standard Problem Nr. 43
ICONE 10-22722, Tenth International Conference on Nuclear Engineering Hyatt Regency Crystal City, Arlington, Virginia, USA April 14-18, 2002, CD-ROM

Hüller, J.; Pham, M. T.; Howitz, S.
Thin layer copper ISE for fluidic microsystem
9th International Meeting on Chemical Sensors, 7-10 July 2002, Boston USA, Abstract book p. 173

Ivanov, A. A.; Abdrashitov, G. F.; Anikeev, A. A.; Bagryansky, P. A.; Deichuli, P. P.; Karpushov, A. N.; Korepanov, S. A.; Lizunov, A. A.; Maximov, V. V.; Murakhtin, S. V.; Smirnov, A. Yu.; Zouev, A. A.; Noack, K.; Otto, G.
GDT Device: Recent Results and Future Plans for GDT Upgrade
4th International Conference on Open Systems for Plasma Confinement, July 1-4,2002, Jeju Island, Korea, Proceedings in: Transactions of Fusion Science and Technology, 43 (2003) 51

K.C.J. Ketelaar, W.J.M. de Kruijf, T. van der Hagen, A. Manera, G. Avakian, P. Gubernatis, D. Caruge, G. Yadigaroglu, G. Dominicus, U. Rohde, H.-M. Prasser, F. Castrillo, M. Huggenberger, D. Hennig, J.L. Munoz-Cobo, C. Aguirre,
Natural Circulation and Stability Performance of BWRs (NACUSP)
Proceedings FISA 2001 EU Research in reactor safety, Luxembourgh, 12-15 november 2001, EUR 20281, European Communities, 2002, pp. 535-546

Kliem, M.
Experimental analysis of crossflow in the reactor core geometry.
Annual Meeting on Nuclear Technology 2002, Stuttgart, Germany, May 14-16, 2002 Proceedings pp. 55-58

Kliem, S.; Prasser, H.-M.; Grunwald, G.; Rohde, U.; Höhne, T.; Weiß, F.-P.
ROCOM experiments on the influence of density differences on the coolant mixing inside the reactor pressure vessel of a PWR
Annual Meeting on Nuclear Technology 2002, Stuttgart, Germany, May 14-16, 2002 Proceedings pp. 65-69

Kliem, S.; Prasser, H.-M.; Höhne, T.; Rohde, U.
Development and application of a fast running model for the description of coolant mixing inside the pressure vessel of pressurized water reactors
Int. Conf. on the Physics of Reactors PHYSOR 2002,Seoul, Korea, 6.-10.10.2002, Proc. CD-ROM paper 5D-04

Knebel, J.; Prasser, H.-M.; Hoffmann, P.-B.; Hüttmann, A.; Hansen, W.; Herrmann, D.; Böhmert, J.
Sektionsberichte - Jahrestagung Kerntechnik 2002
atomwirtschaft, Sektionsbericht, 47. Jahrgang, Heft 7, S. 475, Juli 2002

Kozmenkov, Y.; Mittag, S.; Rohde, U.; Grundmann, U.; Weiss, F.-P.; Vanttola, T.; Langenbuch, S.; Ionov, V. S.; Petkov, P.
VALCO: Validation of transient analysis codes for VVER by using measurement data
Proceedings of the 12th Symposium of Atomic Energy Research, Sunny Beach (Bulgaria), September 23-27, 2002, Proc. pp. 361-381

Krepper, E.
Application of CFX for modelling of natural convection and of subcooled boiling
CFX-Update No.22, Autumn 2002, p. 27

Krepper, E.; Aszodi, A.; Weiß, F.-P.
Experimental and Numerical Investigations of Heating Up Processes of Fluids in Large Pools
ASME Fluids Engineering Division Summer Meeting, Montreal July 2002, Conference-CD paper 31406

Krepper, E.; Hicken, E. F.; Jaegers, H.
Investigation of natural convection in large pools on the example of heating up the secondary side of an emergency condenser
International Journal of Heat and Fluid Flow Vol. 23 (2002) pp. 359-365

Krepper, E.; Prasser, H.-M.
Experimental and numerical investigation of one and two-phase natural convection
HEAT 2002: Third International Conference Transport Phenomena in Multiphase Systems, Baranow Sandomierski, Poland, June 24-27, 2002, pp. 333-339

Kuechler, R.; Noack, K.
Transport of reacting solutes through the unsaturated zone
Transport in Porous Media 49 (2002) 361-375

Lucas, D.; Krepper, E.; Prasser, H.-M.
Evolution of flow patterns, gas fraction profiles and bubble size distributions in gas-liquid flows in vertical tubes
HEAT 2002: Third International Conference Transport Phenomena in Multiphase Systems, Baranow Sandomierski, Poland, June 24-27, 2002, pp. 341 - 348

Lucas, D.; Krepper, E.; Prasser, H.-M.
Experimental high-resolution database for co-current air-water flow in a vertical pipe
40th European Two-Phase Flow Group meeting, Stockholm, Sweden, June 10-13, 2002, Paper C4

Pätzold, O.; Grants, I.; Wunderwald, U.; Jenkner, K.; Cröll, A.; Gerbeth, G.
Vertical gradient freeze growth of GaAs with a rotating magnetic field
Journal of Crystal Growth 245 (2002) 237-246

Prasser, H.-M.
Fast visualization of transient two-phase flows and mixing processes in single phase flows by means of electrode-mesh sensors
CHISA-2002, 15th International Congress of Chemical and Process Engineering, 25 - 29 August 2002, Praha, Czech Republic, Keynote lecture E2.5 (1244), Proc. CD-ROM.

Prasser, H.-M.; Baldauf, D.; Fietz, J.; Hampel, U.; Hoppe, D.; Zippe, C.; Zschau, J.; Christen, M.; Will, G.
Time Resolving Gamma-Tomography for Periodically Changing Gas Fraction Fields
HEAT 2002: Third International Conference Transport Phenomena in Multiphase Systems, Baranow Sandomierski, Poland, June 24-27, 2002, proc. pp. 425-434.

Prasser, H.-M.; Böttger, A.; Schütz, P.; Zschau, J.; Fleischer, S.; Gocht, T.; Hampel, R.
Füllstandswächter zur diversitären Grenzwertmeldung an Siedewasserreaktoren - Entwicklung und Erprobung
Jahrestagung Kerntechnik 2002, Stuttgart, 14.-16. Mai 2002

Prasser, H.-M.; Grunwald, G.; Höhne, T.; Kliem, S.; Rohde, U.; Weiss, F.-P.
Coolant mixing in a PWR - deboration transients, steam line breaks and emergency core cooling injection - experiments and analyses
International Congress on Advanced Nuclear Power Plants (ICAPP), June 9-13, 2002 - Hollywood Florida, USA, Proc. CD-ROM, paper #1214.

Prasser, H.-M.; Krepper, E.; Lucas, D.
Evolution of the Two-Phase Flow in a Vertical Tube - Decomposition of Gas Fraction Profiles according to Bubble Size Classes using Wire-Mesh Sensors
International Journal of Thermal Sciences 41 (2002) pp. 17-28.

Prasser, H.-M.; Zschau, J.; Peters, D.; Pietzsch, G.; Taubert, W.; Trepte, M.
Fast wire-mesh sensors for gas-liquid flows - visualisation with up to 10 000 frames per second
International Congress on Advanced Nuclear Power Plants (ICAPP), June 9-13, 2002 - Hollywood Florida, USA, Proc. CD-ROM, paper #1055.

Prasser, H.-M.; Böttger, A.; Zschau, J.; Dudlik, A.; Schlüter, S.
Cavitation behind a fast acting flap valve and prevention of water hammers
XXXIV. Kraftwerkstechnisches Kolloquium, TU Dresden, 24.-26. September 2002, Vortrag VM8, Kurzfassung in Beitragsmanuskripte, S. 184.

Priede, J.; Gerbeth, G.; Hermann, R.; Behr, G.
Control of the solid-liquid interface during RF-floating zone crystal growth by means of a two-phase inductor
5th International Conference on Fundamental and Applied MHD, Ramatuelle (France), Sept.16-20, 2002, Proceedings V 49-54

Richter, S.; Aritomi, M.; Prasser, H.-M.; Hampel, R.
Approach towards spatial phase reconstruction in transient bubbly flow using a wire-mesh sensor
International Journal of Heat and Mass Transfer 45 (2002) 1063-1075.

Schäfer, F.; Krepper, E.; Prasser, H.-M.; Szabados, L.; Ezsöl, Gy.
Simulation of two surge line break experiments at the PMK-2 Test Facility using the code ATHLET
Annual Meeting on Nuclear Technology, May 14-16, 2002, Stuttgart, Germany

Schaffrath, A.; Krüssenberg, A.-K.; Weiß, F.-P.; Prasser, H.-M.
Die Mehrzweck-Thermohydraulikversuchsanlage TOPFLOW des Forschungszentrums Rossendorf e.V. - Aufbau, Ziele und Perspektiven
Atomwirtschaft-Atomtechnik 47 (2002), Nr. 6, S. 383-388

Schaffrath, A.; Schmeisser, N.; Pietruske, H.; Schubert, S.
Construction of the Multipurpose Thermohydraulic Test Facility TOPFLOW using CAD Applications
Proceedings CAD2002 Corporate Engineering Research, 4-5.03.2002, Dresden, Germany, ISBN 3-86005298-5, 289-298.

Shatrov, V.; Mutschke, G.; Gerbeth, G.
Three-dimensional linear stability analysis of LID-driven MHD cavity flow
5th International Conference on Fundamental and Applied MHD, Ramatuelle (France), Sept.16-20, 2002, Proceedings I 237-242

Stefani, F.; Gerbeth, G.
Contactless methods of velocity determination in conducting fluids
5th International Conference on Fundamental and applied MHD, Ramatuelle (France), Sept.16-20, 2002, Proceedings I 131-136

Stefani, F.; Gerbeth, G.; Gailitis, A.
Lenz's rule liquefied: Understanding magnetic field saturation in the Riga dynamo experiment
5th International Conference on Fundamental and Applied MHD, Ramatuelle (France), Sept.16-20, 2002, Proceedings VI 53-58

Uhlemann, M.; Böhmert, J.; Müller, G.
Einfluss von Wasserstoff auf die Zähigkeit von Reaktordruckbehälterstählen
Jahrestagung Kerntechnik 2002, Tagungsbericht, 14.-16.05.2002, Stuttgart, S. 609

Uhlemann, M.; Böhmert, J.; Müller, G.
Einfluss von Wasserstoff auf die Zähigkeit von Reaktordruckbehälterstählen
2. Workshop "Kompetenzverbund und Kerntechnik" vom 18. - 19. 09. 2002 in Köln, Tagungsband, Vortrag Nr. 19

Ulbricht, A.; Böhmert, J.; Strunz, P.; Dewhurst, C.; Mathon, M.-H.
Microstructural Investigations on Russian Reactor Pressure Vessel Steels by Small Angle Neutron Scattering
Applied Physics A 74, Suppl. 1, 2002, pp. 1128-1130

Ulbricht, A.; Strunz, P.
Evaluation of Irradiation Embrittlement of Reactor Pressure Vessels (RPV)
BENSC Experimental Reports 2001, Hahn-Meitner Institut Berlin, HMI-B 584, p. 208, May 2002

Viehrig, H.-W.; Böhmert, J.; Dzugan, J.
Dynamic Master Curve Issues
Proceedings, MASC 2002: Use and Applications of the Master Curve for Determining Fracture Toughness, June 12 - 14, 2002, Helsinki - Stockholm - Helsinki

Viehrig, H.-W.; Böhmert, J.; Dzugan, J.
Some Issues by Using the Master Curve Concept
Nuclear Engineering and Design 212 (2002) 115-124

Viehrig, H.-W.; Böhmert, J.; Dzugan, J.
Use of Instrumented Charpy Impact Tests for the Determination of Fracture Toughness Values
From Charpy to Present Impact Testing, ESIS-Publication 30, D. Francois, A. Pineau, Eds., Charpy Centenary Conference, 2-5 October 2001, Poitiers, France, Elsevier Science Ltd. and ESIS, 2002, p. 245

Viehrig, H.-W.; Böhmert, J.; Dzugan, J.; Gokhman, A.
Anwendung des Master-Curve-Konzeptes bei dynamischer Belastung
2. Workshop "Kompetenzverbund Kerntechnik", am 18. und 19. September 2002 in Köln, Tagungsband, Vortrag Nr. 11

Viehrig, H.-W.; Böhmert, J.; Ulbricht, A.
Comparison of the Irradiation Effects on Microstructure and Mechanical Properties of VVER-Type RPV Steels
Proceedings of the IAEA Specialists Meeting on Irradiation Embrittlement and Mitigation, Gloucester, England, 14-17 May 2001, p. 121-130

Viehrig, H.-W.; Langer, R.
Application of Master Curve Approach for Rector Pressure Vessel Integrity Assessment
Proceedings of the NATO Advanced Research Workshop On Scientific Fundamentals for the life Time Extension of Reactor Pressure Vessels, held in Kiev, Ukraine, from 22 to 25 April 2002.

Viehrig, H.-W.; Richter, H.; Atkins, T.; van Walle, E.; Scibetta, M.; Valo, Matti J.; Wootton, Malcolm R.; Keim, E.; Debaberis, L.; Horsten, M.
RESQUE: Dependence of Test Results from Reconstituted Specimens with Tolerance Deviations and Variation of End Block Materials
Small Specimen Test Techniques: Fourth Volume, ASTM STP 1418, M. A. Sokolov, J. D. Landes, and G. E. Lucas, Eds., ASTM International, West Conshohocken, PA, 2002, pp. 477 - 488.

Werner, M.
Die Simulation des Teilentlastungs-Compliance-Verfahrens mittels eines Finite-Element-Programms zur Rissfortschrittsberechnung an einer 3-Punkt-Biegeprobe
DVM-Tagung "Werkstoffprüfung 2002", 5.-6.12.2002, Bad Nauheim,

Tagungsband S.312, Wiley-VCH Verlag

Willschuetz, H.-G.; Altstadt, E.; Weiß, F.-P.; Sehgal, B. R.
Analysis and insights about FE-Calculations of the EC-Forever-Experiments
10th International Conference on Nuclear Engineering, Arlington, VA, USA, April 14-18, 2002, CD-ROM

Willschuetz, H.-G.; Altstadt, E.; Weiß, F.-P.; Sehgal, B. R.
Scaled vessel failure experiment analysis and investigation of a possible vessel support
Jahrestagung Kerntechnik 2002, Stuttgart, May 14-16, 2002, Tagungsband S. 173-178

Other oral and poster presentations

Böhmer, B.; Borodkin, G.; Brodkin, E.; Egorov, A.; Konheiser, J.; Kozhevnikov, S.; Manturov, G.; Voloschenko, A.; Zaritsky, S.
ANISN-DORT-ROZ-MCNP-TRAMO Neutron-Gamma Flux Intercomparison Exercise for a Simple Testing Model
13th Seminar on Algorithms and Codes for Neutronics Calculations of Nuclear Reactors, 26-29 October 2002, Obninsk, Rußland

Böhmer, B.; Konheiser, J.; Noack, K.; Stephan, I.
Beiträge der Reaktordosimetrie zu Komponentensicherheit und Integritätsbewertung
2. Workshop des Kompetenzverbundes Kerntechnik zu "Komponentensicherheit und Integritätsbewertung", 18.-19. September 2002, Köln

Böhmert, J.; Große, M.; Ulbricht, A.
Kleinwinkelstreuung - ein vielversprechendes Werkzeug zum Nachweis von Strahlenschäden
Werkstofftag 2002, TU Dresden, Dresden, 04. 10. 2002, eingeladener Vortrag

Eckert, S.; Willers, B.
Erstarrung von Pb-Sn-Legierungen unter Magnetfeldeinfluss
Workshop "Nd-Basis Legierungen" im Rahmen des DFG-Schwerpunktprogrammes "Phasenumwandlung in mehrkomponentigen Schmelzen", IFW Dresden, 1./2.11.2002

Gerbeth, G.
Strömungskontrolle mit Magnetfeldern
Institut für Werkstofftechnik der Universität Bremen, 02.08.02

Gerbeth, G.; Galindo, V.
MHD investigations for material technologies at Forschungszentrum Rossendorf
Vortrag bei Workshop "Use of magnetic fields in crystal growth", Riga (Latvia), June 13-14, 2002

Grants, I.; Gerbeth, G.; Wunderwald, U.; Pätzold, O.; Cröll, A.
Application of a rotating magnetic field to the VGF growth of GaAs: basics of melt control and growth results
Vortrag bei Workshop "Use of magnetic fields in crystal growth", Riga (Latvia), June 13-14, 2002

Grundmann, U.; Rohde, U.
DYN3D - Results for Phase 2 of the BWR TT Benchmark by Using Different Models
OECD/NRC Boiling Water Reactor (BWR) Turbine Trip (TT) Benchmark Third Workshop - Starter Meeting for the VVER -1000 Coolant Transient Benchmark, May 28 - 30, 2002, Forschungzentrum Rossendorf, Dresden

Günther, U.
Krein space features of the MHD alpha² - dynamo operator matrix
5. MHD-Tage, Forschungszentrum Rossendorf, 25-26. 11. 2002

Günther, U.
MHD Dynamo-Operatoren
Lecture given at Bremen University, Department of Mathematics, Applied Analysis Group, June 12-13, 2002, Bremen, Germany

Kryk, H.; Hessel, G.; Schmitt, W.
Arbeiten am Forschungszentrum Rossendorf zum sicherheitsorientierten Monitoring exothermer chemischer Reaktionen
DECHEMA/GVC-Arbeitsausschuss "Sicherheitsgerechtes Auslegen von Chemieapparaten" 54. Sitzung vom 11.-12. Dezember 2002 im DECHEMA-Haus, Frankfurt am Main

Lucas, D.
Experiments and modelling of air/water flows in vertical pipes
Abschlußkolloquium des DFG-Schwerpunktprogramms "Analyse, Modellbildung und Berechnung von mehrphasigen Strömungen", Freyburg/Unstrut, Germany, 23.-25. September 2002

Lucas, D.
Transient flow maps for vertical pipe flow
5th Workshop on Measurement Techniques for Steady and Transient Multiphase Flows, Dresden, Germany, September 18-20, 2002

Schaffrath, A.; Weiß, F.-P.
TOPFLOW - A new multipurpose thermalhydraulic test facility for the investigation of steady state and transient two phase flow phenomena
NUSIM 2002 (11. Meeting of Nuclear Specialists from Slovakia, Czech and Germany), 13.-15.03.2002, Dresden

Stefani, F.; Gerbeth, G.
An inverse glance at MHD
5. MHD-Tage, Forschungszentrum Rossendorf, 25.-26. 11. 2002

Stefani, F.; Gerbeth, G.
Inverse Problems in MHD
Jahrestagung der Gesellschaft für Angewandte Mathematik und Mechanik (GAMM) 2002, Universität Augsburg, 25.-28. März 2002

Ulbricht, A.; Böhmert, J.; Viehrig, H.-W.
Small Angle Neutron Scattering Measurements of the Ageing under Neutron Irradiation and Recovery of Reactor Pressure Vessel Steels and Iron Alloys
Tables Rondes du LABORATOIRE LÉON BRILLOUIN, Thème D: Systèmes désordonnés et Matériaux, CEA/Saclay, FRANCE, 28 Novembre 2002.

VanOuytsel, K.
SAXS near the crack tip in metals
Vortrag am SCK.CEN, 12. März 2002, Mol, Belgien

VanOuytsel, K.
Small Angle Scattering Research at FZ Rossendorf
Vortrag an der TU Delft, 31.10.2002, Delft, Niederlande

VanOuytsel, K.; Böhmert, J.; Müller, G.; Roth, S.; Burghammer, M.
Investigations of the damage structure near the crack tip in Al-alloys by means of small angle x-ray scattering
Posterbeitrag zur XII. International Conference on Small Angle Scattering, 25.-29.08.2002, Venice, Italy

Viehrig, H.-W.
Application of Master-Curve Approach in RPV Integrity Assessment
Arbeitskreis Nucleare Werkstoffe des Paul Scherrer Instituts, Villingen, 28. November 2002

Weier, T.; Gerbeth, G.; Mutschke, G.; Lielausis, O.; Lammers, G.
Control of flow separation using electromagnetic forces
IUTAM Symposium on Unsteady Separated Flows, April 8-12, 2002, Toulouse, France

Weier, T.; Gerbeth, G.; Mutschke, G.; Lielausis, O.; Lammers, G.
Separation Control On A NACA 0015 Hydrofoil Using Lorentz Forces
12th European Drag Reduction Meeting, 18-20 April 2002, Herning, Denmark

Willschütz, H.-G.; Altstadt, E.; Sehgal, B. R.; Weiß, F.-P.
Simulation of Scaled Reactor Pressure Vessel Creep Failure Experiments
NUSIM 02, 11th annual Nuclear Societies Information Meeting, March 13 - March 15, 2002, Dresden

Willschütz, H.-G.; Altstadt, E.; Sehgal, B. R.; Weiß, F.-P.
Validation of a creep and plasticity model for French and German RPV-steels
OLHF Seminar 2002, Madrid, Spain, June 2002; OECD Nuclear Energy Agency

Xu, M.; Stefani, F.; Gerbeth, G.
Numerical experience with the integral equation approach to dynamos in finite domains
5. MHD-Tage, Forschungszentrum Rossendorf, 25-26. 11. 2002

FZR-Reports and other publications

Böhmer, B.; Konheiser, J.; Kumpf, H.; Noack, K.; Vladimirov, P.
Einfluss der Gammastrahlung auf die Schädigung von Druckbehältermaterialien und auf reaktordosimetrische Messungen
Wissenschaftlich-Technische Berichte / Forschungszentrum Rossendorf, FZR-356, Oktober 2002

Franke, E.; Hoppe, D.
Bestimmung der Aktivitätsverteilung in Gebinden mit geringfügig radioaktivem, Material unter Verwendung großflächiger, unkollimierter, feststehender Gamma-Szintillationsdetektoren
Wissenschaftlich-Technische Berichte / Forschungszentrum Rossendorf; FZR-347 Juni 2002

Grundmann, U.; Kliem, S.; Rohde, U.
Qualifizierung des Kernmodells DYN3D im Komplex mit dem Störfallcode ATHLET als fortgeschrittenes Werkzeug für die Störfallanalyse von WWER-Reaktoren - Teil 2
Wissenschaftlich-Technische Berichte / Forschungszentrum Rossendorf; FZR-357 Oktober 2002

Grunwald, G.; Höhne, T.; Kliem, S.; Prasser, H.-M.; Richter, K.-H.; Rohde, U.; Weiß, F.-P.
Versuchsanlage ROCOM zur Untersuchung der Kühlmittelvermischung in Druckwasserreaktoren - Ergebnisse quasistationärer Vermischungsexperimente
Wissenschaftlich-Technische Berichte / Forschungszentrum Rossendorf; FZR-348, Juli 2002

Hessel, G.; Heidrich, J.; Hilpert, R.; Kryk, H.; Roth, M.; Schmitt, W.; Seiler, T.; Weiß, F.-P.
Konzipierung und Erprobung des Zustandserkennungsverfahrens - Bedienungsanleitung von BIMS/MoSys (im Anhang)
Schlussbericht zum BMBF-Fördervorhaben 01RV9802, Forschungszentrum Rossendorf, Dezember 2002

Hessel, G.; Heidrich, J.; Hilpert, R.; Kryk, H.; Roth, M.; Schmitt, W.; Seiler, T.; Weiß, F.-P.
Umweltgerechte Prozessführung und Zustandserkennung in Chemieanlagen mit neuronalen Netzen - Teilvorhaben 2: Konzipierung und Erprobung des Zustandserkennungsverfahrens
Wissenschaftlich-Technische Berichte / Forschungszentrum Rossendorf, FZR-355, Dezember 2002

Hoppe, D.; Fietz, J.; Zippe, C.; Koch, D.
Röntgen-Tomographie mit Hilfe einer Elektronenstrahl-Schweißanlage
Wissenschaftlich-Technische Berichte / Forschungszentrum Rossendorf, FZR-361, November 2002

Mittag, S.; Grundmann, U.; Koch, R.; Semmrich, J.
Erzeugung und Nutzung von Bibliotheken von Zwei-Gruppen-Diffusionsparametern zur Berechnung eines KWU-Konvoi-Reaktors mit dem Reaktordynamik-Programm DYN3D
Wissenschaftlich-Technische Berichte / Forschungszentrum Rossendorf; FZR-346 April 2002

Neumann, J.; Schwarze-Benning, K.; Wack, T.; Deerberg, G.; Schlüter, S.; Hessel, G.; Heidrich, J.; Hilpert, R.; Kryk, H.; Roth, M.; Schmitt, W.; Seiler, T.; Weiß, F.-P.
Umweltgerechte Prozessführung und Zustandserkennung in Chemieanlagen: Teilvorhaben 1: Entwicklung und Validierung von Zustandserkennungswerkzeugen, Teilvorhaben2: Konzipierung und Erprobung des Zustandserkennungsverfahrens
Deutsche Forschungsberichte, UB/TIB Hannover, Elektronische Bibliothek, www.tip.uni-hannover.de, Report 01RV9801 (2002)S. 1-95; www.tip.uni-hannover.de, Report 01RV9802 (2002) S. 1-137

Pietruske, H.; Schaffrath, A.
Entwicklung und Erprobung einer Schnittstelle zwischen der Messdatenerfassungs- und Automatisierungssoftware DIAdem von National Instruments und der Wasser/Dampf Stoffwertedaten-Unterbibliothek Libl97
Wissenschaftlich-Technische Berichte / Forschungszentrum Rossendorf; FZR-352 August 2002

Spengler, C.; Allelein, H.-J.; Breest, A.; Chakraborty, A. K.; Erdmann, W.; Heitsch, M.; Kelmes, I.; Scheuerer, M.; Rastogi, A. K.; Willschütz, H.-G.; Latché, J.-C.
Simulation des Ausbreitungsverhaltens und der Kühlung einer Kernschmelze im Sicherheitsbehälter von LWR-Anlagen
Abschlussbericht, Gesellschaft für Anlagen- und Reaktorsicherheit (GRS (mbH), Reaktorsicherheitsforschung RS 1042, GRS-A-2959, Mai 2002

Stephan, I.; Böhmer, B.
Neutronendosimetrie im Bestrahlungsprogramm Rheinsberg II
Wissenschaftlich-Technische Berichte / Forschungszentrum Rossendorf, FZR-360, November 2002

Voskoboinikov, Roman E.
Analytical Description of Brittle-to-Ductile Transition in bcc Metals. Nucleation of dislocation loop at the crack tip
Wissenschaftlich-Technische Berichte / Forschungszentrum Rossendorf; FZR-344 März 2002

Walter, D.; Schaffrath, A.
Berechnung des Notkondensators des Integralreaktors CAREM
Wissenschaftlich-Technische Berichte / Forschungszentrum Rossendorf; FZR-351 August 2002

Willschütz, H.-G.; Altstadt, E.
Generation of a High Temperature Material Data Base and its Application to Creep Tests with French or German RPV-steel
Wissenschaftlich-Technische Berichte / Forschungszentrum Rossendorf; FZR-353 August 2002

Willschütz, H.-G.; Altstadt, E.
Integral Vessel Failure Experiment Analysis and Investigation of a Possible Vessel Support
Webseite der Arthur-und-Aenne-Feindt-Stiftung, Hamburg (www.feindt-stiftung.de)

Patents

Baldauf, D.; Prasser, H.-M.; Zschau, J.
Anordnung zur Messung der lokalen elektrischen Leitfähigkeit und Temperatur in Fluiden
DE 100 12 938 C2

Eckert, S.; Witke, W.; Gerbeth, G.
Einrichtung zur lokalen Bestimmung von Strömungsgeschwindigkeiten
DE 100 37 331 C1

Hoppe, D.
Anordnung zur tomographischen Bildrekonstruktion
DE 101 21 998 A1

Prasser, H.-M.; Schlüter, S.; Dudlik, A.
Anordnung zur Verhinderung unerwünschter Drücke beim Absperren oder Drosseln der Flüssigkeitsförderung in einer Rohrleitung
US 6 347 783 B1

Prasser, H.-M.; Zschau, J.
Anordnung zur messtechnischen Erfassung einer Projektion des Strahlungsabsorptionsvermögens eines periodisch veränderlichen Messobjekts
DE 101 17 569 C1
WO 02/080772 A1

Willschütz, H.-G.
Abstützvorrichtung für Stahlbehälter
DE 100 41 778 A1
WO 02/16821 A2

Willschütz, H.-G.
Steuereinrichtung für einen Kühlkreislauf
DE 100 41 779 C1
WO 02/17331 A1

Awards

Eberhard Altstadt, Hans-Georg Willschütz

Forschungspreis des FZR 2002

for their work on pressure vessel behaviour under severe accident conditions

Guests

Davidovskyy, Oleg
12.03. – 15.03.2002
Informationszentrum des Staatliches Komitees für kerntechnische Aufsicht der Ukraine/Ukraine

Magas, Konstyantyn Ivanovich
12.03. – 15.03.2002
Informationszentrum des Staatliches Komitees für kerntechnische Aufsicht der Ukraine/Ukraine

Smul's'ky, Volodymyr Volodymyrovich
12.03. – 15.03.2002
Kernkraftwerk Saporoshje/Ukraine

Bleydnykh, Vyacheslav Alexandrovich
12.03. – 15.03.2002
Kernkraftwerk Saporoshje/Ukraine

Manera, Annalisa
25.03. – 03.05.2002
07.10. – 06.12.2002
TU Delft, Niederlande

Anikeev, Dr. Andrei
01.04. – 30.06.2002
09.09. – 2.10.2002
Budker- Institut Novosibirsk/Russland

Borodkin, Gennady
14.04. – 05.05.2002
30.06. – 21.07.2002
03.11. – 02.12.2002
Gosatomnadzor Moskau/Russland

Melnikov, Prof. Vladimir Ivanovich
08.04. – 21.04.2002
16.09. – 22.09.2002
Novgorod Technical University/Russland

Ivanov, Vadim Vladimirovich
08.04. – 21.04.2002
Novgorod Technical University/Russland

Danitcheva, Irina
23.04. – 28.04.2002
Gosatomnadzor Moskau/Russland

Khrennikov, Dr. Nikolay
23.04. – 28.04.2002
Gosatomnadzor Moskau/Russland

Borodin, Dr. Vladimir
19.05. – 04.07.2002
17.11. – 07.12.2002
Kurchatov Institut Moskau/Russland

Adolphe, Xavier
08.06. – 13.06.2002
University Poitiers/Frankreich

Kozhevnikov, Dr. Aleksei
24.06. – 14.07.2002
Kurchatov Institut Moskau/Russland

Tsofin, Vladimir
30.06. – 07.07.2002
GIDROPRESS Podolsk/Russland

Ivanov, Prof. Dr. Alexandre
04.08. – 29.08.2002
Budker Institut Novosibirsk/Russland

Manturov, Dr. Guennadi
22.07. – 22.08.2002
RRC IPPE Obninsk/Russland

Plevachuk, Dr. Yuri
01.08. – 30.09.2002
Institut für Angewandte Physik der Staatlichen Ivan Franko Universität Lviv/Ukraine

Bagryansky, Dr. Petr
09.09. – 03.10.2002
Budker Institut Novosibirsk/Russland

Drobkov, Vladimir
16.09. – 21.09.2002
TU Nishny Novgorod/Russland

Gokhman, Prof. Alexander
05.10. – 16.11.2002
South Ukrainian Pedagogical University Ushinski Odessa/Ukraine

Reddy Vanga, Brahma Nanda
14.10.2002 – 11.01.2003
Purdue University West Lafayette/USA

Ganchenkova, Dr. Maria Gerasimova
21.11. – 10.12.2002
Moscow Engineering Physics Institute, Moskau/Russland

Gailitis, Prof. Dr. Agris
22.11. – 26.11.2002
Institute of Physics Riga/Lettland

Stefanova, Dr. Svetla
25.01. – 02.02.2002
20.07. – 02.08.2002
04.12. – 22.12.2002
Institut für Kernforschung und Kernenergie der Bulgarischen Akademie der Wissenschaften/Bulgarien

Kozmenkov, Yaroslav
07.12. – 14.12.2002
IPPE Obninsk/Russland

Efanov, Dr. Alexandre
07.12. – 14.12.2002
IPPE Obninsk/Russland

Baranaev, Dr. Yury
07.12. – 14.12.2002
IPPE Obninsk/Russland

Peinbergs, Janis
09.12. – 14.12.2002
Institute of Physics Riga/Lettland

Bucenieks, Imants
09.12. – 14.12.2002
Institute of Physics Riga/Lettland

Yakush, Sergey
10.12. – 14.12.2002
Elektrogorsk Research and Engineering Centre/Russland

Melnikov, Prof. Vladimir
10.12. – 14.12.2002
TU Nishny Novgorod/Russland

Myasnikov, Andrey
10.02. – 23.03.2002
22.07. – 01.09.2002
Kurchatov Institut Moskau/Russland

Rogov, Dr. Anatoli
20.05. – 19.08.2002
Vereinigtes Institut für Kernforschung Dubna/Russland

Rjevski, Semen
23.05. – 06.06.2002
NIIEFA St. Petersburg/Russland

Grants, Dr. Ilmars
06.09. – 09.10.2002
Institute of Physics Riga/Lettland

Meetings and workshops

Kick-off meeting EU-Projekt VALCO
Rossendorf, 24. - 25.01.2002

Betriebliche Fernüberwachung ukrainischer Kernkraftwerke
Rossendorf, 12. – 15.03.2002

OECD INRC Workshop
Rossendorf, 28. – 30.05.2002

Use of magnetic fields in crystal growth
Riga (Latvia) , June 13-14, 2002

RSK-Ausschusssitzung
Rossendorf, 26.06.2002

EU-Meeting IMPAM
Rossendorf, 03. – 04.09.2002

Fast Neutron Physics – Internationaler Workshop
Rossendorf, 05.- -07.09. 2002

5. Workshop Messtechnik
Rossendorf, 18. – 20.09.2002

EU-Meeting NACUSP
Rossendorf, 28. – 29.11.2002

5. MHD-Tage Dresden
Rossendorf, 25. – 26.11.2002

Seminars of the Institute

Dr. K. van Ouytsel
Messung der inneren Reibung – Eine Methode zur Untersuchung des Einflusses der Bestrahlung auf Reaktordruckbehälterstähle
17.01.2002

Dr. F. Stefani
Das inverse Problem der Magnetohydrodynamik - Theorie und Anwendung
07.02.2002

Dr. E. Altstadt, H.-G. Willschütz
Modelle für Kühlung und Krustenbildung in einer ausgebreiteten Kernschmelze
21.02.2002

Dr. U. Grundmann
Nachrechnung einer Transiente mit Turbinenschnellschluss an einem Siedewasserreaktor mit DYN3D
21.03.2002

M. Große (PSI Würenlingen)
Materialanforderungen für Flüssigmetall-Spallationstargets
04.04.2002

Dr. Westphal, Dr. Lade (Siemens Axiva GmbH und Co. KG)
Ermittlung sicherheitsrelevanter Kenngrößen verfahrenstechnischer Prozesse und Auslegung von Druckentlastungseinrichtungen – Aktivitäten der Siemens Axiva
12.04.2002

S. Kliem
Experimente zur Kühlmittelvermischung unter dem Einfluss von Dichteunterschieden an der Versuchsanlage ROCOM
18.04.2002

Dr. Altstadt, Dr. Galindo, C. Beckert
Auslegung eines Neutronen-Produktions-Targets an ELBE
23.04.2002

Dr. Gerbeth
Die FZR-Projekte im Sonderforschungsbereich 609 „Elektromagnetische Strömungs-beeinflussung in Metallurgie, Kristallzüchtung und Elektrochemie“
02.05.2002

Prof. Kessler (Karlsruhe)
Transmutation bzw. Zerstörung von Plutonium und minoren Aktiniden des radioaktiven Abfalls durch nukleare Reaktoren
13.06.2002

M. Kliem
Messung von Geschwindigkeitsfeldern in Stabbündeln und CFD-Simulation mit dem Code CFX
27.06.2002

Dr. Dzugan
Evaluation of the residual service life of Shinkansen wheel set
29.08.2002

G. Poss, J. Allelein (Becker Technologies)
Sicherheitsforschung in Deutschland zu Containmentfragen
02.09.2002

C. Beckert
Teilchenflussberechnungen zur Konzeption einer Photoneutronenquelle für Flugzeit-Experimente zur Messung von Neutronenwirkungsquerschnitten an der Strahlungsquelle ELBE
12.09.2002

Dr. J. Zschau, T. Werner
Empfindlichkeitsuntersuchungen am Gittersensor für Objekte mit kleineren Durchmessern als die Maschenweite
29.09.2002

T. Weier
Strömungskontrolle mit oszillierenden Lorentzkräften
10.10.2002

A. Manera (IRI Delft), Dr. Schäfer
Experimental and analytical investigation of flashing-induced natural circulation instabilities
30.10.2002

Dr. M. Werner
Simulation des Teilentlastungsverfahrens zur Risswiderstandsbestimmung mit Finite-Element-Rechnungen
21.11.2002

J. Konheiser
TRAMO-NG: Ein Monte-Carlo Programmsystem zur Berechnung von Neutronen- und Gammafluenzen in der Reaktordosimetrie
05.12.2002

Dr. S. Eckert, V. Galindo, W. Witke
Aluminium-Feinguss mit Magnetfeldkontrolle der Zuströmung
19.12.2002

Lecture courses

Frank-Peter Weiß
Zuverlässigkeit und Sicherheit technischer Systeme
TU Dresden, Fakultät Maschinenwesen
SS 2002 und WS 2002

Udo Rindelhardt
Erneuerbare Energien I und II
Universität Leipzig, Fakultät für Physik und Geowissenschaften
SS 2002 und WS 2002

Departments of the Institute

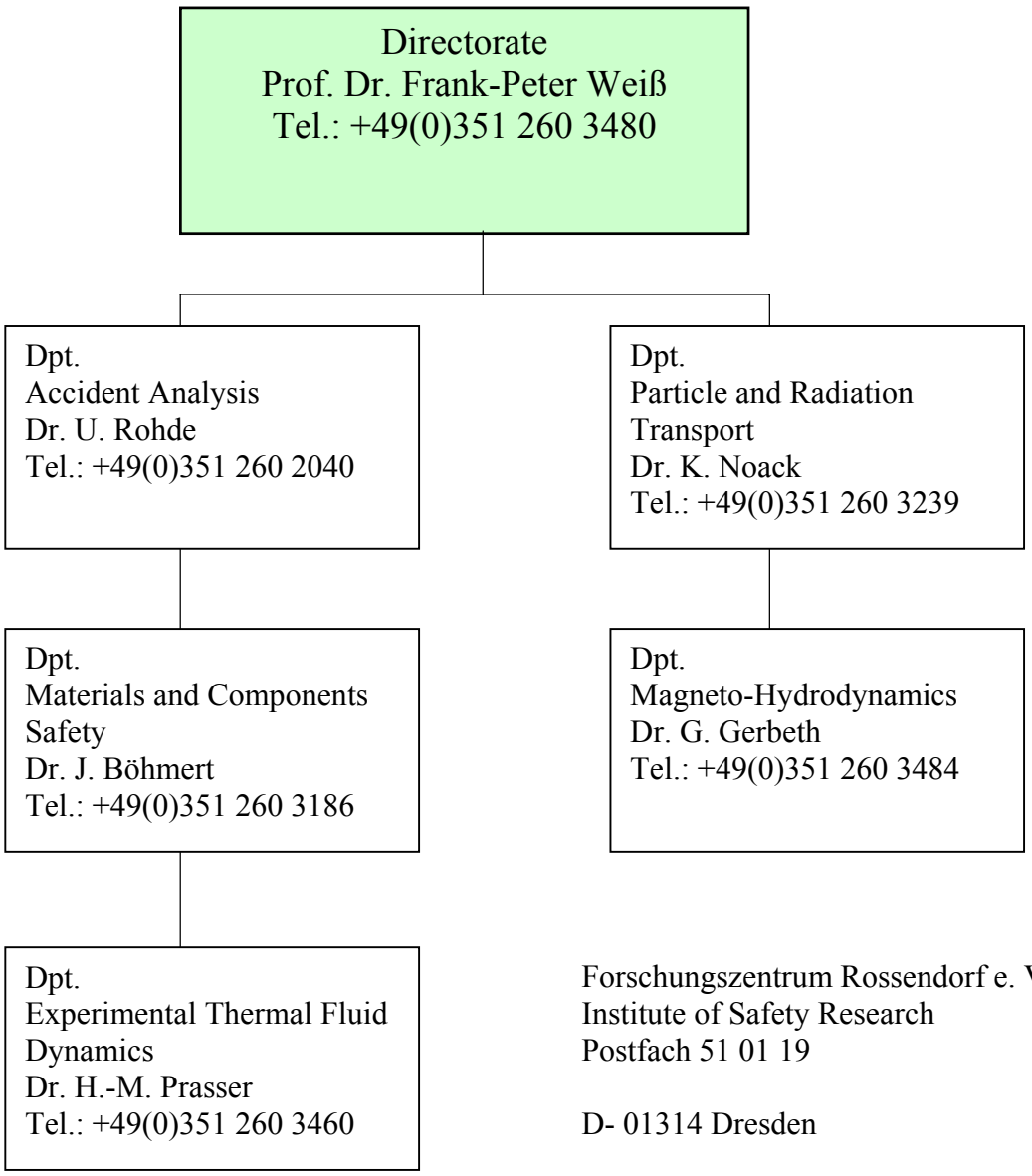

Forschungszentrum Rossendorf e. V.
Institute of Safety Research
Postfach 51 01 19

D- 01314 Dresden

Personnel

Director: Prof. Dr. F.-P. Weiß

Scientific Staff

Altstadt, Eberhard Dr.
Beckert, Carsten
Beyer, Matthias
Böhmer, Bertram
Böhmert, Jürgen Dr.
Böttger, Arnd
Carl, Helmar Dr.
Cramer, Andreas Dr.
Eckert, Sven Dr.
Fietz, Jürgen Dr.
Galindo, Vladimir Dr.
Gerbeth, Günter Dr.
Grahn, Alexander
Grants, Ilmars Dr.
Grundmann, Ulrich Dr.
Grunwald, Gerhard Dr.
Günther, Uwe Dr.
Gundrum, Thomas
Hampel, Uwe, Dr.
Hessel, Günter
Höhne, Thomas
Hoppe, Dietrich Dr.
Hüller, Jürgen Dr.
Kliem, Margarita
Kliem, Sören
Koch, Reinhard Dr.
Konheiser, Jörg
Kozmenkov, Yaroslav
Krepper, Eckhard Dr.
Krüssenberg, Anne-Kathrin Dr.
Kryk, Holger Dr.
Küchler, Roland Dr.
Lucas, Dirk Dr.
Mittag, Siegfried Dr.
Müller, Gudrun, Dr.
Mutschke, Gerd
Neumann, Hartmut Dr.
Noack, Klaus Dr.
Prasser, Horst-Michael Dr.
Rindelhardt, Udo PD Dr.
Rohde, Ulrich Dr.
Schaffrath, Andreas Dr.
Schäfer, Frank Dr.
Schmitt, Wilfried Dr.
Schütz, Peter
Shi, Yun-Mei
Stephan, Ingrid Dr.
Stefani, Frank Dr.
Ulbricht, Andreas
Viehrig, Hans-Werner Dr.
Weier, Tom
Werner, Matthias Dr.
Willschütz, Hans-Georg
Witke, Willy
Zschau, Jochen Dr.
Zippe, Cornelius Dr.
Xu, Mingtian

PhD Students

Krepel, Jiri
Salahura, Gheorge
Zhang, Chaojie

Technical Staff

Baldauf, Dieter
Behrens, Sieglinde
Berger, Torsten
Bombis, Doris
Borchardt, Steffen
Erlebach, Stephan
Forker, Klaus
Futterschneider, Hein
Kunadt, Heiko
Leonhardt, Wolf-Dietrich
Leuner, Bernd
Lindner, Klaus
Losinski, Claudia
Mansel, Catrin
Nowak, Bernd
Pietzsch, Jens
Richter, Annett
Richter, Henry
Richter, Joachim
Richter, Petra
Rott, Sonja
Russig, Heiko
Schleßiger, Heike
Schneider, Gisela
Skorupa, Ulrich
Tamme, Günter
Tamme, Marko
Walter, Denis
Webersinke, Steffen
Weiß, Rainer
Zimmermann, Wilfried